UNIVERSIDAD COMPLUTENSE DE MADRID
FACULTAD DE CIENCIAS FÍSICAS

TESIS DOCTORAL

Estudio de la radiopureza del argón subterráneo para DarkSide-20k e I+D+i en detectores basados en gases nobles para investigaciones de eventos raros

Underground argon radio-purity studies for DarkSide-20k and R&D on noble gas detectors for rare-events investigations

MEMORIA PARA OPTAR AL GRADO DE DOCTOR

PRESENTADA POR

Edgar Sánchez García

Directores

Pablo García Abia
Luciano Romero Barajas
Roberto Santorelli

Madrid

UNIVERSIDAD COMPLUTENSE DE MADRID

FACULTAD DE CIENCIAS FÍSICAS

TESIS DOCTORAL

Estudio de la radiopureza del argón subterráneo
para DarkSide-20k e I+D+i en detectores
basados en gases nobles para
investigaciones de eventos raros

Underground argon radio-purity studies for
DarkSide-20k and R&D on noble gas
detectors for rare-events investigations

MEMORIA PARA OPTAR AL GRADO DE DOCTOR

PRESENTADA POR

Edgar Sánchez García

DIRECTORES

Pablo García Abia

Luciano Romero Barajas

Roberto Santorelli

Underground argon radio-purity studies for DarkSide-20k and R&D on noble gas detectors for rare-events investigations

---

Estudio de la radiopureza del argón subterráneo para DarkSide-20k e I+D+i en detectores basados en gases nobles para investigaciones de eventos raros

Ph. D. Thesis submitted by

Edgar Sánchez García

for the degree of Doctor of Physics

Supervisors:

Pablo García Abia

Luciano Romero Barajas

Roberto Santorelli

Centro de Investigaciones Energéticas, Medioambientales y Tecnológicas

Facultad de Ciencias Físicas
Universidad Complutense de Madrid

Madrid, February 2021

¡Qué gran tónico sería para el novel observador
el que su maestro, en vez de asombrarlo
y desalentarlo con la descripción de las cosas
acabadas, le expusiera el pasado embrionario de
cada invención científica, la serie de errores
y tanteos que le precedieron, y los cuales
constituyen, desde el punto de vista humano,
la verdadera explicación de cada descubrimiento,
es decir, lo único que puede persuadirnos de que
el descubridor, con ser un ingenio esclarecido
y una poderosa voluntad, fue al fin y al cabo
un hombre como todos!

Santiago Ramón y Cajal

Agradecimientos

Cuando empecé la tesis hace ya más de 4 años no me imaginaba terminándola en estas circunstancias. Ha sido un trabajo duro llegar hasta aquí, pero muy enriquecedor y, sin lugar dudas, no podría haberlo hecho sin el apoyo de muchas personas. Espero poder recoger en las siguientes líneas a todas y todos, y si me olvido de alguien espero que me disculpe.

En primer lugar, quiero agradecer a mis directores Luciano, Pablo y Roberto por sus consejos y apoyo durante estos años. He tenido la suerte de aprender mucho de cada uno de ustedes y les estoy realmente agradecido por ello. Gracias por el tiempo dedicado a discutir y compartir resultados y por darme la oportunidad de participar en tantos congresos relevantes. También me gustaría dedicar unas palabras a Vicente, al cual considero mi cuarto director de tesis. Te agradezco enormemente todas las veces que me has animado para continuar en los momentos más complicados. Finalmente, quiero agradecerle a Rodrigo, José Manuel y Juanjo por su apoyo en todas las actividades de laboratorio durante estos años, así como a todo el personal del CIEMAT que ha facilitado mi día a día en este centro.

I would like to thank all the DarkSide members for their constant support and collaboration. I would like to give special thanks to people from the DArT, Proto-0 and Software working groups. It has been a pleasure to work together over the years and I wish you a successful future.

A lo largo de estos años, el resto de estudiantes de doctorado del CIEMAT se han convertido en mucho más que compañeras y compañeros de trabajo. Hemos compartido muchísimas experiencias dentro y fuera del despacho, y aunque no creo que sea capaz de mostrarles todo mi agradecimiento voy a intentarlo. Gracias a Manueliño, con quien he compartido muchas noches de cervezas, risas y discusiones sobre la vida. Otro enorme gracias para Martín, aunque ambos queremos ver el mundo arder, creo que tu apoyo ha sido fundamental estos años. Las risas que nos hemos echado juntos tienen un valor incalculable. Por supuesto, otro enorme agradecimiento para Diana. Hemos hecho muchos viajes juntos (algunos accidentados), me has acogido en fin de año y siempre has sabido animarme con una sonrisa cada vez que te visitaba en tu despacho. Por todo ello te estoy enormemente agradecido. Grazie a Chiara, per tutte le nostre discussioni sull'argon, i divertenti viaggi in macchina e i tuoi deliziosi tiramisù. E anche se non ti piace la pizza con l'ananas e pensi che non si possa aggiungere la panna alla carbonara, sono molto affezionato a te. Otro gracias para Ananana, aunque me meta mucho contigo sabes que te tengo mucho cariño. Además, nunca será lo mismo ir a una casa rural sin ti. Muchas gracias a Mab por descubrirme tantas cosas nuevas en la vida y todos los buenos ratos que hemos pasado. Gracias a Irene (Hilaria) por animarme todas las mañanas son tu optimismo. Muchas gracias a Héctor, por todos los planes que hemos hecho y por entender mis palabrejas raras guanches. Espero que sigamos viéndonos durante

muchos años cuando estemos en Tenerife. Gracias a Iker por encargarte siempre de todas las peleas con el edificio 1, creo que no podríamos tener un mejor representante para los estudiantes. Gracias a Miguel Cárdenas y a MA por sus sabios consejos siempre. Muchas gracias a Iván (Barbas) por todas las risas durante estos años. Gracias a Mar, por tantas anécdotas divertidas y a José por las discusiones sobre argón que hemos tenido. Gracias a Carmen y a Molero por formar parte de tantos planes divertidos durante estos años, aunque algunos me hayan traumatizado de por vida como el del ViñaRock. Gracias a Sergio y a Adri por las amenas conversaciones dentro y fuera del despacho. Gracias a Iván (Muchachito) por todas las noches de fiesta perreando mobiliario urbano. Gracias a Juan, a Irene (CTA) y a David, por todas las charlas durante el café. También quería agradecer a Julia, te he cogido un gran aprecio, aunque hayas llegado hace muy poco. Al resto de estudiantes nuevos del CIEMAT: Ludovico, Rodrigo... les deseo todo lo mejor y espero que aprovechen estos años no solo para aprender sino para divertirse tanto como lo he hecho yo.

Quiero agradecer a mis amigos Joel, Emilio, Rafa, Nerea y Aythami, que han sido un apoyo desde mucho antes que empezara esta aventura. Especialmente quiero agradecer a Bárbara, aunque te hayas incorporado casi al final de esta etapa, tu apoyo incondicional ha sido increíble. Soy una persona muy afortunada por haberte podido tener al mi lado durante este tiempo y estoy seguro de que el futuro nos deparará cosas aún mejores.

Finalmente, este párrafo se lo quiero dedicar a las dos personas más importantes de mi vida, mis padres. Quiero agradecerle a mi padre Domingo, por inspirarme durante toda la vida, tú eres la razón de que haya aprendido a apreciar la ciencia de la forma en que lo hago. Mi mayor agradecimiento es hacia mi madre Olgui, quien ha sido el mayor apoyo durante toda mi vida. De verdad eres una inspiración constante, me has aportado la mayoría de valores que tengo y cada día intento parecerme un poco más a ti. Todo esto no podría haberlo logrado sin ustedes, les quiero mucho a ambos.

Quiero terminar con una frase de uno de mis mayores referentes en el mundo de la física, Richard Feynman: “As I get older, I realize being wrong is not a bad thing like they teach you in school. It is an opportunity to learn something”.

Contents

Summary **15**

Resumen **17**

Introduction **21**

1 Dark matter direct detection **23**
1.1 Dark matter evidences and candidates 23
1.2 WIMP dark matter searches 28
1.2.1 Direct detection 29
1.3 Sensitivity of direct detection experiments 33
1.4 Direct searches status 36
1.5 Sensitivity prospects 38

2 Noble liquid detectors for rare event searches: DarkSide-20k **41**
2.1 Noble liquid detectors 41
2.2 Liquid argon time projection chambers 44
2.2.1 Light and charge propagation 46
2.3 Review of the VUV scintillation light detection technologies 48
2.4 DarkSide-20k experiment 51

3 DArT, a detector for measuring the ^{39}Ar depletion factor **57**
3.1 Underground argon in DarkSide-20k 57
3.2 The DArT experiment 58
3.2.1 Photo-electronics 61
3.2.2 Cryogenics 61
3.3 Signal and background studies 63
3.4 Light response simulation 66
3.5 Simulation of the electronic response 68
3.6 Sensitivity to the **^{39}Ar** signal 70
3.7 Systematic uncertainties 70
3.8 Conclusions 74

4 Construction and commissioning of DArT **75**
4.1 DArTeye characterization 75
4.1.1 Determination of the I-V curves 76
4.1.2 Measurement of the dark currents 77
4.1.3 Characterization of the PDMs with a LED source 80
4.2 DArT commissioning on surface 82

4.3 Characterization with atmospheric argon 83
4.3.1 Energy calibration with the ^{222}Rn decay chain 88
4.4 Upgrade of DArT detector: EDArT 90

5 Spectroscopic studies with argon and xenon gas at high pressure 93
5.1 Brief review of the scintillation in noble gases 94
5.2 Experimental setup 96
5.3 Wavelength-resolved UV/VUV emission with a ^{241}Am source 99
5.4 Spectroscopic analysis of the argon scintillation as a function of the gas pressure 102
5.5 Electric field dependence of the scintillation and spectroscopic studies of the electron-ion recombination 107
5.6 First evidence of the third continuum emission with a β source 108
5.7 Pulse shape discrimination of α and β events in argon gas 110
5.8 Spectroscopic studies with xenon gas 111
5.8.1 Preliminary results with α and β sources 113

6 Experimental aspects of the positive ion current on large size Argon detectors 117
6.1 Secondary recombination in liquid argon detectors 118
6.1.1 Underground TPC 120
6.1.2 Surface TPC 122
6.1.3 Gas amplification 126
6.2 The ARION experiment 127
6.2.1 Test with a continuous ion current 129
6.2.2 Test with ion pulses 132

Conclusions 137

List of Figures

1.1 Galaxy rotation curve . . . 25
1.2 Bullet cluster image . . . 26
1.3 AMS excess in the positron flux . . . 29
1.4 CTA predicted sensitivities for dark matter searches . . . 30
1.5 Differential recoil spectrum for different target materials . . . 31
1.6 Form factor correction as a function of the recoil energy . . . 34
1.7 Cross section for different energy thresholds computed curves . . . 35
1.8 Cross section for different v_{esc} and ρ_χ values . . . 36
1.9 Sensitivity plot for spin-independent WIMP searches . . . 37
1.10 Sensitivity of current and planned spin-independent direct dark matter detection experiments . . . 39

2.1 Dual-phase electroluminescence LAr-TPC scheme . . . 45
2.2 VUV attenuation length dependence of the concentration of impurities in LAr . . . 46
2.3 Drift velocity as a function of the electric field . . . 47
2.4 Photo of PMT and SiPM . . . 49
2.5 Photoelectron spectrum of PMT and SiPM . . . 50
2.6 Light reflectance in the VUV range for different materials . . . 51
2.7 . . . 52
2.8 DarkSide-20k photodetection module and motherboard . . . 53
2.9 Proto-0 photo . . . 55

3.1 DArT detector in ArDM cryostat . . . 59
3.2 Sketch of the inner structure of DArT . . . 60
3.3 Inner acrylic structure lateral view. Top acrylic cap and support disk with the photo-detector module installed . . . 60
3.4 Images of the front and back sides of the front-end boards housing the SiPM for light readout . . . 61
3.5 Schematics of the gas handling and cryogenic system for the operation of DArT . . . 62
3.6 DArT geometry in G4DS . . . 64
3.7 Internal and external γ background spectra in ArDM and DArT expected per week . . . 64
3.8 Total background and contribution of main components . . . 66
3.9 Expected untagged background events in DArT with the lead shield and without in one month of data taking . . . 67
3.10 Collection uniformity in DArT . . . 68
3.11 Simulated pulses for α and β events assuming a response time of 8 ns 69

3.12 Simulated pulses for α and β events assuming a response time of 540 ns 69
3.13 DArT saturation and linearity 70
3.14 Photo-electron spectra corresponding to one week of data taking, for an ^{39}Ar $DF = 10$ without lead shield and for $DF = 1400$ with lead shield 71
3.15 Uncertainty expected per week for different argon depletion factors . 71
3.16 DArT calibration 73

4.1 Experimental setup for DArTeye characterization 76
4.2 Schematics of the DArTeye board 76
4.3 I-V curve for DArTeye at 300 K and 77 K 77
4.4 Typical dark current pulse detected on a PDM 78
4.5 Distribution of the RMS of the signals calculated in the pre-trigger region 78
4.6 DArTeye SPE distribution 79
4.7 DArTeye SPE maximum and integrated charge fit 80
4.8 Average value of the Gaussian fitted with respect to the number of photoelectrons detected for the maximum height of the pulse and the integrated charge with a 7 V OV 80
4.9 Average pulse, generated using the LED with a 10 ns wide excitation signal 81
4.10 Gain of maximum pulse height at different overvoltage values 82
4.11 Example of a saturated pulse induced by the LED 82
4.12 Scheme of the DArT cryogenic system for surface tests 83
4.13 Temperature-pressure equilibrium curve for LN_2 84
4.14 Setup of the DArT cryogenic tests on the surface during the filling operations 84
4.15 DArT saturation and PDM integrated charge 85
4.16 DArT liquid argon purity 86
4.17 Pulse shape discrimination in LAr 86
4.18 Typical pulse detected for an α-decay, a *beta*-decay and a cosmic muon 87
4.19 BiPo coincidence 88
4.20 Light yield estimated with the different α-peaks of the ^{222}Rn chain. Dependence of the light yield with the mylar reflectivity 89
4.21 DArT energy spectrum 90

5.1 High pressure experimental setup 97
5.2 Light transmission as a function of wavelength, for the windows and filters used in the experiment. Quantum efficiencies of the PMTs used in the detector. 98
5.3 Integrated charge signal of the four different PMTs used in the experiment. Asymmetry between the two R7378 PMTs for different pressures 99
5.4 Typical Ar scintillation signals from 5.5 MeV α-particle interaction detected in three spectral regions, with argon gas at 1.5 bar 100
5.5 Pulse shapes of the argon scintillation signals averaged over 3×10^4 events per PMT type, registered with the ^{241}Am source in Ar at 1.5 bar 101

5.6 Integrated charge spectrum obtained in the PMT with the wavelength shifter compared with the sum of the spectra in the UV2 and UV3 regions. Average argon pulse detected with the TPB and sum of the UV2 and UV3 pulses at 1.5 bar . . . 102
5.7 Mean α signal detected in the different spectral ranges as a function of the pressure. Variation with the pressure of the fast component (first 90 ns) of the argon scintillation . . . 103
5.8 Typical Ar scintillation signals from 5.5 MeV α-particle interaction detected in three spectral regions, for argon gas at 16 bar . . . 104
5.9 Average signals in the 1.5-16 bar pressure range for the UV2 and UV3 regions . . . 105
5.10 Fit of argon scintillation pulse at 1.5 bar in the UV3 region. Dependence of the emission time constant with pressure in the 1.5 to 16 bar range . . . 105
5.11 Fit of argon scintillation pulse at 1.5 bar and 16 bar in the UV2 region. 106
5.12 Dependence of the excimer formation time constant and singlet de-excitation lifetime with pressure. Dependence of the luminescence with the electric field intensity in the UV2 and UV3 regions . . . 107
5.13 Mean pulse shape of the UV2 and UV3 signals with and without electric field with argon at 10 bar . . . 108
5.14 Integrated charge for events collected without and with the ^{90}Sr/Y β source . . . 109
5.15 Typical Ar scintillation signals detected for a β event in two spectral regions, with argon gas at 20 bar . . . 110
5.16 F_{90} respect to the total integrated charge with ^{241}Am and ^{90}SrY sources . . . 111
5.17 Fprompt respect to the total integrated charge with the TPB-PMTs at 21 bar . . . 111
5.18 High pressure xenon gas experimental setup . . . 112
5.19 Photo of the 4 R7378A phototubes in the PTFE support structure and drift field cage . . . 113
5.20 Typical Xe scintillation signals from 5.5 MeV α-particle interaction detected in two spectral regions, with xenon gas at 2 bar . . . 113
5.21 Relative intensity of the ^{241}Am peak in the UV and UV4 ranges as a function of the electric field. . . . 114
5.22 Relative intensity of the ^{90}Sr/Y mean value in the UV and UV4 ranges as a function of the electric field. . . . 115

6.1 Configuration of the drift lines near a positive ion placed at (0,0) for a nominal drift field of 1 kV/cm . . . 119
6.2 Recombination probability in underground TPC . . . 123
6.3 Recombination probability in surface TPC with vertical and horizontal electric field . . . 125
6.4 Design and photo of the ARION internal structure . . . 127
6.5 Photo of the two level sensors installed in ARION. Filling rate estimated with both sensors . . . 128
6.6 ARION geometry implemented in COMSOL . . . 129
6.7 Simulation of the electric field in detector with argon gas . . . 130

6.8 Simulation of the electric field in detector filled with liquid argon . . 131
6.9 Evolution of currents measured in the plane, cathode, anode, T-SR and B-SR 131
6.10 Mean value of current generated at cathode and anode for different initial vacuum conditions 132
6.11 Collection efficiency respect to the LAr level 133
6.12 Circuit to generate the ion pulse at the needle. Double coplanar grid at the cathode 133
6.13 Average signal introduced to the anode and detected at the cathode. Average signal detected at the cathode with a drift field of 300 V/cm and without it 135
6.14 Drift velocity of the ions in argon gas at room temperature with respect to the intensity of the drift field 135

List of Tables

2.1 Comparison of physical properties of noble liquids 42

3.1 Radio-impurities of materials and external fluxes 65

4.1 Number of signal events, background events and S/B in a week of operation for DArT and EDArT, operating in single and dual-phase . 91

5.1 Definition of the UV2 and UV3 spectral ranges 99

Summary

There are strong pieces of evidence suggesting that ordinary matter, composed by baryons and leptons, is only the 5 % of the energy-matter content of the Universe. It is necessary to include two new components to account for all the energy-matter density in the Universe and thus explain astrophysical observations on a cosmological scale. The first one is a new, collision-less and non-luminous type of matter, called dark matter (DM), whose interactions with ordinary matter are mainly through the gravitational force. The second one is a uniformly distributed component called dark energy, which is thought to be responsible for the accelerated expansion of the Universe. According to the latest PLANCK satellite data, the dark energy accounts for 69 % of the content of our Universe and the dark matter for the 27 % [1]. The nature of dark matter and dark energy is one of the most relevant problems in current physics.

Although there are different possible explanations for the origin of dark matter component, a very attractive hypothesis comes from particle physics in the form of thermal relic particles produced during the Big Bang that naturally freeze-out with the right abundance and that are present now in the halos surrounding the galaxies. These are the so-called weakly interacting massive particles (WIMPs), which do not have electromagnetic charge and only interact via weak or gravitational force.

During the last years, different experiments have tried to detect this hypothetical particle, establishing lower interaction-rate limits and rejecting the different hypotheses. The time projection chambers (TPCs) based on noble elements have established the strongest dark matter limits for WIMPs with masses above 5 GeV/c^2, demonstrating its potential for dark matter searches.

This thesis was developed within the DarkSide-20k experiment [2], a TPC with a detection volume of 50 tonnes of liquid argon. The sensitivity limits of the experiment for an exposure of 200 tonnes$\times$ year are at cross sections of 8 $\times 10^{-48}$ cm^2 and 7 $\times 10^{-47}$ cm^2 for WIMP masses of 1 TeV/c^2 and 10 TeV/c^2 respectively. DarkSide-20k will dominate the spin-independent searches in the 10 GeV/c^2 to 100 TeV/c^2 mass range for WIMPs over the next decade.

One of the keys to obtaining these challenging results is the use of underground argon (UAr). The isotope ^{39}Ar produces a β decay with an end-point of 564 keV. It is found in atmospheric argon (AAr) at a rate of 1 Bq/kg. It is produced mainly by the interaction of cosmic rays with argon atoms. For this reason, the argon extracted from underground wells has a significantly smaller quantity of this isotope. The DarkSide-50 experiment was the first to operate with UAr and measured an activity of 0.73 mBq/kg of ^{39}Ar [3]. However, the high levels of ^{85}Kr (2.81 mBq/kg) measured in this experiment would indicate a possible air contamination along the complex process of argon extraction and purification.

A crucial point for the DarkSide collaboration is the characterization of the

different argon batches that will be used to fill DarkSide-20k. A novel detector, called DArT, will measure small samples of UAr (approximately 1 L) in short periods of time (few days) with an error below 10%. DArT will be installed in the Canfranc Underground Laboratory (LSC) on summer 2021.

In this work, an ^{39}Ar activity equal to or less than that measured by DarkSide-50 is assumed as the baseline. The number of signal events expected is very small and it is necessary to reduce the number of background events substantially. For this reason, DArT will be installed inside Argon Dark Matter (ArDM), a detector of 1 tonne of liquid argon, which will act as an active veto and at the same time will provide the necessary cryogenic conditions for the experiment.

The CIEMAT-DM group plays a major role in the design and construction of-DArT in ArDM. In particular, my work has consisted in optimizing the DArT design with the aim of achieving the highest possible sensitivity, within the specifications required by the DarkSide-20k experiment. In this context, I have developed several simulations using tools such as GEANT4. The main results of this work have been the basis of the DArT Technical Design Report [4] presented and approved by the LSC Scientific Committee in 2019.

The installation of DArT in the LSC was planned in 2020, but due to the impact of COVID-19 it has been delayed until 2021. With the aim of minimising the impact of the pandemic on the experiment time schedule, the commissioning of DArT on surface has been carried out at CIEMAT. Specifically, I have participated in the detector assembly, the first data collection and their corresponding analysis. In addition, I have been in charge of the characterization of the photodetection modules (PDMs) produced for DArT.

Apart from the work done within the DarkSide collaboration, I have been involved in two other lines of research related to R&D for liquid argon detectors. The first one is the development of a photon wavelength particle detector, to study a novel particle discrimination technique in noble gases. I have successfully built and operated this high pressure argon gas chamber up to 21 bar, studying features of the argon scintillation which are relevant for a spectroscopic identification of the particle interactions.

The second research line is related to the study of the effects produced by the positive ions produced in large liquid argon detectors. In a time projection chamber, the accumulation of a volume positive charge is the effect of the large difference between the drift velocity of the electrons and the five orders of magnitude slower ions. This space charge is expected to distort the electric field and to produce secondary recombination of ions and electrons. I have performed theoretical calculations of the secondary recombination probabilities expected in liquid argon detectors operating in single and dual phase, both on the surface and underground. In addition, I have built a detector to study the effects associated with space charge. In particular, I have investigated the ion feedback from the gas to the liquid phase and measured the drift velocity of the ions in gaseous argon.

The most relevant results of this thesis are published in high impact journals [5, 6]. My thesis has been financed by the Ministry of Economy and Competitiveness through the MDM-2015-0509-16-3 support.

Resumen

Hay evidencias significativas que sugieren que la materia ordinaria compuesta por bariones y leptones, representa solo el 5 % del contenido de energía-materia del Universo. Para dar cuenta de toda la densidad de energía-materia y explicar las observaciones astrofísicas a escala cosmológica es necesario incluir dos nuevos componentes. La primera es un nuevo tipo de materia, no luminosa y que no sufre colisiones, llamada materia oscura (DM), cuyas interacciones con la materia ordinaria son principalmente a través de la fuerza gravitatoria. La segunda es una componente uniformemente distribuida llamada energía oscura, que se le atribuye ser responsable de la expansión acelerada del Universo. Según los últimos datos del satélite PLANCK, la energía oscura representa el 69 % del contenido de nuestro Universo y la materia oscura el 27 % [1]. La naturaleza de la materia oscura y la energía oscura es uno de los problemas más relevantes en la física actual.

Aunque hay diferentes explicaciones posibles para el origen de la materia oscura, una hipótesis muy atractiva proviene de la física de las partículas en forma de reliquias térmicas producidas durante el Big Bang, que se desacoplan de forma natural, con la abundancia adecuada y están presentes actualmente en los halos que rodean a las galaxias. Se trata de las llamadas partículas masivas débilmente interactuantes (WIMPs), que no tienen carga electromagnética y sólo interactúan a través de la fuerza débil o gravitatoria.

Durante los últimos años, diferentes experimentos han tratado de detectar esta hipotética partícula, estableciendo límites más bajos para la sección eficaz y rechazando varias hipótesis propuestas. Las cámaras de proyección temporal (TPCs), basadas en elementos nobles han establecido los límites más fuertes para WIMPs con una masa superior a 5 GeV/c^2, demostrando su potencial para la detección de materia oscura.

Esta tesis se ha realizado dentro del experimento DarkSide-20k [2], una TPC con un volumen de detección de 50 toneladas de argón líquido. Los límites de sensibilidad del experimento para una exposición de 200 toneladas$\times$ año son secciones eficaces de 8 $\times 10^{-48}$ cm^2 y 7 $\times 10^{-47}$ cm^2 para masas de 1 TeV/c^2 y 10 TeV/c^2 respectivamente. DarkSide-20k dominará las búsquedas independientes de spin en el rango de masas para los WIMPs de 10 GeV/c^2 a 100 TeV/c^2 durante la próxima década.

Una de las claves para obtener estos desafiantes resultados es el uso de argón subterráneo (UAr). El ^{39}Ar es un isótopo que produce un decaimiento β con un end-point de 564 keV. Se encuentra a razón de 1 Bq/kg en el argón atmosférico. Se produce principalmente en el argón atmosférico por la interacción de rayos cósmicos con los átomos de argón. Por esto, el argón extraído de pozos subterráneos tiene una cantidad significativamente menor de este isótopo. El experimento DarkSide-50 fue el primero en operar con UAr y midió una actividad de 0.73 mBq/kg de ^{39}Ar [3]. Sin embargo, los altos niveles de ^{85}Kr (2.81 mBq/kg) medidos en este experimento,

podrían indicar una posible contaminación de aire a lo largo del complejo proceso de extracción y purificación del argón.

Un punto crucial para la colaboración DarkSide es la caracterización de las distintas remesas de argón que serán utilizadas para llenar DarkSide-20k. Un novedoso detector llamado DArT medirá pequeñas muestras de UAr (aproximadamente 1 L) en cortos periodos de tiempo (pocos días) con un error menor al 10 %. DArT será instalado en el Laboratorio Subterráneo de Canfranc (LSC) en verano de 2021.

En este trabajo, se asume como referencia una actividad de ^{39}Ar igual a la medida por DarkSide-50 o incluso menor. El número de eventos de señal esperado es muy pequeño y es necesario reducir el número de eventos de fondo dramáticamente. DArT será instalado dentro de Argón Dark Matter (ArDM), un volumen de 1 tonelada de argón líquido, que actuará como veto activo y al mismo tiempo proporcionará las condiciones criogénicas necesarias para el experimento.

El grupo de materia oscura del CIEMAT juega un papel principal en el diseño y construcción de DArT. En particular, mi trabajo ha consistido en la optimización del diseño de DArT con el objetivo de alcanzar la sensibilidad más alta posible dentro de las especificaciones requeridas por el experimento. Para ello, he desarrollado diversas simulaciones utilizando herramientas como GEANT4. Los resultados principales de este trabajo han sido la base del DArT Technical Design Report [4] presentado y aprobado por el comité científico del LSC en 2019.

La instalación de DArT en el LSC estaba prevista para finales de 2020, pero debido al impacto de la COVID-19 se ha retrasado hasta 2021. Con el objetivo de minimizar el impacto de la pandemia sobre la planificación temporal del experimento, se han realizado pruebas en superficie en el CIEMAT. Concretamente, he participado en el montaje, en la primera toma de datos y en su correspondiente análisis. Además, he sido responsable de la caracterización de los módulos de fotodetección (PDMs) producidos para DArT.

Aparte del trabajo realizado dentro de la colaboración DarkSide, he estado involucrado en otras dos líneas de investigación relacionadas con I+D+i para detectores de argón líquido. La primera es el desarrollo de un detector de partículas sensible a la longitud de onda, con el objetivo de estudiar una novedosa técnica de discriminación de partículas en gases nobles. He construido y operado con éxito esta cámara de alta presión con argón gas hasta 21 bar, estudiando las características de centelleo que son relevantes para una identificación espectroscópica de las interacciones de las partículas.

La segunda línea de investigación está relacionada con el estudio de los efectos producidos por los iones positivos acumulados en los grandes detectores de argón líquido. En una cámara de proyección temporal, la acumulación de un volumen de carga positiva, se produce como efecto de la gran diferencia entre la velocidad de deriva de los electrones y los iones, cinco órdenes de magnitud más lentos. Se espera que esta carga espacial distorsione el campo eléctrico y produzca recombinación secundaria de iones y electrones. He realizado cálculos teóricos sobre las probabilidades de recombinación secundaria en detectores de argón líquido operando en fase única y doble, tanto en superficie como bajo tierra. Además, he construido un detector para investigar efectos asociados con la carga espacial de forma específica. En concreto, he estudiado la retroalimentación de iones desde la fase gaseosa a la líquida y he medido la velocidad de deriva de los iones en argón gaseoso.

Los resultados más relevantes de esta tesis están publicados en varias revistas

de alto impacto [5, 6]. Mi tesis ha sido financiada por el Ministerio de Economıa y Competitividad a través de la ayuda MDM-2015-0509-16-3.

Introduction

There are strong pieces of evidence suggesting that ordinary matter, composed by baryons and leptons, is only the 5 % of the energy-matter content of the Universe. It is necessary to include two new components to account for all the energy-matter density in the Universe and thus explain astrophysical observations on a cosmological scale. The first one is a new, collision-less and non-luminous type of matter, called dark matter (DM), whose interactions with ordinary matter are mainly through the gravitational force. The second one is a uniformly distributed component called dark energy, which is thought to be responsible for the accelerated expansion of the Universe. According to the latest PLANCK satellite data, the dark energy accounts for 69 % of the content of our Universe and the dark matter for the 27 % [1]. The nature of dark matter and dark energy is one of the most relevant problems in current physics.

Although there are different possible explanations for the origin of dark matter component, a very attractive hypothesis comes from particle physics in the form of thermal relic particles produced during the Big Bang that naturally freeze-out with the right abundance and that are present now in the halos surrounding the galaxies. These are the so-called weakly interacting massive particles (WIMPs), which do not have electromagnetic charge and only interact via weak or gravitational force.

During the last years, different experiments have tried to detect this hypothetical particle, establishing lower interaction-rate limits and rejecting the different hypotheses. The time projection chambers (TPCs) based on noble elements have established the strongest dark matter limits for WIMPs with masses above 5 GeV/c^2, demonstrating its potential for dark matter searches.

All the Collaborations pursuing first-generation liquid argon detectors, ArDM [7], DarkSide-50 [8], DEAP-3600 [9], and MiniCLEAN [10], recently merged into the Global Argon Dark Matter Collaboration (GADMC [11]) with more than 400 researchers, to pursue together the proposed DarkSide-Low Mass (1 tonne), DarkSide-20k (50 tonnes) and Argo (300 tonnes) experiments, aiming at investigating WIMP masses above 1 GeV/c^2 with cross sections down to the neutrino floor [2].

One of the key points that will make this extraordinary result possible is the use of underground argon not exposed to cosmic rays with a reduced ^{39}Ar activity, the main background source in multi-ton liquid argon detectors. It is crucial for the DarkSide collaboration to characterize the different argon batches that will be used to fill DarkSide-20k. For this purpose, a novel detected called DArT is being installed in the Canfranc Underground Laboratory (LSC). DArT will measure small samples of UAr (approximately 1 L) in short periods of time (few days) with a sufficient sensitivity to estimate the activity of ^{39}Ar with an statistical uncertainty less than 10%.

The CIEMAT dark matter group has a leading role within DarkSide-20k, and

is one of the main groups involved in the design, construction and operation of DArT. In particular, my work has consisted in optimizing the design of DArT with the aim of obtaining the highest possible sensitivity within the requirements set by the DarkSide-20k experiment. This work has resulted in a publication [5] and is described in Chapter 3. In addition, in Chapter 4 the characterization of the photo detection modules (PDMs) developed for DArT and of the commissioning of the detector on surface at CIEMAT is explained.

Apart from the work within DarkSide-20k, I have been involved in other two R&D investigations for noble liquid detectors. The first one, described in Chapter 5, consists in the development of a novel technique for particle discrimination using the wavelength emission of the argon and xenon scintillation. This technique has been demonstrated with a high pressure noble gas detector, using α and β radioactive sources. The studies carried out in argon gas have resulted in a publication [6].

The second investigation is related to the study of the space charge effects in liquid argon detectors. The impact of the positive ions accumulated in large noble liquid detectors operating at single and dual phase is presented in Chapter 6. A setup has been built in order to characterize the ion feedback from the gas to the liquid phase and to measure the ion drift velocity. An article with my investigations on this subject is in preparation.

Chapter 1

Dark matter direct detection

The Universe has fascinated human beings for centuries. Although throughout the ages a wide variety of experiments and observations have improved our understanding of the Universe, its contents remains a mystery. The ordinary baryionic matter, described by the current Standard Model of Particle Physics, which accounts for only the 5% of the Universe energy-matter density. The remaining 95% is in the form of vacuum energy (dark energy) thought to be responsible for the accelerated expansion of the Universe, and in the form of invisible matter called dark matter. Different strong evidences suggest that this form of matter, which account of 85% of the matter of the Universe, is electrically neutral and non-baryonic.

The nature of the dark matter component of the Universe is one of the most important unsolved problems in physics. In this chapter, I will briefly present the different pieces of evidence that motivated the introduction of the dark matter hypothesis and some proposed candidates, the detection techniques, and the current status of the direct and indirect dark matter searches. The expected sensitivity for a hypothetical WIMP particle will be evaluated and the prospects for direct detection searches will be presented.

1.1 Dark matter evidences and candidates

The first astrophysical evidence supporting the presence of dark matter was found in 1933 by the Swiss astronomer Fritz Zwicky. He studied the redshifts of various galaxy clusters, groups of galaxies gravitationally bounded, and noticed a large scatter in the apparent velocities of eight galaxies within the Coma Cluster, with differences that exceeding 2000 km/s [12].

Considering the system in equilibrium, the virial theorem gives a relationship between the mean velocity of the galaxies and the mass of the cluster:

$$< T >= -\frac{1}{2}\sum_{i=1}^{N} < F_i \cdot r_i >, \tag{1.1}$$

where $< T >$ is the average kinetic energy and F_i the force applied to the particle i in the position r_i. If the force between any two particles of the system results from a potential energy $V(r) = ar^n$ that is proportional to some power n of the interparticle distance r. In particular, for the gravitational potential $V(r) \approx r^{-1}$,

Eq. (1.1) becomes:

$$2 < T >= - < V > . \tag{1.2}$$

Eq. (1.2) relates the average kinetic energy to the total gravitational potential energy. Assuming the potential energy of the cluster, $V \approx -GM^2/R$, with radius R and mass M:

$$M(R) = \frac{2v^2 R}{G}, \tag{1.3}$$

where v^2 is the dispersion velocity and G is the gravitational constant. For the Coma cluster, the result is a total dynamically inferred mass within an Abell radius (equivalent to 2.14 Mpc) [13] of:

$$M_{tot} \cong 6.8 \times 10^{14}\ \mathrm{h^{-1}M_{\odot}}, \tag{1.4}$$

where $h = H_0/100\ \mathrm{kms^{-1}Mpc^{-1}}$ is the Hubble parameter. Its present value according to latest PLANCK results is $H_0 = 67.4 \pm 0.5$ [1]. The mass-to-light ratio, M/L, is the quotient between the total mass of a spatial volume and its luminosity. A value of $M/L \simeq 216$ is obtained using Eq. (1.4) and the measured brightness of the Coma cluster. Therefore, the total mass required to explain the dynamics of the galaxy is much higher than the masses of their luminous constituents, which supports the hypothesis of a dark matter component.

The rotational curves of galaxies, i.e. the circular velocity profile of the stars and gas in a galaxy, as a function of their distance from the galactic center, played a particularly important role in the discovery of dark matter. For a circular orbit, considering Newtonian physics, the gravitational force is equal to the centripetal acceleration due to the curved trajectory described by the body:

$$m\frac{v^2}{r} = \frac{mMG}{r^2} \rightarrow v = \sqrt{\frac{GM}{r}}. \tag{1.5}$$

Therefore, it is expected that for a uniform mass distribution the velocity should decrease as $r^{-1/2}$. Four decades after Zwicky's initial observations, Rubin, Ford, Thonnar, and others began to use new spectroscopic techniques to analyze the rotation curves of galaxies [14]. The Doppler shift of the 21 cm emission line from neutral hydrogen provides information on the rotational velocity of the stars in the galaxy disk. This is especially interesting is spiral galaxies, in which the rotation curve gives a direct measurement of the radial distribution of the total mass.

The rotational curves of different galaxies are presented in Fig. 1.1. The rotation velocity remains constant for stars that are far from the center of the galaxy, thus the mass has to increase with the radius and this mass can not be luminous matter. The velocity curve behaviour can be explained by assuming the presence of a dark matter component in the halo of the galaxy.

The dark matter halo of a galaxy envelops the galactic disc and extends well beyond the edge of the visible galaxy. The Standard Halo Model (SHM) consists in a spherical halo with a Maxwellian velocity distribution for dark matter. The density distribution, $\rho(r)$, as function of the radius, r, is given by:

$$\rho(r) = \rho_0 \left[1 + \left(\frac{r}{r_c}\right)^2\right]^{-1}, \tag{1.6}$$

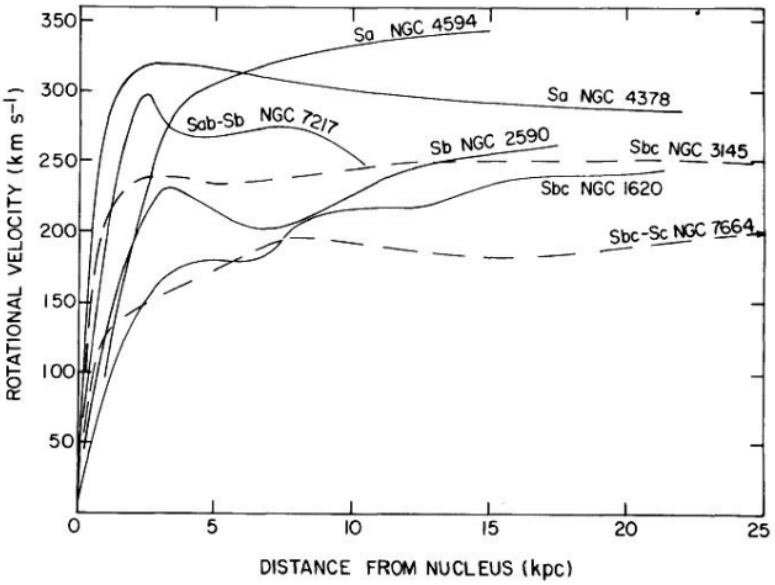

Figure 1.1: Rotation curves of seven galaxies of different Hubble types. At some tens of kpc the Keplerian fall is not observed [15].

where ρ_0 is the central halo density and r_c the halo core radius. Assuming that the velocity curve is flat in the midplane, the data imply a local dark matter density of $\rho_\chi = 0.3 \pm 0.1$ GeV/c^2 [16]. However, a new ρ_χ value of 0.55 ± 0.17 GeV/c^2 has been proposed recently [17] based on recent investigations using the vertical kinematics of stars [18, 19]. The velocity curves are perfectly reproduced after including this dark-halo model, thus pointing out the necessity of a dark matter component electrically neutral in the galactic halo to explain the data.

Until a few decades ago, there was little observational information on the spatial distribution of dark matter. Gravitational lensing, predicted by Einstein equations of General Relativity, is a powerful tool to obtain detailed maps of the dark matter distribution in the galaxy clusters. It is based on the fact that the presence of high gravitational fields bends and amplifies the light the light coming from objects behind them [20]. This effect is known as gravitational lensing. The Bullet Cluster (Fig. 1.2) is an especially interesting astrophysical object, as it was formed by the collision of two large clusters of galaxies. During the collision, the hot gas from each of them suffered a dragging force that reduced its velocity when it passed through the gas from the other cluster. On the other hand, the dark matter, which only interacts gravitationally was not affected by the collision. This results in two well separated regions for both components.

The Cosmic Microwave Background (CMB) radiation is an isotropic radiation produced 3.8×10^5 years after the Big Bang, when the temperature of the Universe decreased enough to allow electrons and protons to form hydrogen and making the Universe transparent to radiation [22, 23]. This radiation is extremely homogeneous with some tiny fluctuations in the temperature, of the order of 10^{-5} . These fluctuations, measured by [1, 24, 25], were originated during the inflationary period of the Universe expansion and are very sensitive to the parameters of the cosmological model. The composition of the energy-matter of the Universe from the latest

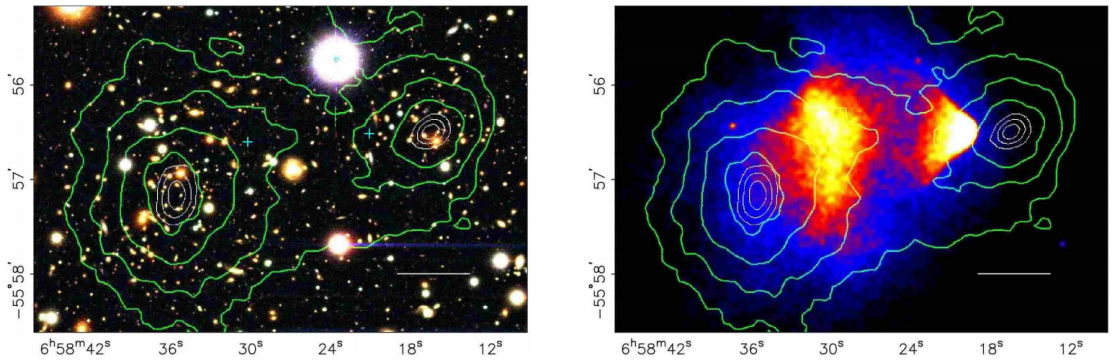

Figure 1.2: (Left) The bullet cluster color image from the Magellan images. (Right) X-ray image of the bullet cluster, obtained in a 500 second exposure with Chandra. The white bar represents a distance of 200 kpc at the location of the cluster. The green contours denote the reconstructed lensing signal, proportional to the projected mass in the system [21].

PLANCK data is [1]:

$$\begin{aligned} \Omega_m &= 0.3147 \pm 0.0024, \\ \Omega_b &= 0.0492 \pm 0.0003, \\ \Omega_c &= 0.2642 \pm 0.0026, \\ \Omega_\Lambda &= 0.6847 \pm 0.0073, \end{aligned} \tag{1.7}$$

where $\Omega_m = \Omega_c + \Omega_b$, is the matter density, Ω_b is the ordinary baryonic matter density, Ω_c the dark matter, and Ω_Λ the dark energy. Dark energy and dark matter account for 95% of the energy-matter content in the Universe. This result is especially interesting when compared with the Ω_b obtained from the Big Bang nucleosynthesis (BBN). It predicts the abundances of the light elements, such as deuterium (D), helium (^{3}He, ^{4}He) and lithium (^{7}Li), which were synthesised at the end of the first three minutes of the existence of the Universe. The synthesis of these elements is sensitive to physical conditions in the early radiation-dominated era of the Universe, in which weak interactions were in thermal equilibrium. The baryon content is estimated to be [26]:

$$0.046 \leq \Omega_b \leq 0.055 \text{ (at 95\% confidence level (C.L.))}, \tag{1.8}$$

a result which is in remarkable agreement with the value obtained by the CMB (Eq. (1.7)).

Nowadays, the so-called ΛCDM-model is well established. From $\Omega_m \gg \Omega_b$, it is inferred that 85% of the matter of the Universe is non-baryonic. Additionally, the excess in the mass-to-light ratio indicates that most matter in galaxies is optically dark.

The strong evidences that we have reviewed so far lead us to conclude that dark matter is electrically neutral and non-baryonic. However, its composition is a mystery and different hypotheses have been proposed to account for the missing mass of the Universe, yielding a variety of dark matter candidates. Some of them, like the massive astrophysical compact halo objects (MACHO), have been discarded

with the current observations. Other alternatives such as theories that modify the Newtonian gravity (MOND [27]), have some difficulties reproducing observations like the Bullet Cluster or CMB in a simple way.

A hypothesis that attracts significant attention is a new kind of non-baryonic weakly interactive elementary particle. Some properties of these candidates are inferred from astrophysical and cosmological observations. They must be stable enough to be present in the actual Universe, electrically neutral and massive enough to account for the measured Ω_c. They are classified in three categories based on their temperature at the time of galaxy cluster formation [28]:

- Hot dark matter (HDM): weakly interacting particles that decoupled from radiation being relativistic.
- Cold Dark Matter (CDM): weakly interacting particles that were non relativistic at the epoch of galaxy formation.
- Warm Dark Matter (WDM) that constitutes an intermediate case between the previous ones.

The dark matter abundance and composition have influence in the Large Scale Structure (LSS) formation. The CDM particles allow small clumps of matter join to form larger structures. On the other hand, HDM would have prevented the formation of high density regions. Therefore, CDM candidates are favoured by current observations [29, 30].

Let us suppose that this new elementary particle is a stable and neutral weakly interacting massive particle (WIMP), produced during the Big Bang and currently present in the halo surrounding the galaxy. For temperatures of the Universe, T, greater than the WIMP mass, the number density of these particles at equilibrium is proportional to T^3. In this epoch, WIMPs are abundant and rapidly convert into lighter particles and vice versa. However, as the Universe evolves, its temperature decreases and, after it drops below the WIMP mass, the equilibrium abundance is exponentially suppressed. At this point, WIMPs cease to annihilate efficiently, falling out of equilibrium, and naturally freezing-out, leaving as remnant a relic cosmological abundance. Additionally, considering a WIMP cross section of the order of the electroweak-symmetry breaking scale (M_{EW}), they match the current dark matter relic density, $\Omega_c = 0.26$.

Neutrinos are in fact the first "dark matter candidate" detected. They are known to have mass from the observation of neutrino flavour oscillations [31, 32]. However, there are observational limits from cosmology on the value of the sum of the neutrino masses. In particular, from PLANCK, $\sum m_v < 0.12$ eV [1], which corresponds to a contribution to the energy density, $\Omega_v < 0.003$, much lower than the dark matter density previously reported. A fourth neutrino type that would interact weakly with the other three families, called sterile neutrino, has been proposed as WDM. Reactor and short baseline neutrino experiments have suggested the detection of this particle [33, 34] during the last years.

WIMPs are an specially attractive candidate since they arise naturally from well motivated extensions of the SM of Particle Physics. They are CDM and reproduce the currently observed relic abundance in the Universe. The range of their expected masses is in the 10 GeV/c^2 to a few TeV/c^2 region. The supersymmetry theory

(SUSY) is an extension of the SM which explains the huge ratio between Planck mass, M_P, and the electroweak scale, $M_P/M_{EW} \sim 10^{16}$, the so-called hierarchy problem, and it provides several suitable dark matter candidates as the neutralino or the gravitino. However, the Large Hadron Collider (LHC) has not detected any signals of supersymmetric particles yet [35].

Although the WIMP hypothesis is a very attractive solution, there are other explanations which come from the particle physics. The axion is an elementary particle that was proposed in the 1970s to solve another unrelated problem, CP violation in Quantum Chromodynamics (QCD). A global symmetry is introduced and spontaneously broken, the Goldstone boson is the axion and it gets the mass from the QCD anomaly. The mass range in which the axions are suitable dark matter candidates has been constrained by different experiments, as ADMX, to very light masses in the range $\mu\text{eV} \leq \text{m} \leq 0.01$ eV [36].

During the last years, there has been an increasing interest in the primordial black holes (PBH) as a possible solution to the dark matter problem. PBHs, predicted by General Relativity, are a hypothetical type of black hole that formed soon after the Big Bang. In the early Universe, high densities and heterogeneous conditions could have led sufficiently dense regions to undergo gravitational collapse, forming black holes. Since PBHs are formed in the radiation-dominated era, they are not subject to the well-known big-bang nucleosynthesis (BBN) constraint that baryons can have at most 5% of the critical density. Different experiments have provided strong limits to the mass of PBHs during the last decades [37, 38]. A wider mass spectrum that would relax these limits has been proposed recently [39, 40].

1.2 WIMP dark matter searches

There are different approaches for the experimental detection of WIMPs, e.g. the interaction of a WIMP particle with a target nucleus, the detection of the products of their annihilation, and the production of WIMPs in collisions at high energy. The different WIMP detection strategies are complementary. Assuming the detection of a dark matter candidate in any experiment, confirmation from other different searches is necessary to claim the discovery and measure the mass and cross-section of the new particle.

Indirect detection experiments are based on the search of WIMP-pair annihilation products, such as gamma rays and neutrinos, and the relative flux of particles and antiparticles [41]. These particles are detected by space-based detectors (PAMELA [42], Fermi-LAT [43], AMS [44]), Cherenkov telescopes (MAGIC [45], H.E.S.S. [46], CTA [47]), or by neutrino experiments (ANTARES [48], IceCube [49], Super-Kamiokande [50]). The energy available in the annihilation process is the WIMP-pair rest mass due to its cold nature. Therefore, the indirect detection experiments search for an excess of photons, anti-matter, positrons, or neutrinos at energies between 1 GeV/c^2 and 10 TeV/c^2. PAMELA has reported an excess in the positron flux over the predictions [51]. This rise has been confirmed by other experiments as AMS [52, 53]. The positron flux in the 0.5-1000 GeV/c^2 range is displayed in Fig. 1.3. It is necessary to include a new positron source term to describe the positron spectrum at high energies. It is the contribution of the source term that leads to the observed excess of the positron flux above 25 GeV/c^2. This new positron source could be interpreted as dark matter annihilation or other new

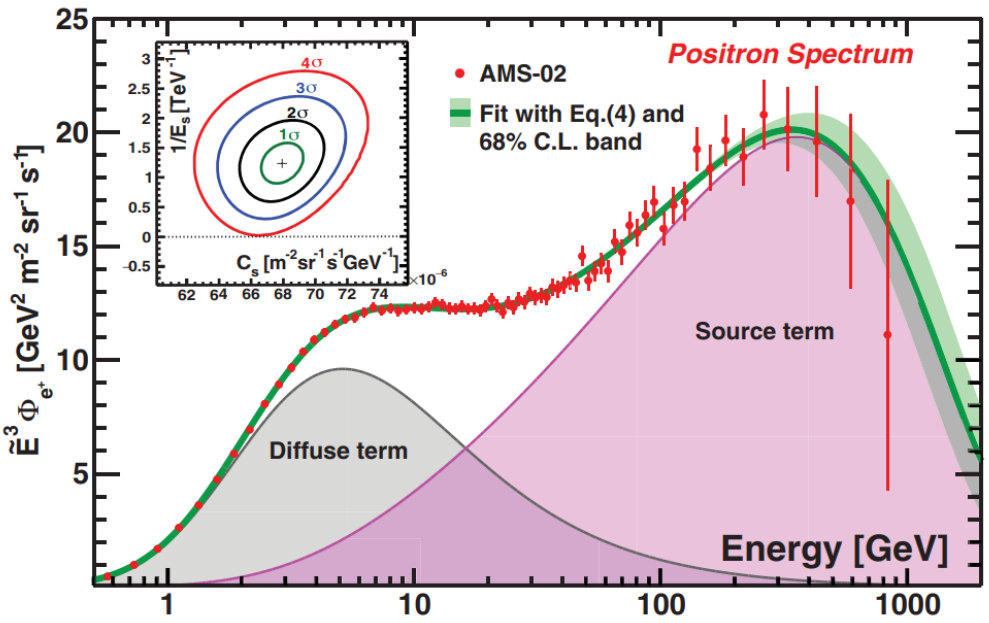

Figure 1.3: Positron flux in the energy range 0.5-1000 GeV/c^2 measured by the AMS satellite experiment. The red data points are the measured positron flux values. The source term contribution is represented by the magenta area [54].

astrophysical source, as pulsar emission [54].

Cherenkov telescopes, such as MAGIC or the Cherenkov Telescope Array (CTA) detect showers of secondary particles produced by the interaction of incident high energy gamma rays with the atmosphere. CTA will be the major global observatory for very high energy gamma-ray astronomy over the next decade and it will have a strong dark matter program. The sensitivity predictions for different targets in the W^+W^- channel are summarized in Fig. 1.4.

Another possible detection method is the production of WIMPs at high energy colliders like the Large Hadron Collider (LHC) at CERN produced by the reaction $q\bar{q} \rightarrow \chi\bar{\chi}$. Since the WIMPs are electrically neutral and would only undergo weak interactions, the signature of dark matter expected in colliders events is a large amount of transverse missing energy. Therefore, events with an energetic jet and large missing transverse momentum in the final state, usually referred as monojet-like events, constitute a clean and distinctive signature in searches for new physics beyond the SM at colliders, such as SUSY [57].

The LHC has put many relevant constraints on theoretical parameters, although they have not provided any hint about the dark matter nature. However, there are many model dependencies on these analyses making difficult to draw general conclusions.

1.2.1 Direct detection

The direct detection experiments are based on the interaction of WIMPs from the local dark matter halo with target nuclei of experiments on Earth. WIMPs do no interact electromagnetically (weak force) and are not relativistic thus, they are expected to recoil elastically on the nuclei, producing nuclear recoils (NR). On the

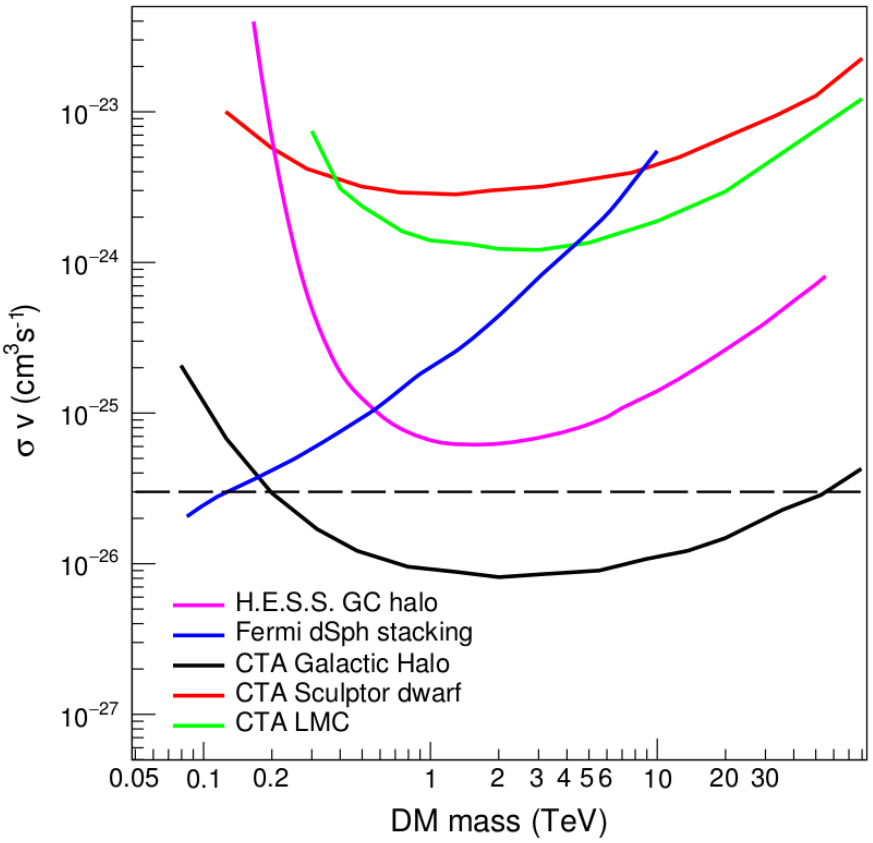

Figure 1.4: Comparison of predicted sensitivities for the targets of: the Milky Way Galactic halo; the Large Magellanic Cloud (LMC) and the dwarf galaxy Sculptor. The CTA sensitivity curves use the same method and W^+W^- annihilation modes for each target and the same dark matter profile. The sensitivities for the three targets are all for 500 hours taking into account the statistical errors only. The H.E.S.S. results come from the Galactic halo for the W^+W^- channel [55] and the Fermi-LAT results come from dwarf spheroidal galaxies for the W^+W^- channel [56]. The horizontal dashed line indicates the thermal cross section at 3×10^{-26} cm^3.

contrary, β and γ particles from radioactivity interact with the electrons of the target atoms, giving rise to electron recoils (ER).

A simple model for the distribution of WIMPs in our galaxy suggests that they should gather in a spherical isothermal halo. The solar system moves through this halo with a speed of 220 km/s [17]. Considering WIMPs with a mass, m_χ, and an initial kinetic energy $E_0 = \frac{1}{2} m_\chi v_0^2$, a nucleus of mass m_N will recoil at a scattering angle θ, with an energy E_R is given by:

$$E_R = \frac{\mu_\chi^2 v_0^2 (1 - cos\theta)}{m_N}, \tag{1.9}$$

where $\mu_\chi = \frac{m_\chi m_N}{m_\chi + m_n}$ is the reduced mass of the WIMP-nucleus system and v_0 is the speed of the incoming WIMP. Considering a WIMP of mass $m_\chi \approx 100$ GeV/c^2 with $v_0 \approx 200$ km/s, and argon as the target nucleus, $m_N \approx 40$ GeV/c^2, the expected recoil energy is very low, of the order of tens of keV. For this reason, low energy thresholds are necessary in dark matter experiments to increase the sensitivities for

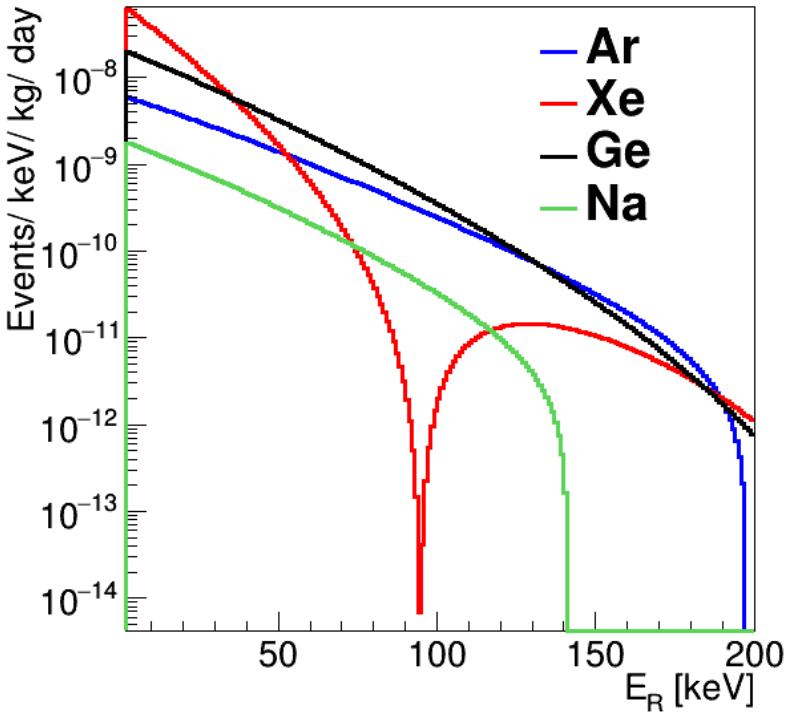

Figure 1.5: Expected event rate per keV, per kg of target and day as function of E_R, for different target materials (Xe, Ar and Na) considering a WIMP-nucleon cross section of 10^{-45} cm^2 and a WIMP mass of 1 TeV/c^2.

the detection of WIMPs.

The expected event rate per keV, per kg of target and day as a function of the recoil energy is depicted in Fig. 1.5, where a WIMP-nucleon cross section of 10^{-45} cm^2 and a WIMP mass of 1 TeV/c^2 are assumed. The expected rate for dark matter direct detection in liquid argon is of the order of 10^{-7}-10^{-10} events/day/kg/keV. Therefore, it is necessary to build detectors with volumes on the tonne scale for the detection of WIMPs.

The expected rate of WIMP signals is very low, of the order of a few events per year per tonne. Therefore, ultra-low background experimental conditions are required in dark matter direct searches. The main backgrounds are:

- Cosmic-rays and cosmogenic neutron radiation. Cosmogenic neutrons are produced by muon spallation reactions with the detector materials. Neutrons can interact with nuclei in the detector via elastic scattering, yielding nuclear recoils which can mimic a WIMP. To mitigate this problem, dark matter experiments are typically placed in deep underground laboratories. The rock coverage reduces the muon flux and so the number of muon-induced neutrons. The hadronic component of the cosmic ray flux is also rendered negligible by a few tens of meter water equivalent.

- Environmental γ-ray radiation. Most of the background due to γ-ray radiation originates from the decays in natural uranium and thorium chains, as well as from decays of common isotopes such as ^{40}K, ^{60}Co and ^{137}Cs, which are present in the rock of the cavern. It is reduced by surrounding the detector

with materials with high atomic number and high density (i.e. good stopping power). Additionally, detectors have passive or active shields which moderate and tag the external radiation, respectively.

- Internal backgrounds. Radiogenic neutrons are emitted in (α,n) and spontaneous fission reactions from natural radioactivity. Additionally, γ-ray radiation is originated in the detector components. For noble gases, the dominant internal background consists of isotopes that can be activated by cosmogenic activity and α decays mainly produced in the ^{222}Rn chain on the internal surfaces of the detector. They are suppressed selecting materials with low traces of radioactive contaminants, to reduce the rate of α and γ-ray emission, and spontaneous fission.

Three different signals can be measured from nuclear recoil interactions in the target medium: scintillation (photons), ionization (electrons) and heat (phonons). The new generation of dark matter experiments usually exploit two of these signatures at the same time (as ionization and scintillation) to improve the particle identification techniques and separate the expected WIMP signal from background events. Different target materials as inorganic crystal scintillators (CRESST [58], CDMS [59], ANAIS [60], DAMA/LIBRA [61]), liquid noble elements (DEAP-3600 [9], DarkSide-20k [2], ArDM [7], XENON1T [62]), and bubble chambers (PICO [63]) are typically used for the WIMP direct detection searches.

Another important experimental signature for WIMPs discovery is the annual modulation in the WIMP event rate. The Earth velocity in the galactic frame, can be divided into three contributions: the rotational velocity of the galactic disk, the velocity of the Sun with respect to the disk and the motion of the Earth with respect to the Sun. The tangential velocity of the Sun around the galactic centre, 220 km/s, is an order of magnitude larger than Earth speed around the Sun of approximately 30 km/s, thus this last term is usually neglected in most of the studies. However, it would give rise to a seasonal effect in the WIMP flux detected on Earth, and therefore in the interaction rate.

The direction vector of the Earth plane orbit around the Sun is tilted 60° with respect to the Sun propagation direction. As a result, the velocity of the Sun relative to the WIMP flux has a variation of $\pm$ 15 km/s. Therefore, the WIMP flux detected on Earth has a seasonal variation, thus giving an annual modulation effect in the WIMP event rate that can be used for dark matter searches [64].

The different type of experiments compete to achieve the highest sensitivity and the lowest possible values of the WIMP-nucleon cross-section. Typically, the sensitivity of the direct detection experiments is expressed in terms of the WIMP-nucleon cross section (cm^2) versus the WIMP mass (GeV/c^2). To be able to compare results coming from different experiments with distinct target materials, the cross section is defined as the WIMP scattering off a target nucleon (instead of nucleus).

The elastic scattering of a WIMP off a nucleus can occur via spin-dependent or spin independent channels since the contribution of several nucleons to the scattering cross section will not always be added coherently. In the spin-dependent case, only the unpaired nucleon will have a remarkable contribution to the interaction, while in the spin-independent all contributions for different nucleons are considered. Consequently, the cross section expression will vary depending on the type of interaction.

The difference between spin-independent and spin-dependent interactions provides an important cross check in the case of a positive dark matter signal. The abundance of odd atomic number isotopes is negligible in natural argon, thus only spin-independent signals can be observed. On the other hand, there are two isotopes in xenon with an odd atomic number of nucleons, ^{129}Xe and ^{131}Xe, allowing spin-dependent searches.

1.3 Sensitivity of direct detection experiments

The interaction rate of WIMPs with ordinary matter depends on several parameters, like the WIMP velocity distribution and density, and the material-dependent nuclear form factor. Corrections due to finite galactic escape velocity, v_{esc}, and the annual modulation of the signal due to Earth's motion around the Sun are introduced. The latter correction depends on three variables, the Earth velocity around the Sun, v_E, the Solar System velocity in the galaxy, v_0, and the minimum initial WIMP velocity, v_{min}, to produce an energy recoil of E_R.

A full analytical computation of the differential WIMP recoil energy spectrum has been developed, to evaluate the expected sensitivity for the next generation of dark matter experiments [65]:

$$\frac{dR(v_E, v_{esc})}{dE_R} = \frac{2N_0}{\sqrt{\pi}} \frac{\rho_\chi}{m_\chi A} v_0 \left[erf\left(\frac{v_{esc}}{v_0}\right) - \frac{2v_{esc}}{\sqrt{\pi} v_0} e^{-(v_{esc}/v_0)^2} \right]^{-1} \frac{1}{E_0 r}$$
$$\left[\frac{\sqrt{\pi} v_0}{4 v_E} \left(erf\left(\frac{v_{min} + v_E}{v_0}\right) - erf\left(\frac{v_{min} - v_E}{v_0}\right) \right) - e^{-(v_{esc}/v_0)^2} \right] \sigma_n(q r_n) \ , \tag{1.10}$$

where N_0 is the Avogrado number, A the atomic number of the target nucleus, σ_N the WIMP-nucleus cross section and E_0 the initial kinematic energy. The dependence of this equation with the energy recoil, E_R, comes from $v_{min} = \sqrt{\frac{E_R}{E_0 r}} v_0$. A kinematic factor, r, related to the mass of the WIMP-nucleus system is introduced for simplification:

$$r = \frac{4 m_\chi m_N}{(m_\chi + m_N)^2} \ . \tag{1.11}$$

The Eq. (1.10) is calculated in the zero momentum transfer approximation, with a cross section σ_0. A form factor, $F(q r_n)$, is introduced to consider the momentum transfer between the nucleus and the WIMP. The scattering cross section behaves as:

$$\sigma(q r_n) = \sigma_0 F^2(q r_n). \tag{1.12}$$

Considering the distribution proposed by Helm [66]:

$$F(q r_n) = 3 \ \frac{j_1(q r_n)}{q r_n} \ e^{-(qs)^2/2} \ , \tag{1.13}$$

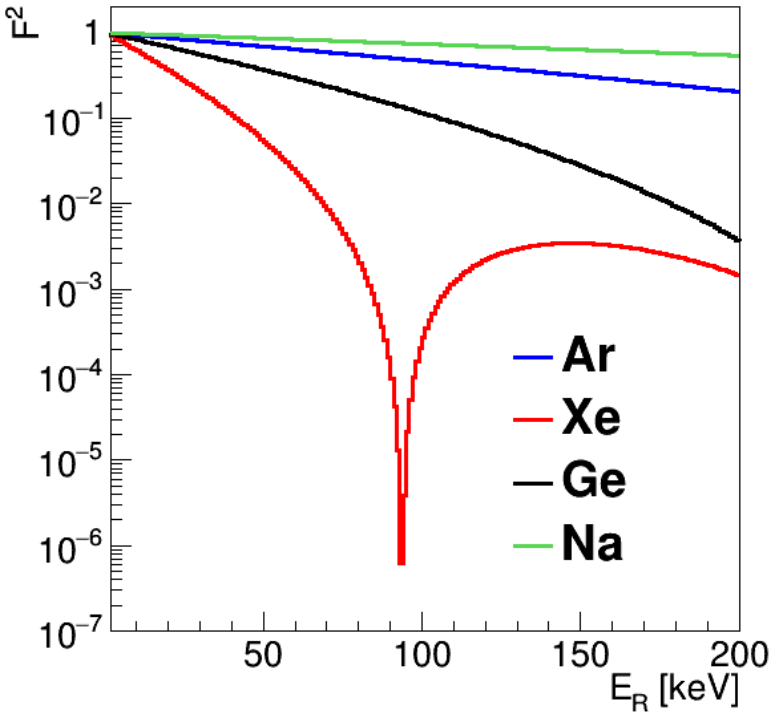

Figure 1.6: Form factor correction as a function of the recoil energy for different target materials.

where r_n is the effective nuclear radius, q is the WIMP-nucleus momentum transfer, $j_1(qr_n)$ is the Bessel function and s accounts for the nuclear skin thickness.

The form factor correction is displayed in Fig. 1.6 as a function of the recoil energy, for the different materials. Those with a large atomic number have a remarkable influence on the form factor.

Expressing Eq. (1.10) as a function of the WIMP-nucleon cross section, σ_n, is important to compare the results from experiments using different target materials:

$$\sigma_n = \frac{1}{A^2}\left(\frac{\mu_N}{\mu_n}\right)^2 \sigma_N \ . \tag{1.14}$$

It is convenient to calculate the WIMP cross section as a function of the WIMP mass. In case of lack of a dark matter positive signal, the number of events detected in a given energy range are used, together with an estimate of the background events, to set limits on the cross section as function of m_χ. Therefore, it is necessary to isolate σ_n from Eq. (1.10) and consider the integrated event rate over a recoil-energy range, $E_{th} = [E_1, E_2]$, defined by the lower and upper energy threshold. Since it is not possible to integrate Eq. (1.10) analytically with respect to E_R, it is calculated numerically for a full range of different m_χ values, so we obtain σ_n as follows:

$$\sigma_n = \frac{R(v_E, v_{esc})}{\int_{E_1}^{E_2} f(E_R)\, dE_R} \ , \tag{1.15}$$

where $R(v_E, v_{esc})$, expressed in units of $\mathrm{keV}^{-1}\mathrm{kg}^{-1}\mathrm{day}^{-1}$, is directly given by the experimental exposure. The result of Eq. (1.15) is compared with numerical approximations performed with public domain software tools for dark matter related

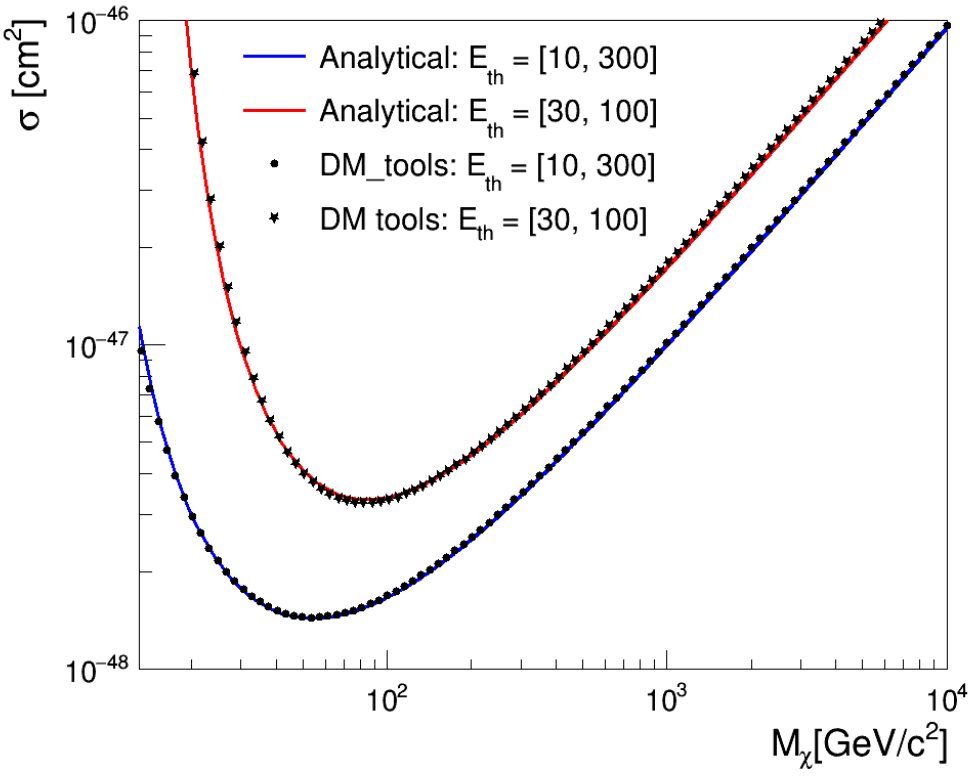

Figure 1.7: Cross section for different energy thresholds considering an exposure of 200 tonne × year. The curves computed analytically with Eq. (1.15) (solid lines) are in excellent agreement with the predictions obtained from the dark matter online tools (dotted lines).

calculations [67]. The comparison is done in two energy ranges as presented in Fig. 1.7, which shows an excellent agreement with the theoretical calculation.

The influence of the lower energy threshold in the evaluation of the expected experimental sensitivity is remarkable. This lower threshold effect is due to the approximately exponential form of the differential spectrum, which imposes low energy thresholds for the detectors to be sensitive to low WIMP masses.

These results are obtained assuming the SHM ($\rho_\chi = 0.3$ GeV/c^2, $v_{esc} = 544$ km/s and $v_0 = 220$ km/s). However, the new data provided by Gaia [68] suggest the need of a new dark matter term, requiring a bi-component model to correctly describe the Milky Way stellar dynamics. For experiments without directional sensitivity, though, it is enough to use the SHM with updated values of v_{esc} and ρ_χ [17].

The impact of these new parameters in a liquid argon detector with a exposure time of 200 tonne × year, is evaluated in Fig. 1.8 using the analytic code described before. The value of v_{esc} is updated from 544 km/s to 528 km/s and that of ρ_χ from 0.3 GeV/c^2 to 0.55 GeV/c^2.

The impact of the new v_{esc} value on the sensitivity is reduced. Only small variations are observed for $m_\chi <$ GeV/c^2. On the other side, the updated ρ_χ significantly increases the cross section sensitivity from 9 $\times 10^{-47}$ cm^2 to 3 $\times 10^{-48}$ cm^2 for a WIMP mass of 50 GeV/c^2.

In conclusion, the validity of the theoretical development has been tested and the impact of updating the astrophysical parameters in accordance with the new

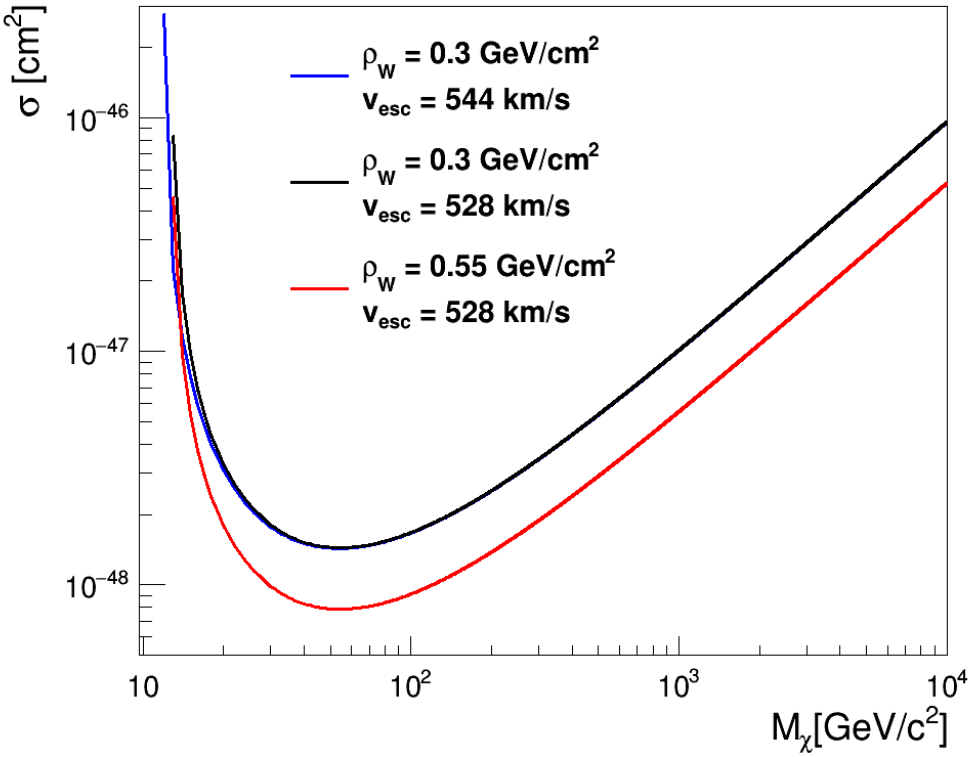

Figure 1.8: Cross section for different v_{esc} (black) and ρ_χ values (red), considering an exposure of 200 tonne × year and an energy range from 10 to 300 keV.

Gaia measurements has been evaluated. Although the SHM is still valid and the impact of v_{esc} is small, our results suggest that an ρ_χ update affects the expected sensitivity considerably.

1.4 Direct searches status

The DAMA/NaI and DAMA/LIBRA experiments claim a dark matter discovery [69]. These experiments, located in the Laboratori Nazionali del Gran Sasso (LNGS), have measured the WIMP annual modulation signature using an array of high radiopure NaI crystals. Recently, DAMA/LIBRA has released a summary of the results obtained with the total cumulative exposure of 2.46 tonne × year that gives evidence of an annual modulation with a statistical significance of 12.9 σ in the 2-6 keV energy range. They attribute this rate variation to a possible dark matter modulation signal [70].

Noble liquid detectors as XENON1T and DarkSide-50 have obtained results that are in clear disagreement with the claims from the annual modulation analysis. The ANAIS-112 [60] and COSINE-100 [71] experiments are aiming to replicate the results of DAMA/LIBRA using the same technique. ANAIS-112 consists of a 112 kg NaI detector located in the Canfranc Underground Laboratory (LSC). The data from the exposure of 0.22 tonne × year are compatible with the absence of modulation, and incompatible with a statistical significance of 2.6 σ in the 1-6 keV energy interval [72].

The sensitivity of current WIMP direct detection experiments is in Fig. 1.9, where the WIMP-nucleon cross section as a function of the incident WIMP mass

is represented. The lines correspond to the exclusion limits set by different experiments at the 90% C.L. The shape of the exclusion curves is determined by the kinematics of the WIMP-nucleon scattering. The parameter space is limited from below due to the so-called neutrino floor, a region where coherent scattering of solar, atmospheric, and supernova neutrinos with nuclei limits the sensitivity of direct detection experiments [73].

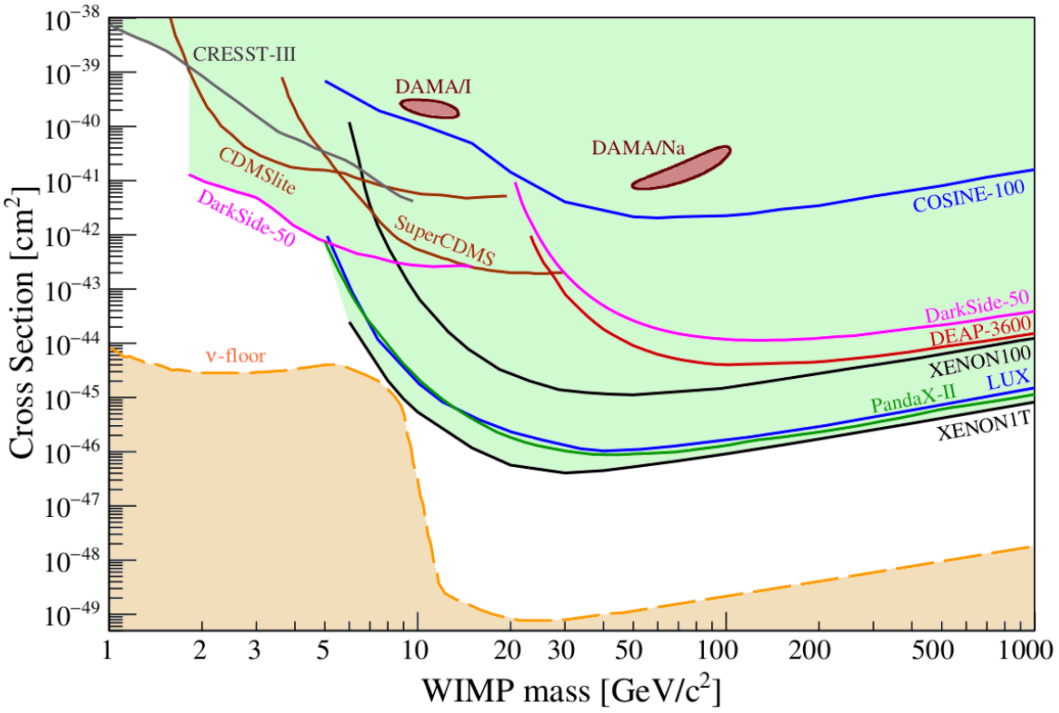

Figure 1.9: Parameter space accessible experimentally for spin-independent WIMP searches. The space above the lines is excluded at the 90% C.L. The two contours for DAMA interpret the observed annual modulation in terms of scattering of WIMPs with iodine (I) and sodium (Na), respectively [74]. The dashed line limiting the parameter space from below represents the neutrino floor.

Due to their ability to reach extremely low energy thresholds well below 1 keV, the cryogenic experiments using Ge-crystals (EDELWEISS [75], (Super)CDMS [59]) or scintillating $CaWO_4$-crystals (CRESST [58]) are very sensitive to low-mass WIMPs. CRESST-III is currently placing the most stringent constraints below 1.8 GeV/c^2 [76] extending the mass range down to 0.16 GeV/c^2.

In 2018, the DarkSide collaboration published the world's best upper limit at low masses, between 1.8 GeV/c^2 and 6 GeV/c^2 using a LAr target depleted in ^{39}Ar [77]. The result is based on the ionization signal only, which allows reducing the analysis threshold to 0.1 keV.

Additionally, it has been proposed recently that the reach of WIMP detectors could be extended further into the sub-GeV region by exploiting the Migdal effect [78].

On the other hand, the high mass WIMP region is dominated by massive noble liquid experiments. DEAP-3600 has reported the current most sensitive limit for liquid argon detectors setting a WIMP-nucleon scattering cross sections above 3.9×10^{-45} cm^2 (1.5×10^{-44} cm^2) for WIMPs with a mass of 100 GeV/c^2 (1 TeV/c^2)

at 90% C.L., assuming the standard WIMP halo model [79]. Among all dark matter detectors to date, the XENON-1T collaboration has obtained the most sensitive limits on spin-independent interactions of high-mass WIMPs with nuclei, using a xenon target to place a limit on the WIMP-nucleon interaction cross section of 4.1×10^{-47} cm^2 for a WIMP mass of 30 GeV/c^2 at 90% C.L. [80].

The Global Argon Dark Matter Collaboration [11] (GADMC) was founded by scientists from ArDM [7], DarkSide-50 [8], DEAP-3600 [9], and MiniCLEAN [10] to pursue a sequence of future experiments, starting with DarkSide-20k [2].

1.5 Sensitivity prospects

A dark matter experiment expecting one background event will need up to 3 times more WIMP interactions to claim a detection, compared to an experiment free of background [2]. The silicon photomultiplier (SiPM) and the underground argon technologies will allow the GADMC to construct a massive detector with an extremely low number of background events expected in the full exposure (0.1 neutrons in 10 years). This will allow DarkSide-20k and the next experiments of the GADMC to dominate the dark matter direct searches during the next decade with the sensitivity to reach the neutrino floor.

The sensitivity of current and upcoming WIMP direct-detection experiments is displayed in Fig. 1.10. The solid lines correspond to the sensitivity curves for different exposure times of future experiments, while the dashed lines are the neutrino floor regions for argon and xenon targets. DarkSide-20k, with an exposure time of 200 tonne $\times$ year, is an extremely low background experiment. Its sensitivity curve at 90% C.L. for WIMP masses of 1 TeV/c^2 and 10 TeV/c^2 reaches cross sections of 8×10^{-48} cm^2 and 7×10^{-47} cm^2, respectively. The next generation of xenon experiments in construction, XENONnT and LZ, are expected to have slightly lower sensitivity than DarkSide-20k, 2×10^{-47} cm^2 (2×10^{-46} cm^2) for 1TeV/c^2 (10 TeV/c^2) WIMP mass [81, 82].

Another two multi-ton projects have been proposed recently to start operation during the next decade: DARWIN [84] (liquid xenon) and ARGO [11] (LAr), which will explore the experimentally accessible parameter space for WIMPs in a wide mass-range, down to the neutrino floor. New techniques exploiting the directionality of incident particles have been suggested in recent times [85, 86], to surpass this limitation of direct detection experiments.

Liquid argon and xenon detectors are complementary. It is fundamental to have different target materials in case of a positive dark matter signal, in order to characterise a potential signal.

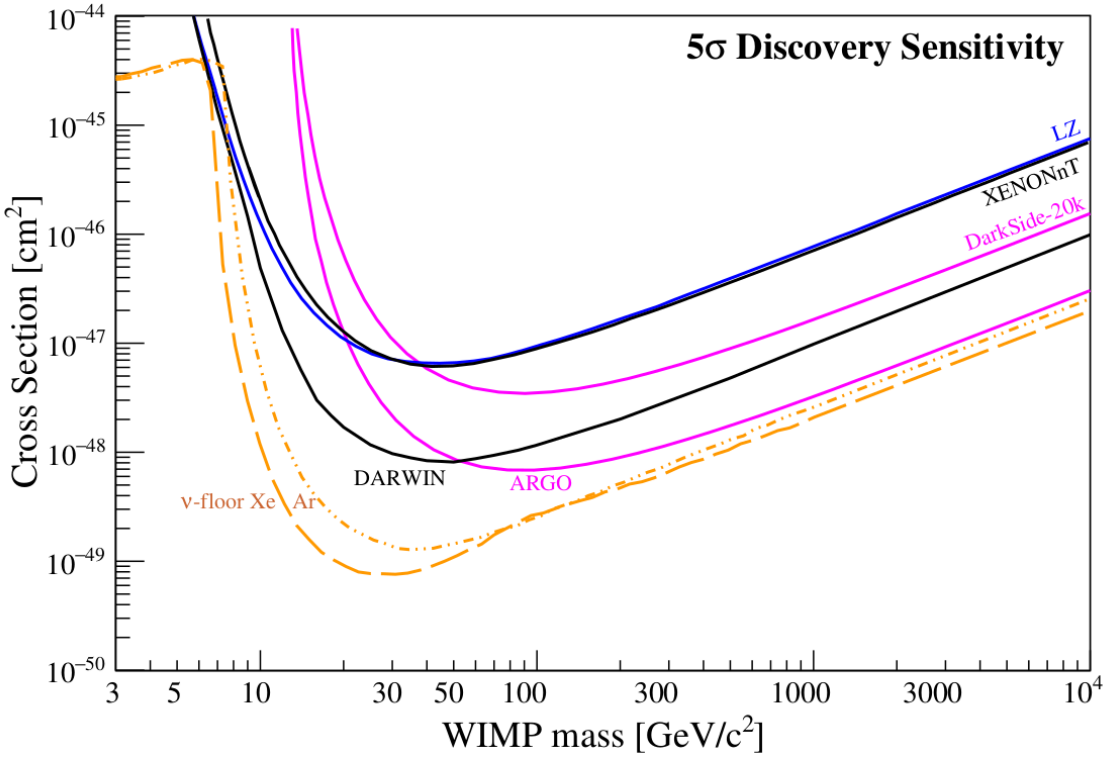

Figure 1.10: Discovery potential at the 5 σ statistical significance of current and planned spin-independent direct dark matter detection experiments [83].

Chapter 2

Noble liquid detectors for rare event searches: DarkSide-20k

Noble liquid technology has been widely used in recent years in particle and astroparticle physics experiments. In particular, the last decade has witnessed an enormously increasing interest in argon and xenon based Time Projection Chambers. This technology has the potential to provide the sensitivity and detector-mass scalability required for neutrino physics and rare event searches.

Liquid noble detectors based on argon or xenon can be designed to operate in single-phase (liquid) or dual-phase (liquid-gas). Both detect the scintillation and the ionization signal, providing a powerful tool for particle identification and background discrimination. In dual-phase detectors is possible to reach lower thresholds in terms of ionization signal.

This thesis was developed within the DarkSide-20k experiment, a dual-phase TPC with a detection volume of 50 tonnes of liquid argon, which is currently under construction at the LNGS. DarkSide-20k is designed to dominate the spin-independent searches in the 10 GeV/c^2 to 100 TeV/c^2 mass range for WIMPs over the next decade.

In this chapter, I present a review of the light and charge production mechanisms in liquid argon (LAr) and liquid xenon (LXe), as well as their propagation and detection in large liquid argon TPCs. Finally, I describe the DarkSide-20k experimental setup.

2.1 Noble liquid detectors

The high scintillation yield of noble liquids permits to establish low detection thresholds for particle interactions, of the order of the keV. Additionally, they are available in large amounts and argon, in particular, is the third most abundant gas in the atmosphere (934 ppm). They can be easily purified, making it possible to build tonne scale detectors with long electron drift distances.

These aspects, together with the unique background discrimination made possible by particle identification and 3D event reconstruction capabilities, makes noble liquids ideal materials for the next generation of neutrino [87, 88, 89] and dark matter direct search experiments [90, 91, 92, 93]. The characteristics of the main noble elements used in rare events searches are summarized in Table. 2.1.

Liquid xenon and liquid argon are excellent scintillators in response to particle

Table 2.1: Comparison of some physical properties of noble liquids that are relevant for dark matter detection [94].

Parameter	**Neon**	**Argon**	**Xenon**
Atomic number	10	18	54
Atomic mass	20.2	40.0	131.3
Boiling point (b. p.) [K]	27.1	87.3	165.0
Liquid density at b. p. [g/cm^3]	1.21	1.40	2.94
Scintillation yield [γ/keV]	7	40	46
Scintillation wavelength [nm]	78	128	172
Primary ionization [e^-/keV]	46	42	64
Energy to generate an ion pair [eV]	-	23.6	15.6
Abundance in the atmosphere [ppm]	18.2	934	0.09
Price	$$	$	$$$$

interactions, with high light yields, 46 γ/keV and 40 γ/keV, respectively. The light yield of liquid neon, LNe, is 7 γ/keV. For this reason, LAr and LXe are the main target materials for neutrino and dark matter detection experiments. The most relevant difference between them is related to the details of the scintillation emission. Its primary component has a wavelength of 128 nm (in the VUV region of the electromagnetic spectrum), while in LXe it is 172 nm (VUV).

In rare gases, the energy deposited by radiation is expended in the production of a number of electron-ion pairs, N_i, excited atoms, N_{ex}, and free electrons with a kinetic energy lower than the energy of the first excited level, known as sub-excitation electrons. The energy transferred by a particle to the medium, E_0, is expressed in terms of ionization, excitation and sub-excitation electrons by an energy balance equation [95]:

$$E_0 = N_i E_i + N_{ex} E_{ex} + N_i \epsilon \ , \tag{2.1}$$

where E_i and E_{ex} are the mean energies to ionize and excite an atom and ϵ is the mean energy of sub-excitation electrons after the last collision to result in either excitation or ionization. The free electrons with energy below ϵ only induce elastic collisions with the target atoms, increasing the temperature of the medium. The value of ϵ lies between 6.3 eV and 7.7 eV for LAr and between 4.7 eV and 5.2 eV for LXe [96]. The W-value is defined as the average energy required to produce one electron-ion pair, and is given by:

$$W = \frac{E_0}{N_i} = E_i + \frac{N_{ex}}{N_i} E_{ex} + \epsilon \ . \tag{2.2}$$

The W-values are inferred in [97, 98] for LAr and LXe to be 23.6 eV and 15.6 eV, respectively. LXe has the smallest W-value, hence the largest ionization yield of all liquid rare gases.

In general terms, the mechanism of primary scintillation is similar for LAr and LXe. The light production mechanism relies on the collision among excited and ground state atoms, forming excited molecular states, called excimers. They are produced in a very short time scale (below the ns scale), suppressing the direct de-excitation of the atoms. A more detailed explanation of the noble gas scintillation mechanisms is presented in Chapter 5.

The excimers are formed in singlet $^1\sum_u^+$ (from P_1^3) and triplet $^3\sum_u^+$ (from P_2^3) states, depending on how the spin of the electron and the argon dimer couple. Scintillation photons are emitted in the transition from one of these two lowest molecular excited states to the ground state $^1\sum_g^+$ [99].

The direct transition from the triplet state to the ground state is forbidden, and the decays are possible through the mixing between the $^3\sum_u^+$ and the $^1\prod_u$ states via spin-orbital coupling [100]. This transition is characterized by a longer lifetime with respect to the singlet state, 1.6 μs with respect to 7 ns in LAr and 22 ns with respect to 4 ns in LXe. In the case of liquid xenon, the time difference is lower because the spin-orbital coupling becomes stronger for heavier molecules. As the ground state for these transitions of the excimer is not bound, it decays to two neutral argon/xenon atoms. The re-absorption of the photons is excluded by the absence of excimer molecules and atoms with low enough excited states, hence the scintillation photons are free to leave the liquid.

The ratio of the intensities of the singlet and the triplet transitions depends on the incident particle type, its energy and the density of excited atoms. From the practical point of view, the higher the excitation density is, the more prompt singlet photons are observed, thus a pulse shape analysis of the scintillation light can be used to discriminate the incident particle types.

Besides direct excitations, the alternative luminescence process involves recombination of the ionization electrons with positive ions. Molecular ions are formed after a short period of time (of the order of the ps) by the ionized noble gas atoms [101], suppressing the direct electron-atom recombination. The recombination between ionization electrons and the molecular ions leads ultimately to the formation of the same excimers produced by the direct excitation channel. As a consequence, the emitted light is characterized by the same wavelength.

The charge recombination along the particle track plays a very important role in determining the response to radiation. The electron-ion pairs can either partially recombine, producing additional light, or can be separated through a drift field and then collected. The average energy loss of the particle along its path through the liquid determines both the shape of the light pulse and the ratio between the scintillation and the ionization signals, which are the signatures typically used to discriminate, for example, between heavy ionizing particles, like α or recoil nuclei, and electrons [102].

The recombination process can be described assuming that a dense plasma of positive and negative ions is formed along tracks for ionising particles [103]. In the absence of an electric field, practically all the electrons-hole pairs created initially recombine and give rise to the recombination luminescence. For low-density tracks, some electrons escape the recombination even at zero fields. The scintillation light decreases by a factor 3 in liquid argon when a high electric field (10 kV/cm) is applied. The relative contribution of the recombination component to the total light yield has been measured to be 65% in liquid argon [104].

The required intensity of the electric field applied to avoid the recombination is larger for particles with higher linear energy transfer (LET). For low-LET 1 MeV electrons, 90% of the charge is collected with a few kV/cm [101], while for α-particles a field of 20 kV/cm is needed to collect 20% of the charge.

The Jaffe model describes the recombination of positive and negative ions with equal mobilities [105] in a column of target material. The charge dependence with

the electric field intensity, E, has the following expression:

$$Q(\epsilon) = \frac{Q_0}{1 + k/E} \ , \tag{2.3}$$

where Q_0 is the initial charge generated in the particle interaction, and the constant k characterizes the recombination strength.

2.2 Liquid argon time projection chambers

The Time Projection Chamber proposed by David Nygren in 1974 [106], is an evolution of George Charpak's Multi-Wire Proportional Chamber [107]. Crossing charged particles ionise the detection medium, which was gaseous in the original design. An electric field is applied to prevent the recombination of the ions and the electrons. These electrons drift towards a 2D readout plane. The charge readout is triggered by a scintillation light readout, also providing accurate timing of an event. This allows to measure the time for the ionisation electrons to reach the readout plane. As the drift speed of charged particles in the detection medium is constant, provided it is known, the coordinate in the drift direction is calculated from the drift time.

While gaseous TPCs already provide very accurate tracking, they have the disadvantage that the target mass of the detection medium is quite low, resulting in a low interaction rates. In 1977, C. Rubbia proposed the usage of LAr as a detection medium to solve this problem [108].

A liquid argon Time Projection Chamber (LAr-TPC) consists of a detection volume filled with liquid in an electric field with a position-sensitive charge readout and a light collection system. The ion/electron pairs generated in LAr either recombine, producing light, or are separated through a drift field, thus migrating to the anode and cathode, respectively. The LAr-TPCs can be designed to operate in single-phase (liquid) or in dual-phase (liquid-gas).

In LAr-TPCs, both ionisation and scintillation signals are detected. When a particle interacts within the active volume of the detector, it produces a primary scintillation signal (S1), as well as electrons from the ionisation. The generated electrons do not recombine due to the electric field applied and they are drifted towards the anode. In single-phase LAr-TPCs, the charge measurement is done through the induction or the collection of the electrons on thin wires directly placed in the liquid. In dual-phase LAr-TPCs, the electrons are extracted into the gas phase by a stronger field that allows surpassing the liquid-gas potential barrier. The electrons are accelerated in the gas phase in this high electric field, generating a proportional electroluminescence scintillation signal (S2), which is mainly detected by the light sensors on the top. A sketch of a typical dual-phase electroluminescence detector is presented in Fig. 2.1-left. If a much larger electric field is applied to the gas phase, an avalanche of secondary electrons will occur. The amplified charge is detected by a readout plane on the top.

The single-phase TPCs are the current preferred option for next-generation neutrino experiments [109]. Their operation and design are much simpler than dual-phase detectors and they have been proved successfully at large sizes [110]. On the other hand, the dual-phase electroluminescence TPC provides a lower energy threshold using the ionization signal. Since WIMP interactions are typical of the

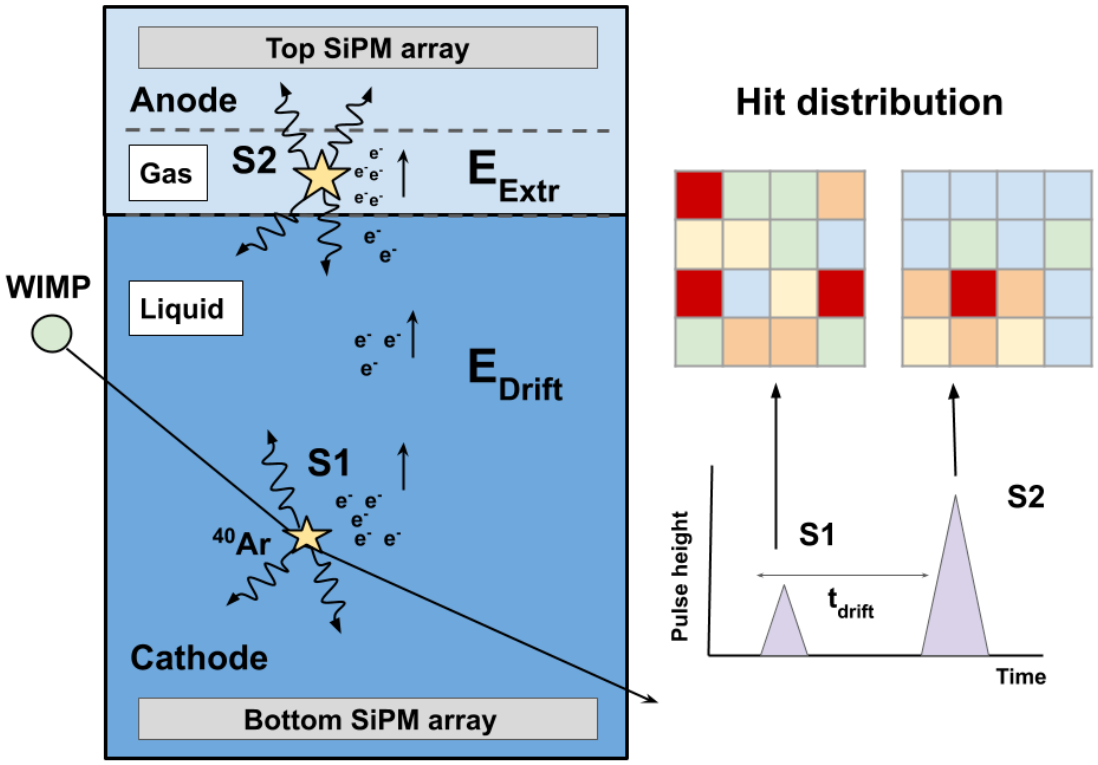

Figure 2.1: (Left) Dual-phase electroluminescence LAr-TPC scheme. A uniform electric field is applied between the anode and the cathode. The scintillation signal is detected by the photosensors (S1), the electrons are drifted to the anode (direction of arrows) and extracted to the gas phase, producing the electroluminescence signal (S2). (Right) Hit distribution over the photosensor plane for S1 and S2 signals.

order of keV, they are the most popular option for future dark matter experiments as DarkSide-20k [2] or DARWIN [84].

The light pattern detected by the photosensors for S1 and S2 signals is depicted in Fig. 2.1-right. The X-Y position reconstruction with millimeter resolution [111] is possible since the electron diffusion is small in liquid. Additionally, considering that the drift velocity of electrons in the LAr has been precisely measured as a function of the drift field, the time difference between the S1 and S2 signals, t_{drift}, provides the Z coordinate (along the electric field) of the position of the interaction event.

Cosmogenic neutrons and radiogenic neutrons are two of the main backgrounds in dark matter experiments, because they interact with nuclei in the detector via elastic scattering, producing nuclear recoils which can mimic a WIMP signal (see Chapter 1). The 3D position reconstruction allows the identification of multiple-scattering events, rejecting neutrons as possible positive signals. At the same time, it permits to select a LAr fiducial volume inside the active region, using the argon around it as shielding. This technique is specially efficient for background events coming from the inner surface of the detector, as α decays produced in the ^{222}Rn decay chain. Additionally, the possibility of detecting both scintillation and ionisation signals provides a powerful tool for particle identification and background discrimination, since the ratio of these two signals is different for nuclear recoils, generated by WIMPs or neutron interactions, and electronic recoils, produced by

electrons and γs. This technique is complementary to pulse shape analysis of the scintillation light used to discriminate the incident particle types.

2.2.1 Light and charge propagation

Next generation dark matter and neutrino experiments are expected to have large active volumes to improve their sensitivities, in which the propagation of the scintillation light and the electrons drifted over long distances will play a fundamental role. Although the noble atoms are transparent to their own scintillation light, two processes can contribute to a finite photon attenuation length in noble liquids: absorption by impurities and quenching of the excimer. Residual molecules in Ar/Xe, mainly O_2, N_2 and H_2O (impurities), can dissipate the energy of the excimers through non-radiative channels, affecting the total light yield of the detector. The observation of this phenomenon is reported in [112, 113], with the addition of small concentrations of N_2 and O_2 (above 0.1 ppm). This effect is independent of the detector size.

Additionally, the impurities can capture the VUV photons, reducing the scintillation triplet lifetime and the light yield. The VUV attenuation length for impurities dissolved in LAr is depicted in Fig. 2.2 assuming different molecular absorption cross sections [114]. This effect is more relevant for large detectors.

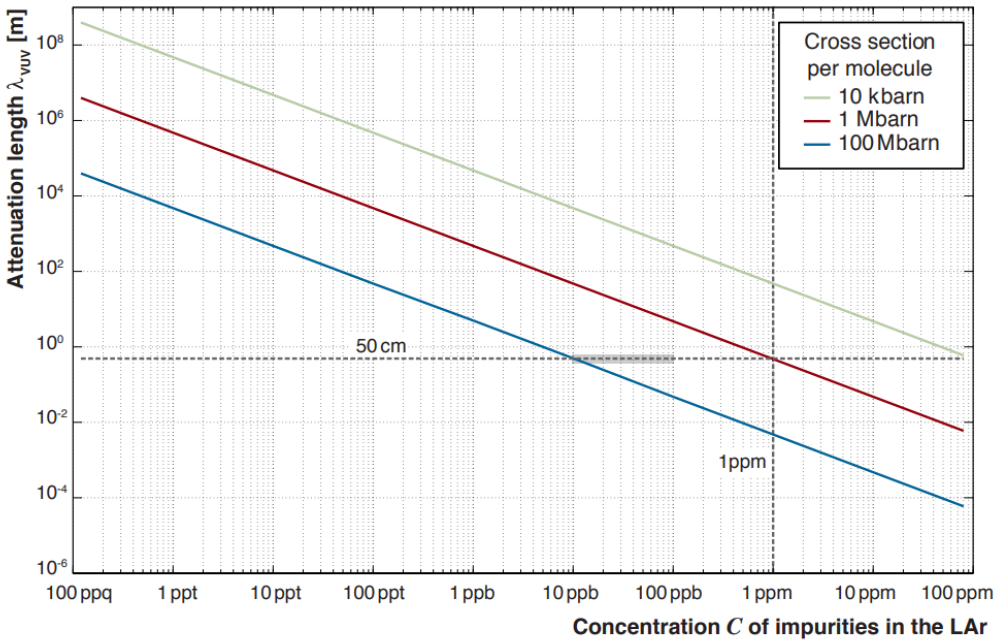

Figure 2.2: Dependence of the VUV attenuation length on the concentration of impurities in LAr. The diagonal lines represent molecular cross sections of 0.01, 1 and 100 Mbarn, respectively. These values are consistent with those expected for the impurities usually present in LAr.

In LAr-TPCs, the electrons produced by the interactions of particles in the liquid are drifted over long distances by a uniform electric field. The detectable fraction of ionization charge depends on the electronegative impurities present in LAr since, some of them as O_2, N_2 and CO_2, capture the ionisation electrons [115]. The number

of free electrons decreases with time due to their interaction with impurities following an exponential law:

$$N_e(t) = N_e^0 e^{-t/\tau_e}, \tag{2.4}$$

where τ_e is the lifetime of the drifting electrons, and N_e^0 is the initial number of electrons that do not recombine. The probability that the electron attaches to a neutral molecule, called attachment rate coefficient, is different for each impurity. The argon purity is usually expressed as a function of the oxygen equivalent concentration $[O_2]_{eq}$. Assuming that all the argon contamination is due to oxygen, the electron lifetime is estimated to be [116]:

$$\tau_e(\mu s) = \frac{300}{[O_2]_{eq}(\text{ppb})}. \tag{2.5}$$

The electron drift velocity depends of the electric field applied and the argon temperature (Fig. 2.3). It is inferred from Eq. (2.4) that the number of free electrons reaching the cathode depends on the time to travel the drift distance. Therefore, it is possible to reduce the purity requirements increasing the drift field intensity.

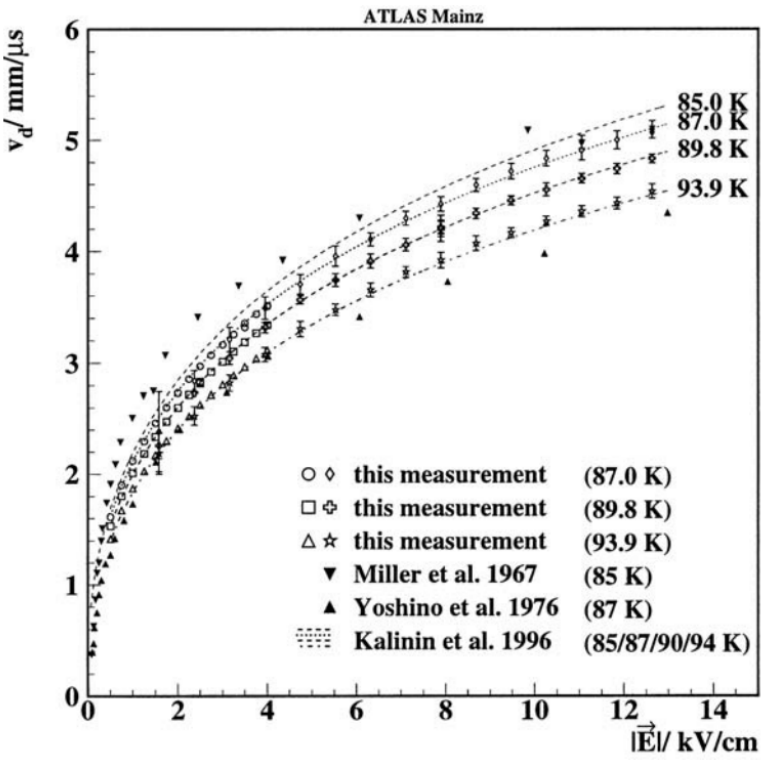

Figure 2.3: The drift velocity, v_d, is represented as function of the electric field, for different liquid argon temperatures [117].

Another important aspect of the charge propagation in LAr-TPCs is the electron diffusion, which limits the spatial resolution of tracks with long drift distances. Diffusion in noble elements is much lower in the liquid than in the gas phase. The diffusion process is modeled with two coefficients: the transverse diffusion, D_T, and the longitudinal diffusion, D_L. The spread of the initially point-like electron cloud

over a distance L can be estimated using:

$$\sigma_X = \sqrt{\frac{2LD}{v_e}} = \sqrt{\frac{2L(D_L^2 + D_T^2)^{1/2}}{v_e}}. \tag{2.6}$$

At 500 V/cm electric field, the diffusion coefficients have been estimated to be D_L = 7.2 cm^2/s and D_T = 12.0 cm^2/s [118]. With these values, the smearing expected in LAr over a drift length of 1 m is 1.3 mm. This smearing will affect the position resolution of dark matter and neutrino detectors and it will increase with the drift distance.

2.3 Review of the VUV scintillation light detection technologies

A central aspect of argon and xenon TPCs is the efficient collection and detection of the vacuum ultraviolet (VUV) scintillation photons and the electroluminiscence signals, which makes available the calorimetric data, the time information necessary for the 3D event reconstruction and the particle identification capability required for background events rejection.

The VUV light is usually detected using photosensors as photomultiplier tubes (PMTs) or silicon photomultipliers (SiPMs). The SiPMs are solid-state single-photon sensitive devices based on Single-Photon Avalanche Diodes (SPAD) [119] implemented on a common silicon substrate. Every SPAD in a SiPM operates in Geiger mode and is coupled with the others by quenching resistors. Each module comprising an independently operating unit of SPAD and a quench resistor is referred to as a microcell. The size of a microcell varies from 10 μm to 100 μm and the number of microcells per device ranges from several hundred to several tens of thousands. All of them are connected in parallel to one common cathode and one common anode output.

In SiPMs, the photon is absorbed in the silicon and creates an electron-hole pair. Applying a reversed bias voltage, the charge carried is accelerated to a point where it creates secondary charge pairs through a process called "impact ionization". The silicon breakdowns and becomes conductive, effectively amplifying the original electron-hole pair into a macroscopic current flow through the microcell. This process is called Geiger avalanche. The voltage drops across the quench resistor, reducing the bias voltage to a value below the breakdown, thus quenching the photocurrent and preventing further Geiger-mode avalanches from occurring. Once the photocurrent is quenched, the voltage recharges to the nominal bias value. The time it takes for the microcell to recharge to the full operating voltage is called the "recovery time" [120]. The Geiger avalanche is confined to the single microcell where it started. During the avalanche process, all other microcells remain fully charged and ready to detect photons.

The SiPMs have several advantages with respect to the PMTs. For their operation, they are supplied typical voltages between 20 V and 100 V, being 15 to 75 times lower than the voltage required for a traditional PMT operation. Their geometry is more compact, reducing the amount of mass in low background experiments, and they are easily scalable to large areas. Additionally, they offer an excellent single photon resolution and a very high signal-to-noise ratio.

To successfully employ SiPMs in rare-event searches, low dark count rates are required to minimise the rate of accidental coincidences at low energy thresholds. Also, a gain in the order of 10^6 is needed to achieve a high single photoelectron (SPE) detection efficiency. Pictures of a 8" liquid argon PMT and a 25 cm^2 active area SiPM developed by DarkSide-20k are displayed in Fig. 2.4. A comprehensive review of advances in solid state photon detectors is found in [121].

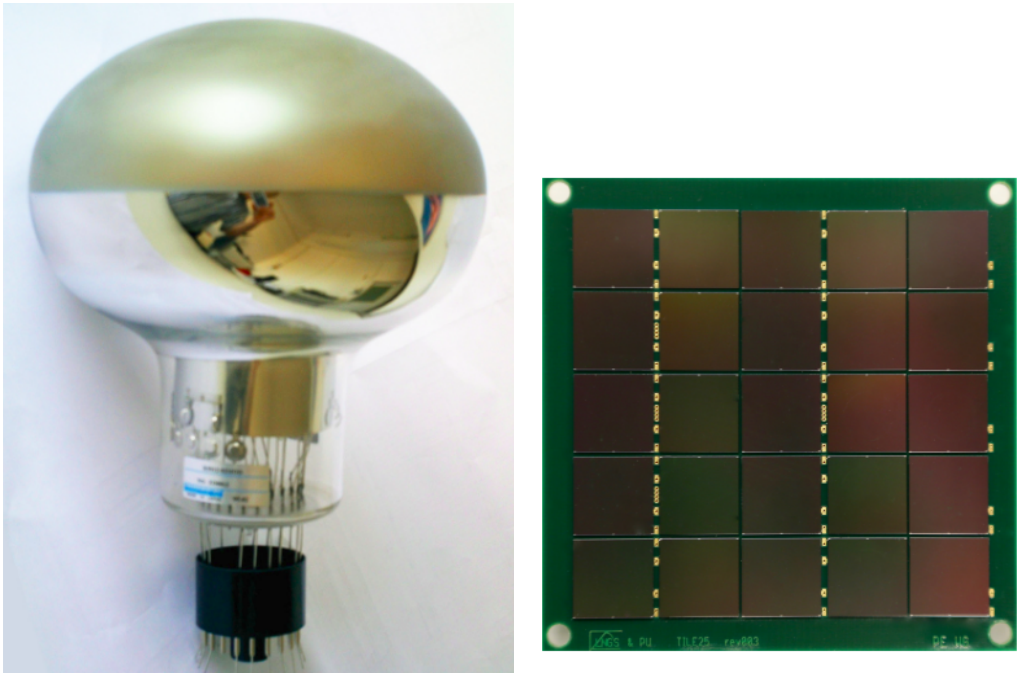

Figure 2.4: Photo of a 8" liquid argon PMT (left) and a 25 cm^2 active area SiPM (right).

The SPE spectrum obtained during the calibration of the PMTs described in chapter 5 is depicted in Fig. 2.5-top, using dark current events. The measured spectrum is successfully reproduced with the sum of several correlated Gaussian functions. The first one corresponds to the average noise level and the following ones to the number of detected photoelectrons (PE). The SPE spectrum measured for a SiPM developed by DarkSide-20k is shown in Fig. 2.5-bottom. A significant improvement is observed in the peak identification for each photoelectron in the SIPM in comparison with the PMT. The SiPMs allow photon counting, improving the energy resolution and reducing the energy threshold to the 1 PE level.

The light collection effiency is increased using materials with high reflectivity at the scintillation light wavelength. Data on the reflectivity of some relevant materials for wavelengths shorter than 200 nm are represented in Fig. 2.6. Freshly deposited aluminium presents the highest reflectance, although it rapidly degrades when is exposed to air. The surfaces can be protected from oxidation using MgF_2, conserving a high reflectance in the VUV range. PTFE is typically used in xenon experiments, which report a reflectance between 85% and 90% for the scintillation light in liquid xenon.

It is complicated to develop photosensors and reflectors with high enough quantum efficiency (QE) and reflectivity in the VUV-UV range, where the argon and xenon scintillation light emission is produced. The most common solution is to use

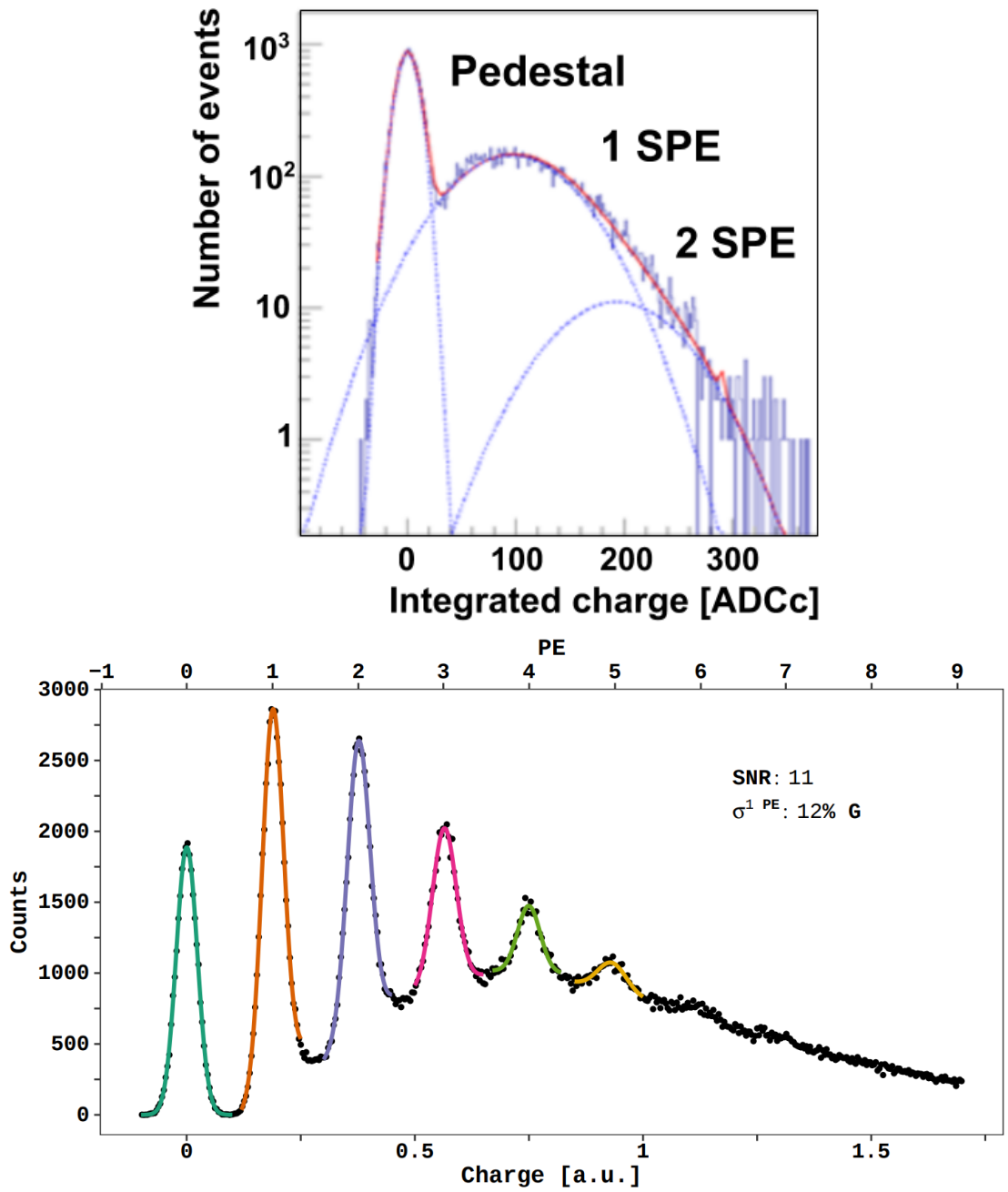

Figure 2.5: Photoelectron spectra of the 1" Hammamatsu R6095 PMT (top) and the 24 cm^2 SiPM photosensor (bottom), both using a fixed window integration [122]. The solid lines represent a Gaussian fit to the photoelectron peaks and the baseline.

wavelength shifting materials, which absorb VUV and re-emit the light at longer wavelengths. The tetraphenyl butadiene (TPB) is an organic molecule that converts the UV light to the 380 nm-450 nm wavelength range, with an efficiency close to 1 [126]. TPB is usually evaporated over photosensors and reflectors in liquid argon detectors, to improve the light collection efficiency. Albeit TPB has been widely used in dark matter and neutrino experiments, its evaporation over large areas, transportation and storage are a complex process. Additionally, the TPB coating can be degraded during operations [127]. For this reason, new alternatives have been proposed over the last years, as the polyethylene naphthalate (PEN) [128].

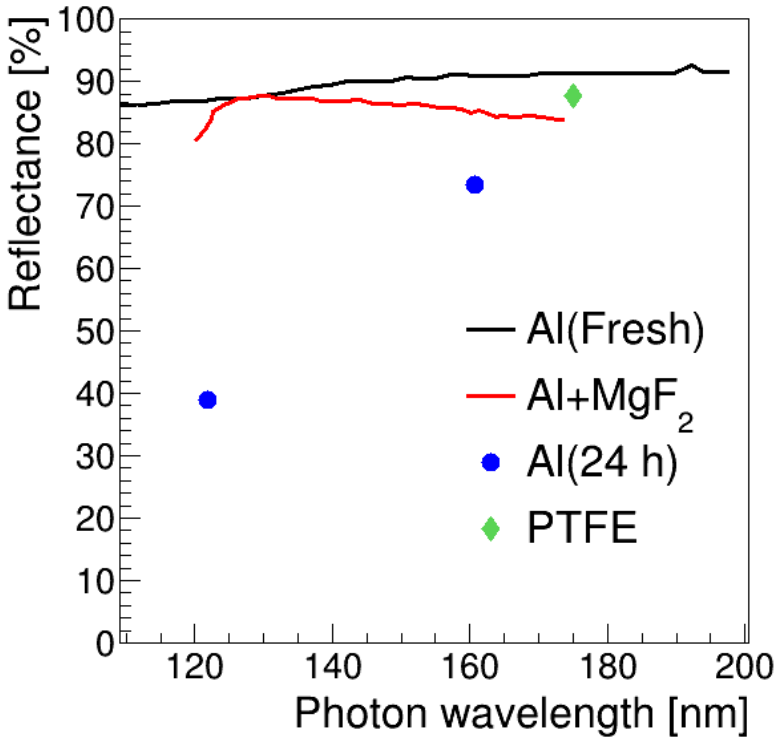

Figure 2.6: Light reflectance in the VUV range for different materials. The aluminium data are from [123] and the data for aluminium protected with MgF_2 (deposited by evaporation) from [124]. Measurements with polished PFTE illuminated with a Xe scintillation light in vacuum are reported in [125].

The PEN conversion efficiency has been reported to be close to 60% and it can be found in the market as large area sheets or rolls.

2.4 DarkSide-20k experiment

DarkSide-20k [2] is the first experiment of the GADMC. It consists in a dual-phase LAr-TPC with an active volume of 50 tonnes of low-radioactivity argon from an underground source (UAr). The TPC is housed within a ProtoDUNE-style membrane cryostat [129], that acts as veto. The goal of DarkSide-20k is to detect WIMPs [2] from their expected scintillation light and ionisation charge signals, which provide a particle identification tool and a powerful discrimination method between nuclear recoils and electron recoils.

The DarkSide-20k experiment construction is planned to being in 2021 in the Hall-C of the Gran Sasso National Laboratory (LNGS), at a depth of approximately 3500 meters water equivalent. A 3D schematic view of the DarkSide-20k detectors is in Fig. 2.7.

The inner detector is a dual-phase LAr-TPC, contained within an ultra-pure acrylic (PMMA) 350 cm tall vessel in form of an octagonal prism. The vessel hermetically encloses the ultra-pure liquid argon target and a thin layer of argon gas, sitting in the ullage above the liquid. On the sides of the vessel, there are eight vertical reflector panels supported by the PMMA sidewalls. At the top and bottom of the vessel, two PMMA windows separate the active volume from the

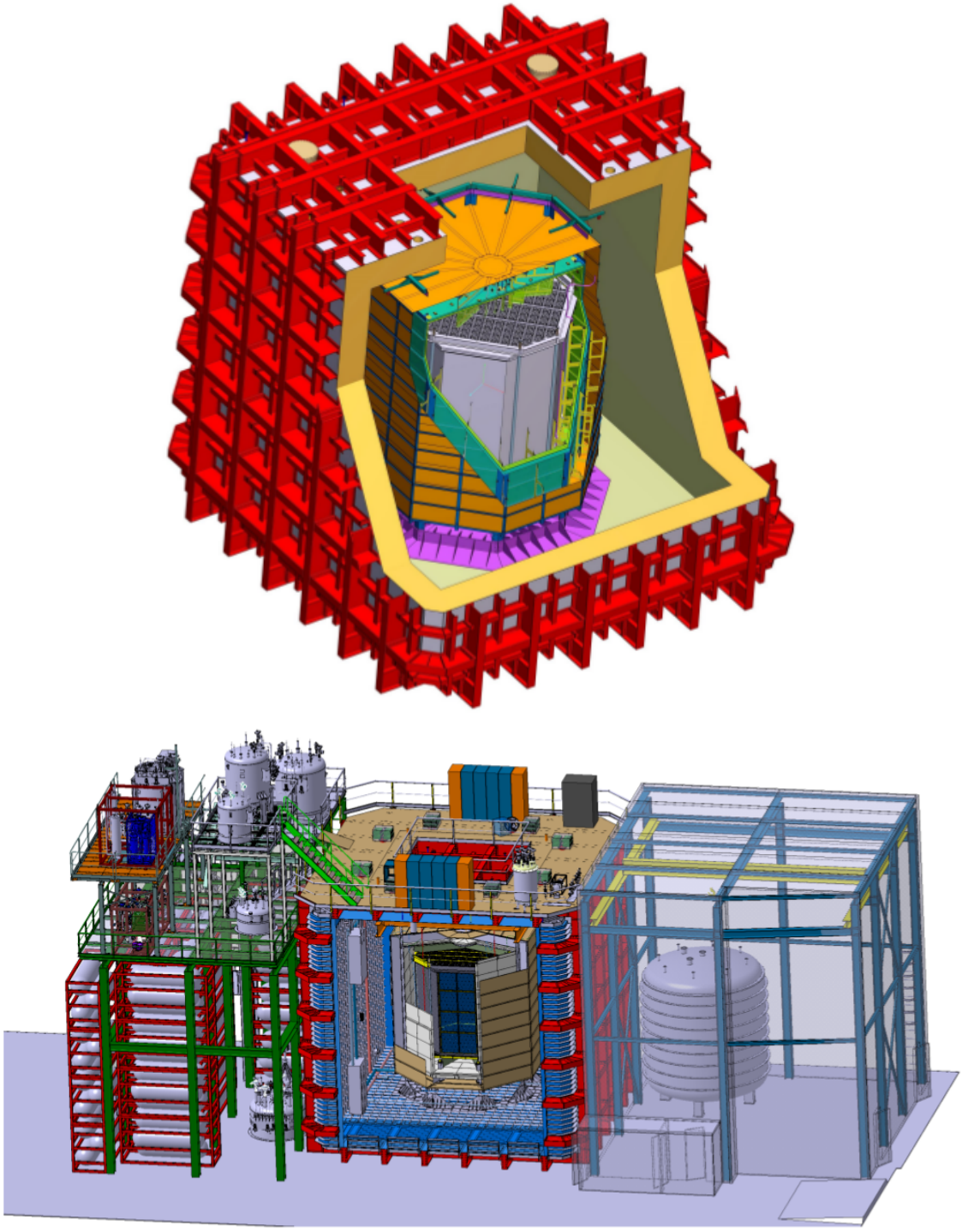

Figure 2.7: (Top) Illustration of the DarkSide-20k experiment. From the center out: UAr target, acrylic (PMMA) vessel (gray), inner active atmospheric argon veto, Gd-loaded acrylic shell (green), outer active atmospheric argon veto, copper vessel (gold), passive atmospheric argon shielding, ProtoDUNE-like cryostat (yellow, red), plastic neutron thermalization sheets (not shown). The TPC rests on a temporary support structure (purple). When the detector construction is complete, it will be suspended from the cryostat roof (not shown). (Bottom) CAD rendering of the DarkSide-20k experiment in the Hall C of LNGS.

photodetector planes.

The TPC drift field within the active volume is established using thin octagonal strips of poly(3,4-ethylenedioxythiophene) polystyrene sulfonate (also known as PEDOT:PSS and commercialized under the name Clevios TM [130]) coated directly on the PMMA sidewalls. Clevios will also coat the internal surfaces of the top and bottom acrylic windows that serve as the anode and cathode of the TPC. A third electrode, a wire grid, is located a few millimeters below the liquid-gas interface and will separate the TPC drift region (which is the target volume for WIMP interactions) from the extraction region and the gas pocket, where ionization electrons extracted from the target volume are accelerated to produce an electroluminescence signal. Tetraphenyl butadiene, coated on all internal surfaces of the inner detector, converts the prompt scintillation and delayed electroluminescence VUV light to a wavelength efficiently detectable by silicon photomultipliers. The argon volume is read out by 8280 SiPM-based Photodetector Modules (PDM) through the top and bottom windows of the acrylic vessel (Fig. 2.8-left).

The PMMA vessel is contained within the outer cage, which ensures the vessel's stability and provides optical isolation of the internal argon volume from the veto detector. The walls of the outer cage consist of PMMA and enhanced specular reflector (ESR) foil tiles fixed to anchor points on the outer wall of the PMMA vessel. The reflector tiles bounce the waveshifted light produced in the veto region back towards the veto, isolating the TPC SiPMs. The top and bottom caps of the cage prevent light from penetrating the space between adjacent SiPM modules and will be anchored to a series of copper fixtures that also act as the SiPM motherboard holders (Fig. 2.8-right).

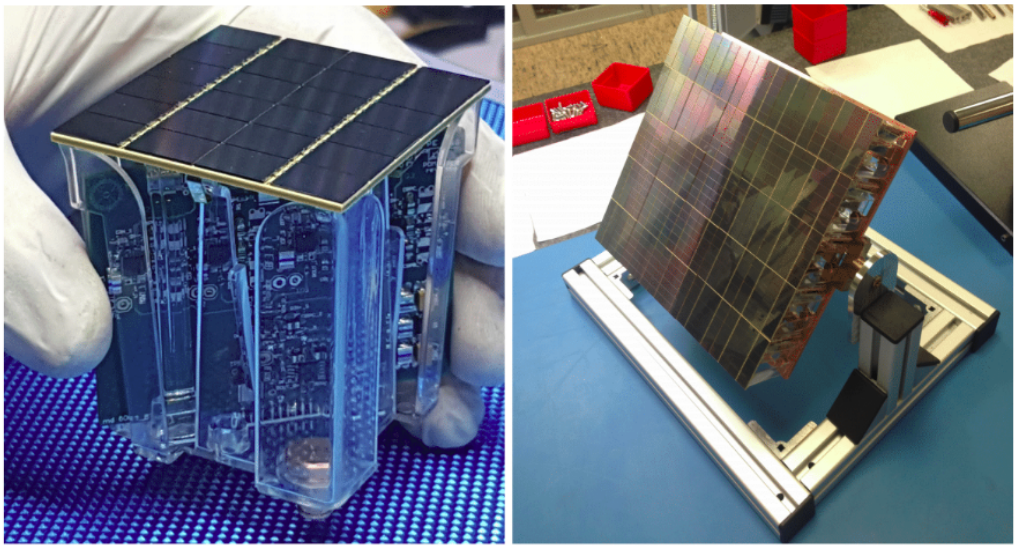

Figure 2.8: (Left) Picture of the first PDM consisting of 24 SiPMs together with the front-end electronics board. (Right) Photo of the first motherboard (MB) assembled with 25 PDMs.

The active outer veto detector is composed of two instrumented atmospheric argon (AAr) volumes that sandwich a passive Gd-loaded PMMA shell, which moderates and and captures (α, n) neutrons from residual impurities in the LAr-TPC resulting in the emission of multiple γ-rays. The γ-rays interact in the AAr layers and cause scintillation light that is detected, providing an efficient neutron veto sur-

rounding the TPC, enabling the efficient tagging of neutrons that scatter or capture within the UAr target. The ProtoDUNE-like cryostat will be surrounded by layers of plastic to moderate cosmogenic and radiogenic neutrons from the rocks surrounding LNGS Hall C (not shown in Fig. 2.7).

The DarkSide-20k experiment is designed to have ultra-low background rates and the ability to tag these events in situ. DarkSide-20k is planned to operate with "zero" instrumental backgrounds within the 20.2 tonne fiducial volume, meaning all sources of background besides neutrino scatters can be reduced to less than 0.1 events in a ten years run. All background events from electromagnetic interactions will be removed by a combination of pulse shape discrimination (PSD) using the primary scintillation pulse and a comparison of the primary and secondary scintillation signals (see [2] for details on suppressing background from ^{222}Rn, ^{220}Rn, and their progeny). Neutrons will be tagged using the outer veto detector, which means DarkSide-20k will perform a high efficiency measurement of the radiogenic neutron background during its operation. Any signal measured within the fiducial volume in excess of the expected coherent elastic neutrino-nucleus scattering background can therefore be unambiguously attributed to dark matter interactions. The sensitivity can be further improved by relaxing the instrumental background-free requirement and analyzing the full 49.7 tonne active volume of the detector using a profile-likelihood ratio analysis [131]. DarkSide-20k will operate for ten years, collecting a 1000 tonne $\times$ year exposure (200 tonne $\times$ year fiducial). It will be the first experiment to observe coherent elastic neutrino-nucleus scattering from atmospheric neutrinos, with 3 events expected for the 200 tonne $\times$ year fiducial exposure.

One of the keys to obtaining these challenging results is the use of underground argon. The isotope ^{39}Ar produces a β decay with an end-point of 564 keV. It is found in atmospheric argon at a rate of 1 Bq/kg. It is produced mainly by the interaction of cosmic rays with argon atoms. For this reason, the argon extracted from underground wells has a significantly smaller quantity of this isotope. The DarkSide-50 experiment was the first to operate with UAr and measured an activity of 0.73 mBq/kg of ^{39}Ar [3].

There is a worldwide effort led by the GADMC collaboration whose goal is the procurement of UAr for rate event searches. The Urania plant will extract at least 50 tonnes of low-radioactivity UAr for DarkSide-20k, at a rate of 300 kg/day, from the Kinder Morgan Doe Canyon Facility in Cortez, Colorado, USA, which is the same source of UAr that was used for the DarkSide-50 detector. The concentration of ^{39}Ar should be ensured to have at least the same reduction factor as measured in DarkSide-50. The extraction plant is optimized to achieve an UAr purity better than 99.9%.

The majority of the liquid UAr extracted by Urania will be sent to the appropriate cryogenic vessels for shipment to Sardinia, where it will undergo final chemical purification up to 99.999% purity in the ARIA plant [132]. ARIA consists of two 350 m tall distillation columns of different processing diameters, Seruci-I and Seruci-II, located in a refurbished carbon mine shaft in Sardinia, Italy. It will process about 150 kg/day of argon to achieve a purity level enough to operate DarkSide-20k. Although not its primary goal, it will also be the test bench to perform active depletion of ^{39}Ar from the UAr to possibly provide depleted argon (DAr) targets for LAr detectors. It is designed to separate ^{39}Ar from ^{40}Ar by exploiting the tiny difference in the relative volatility of the two isotopes.

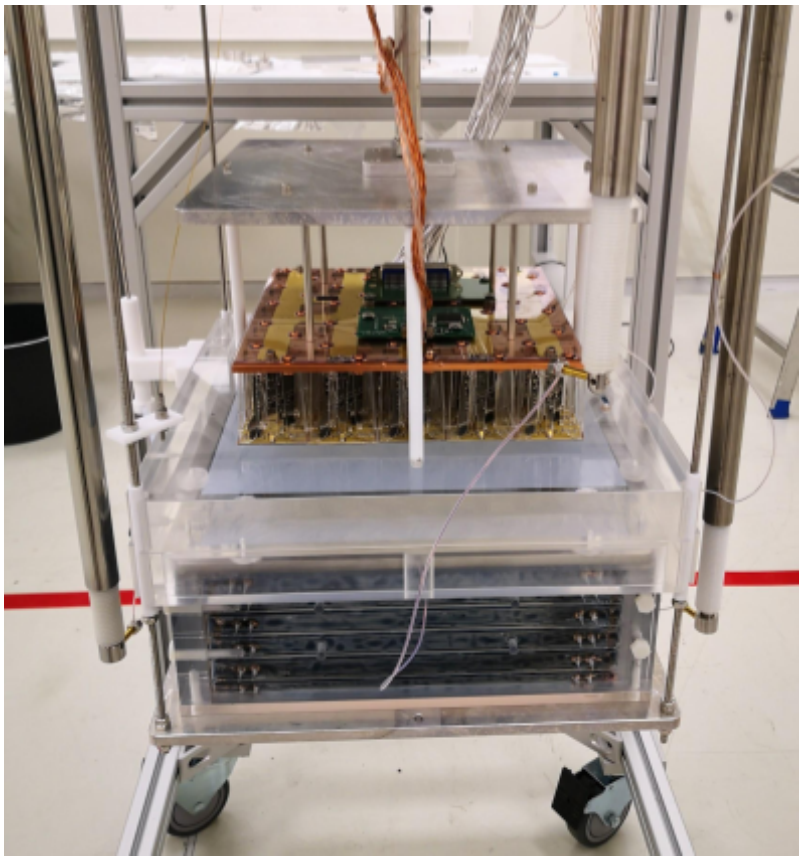

Figure 2.9: Proto-0 detector at CERN.

In November 2019, the first prototype of DarkSide, Proto-0, was succesfully operated for several weeks at CERN, with the aim of validating the SiPM technology prior to the large-scale construction of DarkSide-20k. It consists in a dual-phase detector with a volume of a 60 L of liquid atmospheric argon. The light is detected by a 35.2×35.2 cm^2 MB, containing 25 PDMs, placed on top of an acrylic vessel. A picture of the setup after its assembly is shown in Fig. 2.9.

In particular, I have contributed to the assembly of Proto-0 and the data collection at CERN, the analysis software development and the detector characterization. In addition, I have developed the database for Proto-0 to monitor the MB stability over time.

The next step before starting full-scale production of DarkSide-20k is the operation of Proto-1, a dual-phase detector with a volume of 1 tonne of liquid argon, which is planned for 2022.

Chapter 3

DArT, a detector for measuring the ^{39}Ar depletion factor

Large liquid argon detectors offer one of the best avenues for the detection of galactic WIMPs via their scattering on atomic nuclei. The liquid argon target allows exquisite discrimination between nuclear and electron recoil signals via pulse-shape discrimination of the scintillation signals. Atmospheric argon (AAr), however, has a naturally occurring radioactive isotope, ^{39}Ar, a β emitter of cosmogenic origin.

The use of argon extracted from underground wells, deprived of ^{39}Ar, is key to the physics potential of large detectors. The DarkSide-20k dark matter search experiment will operate a dual-phase time projection chamber with 50 tonnes of radio-pure underground argon (UAr), that was shown to be depleted of ^{39}Ar with respect to AAr by a factor larger than 1400 [3].

Assessing the ^{39}Ar content of the UAr during extraction is crucial for the success of DarkSide-20k, as well as for future experiments of the GADMC. This will be carried out by the DArT experiment, a small chamber made with extremely radio-pure materials that will be placed at the center of the ArDM detector, in the Canfranc Underground Laboratory (LSC) in Spain. The ArDM LAr volume acts as an active veto for background radioactivity and it will provide the cryogenics conditions necessary to operate with liquid argon. The DArT project is described in this chapter, including the chamber design, construction, and expected performance [5].

3.1 Underground argon in DarkSide-20k

The detection properties of LAr are particularly favourable for the rejection of radioactive backgrounds that produce electron recoils. In experiments searching for WIMPs, there is significant difference between the time distribution of the scintillation signals produced by these interactions compared to that of nuclear recoil events. The DEAP-3600 experiment, with 3200 kg of LAr, has demonstrated an exceptional pulse shape discrimination against such background, projected to be over 10^9 [133].

The DarkSide-50 experiment has demonstrated the background-free capability of the dual-phase time projection chamber technique [134]. The dual-phase method also allows to search for lighter WIMPs (m_χ<10 GeV/c^2) using the electroluminescence signal alone, as demonstrated by DarkSide-50 [90, 135]. With careful control of the electron recoil background, a multi-ton LAr detector has the potential to reach the neutrino floor due to solar neutrino interactions, via coherent elastic scattering

on target nuclei, in this low mass region.

A potentially limiting factor for the sensitivity of LAr-based experiments is the presence of the ^{39}Ar radioactive isotope, present at a rate of 1 Bq/kg in atmospheric argon. One of the key enabling technologies of the GADMC program is the argon target obtained from the high-throughput extraction of low-radioactivity argon naturally depleted in ^{39}Ar from underground sources (UAr) via the Urania plant in Cortez (USA). Urania will deliver 330 kg/day of UAr with 99.99% purity. The underground argon will be further purified chemically to detector-grade argon in Aria at the rate of 1 tonne/day. Aria is a 350 m cryogenic distillation plant currently being commissioned in Sardinia, Italy. Although not its primary goal, Aria can also be operated in isotope-separation mode to achieve a 10-fold suppression of ^{39}Ar per pass at a rate of 10 kg/day [132].

The DArT in ArDM experiment at the Canfranc Underground Laboratory (LSC), Spain, will measure the ^{39}Ar content in batches of the UAr delivered by Urania and Aria. In the shielded environment of the LSC, DArT in ArDM will be sensitive to very high depletion factors of ^{39}Ar, of the order of 1000. These measurements are crucial for the DarkSide-20k physics program and for the future experiments of the Global Argon Dark Matter Collaboration.

3.2 The DArT experiment

The DArT experiment at LSC aims at measuring UAr-to-AAr ^{39}Ar depletion factors of the order of 1000 with 10% precision in one week of running. The ^{39}Ar isotope decays via β emission with an end-point of 565 keV. DArT is a single-phase liquid argon detector, with an active volume of approximately one litre, that will be filled with underground argon samples from Aria. Sampling directly UAr from Urania, with a SAES getter in front, would also be possible. The light produced by ionizing radiation in the active volume will be readout by two 1 cm^2 silicon photo-multipliers (SiPMs) procured from the DarkSide-20k production packaged with the cryogenic readout electronics. DArT will be housed at the centre of the 1 tonne LAr ArDM detector [7, 136] (Fig. 3.1), which will serve as an active veto to tag both internal and external radiation. The ArDM setup will be operated in the single-phase mode with a new set of low-radioactivity photo-multipliers (PMTs), 6 at the top and 7 at the bottom. A reflector foil coated with TPB wavelength shifter will cover the inner surface of the cylindrical barrel to enhance light collection. The cryostat is surrounded by a 50 cm thick polyethylene shielding (not shown in the Fig. 3.1).

Background is largely composed of γ-rays originating from within the detector materials and from the surrounding cavern that are energetic enough to penetrate into the DArT chamber. To minimize the background induced by its intrinsic radioactivity, DArT is built with selected radio-pure materials. In DArT, the LAr is contained inside an outer vessel made of ultra-pure 99.99% Oxygen Free High Conductivity (OFHC) copper. A smaller cylindrical structure made of radio-pure acrylic (PMMA) is inserted in the copper cell and provides the cleanest possible surface for the UAr under test, as well as the support for the SiPM detector assemblies. Following a procedure developed by the DEAP-3600 collaboration [137], the inner surfaces of the acrylic structure directly in contact with the argon are sanded after fabrication to suppress backgrounds deriving from the plate-out of ^{222}Rn daughters.

In order to suppress the impact of external photons from the experimental cavern,

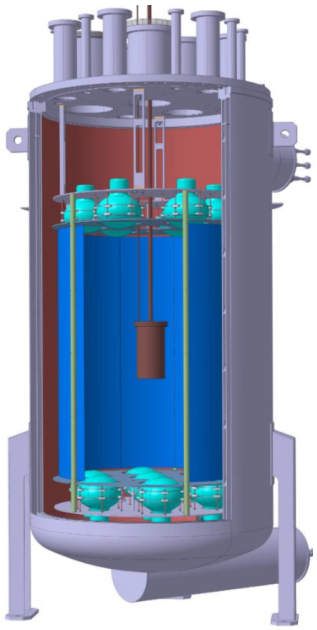

Figure 3.1: DArT detector in the centre of the ArDM cryostat.

which dominate the background budget, a 6 tonne lead shield will be installed around the ArDM vessel, in the hollow space between the ArDM cryostat and polyethylene shielding. The lead shield is a 140 cm height octagonal prism, with 10 cm width walls. In this configuration, the detector will be capable of measuring with high precision the larger ^{39}Ar depletion factors of the UAr batches coming from the Urania plant.

The lateral wall of the copper cylinder is 5 mm thick and the top and bottom caps are 8 mm thick (Fig. 3.2). The top flange allows access to the inner part of the chamber. A 1.5 mm thick indium wire is used to seal the top flange-copper cylinder interface. The contribution of indium to the overall background budget is negligible. The DArT chamber was leak tested at cryogenic temperature, evacuating the system up to 10^{-6} mbar. The DArT instrumentation and services, including SiPM bias and readout, and a level meter signal, are routed through the top flange into a 15 cm long copper pipe leading to the top of the ArDM cryostat. A thinner off axis pipe, that penetrates the copper chamber and extends almost all the way to the bottom, is the argon fill line.

The inner acrylic structure is made of 8 pieces (Fig. 3.3): attachment to the top cover, inner and outer cylinders, 2 SiPM supports, 2 end caps, and facilities support on the bottom. Two 6 mm thick disks cap the inner cylinders in front of the SiPMs. The internal surfaces of these disks and the inner acrylic cylinder are coated with 200 μg/cm^2 wavelength shifter (TPB). The outer surface of the acrylic is wrapped in Vikuiti reflector foil [138]. An additional cylindrical shell (annulus) is used as a filler between the reflector foil and the copper vessel. The outer acrylic parts are attached to the top vessel flange. Two dedicated boards attached to the bottom and top acrylic disk with acrylic screws hold the SiPMs.

Currently the detector construction is almost complete and is in commissioning phase, the DArT experiment is expected to test UAr not only for DarkSide-20k, but also for any future experiment of the GADMC, such as ARGO and a possible tonne-scale detector to search for light dark matter. It is also being considered for

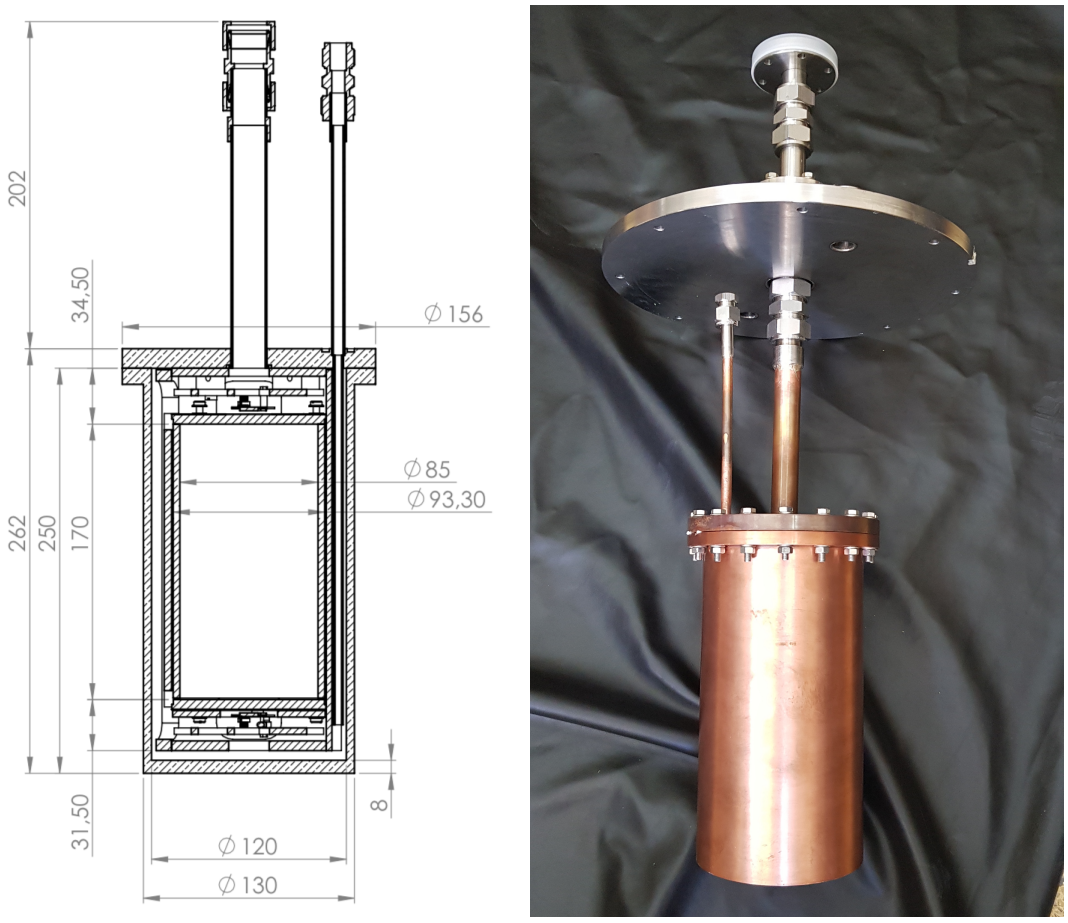

Figure 3.2: (Left) Sketch of the inner structure of DArT. (Right) Picture of the actual detector. The short stainless steel pipes are used in the cryogenic tests, and will be replaced by longer tubes in the final setup.

Figure 3.3: (Left) Inner acrylic structure lateral view. (Right) Top acrylic cap and support disk with the photo-detector module installed.

use by other experiments [139].

3.2.1 Photo-electronics

Scintillation light in DArT will be collected by two photo-detector modules (PDM), specifically designed to maximise the radiopurity and simplify the connections. Each PDE (Fig. 3.4) is based on a module integrating both, a 11.9×7.8 mm^2 SiPM, and the readout electronics in a 15×26 mm^2 PCB. The SiPM cell size is 25 μm, and has a quenching resistor of 10 MΩ at 77 K. These SiPMs are based on the NUV-HD-Cryo technology developed by FBK for DarkSide-20k, which allows low afterpulse at cryogenic temperature with extended over-voltage [140]. The SiPM sensitivity peaks at 400-420 nm, with a photo-detection efficiency above 50% at room temperature. The pre-amplifier is based on the low-noise design developed at LNGS [141]. Overall, a signal-to-noise ratio in excess of 40 is achieved when operated at an overvoltage of 7 V, with a rise time of 2 ns and a total power dissipation of 200 mW.

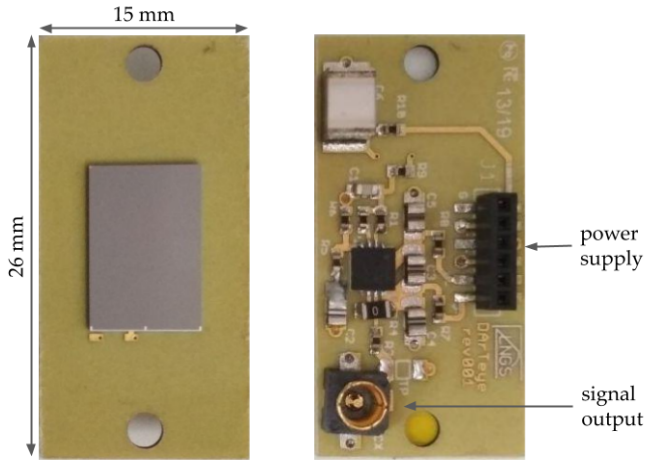

Figure 3.4: Images of the front and back sides of the front-end boards housing the SiPM for light readout.

The energy scale of DArT will be studied with AAr, that provides a well-known, high statistics ^{39}Ar spectrum. The energy resolution will be measured using an ^{83m}Kr gaseous source injected into the argon stream, a method first demonstrated in argon in 2009 [142] and successfully exploited since then in many experiments, including DarkSide-50 [134].

3.2.2 Cryogenics

DArT is connected to the cryogenic system of the experiment through two copper pipes (Fig. 3.2). They are joined with a silver brazing to two stainless steel pipes that go up to a CF200 flange, on top of ArDM, which provides the external connections. The schematics of the gas handling system and cryogenics is in Fig. 3.5. High oxygen traces in the liquid argon would quench the scintillation signal produced in the detector target. Hence, less than 1 ppm of oxygen is left in the chamber before filling it with argon, pumping the system below 10^{-3} mbar at room temperature. The pumping system is equipped with vacuum gauges and a turbo pump connected

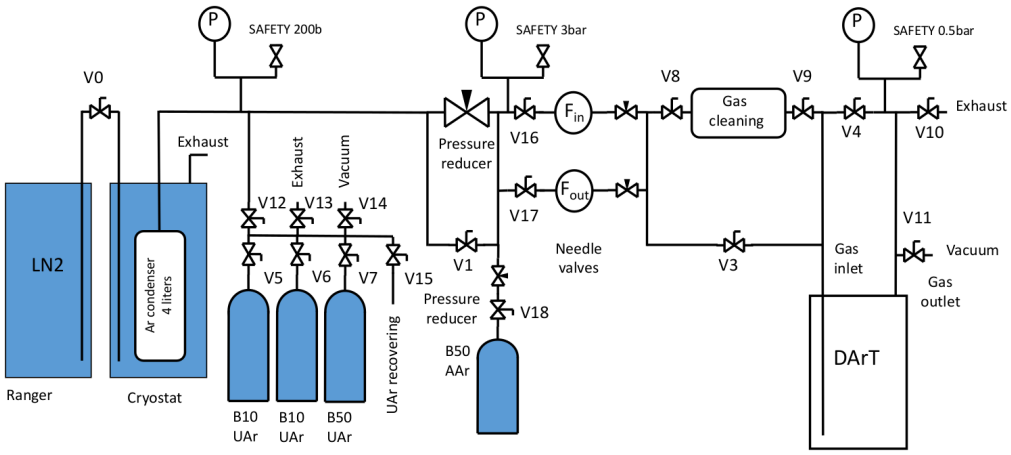

Figure 3.5: Schematics of the gas handling and cryogenic system for the operation of DArT. P indicates mechanical pressure gauges, F stands for flow meters and V denotes valves.

to valve V11. The pump is kept on while the system is warm. The system is proven leak tight at a level better than 10^{-7} mbar ℓ/s.

In normal operational conditions the DArT chamber is kept isolated closing all the in/out valves and reaches the thermal equilibrium with the surrounding liquid argon of ArDM. The pressure inside DArT is very close to the pressure of ArDM which, in order to avoid argon contamination in case of a small leak, is kept at a few mbar above the atmospheric pressure.

DArT will undergo filling and emptying cycles as needed for testing different argon batches. The evacuated DArT chamber is filled by condensing gaseous argon on the walls of the vessel (5 mm thick) and of the copper pipes (1 mm thick), whose external sides are maintained at fixed temperature by the ArDM LAr bath. The filling rate is established by the inflow meter/controller, which supplies the STP argon gas to be cooled and condensed in DArT. Given the high thermal conductivity of copper, a substantial filling rate can be maintained without a significant drop of temperature across the copper walls and without a significant increment of the pressure inside DArT. The limiting factor for filling DArT is the ability of ArDM to dissipate safely to the cryocoolers the heat needed to condense the Ar. The ArDM dissipated heat is limited to a maximum of 20 W. The amount of LAr in DArT is 1.58 liters. To fill DArT, the energy needed for cooling the argon gas to its liquefaction point is 230 KJ, while 355 KJ are needed for its full condensation. The filling level of the DArT chamber is monitored by three PT1000 sensors. These platinum resistors are used as level sensors thanks to the different self-heating of their resistance in gas (with thermal conductance 3.2 mW/K) and liquid (32 mW/K) phases. When filling, the argon flows through a hot getter for its further purification before reaching the DArT chamber.

The time required for filling DArT is at least 8 hours. The expected run time of the experiment ranges from one to several weeks per argon batch, depending on the argon purity. Therefore, one full day for condensing and evaporating the argon in the chamber is not a dominant component in the duty cycle of the experiment.

To empty the DArT chamber, the argon is evaporated and temporarily stored

in a 4 liter condenser bottle, enclosed in an LN_2 cryostat. As the condenser is refrigerated with liquid nitrogen (77 K), the argon converts into solid phase and therefore its saturated vapor pressure is about 260 mbar. This pressure cannot of course be applied directly to the liquid argon in the DArT chamber because the LAr would also freeze. The flow of gaseous argon into the condenser is therefore controlled in such a way that the pressure inside the DArT chamber is higher than the triple point pressure of LAr (682 mbar) and lower than the equilibrium pressure of ArDM. These operating conditions guarantee that neither the LAr will freeze within the DArT chamber nor the gaseous argon will re-condense on the walls on its way out. In particular, the LAr will become overheated and will evaporate on the free surface of the LAr, cooling a layer of liquid beneath the surface. Because of the low thermal conductivity of the LAr, the surface is thermally insulated from the bulk of LAr and the evaporation process is very inefficient. To speed up the evaporation of the LAr, two PT100 platinum resistors, dissipating 3.5 W each, are located near the bottom of the DArT chamber. The work required to evaporate the DArT LAr is 355 kJ, so the chamber is emptied in about 14 hours. When the DArT chamber is empty, the condenser will be full and it may be warmed up. The argon gas is then transferred to a high-pressure storage bottle.

3.3 Signal and background studies

Studies of the physics reach of the experiment are performed with tuned-on-data Monte Carlo simulations based on Geant4 [143], with the simulation framework of the DarkSide-50 experiment (G4DS [144]). This package contains a detailed description of DArT and ArDM layout, including the lead and polyethylene shields. A general view of the ArDM simulated geometry with DArT integrated inside is shown in Fig.3.6.

In the DArT detector, signal events are electron recoils from the β decay of ^{39}Aroccurring within the inner acrylic vessel. These events deposit all their energy in DArT, leaving no signal in the veto detector, ArDM. The range of the energy spectrum in DArT below 600 keV is defined as the *region of interest* (ROI) where the signal events are contained. Background events stem from radioactive decays in the detector materials and in the experimental hall surrounding the detector. They typically produce γ particles that deposit energy in DArT and/or in ArDM via Compton scattering. We assume that nuclear recoils are efficiently rejected using the powerful scintillation pulse shape discrimination technique in LAr. Background events that leave a signal with energy in the DArT ROI are tagged as background and removed from the analysis when they also deposit more than 10 keV in ArDM. If, however, less than 10 keV is deposited in ArDM they will go *untagged* and contribute to the background of the measurement.

The energies deposited in ArDM and DArT per week are shown in Fig. 3.9 with a stacking of the material and external background events. In Fig. 3.9-left, different peaks are clearly visible at 1450 keV, 1700 keV and 2600 keV, compatible with γ^s coming from ^{40}K, ^{210}Bi and ^{206}Tl, respectively. No clearly peaks are observed in the DArT energy distribution, due to the small active volume of DArT, which, in most cases, is not able to fully contain the high energy γ^s.

The amount of ^{39}Ar in an argon sample is determined from fits to the spectral shapes of electron-like recoils in the LAr target expected in the ROI with no coin-

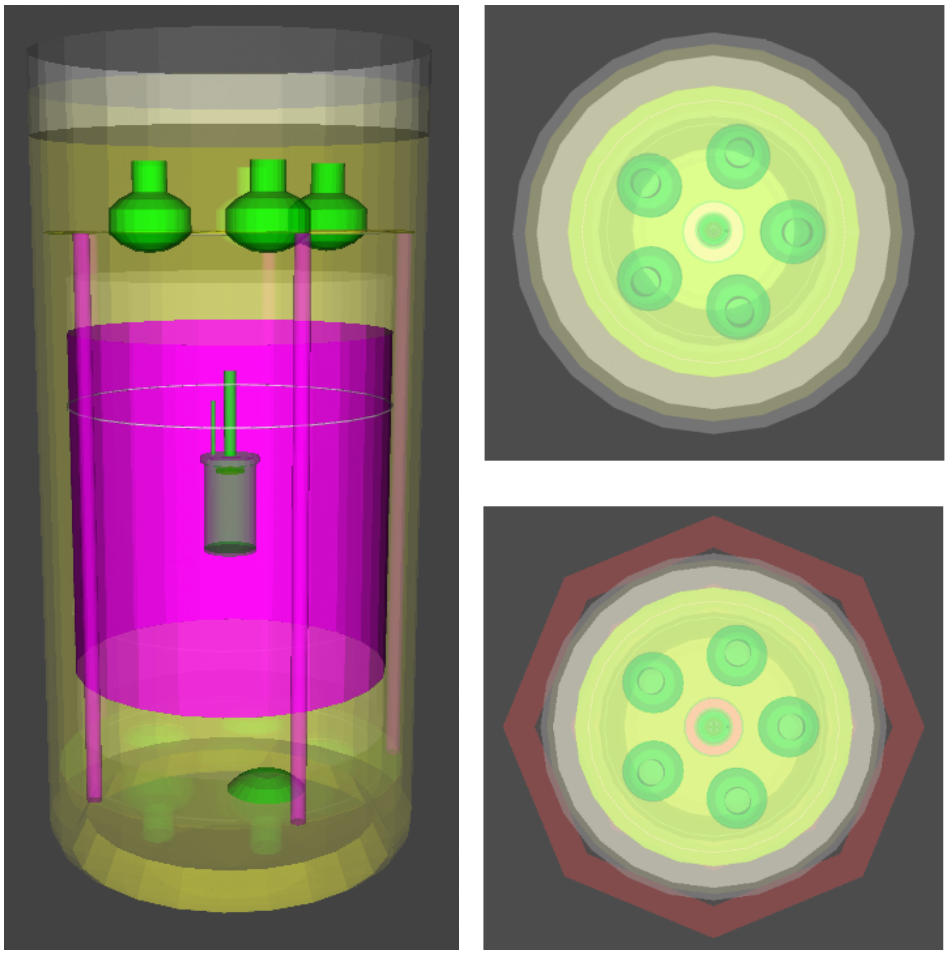

Figure 3.6: Lateral and top views of the ArDM geometry initially implemented in G4DS, with DArT integrated. Down-right: Top view with the lead belt integrated (red) around the ArDM cryostat. An updated geometry is used in the latest simulations, reproducing the actual design of ArDM.

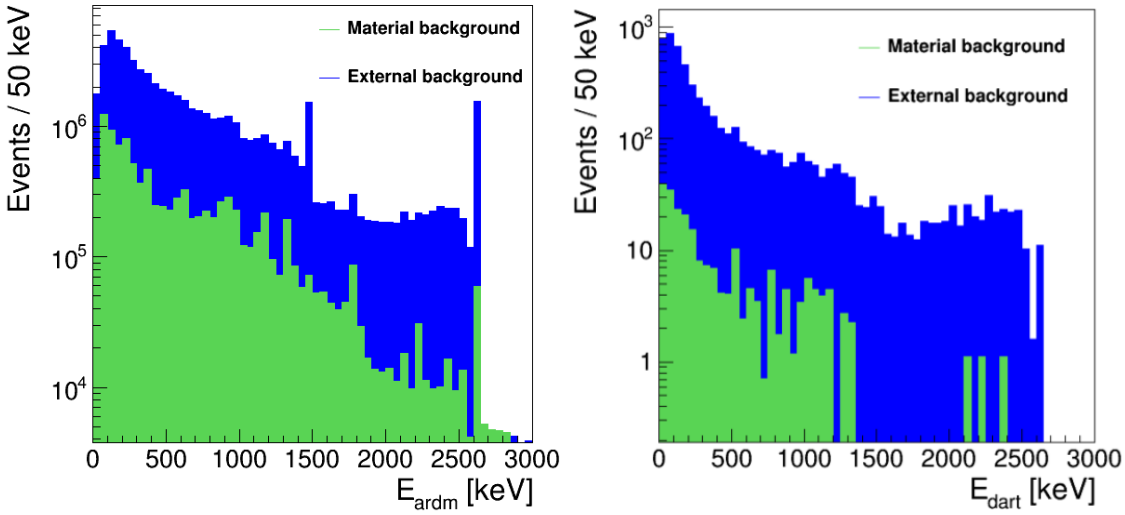

Figure 3.7: Internal (green) and external (blue) γ background spectra in ArDM (left) and DArT (right) expected per week.

cident ArDM tag. The normalization of the background can be constrained by the high-energy region of the DArT energy spectrum, above 600 keV, where no signal events reside and whose rate is assumed constant or predictable in time. Background rates and origin are based on actual assays of screened materials and *in situ* measurements in the underground hall A at LSC. The values for the radio-impurities and masses of internal materials are summarized in Table 3.1, along with the figures for the external background (from outside ArDM).

Table 3.1: Activities (in mBq/kg, except for ^{210}Bi that is in mBq/m^2), masses (kg) and surface areas (cm^2) for the different materials used for ArDM and DArT simulations. As the ^{238}U secular equilibrium in Arlon is broken, the upper, middle and lower parts of the chain are considered. (*) γ flux per cm^2 at the outer surface of the polyethylene shielding of ArDM. (**) Surface in cm^2.

Source		^{238}**U**	^{232}**Th**	^{40}**K**	^{60}**Co**	^{210}**Pb**	^{210}**Bi**	**mass [kg]**
ArDM Cryo		3.42	6.37	1.3	11.21			1630
ArDM PMTs	Base	9176	11043	1978				10.8
	Metal	181	73	371				
	Glass	636	115	53	2			
Lead shield		0.37	0.073	0.31		10		6000
ArDM pillars		0.012	0.04	0.06	0.04			26.5
ArDM rings		3.42	6.37	1.3	11.21			4
PMTs support		3.42	6.37	1.3	11.21			16
Acrylic		0.004	0.005				0.22	1.8
DArT Cu		0.012	0.04	0.06	0.04			6.95
SiPM Arlon	Up	3.8	70	1300				0.001
	Mid	53						
	Low	137						
Solder brazing		1203	406	3090				0.001
External		0.72*	0.13*	0.05*				800700**

The untagged background events per week in DArT are depicted in Fig. 3.8. The different main contributions are represented together with the UAr signal spectrum. The total number of background events per week is 13385 (10300 in the ROI). About 97% of the background comes from sources external to ArDM [145]. For convenience, we have simulated the external background events with an uniform spatial distribution. However, most of the external events that reach DArT come from the sides of the detector, due to the smaller distance that external γ^s have to travel to reach DArT.

To study the performance of the detector reducing the external background a lead belt is simulated around ArDM (Fig.3.6). The total number of background events per week in the ROI with the lead shield is 7210, of which 465 are untagged. The number of expected events from the materials is much lower, 368 per week (299 in the ROI). The DArT fiducial mass is 1.3 kg of LAr. Assuming the ^{39}Ar activity in the UAr measured by DarkSide-50, 0.73 mBq/kg (for a corresponding depletion factor of 1400), we expect 613 signal events per week, yielding a signal-to-background ratio (S/B) of ≈ 0.06, too small to perform a meaningful measurement without the lead shield. The lead shield reduces the external background by a factor about 20,

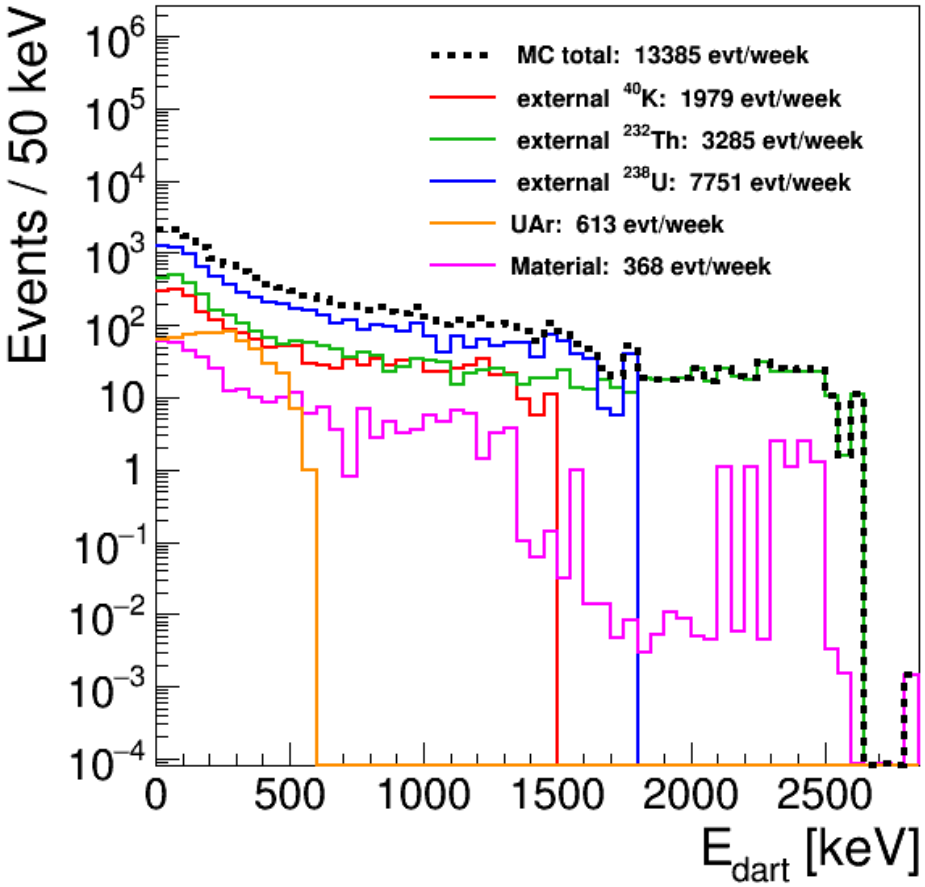

Figure 3.8: Total background (black) and contribution of the main components. The external background has the largest contribution with 13015 events/week. Assuming a DP = 1400, a signal of 614 events/week of ^{39}Ar is expected.

leading to S/B $\approx$ 1.3. The background spectrum per week with and without the lead shield is represented in Fig. 3.9.

The current ArDM single-phase geometry, with 13 PMTs and DArT shading some of the light, will be able to detect events with energies as low as 10 keV. The sensitivity to the ^{39}Ar signal is subject to further optimisation by tuning the ArDM veto energy threshold. The dependence of the number of untagged background events in DArT is calculated as function of such threshold, and is found to be linear with a slope of 8.5×10^{-3}/ keV.

3.4 Light response simulation

The energy deposits in the liquid argon of DArT produce vacuum ultraviolet photons (VUV) that, once converted to visible photons (420 nm) by the TPB, are either detected by the two SiPMs or absorbed elsewhere. The simulation of the propagation of photons to the SiPMs with Geant4 takes into account the optical properties of the detector materials and their interfaces, in particular the acrylic (PMMA), the TPB coating of the internal surfaces, the reflector foil and the SiPM planes. Most of these materials are modelled as pure dielectrics, with the exception of the

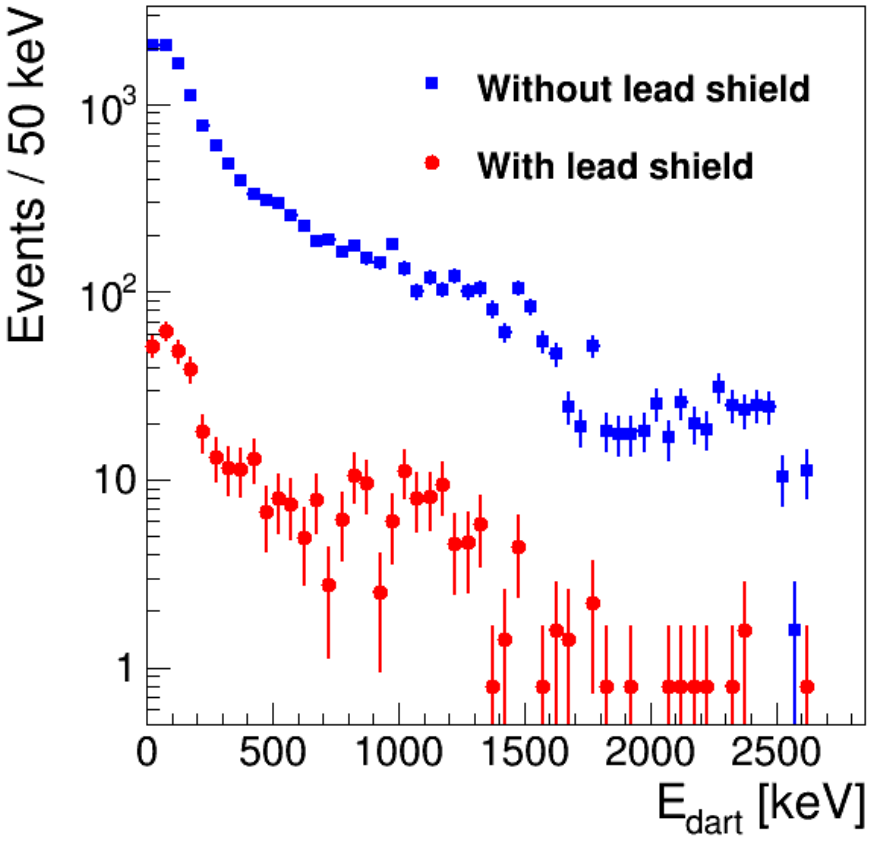

Figure 3.9: Expected untagged background events in DArT with the lead shield (red circles) and without (blue squares) in one month of data taking, assuming a veto threshold of 10 keV.

reflector which is assumed metallic, *i.e.* a surface that photons cannot penetrate. The TPB is assumed to re-emit a single visible photon (VIS) for each absorbed VUV photon with a characteristic time of 1.5 ns. The SiPMs are modelled as dielectrics with an arbitrarily reduced absorption length, in order to fully absorb the transmitted visible photons in a few nanometers. Absorbed photons are converted to photo-electrons, with a photon detection efficiency (PDE) dependent on the incident photon wavelength with a value of 40% at 420 nm. Simulation parameters are tuned according to reference [144].

The light response of the detector is evaluated simulating 20000 ^{39}Ar events in the DArT active volume. The mean energy of the ^{39}Ar β emission is 210 keV. Thus, considering a W-value for producing a VUV scintillation photon in LAr of 19.5 eV, and a quenching factor of 0.95 for electrons [146], on average 10230 photons are produced per event, corresponding to 48.7 VUV-photons/keV. The fraction of visible photons produced per VUV photon is ∼98.5%, which accounts for the tiny absorption of VUV photons in LAr.

The reflector foil is placed on the sides of the active volume and on the top and bottom acrylic caps, around the SiPMs, providing a light collection efficiency largely independent of the event position (Fig. 3.10). The average light collection efficiency is ∼58%, which corresponds to a light yield of 9.5 PE/ keV. For reference, about 3000 PE are recorded per SiPM for energy deposits at the endpoint of the ^{39}Ar

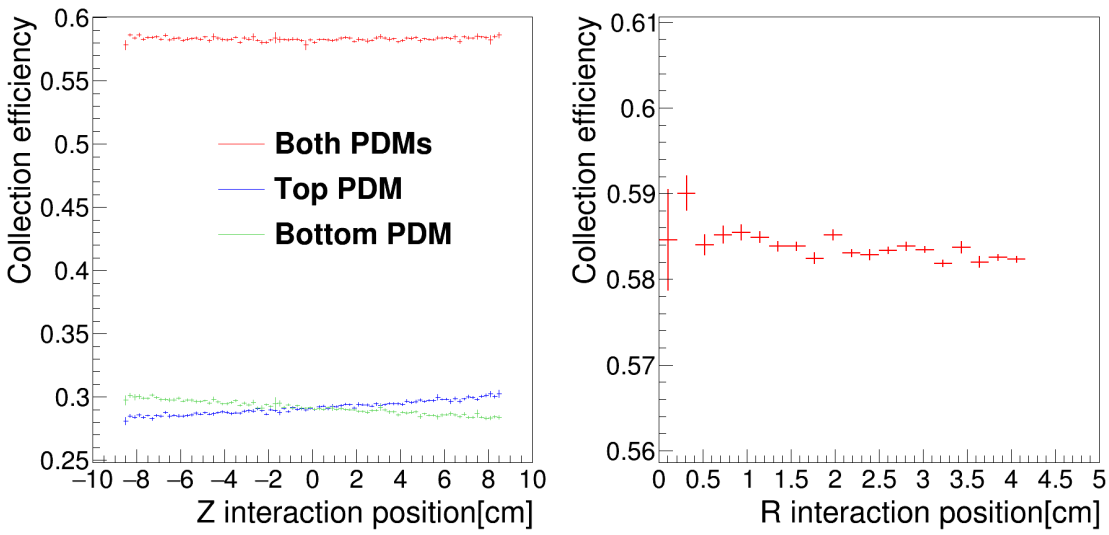

Figure 3.10: Average light collection efficiency vs. height (left) and radius (right) of the interaction position.

spectrum. Approximately, 30% of the scintillation photons are collected in ∼4 ns (the fast component in Ar), that is ∼900 PE, well within the dynamic range of the readout electronics. The slow scintillation component delivers photons over an extended period. If the dynamic range of the light sensors turns out to be insufficient, the LY can be decreased by reducing either the overvoltage of the SiPMs (that is related to the PDE) or the effective area of the reflector.

The energy resolution is calculated with energy deposits from 50 keV up to 800 keV uniformly distributed in the DArT active volume. An energy resolution between 3 % and 6 % is found in the ROI. The SiPM energy resolution is not considered at this point. The final energy resolution is the convolution of both.

3.5 Simulation of the electronic response

The response of the PDM installed in DArT is studied using the DarkSide-20k electronics simulation package. This program contains a set of parameters tuned to simulate the behaviour of the electronics. These parameters are: 15% after-pulsing probability, 20% direct cross-talk between SiPMs cells and 100 Hz of dark current. A gain of 80 ADCc/PE is considered for the simulations. The data acquisition system is simulated as a 14-bit ADC card with a range of 2 Vpp, and a resolution of 5×10^8 samples/s. The acquisition time window is set to 8 μs with a 1 μs pre-trigger time window. The response function of the SiPMs is obtained in specific tests with an LED at CIEMAT (Chapter 4). Two components are distinguished, a Gaussian peak with a width of 4 ns, and a slow exponential signal with a time constant of 540 ns, due to the discharge of the SiPMs (t_{SiPM}). The relative weight of exponential part is 96%.

The simulated signals corresponding to α and β particles collected with a fast optical readout, as a PMT, are presented in Fig. 3.11. As expected, both types of interactions are clearly distinguishable. After checking that the simulation works properly, t_{SiPM} is increased to 540 ns, including the previously mentioned electronic

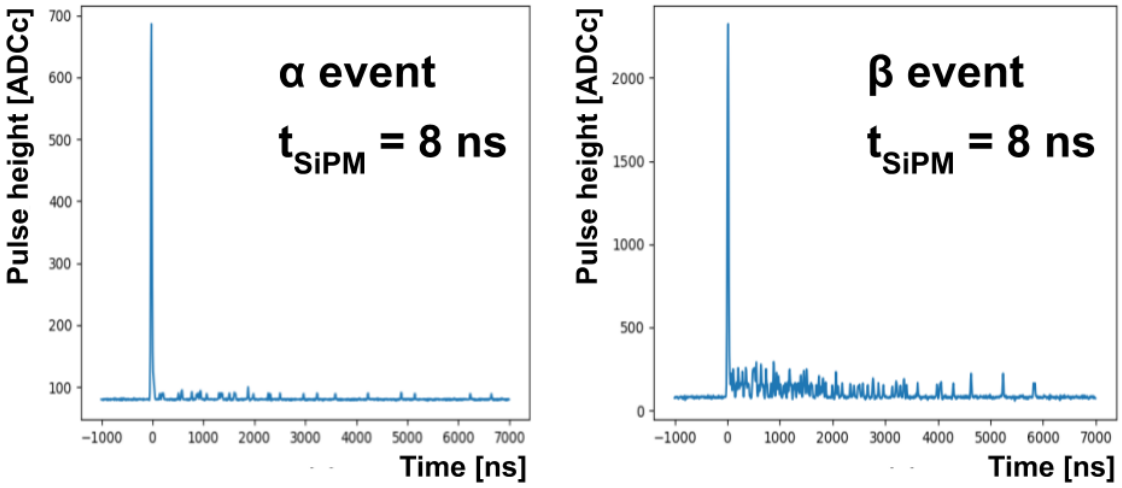

Figure 3.11: Simulated pulses for α (left) and β (right) events assuming a response time of 8 ns.

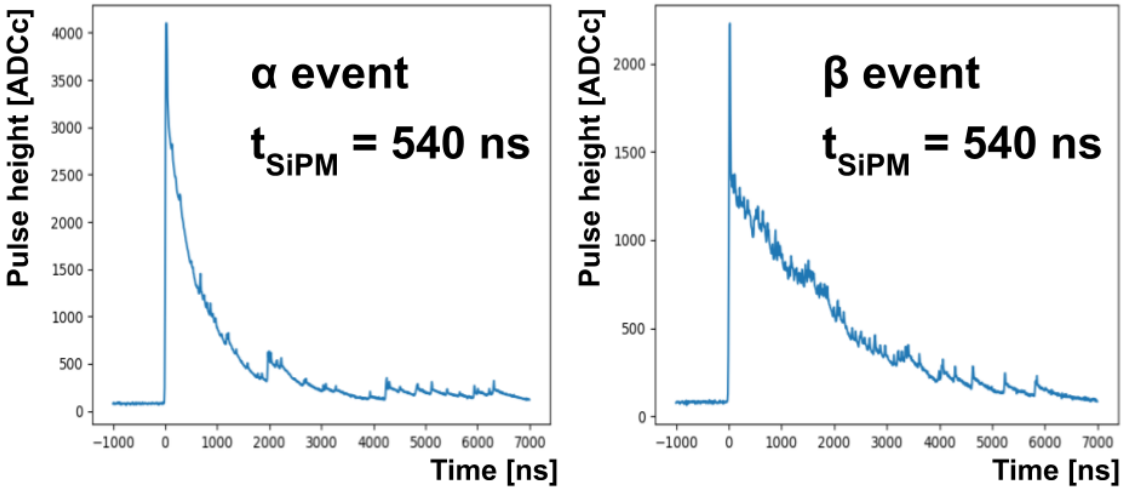

Figure 3.12: Simulated pulses for α (left) and β (right) events assuming a response time of 540 ns.

effects. The result for an α and a β event of 100 keV are shown in Fig. 3.12. The slower response time causes α and β events to produce similar signals, making difficult to perform the pulse shape discrimination, which requires the development of software capable of decoupling the scintillation pulse and the response of the PDM.

By increasing the energy of the incident particle, or in other words the number of incident photons, saturation effects are observed in the electronics. The integrated charge as a function of the deposited energy for β events is shown in Fig. 3.13-left. The linearity of the response is lost above 300 keV. This effect would produce distortions in the shape of the ^{39}Ar spectrum, making difficult to estimate the depletion factor correctly. Therefore, the gain of the PDMs is reduced, increasing the dynamic range by a factor of 20. In this case, the linear response over the entire ROI is recovered (Fig. 3.13-right) probing that the PDMs are suitable for light detection in DArT.

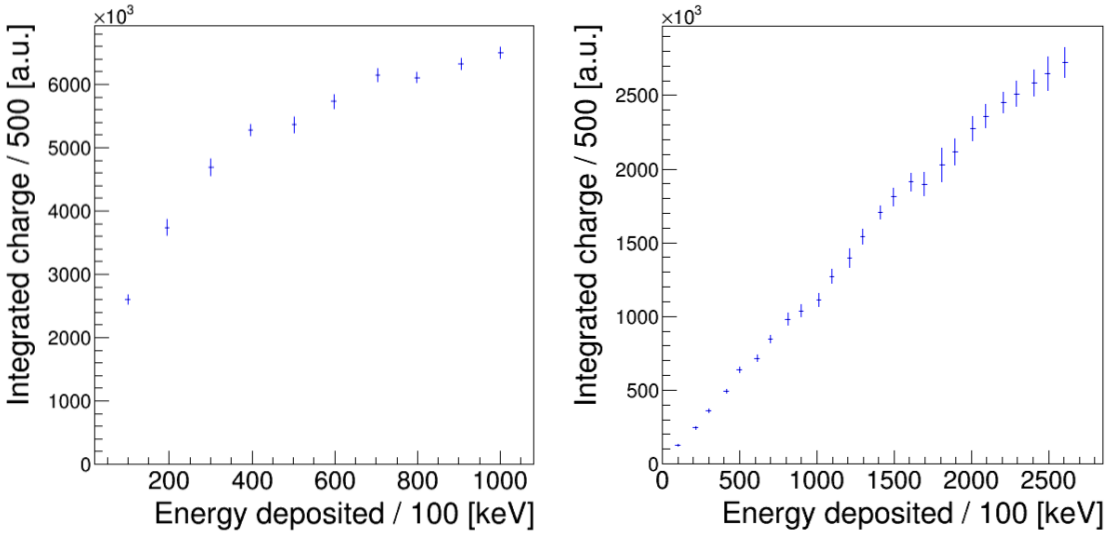

Figure 3.13: Integrated charge with respect to deposited energy for β events with a gain of 80 ADCc/PE (left) and 4 ADCc/PE (right).

3.6 Sensitivity to the ^{39}Ar signal

Using the background values and the light characterization illustrated in the previous sections, we evaluate the DArT sensitivity expected for different ^{39}Ar depletion factors, using a veto threshold of 10 keV. In the following, we calculate both the measurement uncertainty on the depletion factors in case a clear signal is observed and the 90% confidence level (C.L.) upper limits in absence of an excess over the expected background.

A typical photo-electron spectrum, for background and signal events acquired in one week of running of DArT, is displayed in Fig. 3.14 for ^{39}Ar depletion factors of 10 and 1400, respectively. The so-called *simulated data* distribution is a randomized distribution generated from the sum of the signal and background distributions. The ^{39}Ar content is extracted from a fit of the observed shape to the weighted sum of the signal and background distributions. From these fits, the expected statistical uncertainties per week on the measurement of different depletion factors of ^{39}Ar are extracted (Fig. 3.15). In the configuration with the lead shield, the uncertainty is below 1% for a depletion factor (DF) of 10, 1% for $DF = 100$, 7% for $DF = 1400$ and 40% for $DF = 14000$. The upper limit at the 90% C.L. is reached for $DF \approx 6 \times 10^4$. Without the lead shield, the statistical uncertainties increase, typically, by a factor 3, and the 90% C.L. upper limit is $DF \approx 5000$. The 90% one-sided confidence level upper limit (1.28 σ) is depicted in Fig. 3.15 for different depletion factors of ^{39}Ar.

These results assume the knowledge of the spectral shape of the signal and background from the simulations and, therefore, do not include systematic uncertainties.

3.7 Systematic uncertainties

The measurement of the ^{39}Ar depletion factor depends on a variety of factors that, if not accurately constrained, may lead to large uncertainties. Experimental effects

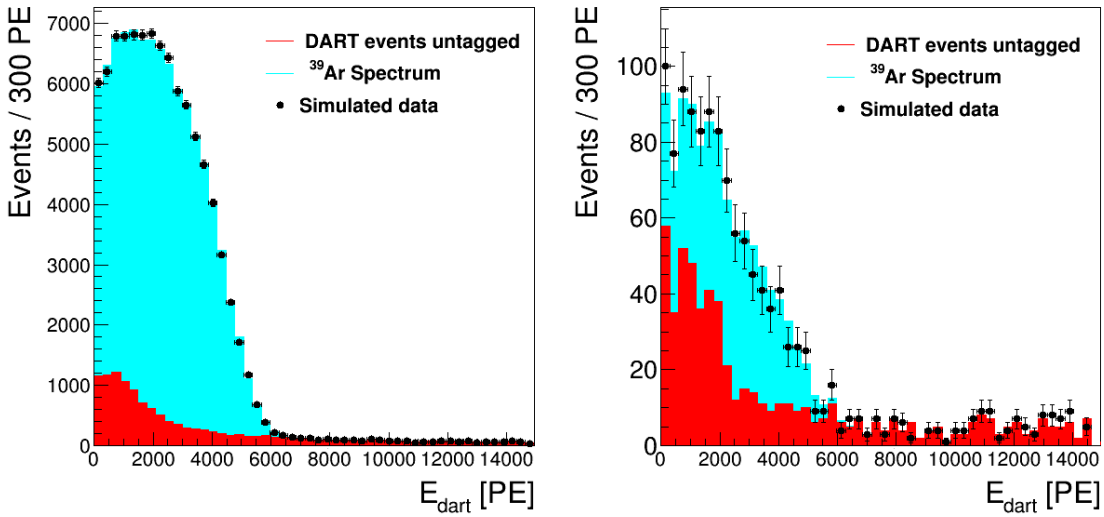

Figure 3.14: Photo-electron spectra corresponding to one week of data taking, (left) for an ^{39}Ar $DF = 10$ without lead shield and (right) for $DF = 1400$ with lead shield. The red (dark) histogram represents the background spectrum, the blue (light) histogram is the ^{39}Ar signal and the black dots denote the simulated data.

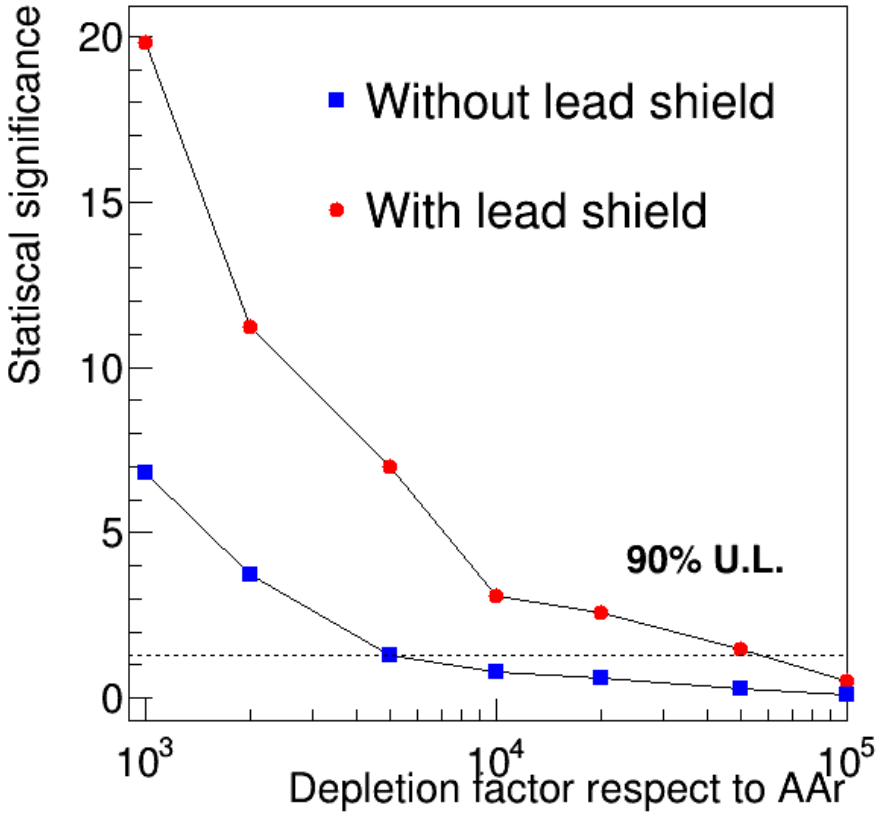

Figure 3.15: Statistic significance expected per week for different argon depletion factors. The 90% upper limit is indicated with a horizontal line. The red points correspond to the configuration with the lead shield and the blue ones without it.

potentially limiting the precision of the measurements are related to the operation of the detector (electronics, light yield, reconstruction software, data analysis) and background sources (from the materials and the walls of the experimental area). Some of these effects can be compensated by long data-taking periods, but not all. In this section, I describe the specific studies performed to understand and limit these effects, and to quantify their impact.

The uncertainties related to electronics are due to effects such as after-pulsing or saturation, which could distort the photo-electron spectrum. The linear response of the DArT data-acquisition system has been found in simulations to be linear up to 2.6 MeV, where the ^{206}Tl peak is present. It is necessary to assess this linearity with real data. In case the actual linearity of the electronic system is compromised by high energy events, there is a margin of operation by tuning the SiPMs overvoltage. Albeit the impact of these effects is expected to be small, specific studies are being performed in the commissioning phase of the detector. The slow response of the PDMs makes necessary to use algorithms that allow the extraction of the photo-electrons in each event and their correct reconstruction. Several such algorithms are being developed in DarkSide-20k. The variation in the reconstruction efficiency with the number of incident photo-electrons is an important uncertainty when obtaining the energy spectrum in DArT. Therefore, it is necessary to study the performance of the event reconstruction algorithm by simulating scintillation pulses with given numbers of photo-electrons, including the various effects of the electronics.

The light response of the detector is a potentially important source of uncertainty. Optical parameters like the ESR film reflectivity, the transmission coefficient of the acrylic walls, and the photon conversion efficiency of the TPB, affect significantly the light yield. Specific studies have been performed with simulations, with preliminary values of these optical parameters. Refined studies are necessary with more realistic values, to quantify the actual uncertainty expected in data.

The precise determination of the ^{39}Ar energy spectrum depends critically on the energy calibration of DArT. The absolute energy scale will be extracted from the energy spectrum of atmospheric argon, which provides a rich sample of ^{39}Ar events. The energy resolution will be measured using an ^{83m}Kr gaseous source injected into the argon stream. It is also possible to use external sources placed in a hole in the polyethylene shielding of ArDM, located at the same height as the midpoint of the DArT active volume.

The use of ^{57}Co source is evaluated, which produce 122 keV γ^s, with a branching ratio of 90%. Only a fraction of the γ^s produced reach detector, depositing in general a fraction of the energy. In a reduced number of cases, the γ reaches DArT, leaving there all its energy. This is verified simulating 10^6 γ^s originating in the polyethylene hole and shot horizontally towards the detector. The spectrum detected in one hour of data taking is presented in Fig. 3.16, both for atmospheric argon and argon with a depletion factor of 10, with and without the lead shield. In this study, the energy resolution is set to 10%, and the light yield is 9 PE/keV, independent of the energy. A clear peak is observed in the spectrum, which is fully contained for 30% of the events that reach DArT. The signal-to-background ratio in the ^{57}Co peak region is 0.5 for atmospheric argon, and 3.5 for depleted argon. From this type of study, we evaluate the activity of the radioactive source necessary to calibrate the detector in a reasonable period of time. In this case, the activity is 100 kBq, below the radiation limits permitted at LSC. More detailed simulations, with γs from the ^{57}Co produced

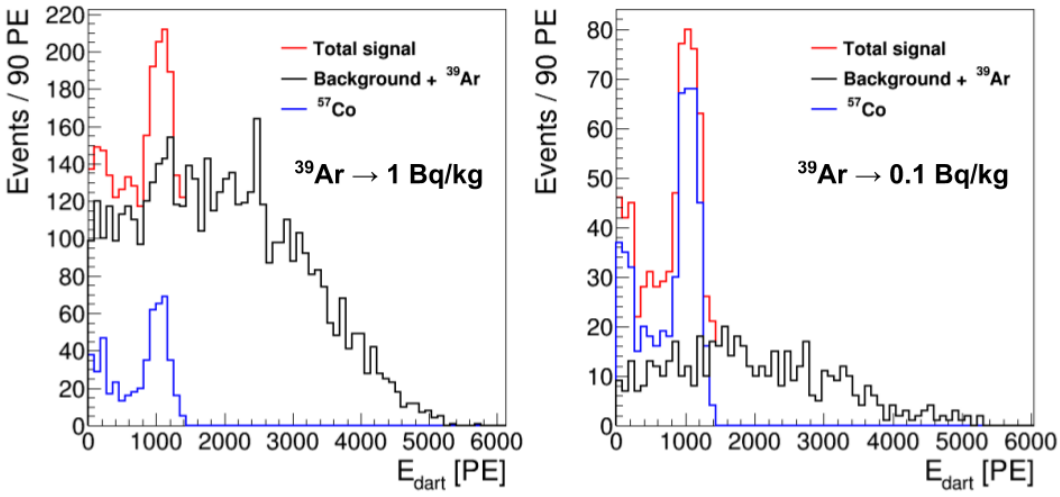

Figure 3.16: Simulation of the energy spectrum with ^{57}Co calibration source, assuming an ^{39}Ar activity of 1 Bq/kg (left) and 0.1 Bq/kg (right).

in a more realistic solid angle, will give more accurate predictions for the activity of the source.

Finally, the impact of the background determination in the measurement of the depletion factor is investigated. The background of DArT and ArDM materials has been thoroughly simulated. The radioactive contamination of the materials has been measured in several extensive campaigns (Table 3.1). The uncertainty in the estimation of the background from materials depends on the mass and radioactive contamination of the different detector components, and on the simulated geometry. Another important source of background are the γ-rays emitted from the surrounding cavern. In the simulation, the spatial distribution of the external background is homogeneous, which may not be strictly the case in the actual cavern.

The uncertainties considered in the determination of the backgrounds from materials and the external γ-ray radiation are 10% and a 30%, respectively. The ^{39}Ar depletion factor extracted from the fit is compared with the value introduced in the simulation, in order to evaluate the impact of these uncertainties. The accuracy of the depletion factor measurement for UAr (0.73 mBq/kg) in one week of data acquisition with the lead shielding, is reduced from 7% to 18% by introducing the aforementioned uncertainties in the background shape. Therefore, it is essential to characterise the background shape in DArT very precisely.

The external background uncertainty can be reduced comparing the spectrum detected without the top part of the ArDM polyethylene shielding and with the detector fully covered. This procedure has been successfully tested by the ArDM collaboration [145]. Another possible strategy is the background characterization with atmospheric argon, in which the amount of ^{39}Ar has been precisely measured. These different methods will make possible to reduce the uncertainties in the background estimations, improving the accuracy of the ^{39}Ar depletion factor measurement.

3.8 Conclusions

We have designed the DArT in ArDM experiment capable of measuring with high precision the amount of ^{39}Ar in the argon that will be used in current and future dark matter search experiments. The detector construction is almost complete and is in commissioning phase. The sensitivity of DArT was studied using a detailed background model and light response simulations. These studies show that our detector will allow us to measure UAr depletion factors in excess of 1000 with a statistical accuracy better than 10% in one week of counting time. The installation of DArT in ArDM at LSC is planned for the summer of 2021. The construction and commissioning of the detector on surface will be described in detail in the next chapter.

Chapter 4

Construction and commissioning of DArT

The construction of DArT started in 2019 at CIEMAT. At the end of 2020, a basic setup was ready, including a cryogenic system, voltage supplies, electrometer, and a LED coupled to a light pulse generator. The first detector integration tests and data taking were performed on the surface using this setup.

In this chapter, I describe the characterisation of the light detection modules produced for DArT, along with along with the analysis of the first DArT data taken with atmospheric argon. These tests are a fundamental milestone in the DArT experimental programme. The next step will be the installation of the detector at LSC, planned for 2021.

4.1 DArTeye characterization

DarkSide has produced ten PDMs specifically designed for DArT. These modules are called DArTeyes. They have been characterized at room temperature and cryogenic conditions in a dedicated test bench at CIEMAT.

The PDMs are mounted individually on a support structure, with an optical fibre placed at a fixed distance of 0.5 cm from the surface of the SiPM. The light from the fibre is incident perpendicularly on the centre of the active area of the SiPM. A fast light signal of 10 ns width is produced with a 400 nm LED coupled to a pulse generator. The intensity of the LED can be adjusted from 0.1 to 3.4 V providing 6 candela (cd) at maximum. The setup is installed inside a cryogenic dewar to perform tests with liquid nitrogen (LN_2). Additionally, the dewar is introduced in a black box to avoid light leaks. The full setup is shown in Fig. 4.1.

The PDMs undergo three temperature cycles (from 300 K to 77 K and back) to validate the stability of the wire bonding and the electronic components in cryogenic conditions. One signal connector was released during the test (over 21 cycles in total). The wire bonding was inspected before and after each cycle with a microscope, no damage being found.

The scheme of the DArTeye electronic board is depicted in Fig. 4.2. The preamplifier is supplied with two fixed voltages of +2.5 V (V_{CC}) and -2.5 V (V_{EE}). The SiPM is reverse polarised with a bias voltage, V_{BIAS}, provided with an independent power supply.

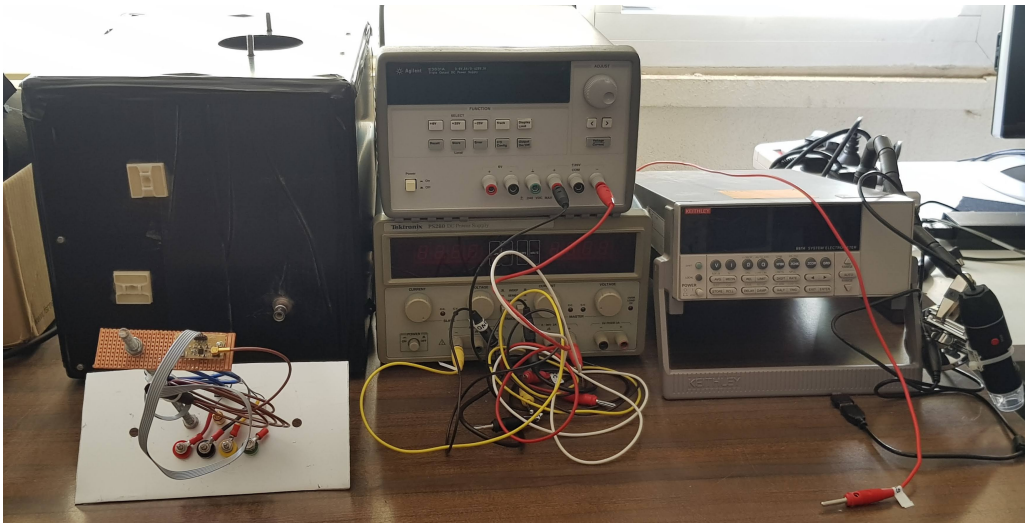

Figure 4.1: Experimental setup for the characterization of the DArTeyes. The devices in the image are, from left to right, black box, PDM support structure, PDM power supply and electrometer.

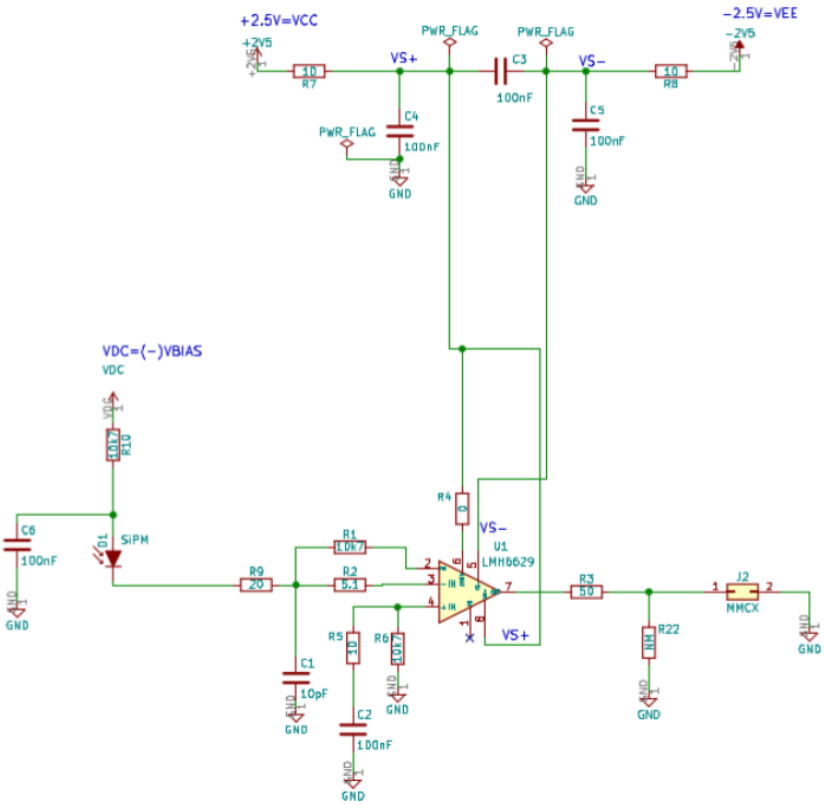

Figure 4.2: Schematics of the DArTeye electronic board.

4.1.1 Determination of the I-V curves

The SiPMs are characterised by measuring the intensity in response to the input voltages applied, the so-called I-V curves. These curves are obtained without an external light source. A key parameter of this characterisation is the breakdown

voltage, V_B, at which the electric field strength generated in the depletion region is sufficient to create a Geiger discharge.

To measure the I-V curves, different values of V_{BIAS} are considered, depending on the breakdown voltage of each SiPM, with a maximum of 40 V. The intensity is measured with a Keithley 6514 electrometer. A custom-made software is used to control the power supply and register the measured values.

The I-V curves, measured both at room temperature and cryogenic conditions (77 K) are presented in Fig. 4.3. The PDM number 6 was damaged during the bonding process and is excluded from the characterization. All the SiPMs have a similar behaviour with a breakdown voltage around -31.5 V and -26 V at 300 K and 77 K, respectively.

After verifying that all the SiPMs are operational, they are characterized using the dark current signals.

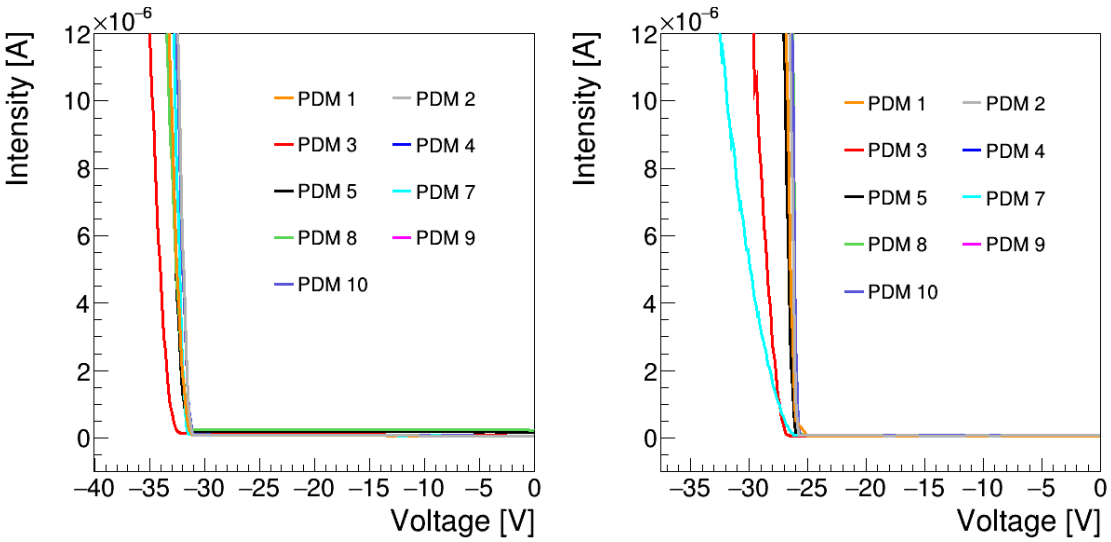

Figure 4.3: I-V curves measured at 300 K (left) and 77 K (right).

4.1.2 Measurement of the dark currents

The PDMs are characterized using dark current signals with the setup fully covered with a black blanket to avoid light leakage into the system. The event rate observed with a threshold of 400 mV on the oscilloscope and an overvoltage of 5 V is around 20 Hz. The results presented in this section are obtained with an overvoltage of 7 V, to increase the signal to noise ratio.

The data acquisition is made with an ADC (DT5725) with a resolution of 14 bits, a dynamic range of 2 V, and a sampling rate of 2.5 $\times$ 10^8 samples/s (4 ns time resolution). The acquisition window is set to 10 μs, with a region of 2.5 μs before the trigger time mark (pre-trigger). The trigger is made on the ADC channel itself with a threshold of 25 ADC counts (ADCc), equivalent to 3 mV.

A typical pulse acquired for an event is shown in Fig. 4.4. The baseline is calculated as the mean value measured in the pre-trigger region. The noise level is estimated from the RMS of the ADC readings in the pre-trigger region, with respect to the baseline (Fig. 4.5). The distribution obtained is mostly symmetric below 0.6 mV, approximately Gaussian, with a very small tail observed up to 1 mV.

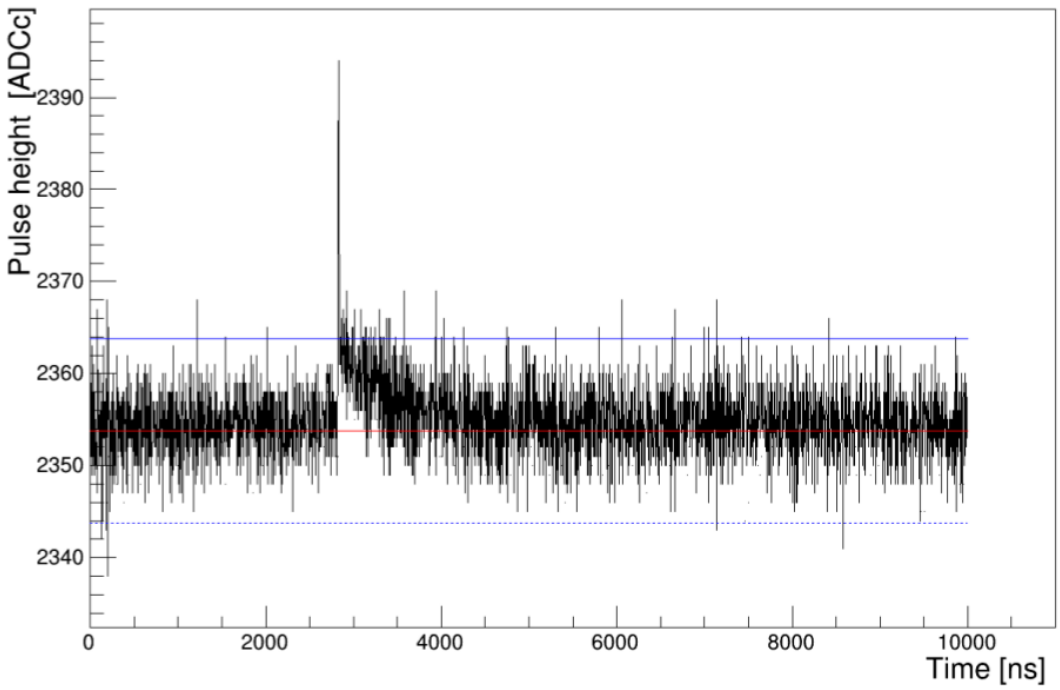

Figure 4.4: Typical dark current pulse detected on a PDM with an overvoltage of 7 V. The red line is the baseline and the blue lines delineate the ADC counts interval used for the calculation of the integrated charge.

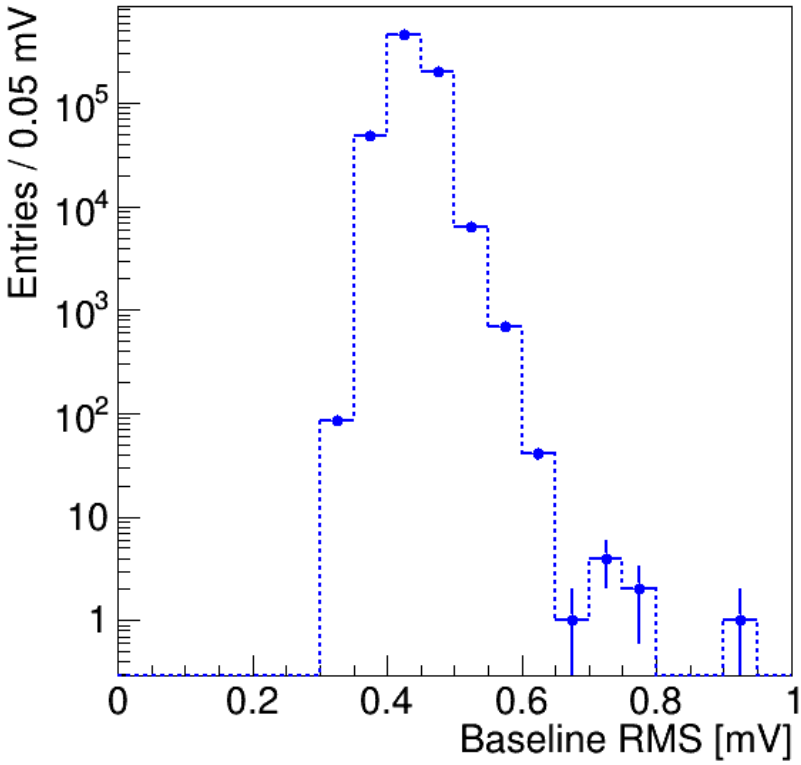

Figure 4.5: Distribution of the RMS of the signals calculated in the pre-trigger region.

The integrated charge is calculated as the integral over two thresholds previously selected in the data processing. The maximum height of the pulse for 10^6 events is presented in Fig. 4.6 as a function of the integrated charge. The two 1D projections of this distribution are displayed in Fig. 4.7. The figures show outstanding peaks, corresponding to the different numbers of photoelectrons detected in the PDMs. The two distributions of Fig. 4.7 are fitted with a sum of Gaussian functions. The difference in the mean values of consecutive peaks is approximately constant. In the integrated charge distribution, the first peak is distorted due to the threshold value set in the ADC, and is excluded from the fit.

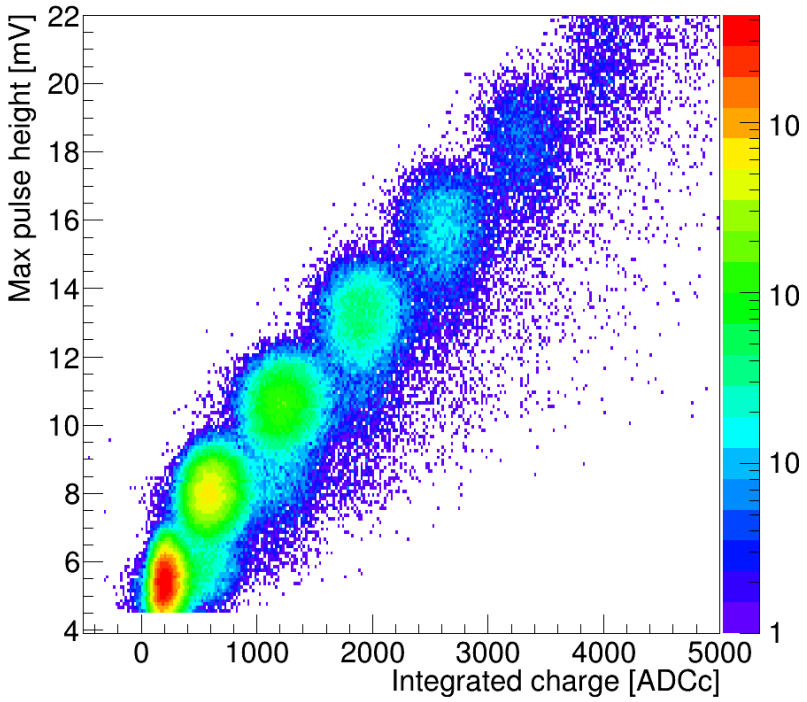

Figure 4.6: Distribution of the maximum pulse height versus the integrated charged, for 10^6 dark current events collected. The structures observed are associated with the number of photoelectrons detected.

To assess the linearity of the PDMs response, the aforementioned mean values are represented as a function of the number of photoelectrons, both for the maximum pulse height and the integrated charge, and linear fits are performed (Fig. 4.8). In the two cases, the slopes obtained in the fits correspond to the single-photoelectron values of those distributions, which are 2.6 ± 0.3 mV for the máximum pulse height and 664 ± 187 ADCc for the integrated charge.

The number of photoelectrons measured using the dark current signals is small. To characterize the different PDMs under similar conditions, it is necessary to use a controlled pulsed light source. The previously described LED calibration system is used for this purpose.

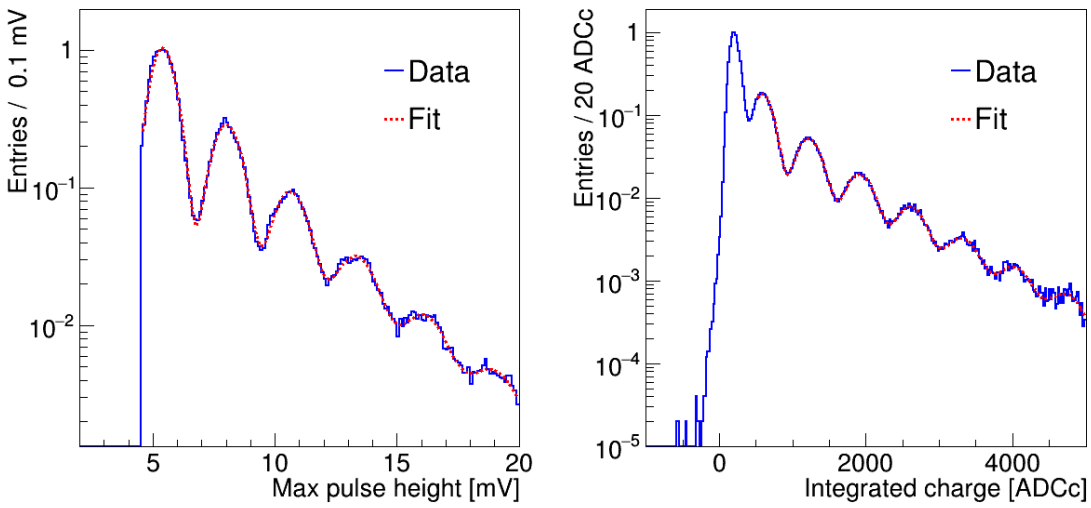

Figure 4.7: (Left) Maximum pulse height and (right) integrated charge distributions, together with the result of the fits to sums of Gaussian functions.

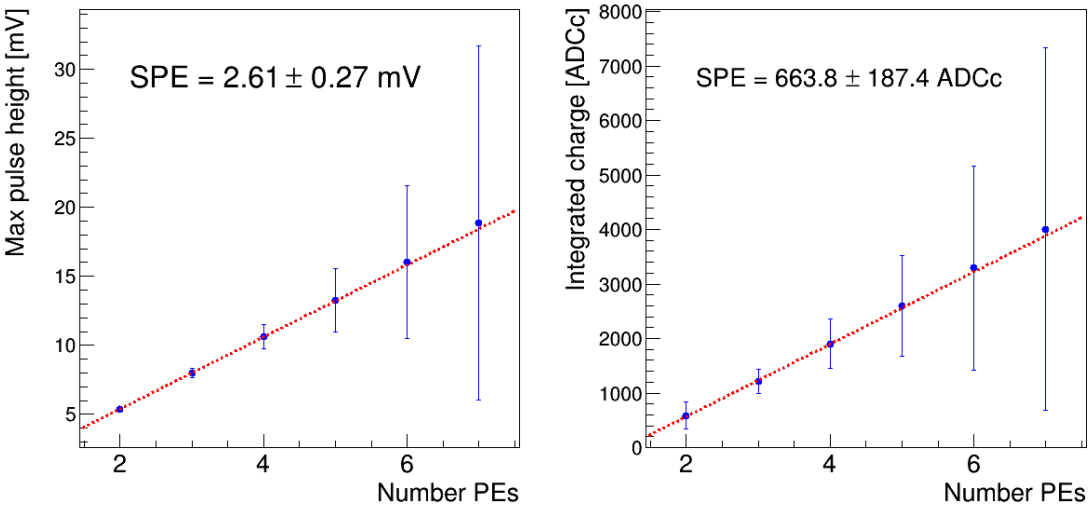

Figure 4.8: Peak values of the Gaussians obtained from the sum-of-Gaussian fits (left) to the maximum pulse height and (right) integrated charge distributions, as functions of the number of photoelectrons. The results of linear fits is superimposed and the y-axis intercepts indicated, together with their statistical uncertainties.

4.1.3 Characterization of the PDMs with a LED source

The system built to calibrate the PDMs consists of a blue LED (400 nm) facing an optical fibre, which transports the light to the front face of the PDM. The LED is excited with a pulse generator, producing fast signals 10 to 20 ns wide, with a variable amplitude. The signal in the pulse generator is replicated and used as the trigger in the ADC. The response function of the PDM with an overvoltage of 7 V is obtained with a 10 ns width LED. The average pulse registered is shown in Fig. 4.9. The signal shape is fitted with the sum of a Gaussian and an exponential function. The latter accounts for the discharge time of the SiPM. A discharge time of 578 ± 8 ns is obtained from the fit. The width of the Gaussian is limited by the

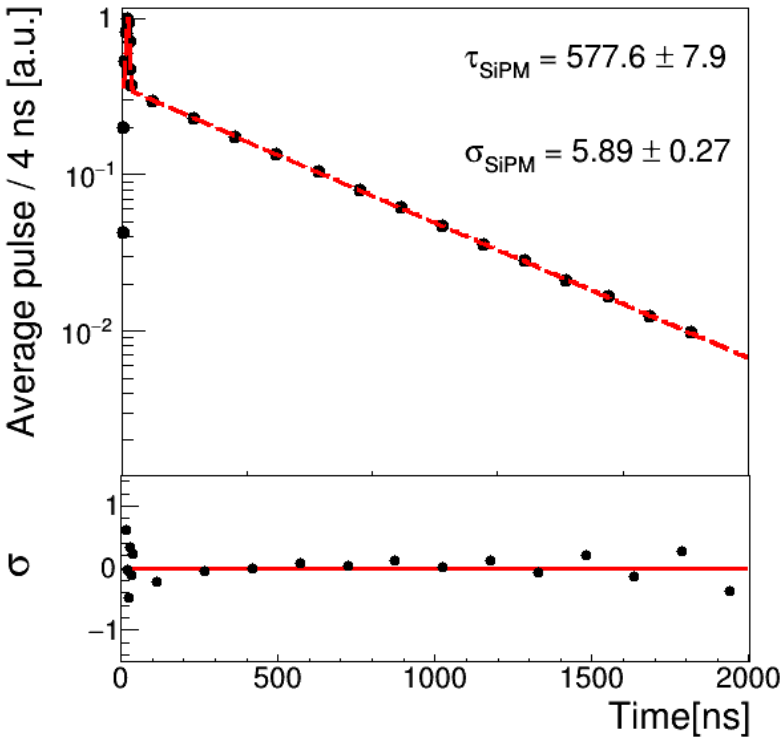

Figure 4.9: Average pulse of 3×10^4 events, generated using the LED with a 10 ns wide excitation signal. The signal is fitted with the sum of a Gaussian and an exponential function. A variable bin width is used in the graph, which is 4 ns up to $t = 200$ ns, and 200 ns from that point onwards.

sampling rate of the ADC (4 ns) and a value of 5.9±0.3 ns is measured. The bottom graph of Fig. 4.9 presents the residuals of the fit.

The dependence of the gain on the overvoltage is studied using LED pulses with the same amplitude and width. The gains for the pulse height and the integrated charge are displayed in Fig. 4.10, normalized to the signals detected with 3 V of overvoltage. A non-linear behaviour is observed, consistent with the shape of the I-V curves.

Another important aspect to study is the saturation in the PDMs. Saturated signals can distort the detected energy spectrum, affecting the measurement of the amount of ^{39}Ar in the argon sample. The study of the dynamic range of the PDMs is performed raising the voltage supplied to the LED, which increases significantly the number of photons emitted. An example of a saturated pulse measured is shown in Fig. 4.11. The signal is distorted in the first ns, deteriorating the capability to perform pulse-shape discrimination. The measured dynamic range, maximum pulse amplitude detected before saturation, is around 500 PE.

The PDMs produced for DArT have been fully characterized. Their response has been studied using dark current signals, and fast signals (10 ns) generated with an LED in a controlled way at 400 nm. The tests have revealed the proper operation of the PDMs at room temperature, and their performance after several cryogenic cycles. Although variations are observed in the response of the different PDMs, all of them satisfy the quality requirements to be used in DArT. The two PDMs with the best performance are installed in the detector.

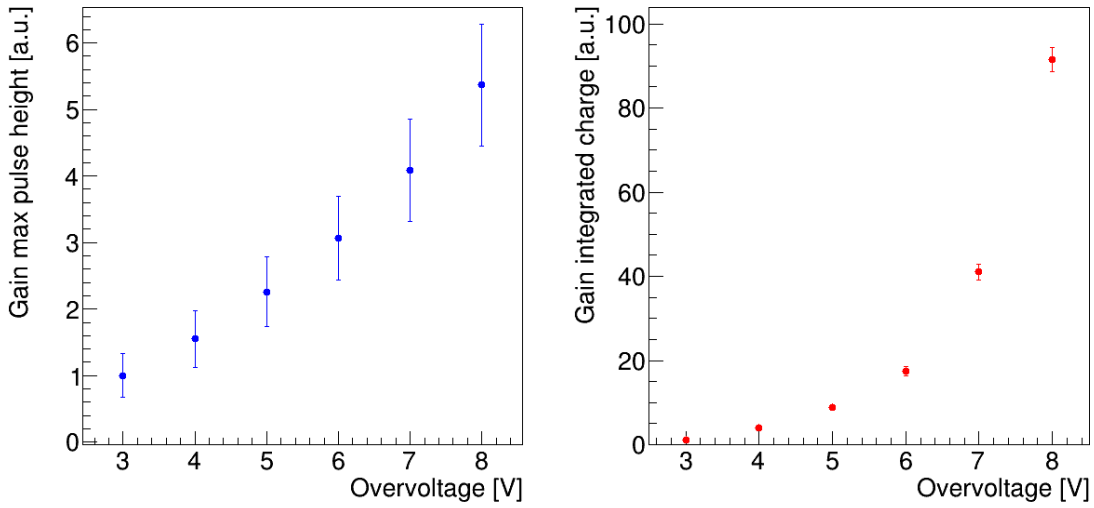

Figure 4.10: Gains of the maximum pulse height (left) and integrated charge (right), as a function of the overvoltage. The gain is normalized to the detected signal with 3 V of overvoltage. The error bars indicate the statistical uncertainties.

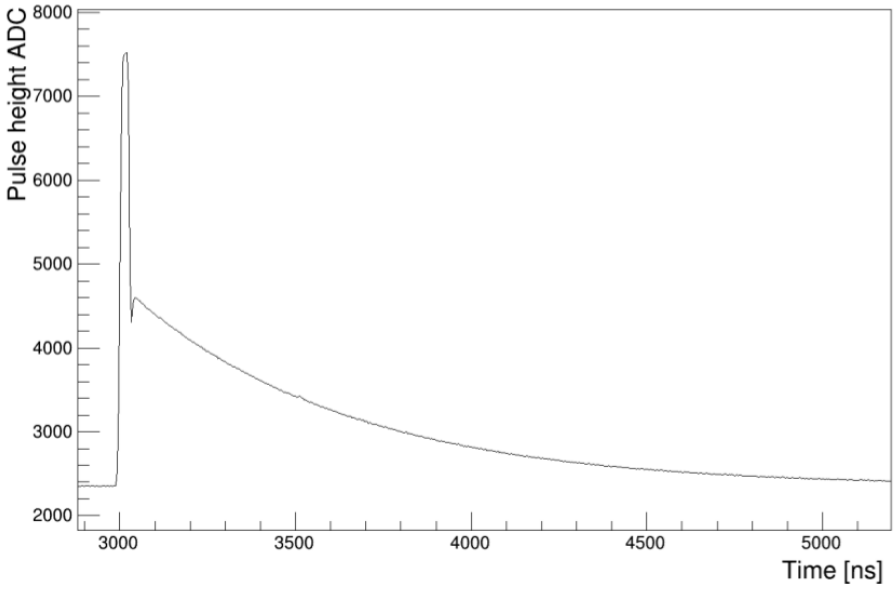

Figure 4.11: Example of a saturated pulse induced by the LED.

4.2 DArT commissioning on surface

The assembly of the DArT test setup at CIEMAT began in November 2020. The main goal of the commissioning of the detector on the surface is to demonstrate that the different elements of DArT are operative and to determine the most relevant optical parameters of the system. It is also crucial to confirm that DArT is capable of performing particle identification.

The cryogenic system used to perform the detector commissioning on the surface is depicted in Fig. 4.12. The active volume of DArT is filled by condensing argon gas, maintaining a constant pressure of 1 bar absolute. DArT is introduced into a pressurized cryostat filled with LN_2 that keeps a stable temperature during the

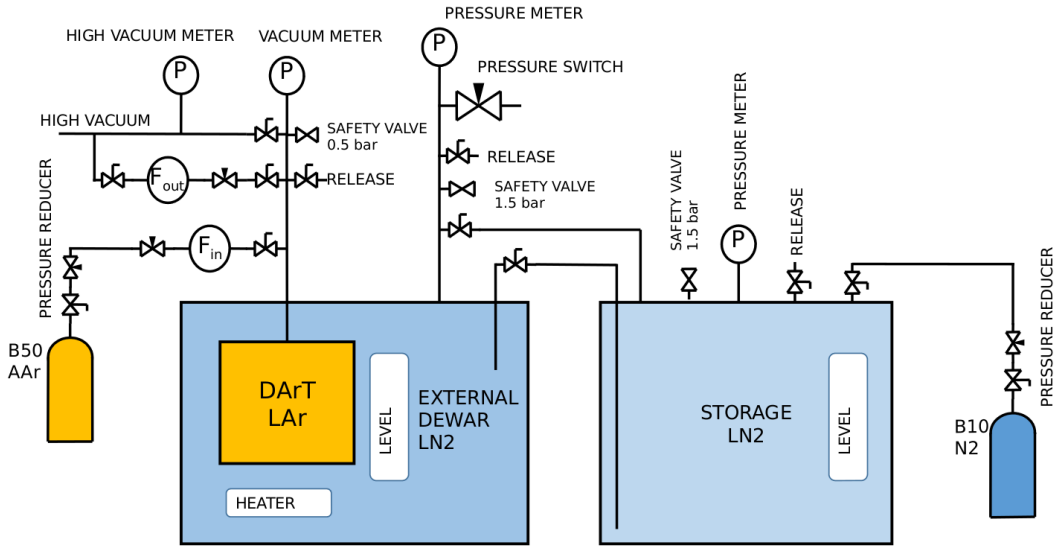

Figure 4.12: Scheme of the DArT cryogenic system for tests on the surface.

operations.

The freezing and boiling temperatures of the liquid argon at 1 bar are 87 K and 83 K, respectively. At this pressure, the LN_2 equilibrium temperature is 77 K, below the argon freezing point. To fill DArT with liquid argon, it is necessary to keep the LN_2 pressure (absolute) in the range from 2 to 2.7 bar (Fig. 4.13). To avoid freezing the argon inside DArT, pressurized LN_2 is introduced into the cryostat using an external tank instrumented with several heating resistors. An external nitrogen gas bottle connected to the bottom of the tank delivers a more efficient transfer of LN_2 between the cryostat and the external tank.

A vacuum level of 1.5×10^{-5} mbar is reached in DArT at cryogenic temperature (83 K) before starting to condense argon. The Fig. 4.14 shows a picture of the test setup at CIEMAT during the filling operations.

The scintillation light produced in the active volume of DArT is detected in the top and bottom PDMs. The signals registered are fed into a fan-in/fan-out module that delivers two replicated output signals. One of the outputs is directed to a 2 V CAEN ADC with a sampling rate of 250 MHz. The other output is used to generate a trigger time mark, obtained from the temporal coincidence of the signals, in a 200 ns window, larger than 2 mV in both PDMs. The data are stored on a local computer and processed with a custom-made software.

4.3 Characterization with atmospheric argon

The results presented in this section correspond to a 60 hour data collection period. Both PDMs are operated at -31.5 V, equivalent to an overvoltage of 5 V. DArT has been filled with argon Alphagaz-2 (with purity at the 1ppm level), maintaining a constant pressure of 1 bar and a temperature of 85 K.

The gains determined for both PDMs in the preliminary tests are applied to convert the acquired signals to photoelectrons detected. The PDM at the top (PDM-Top) has a lower gain than the PDM at the bottom (PDM-Bottom), with an SPE of 100 and 150 ADCc, respectively.

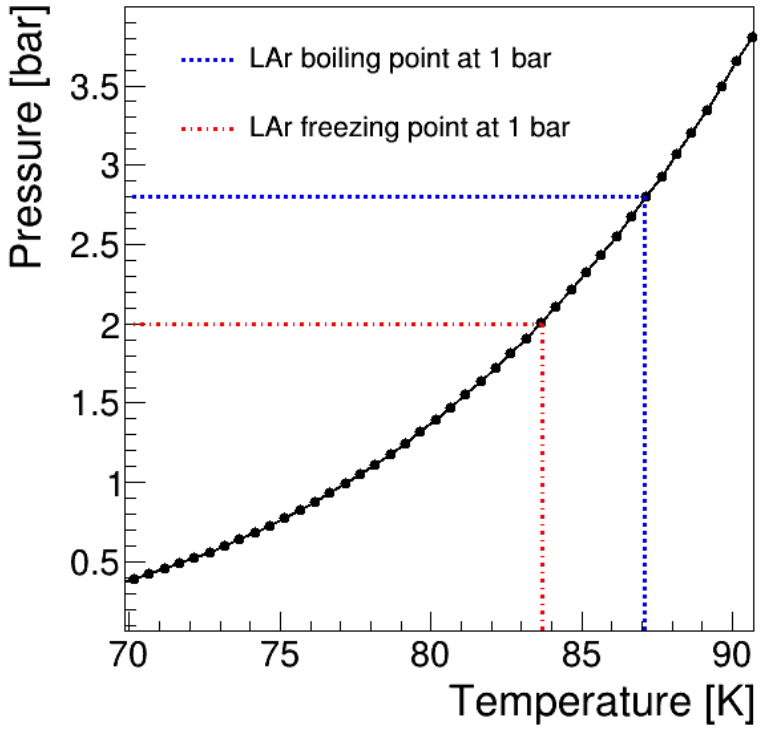

Figure 4.13: Temperature-pressure equilibrium curve for LN_2 [147].

Figure 4.14: Setup of the DArT cryogenic tests on the surface during the filling operations. The devices in the image are, from left to right, vacuum pump, cryostat, external tank, argon bottle and temperature control system.

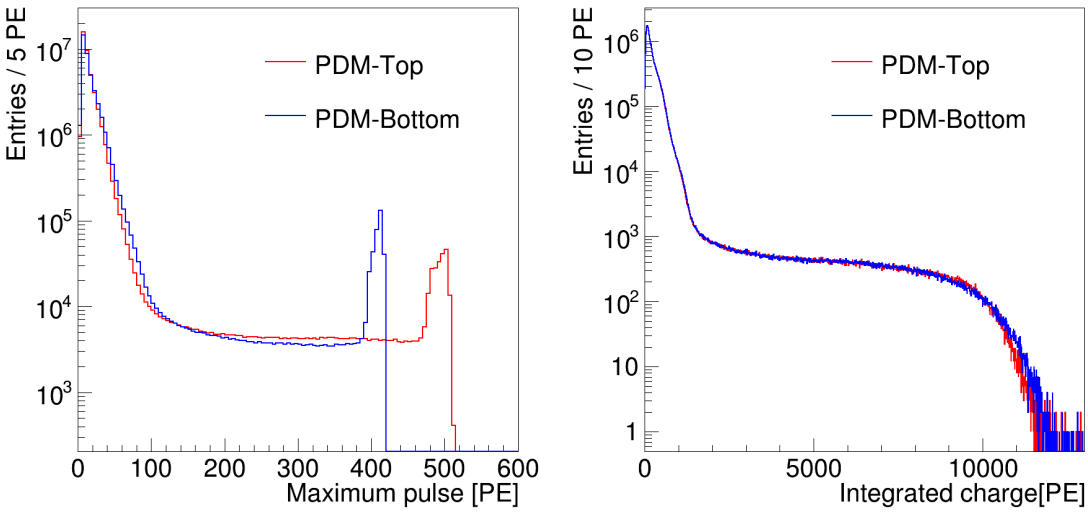

Figure 4.15: (Left) Maximum pulse height in photoelectrons. The PDM-Top (red) has a dynamic range of 500 PE and the PDM-Bottom (blue) of 400 PE.(Right) Integrated charge on both PDMs by applying a cut-off to reject saturated events.

The maximum pulse height is used to study the effects of saturation (Fig. 4.15-left). The PDM-Top saturation is above 500 PE, while the PDM-Bottom has a dynamic range below 400 PE. Individual cuts are applied to both PDMs to reject saturated events. The integrated charge on both PDMs, obtained with a cut that prevents saturation, is shown in Fig. 4.15-right. The spectrum detected in each PDM reaches up to $12\times$ 10^3 PE. Both signals are almost identical, indicating that the light collection in the detector is extremely uniform.

The argon scintillation pulse, averaged over 2×10^4 events, is displayed in Fig. 4.16-left. Only low energy events (below 1000 PE) are considered to avoid saturation effects, using an energy threshold cut. The average pulse is the result of the convolution of the PDM response function (previously estimated) and the argon scintillation profile. The argon purity is estimated with the scintillation triplet lifetime (τ_{slow}), by adjusting the final part of the average pulse to an exponential decay. The purity is stable during the whole data taking period, with an average value of 1053 ± 17 ns (Fig. 4.16-right).

The pulse shape analysis of the scintillation light can be used to discriminate the incident particle types. The ratio of the intensities of the light produced in the first 90 ns with respect to the total provides a powerful particle discrimination technique in liquid argon [133]. The slow response time of PDMs complicates the pulse shape analyses. It is necessary to evaluate the possibility of using the particle discrimination techniques in DArT.

A new variable, F_{640}, is defined as the fraction of the light detected in the first 640 ns of the full pulse. The total integrated charge is represented with respect to the F_{640} value in Fig. 4.17. There are two bands of events, separated by different F_{640} values, similar to that typically obtained in other liquid argon experiments [133, 134]. The upper band with F_{640} values between 0.55 and 0.7 is associated with heavily ionizing particles, while the lower band in the range 0.3-0.45 is due to electron recoil events. This is the first evidence of particle identification with DArT.

In the nuclear recoil band (Fig. 4.17) there is a clump of events clearly isolated,

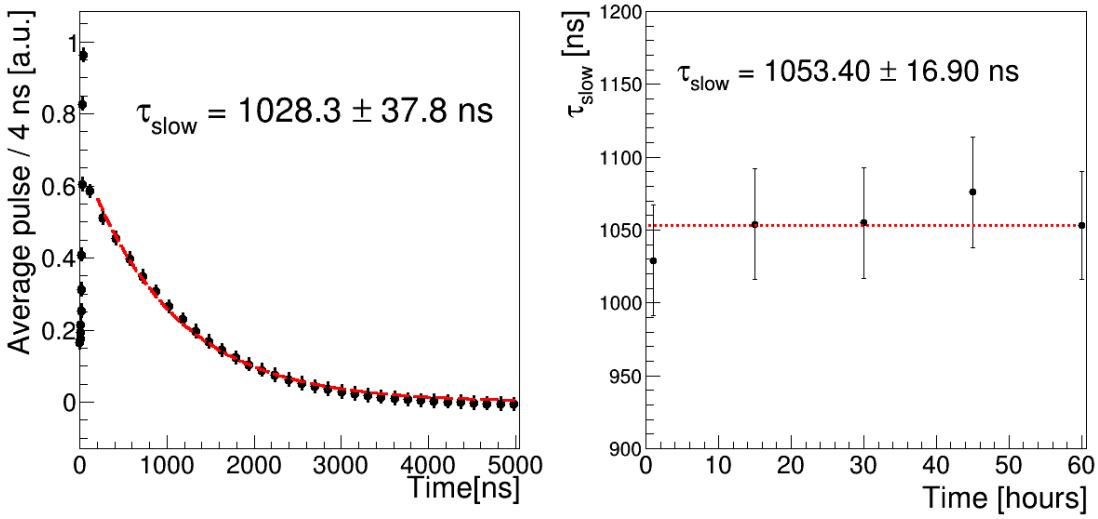

Figure 4.16: (Left) Pulse averaged over 2×10^4 events with an energy lower than 1000 PE. The purity of argon is determined with τ_{slow}, from an exponential fit. (Right) Variation of τ_{slow} with time (each 15 hours). The mean value is indicated in the graph.

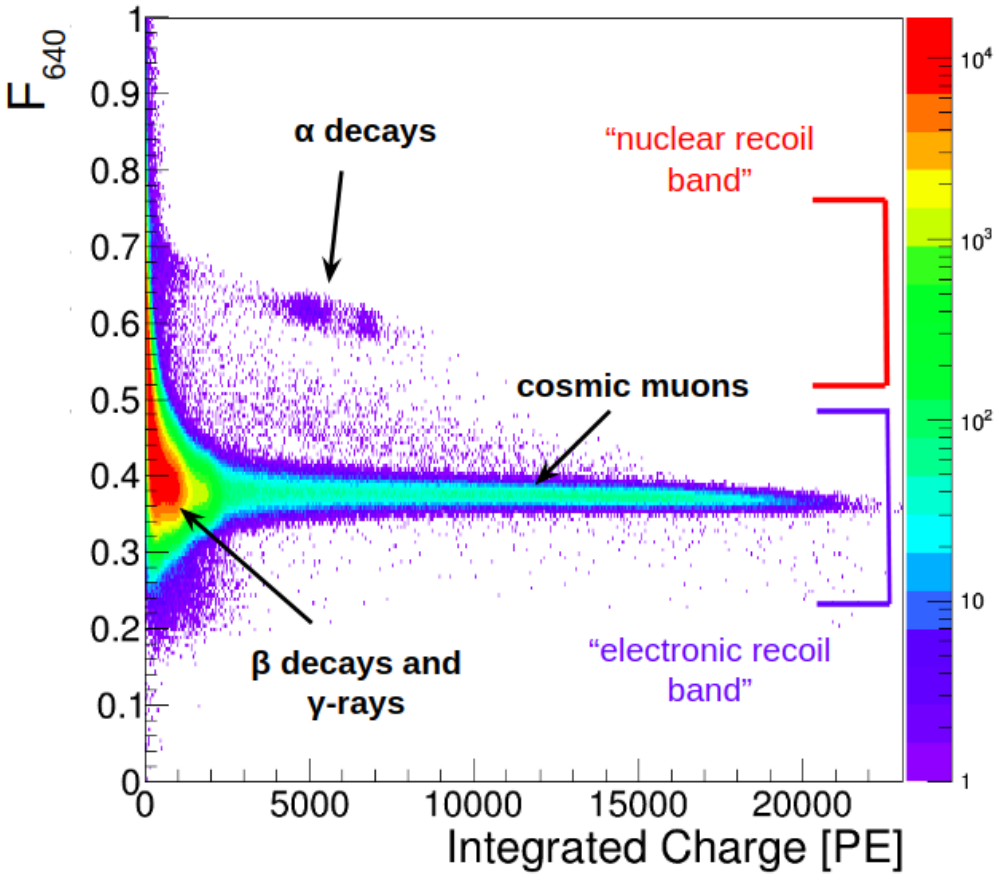

Figure 4.17: Total integrated charge versus F_{640}. There are three distributions of events associated with α-decays, β-decays plus γ-rays, and cosmic muons.

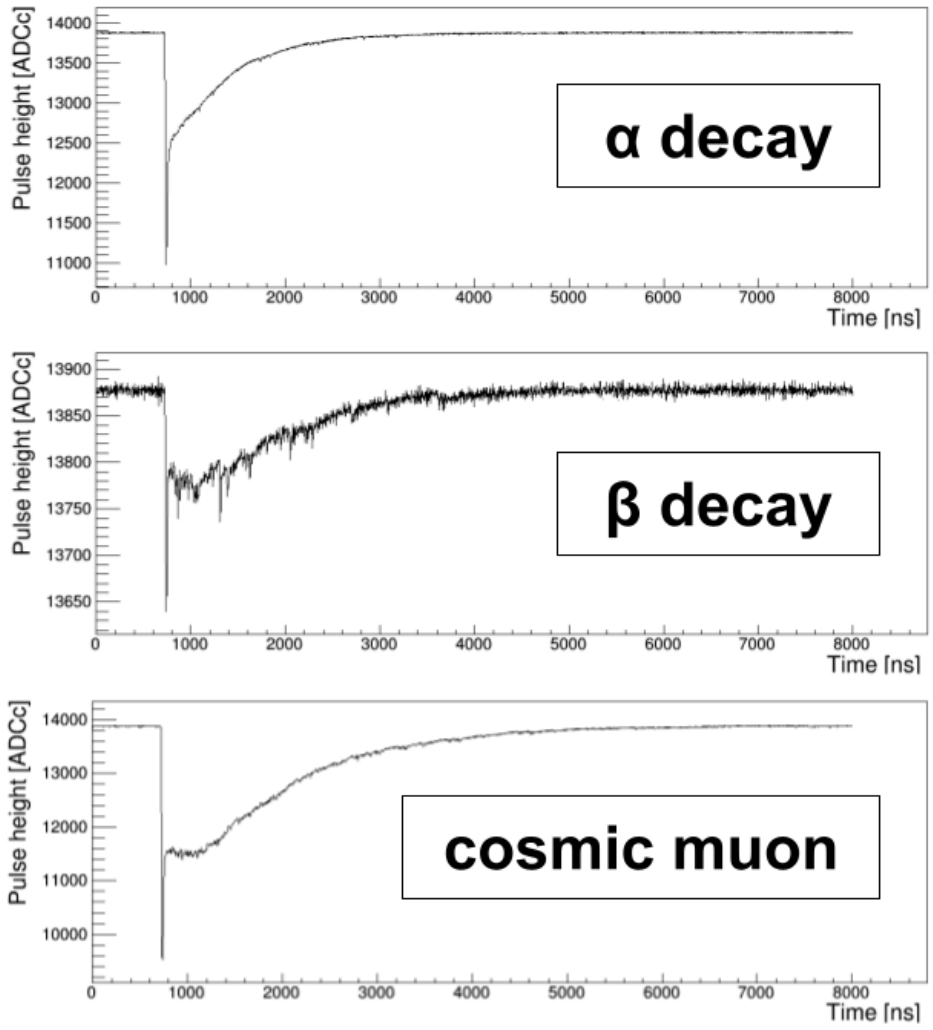

Figure 4.18: Typical pulses detected for (top) an α decay, (middle) a β decay, and (bottom) a cosmic muon.

between 5000 and 10000 PE. The pulse shape of the events detected in this region (Fig. 4.18-top) is consistent with the expectation for a typical α-decay pulse, obtained with simulations (Fig. 3.12). At lower energies, below 3000 PE, the events are consistent with degraded α-decays.

On the other hand, two differentiated distributions of events are observed in the electron recoil band. The first one at low energy (below 3000 PE) is consistent with β-decays of ^{39}Ar and γ-rays of environmental radioactivity. An example of a pulse detected in this region is shown in Fig. 4.18-middle. Also in this case, the agreement with the expectation from simulations is excellent. The second distribution consists of a narrow band of events from 2000 to 20000 PE, consistent with muons produced in cosmic-ray events. These particles produce ionization tracks with lengths depending on the incident angle, depositing on average an energy of 1 MeV/cm (Fig. 4.18-bottom).

4.3.1 Energy calibration with the ^{222}Rn decay chain

Radon accumulates on the internal surfaces of the detector during assembly, filling and emptying operations. The ^{222}Rn decay chain produces three α decays: 5.6 MeV from ^{222}Rn, 6.1 MeV from ^{218}Po and 7.8 MeV from ^{214}Po. The α events are fully contained in the DArT active volume, thus it is possible to study the light yield (LY) and detector resolution using the decays from the ^{222}Rn decay chain. The energy spectrum detected for these events is shown in Fig. 4.19-left. The different peaks observed are consistent with the ones expected from the ^{222}Rn decays.

Another interesting feature of the radon chain is the production of the β-decaying isotope ^{214}Bi, which results in ^{214}Po. The latter produces an α-decay with a half-life time of 164 μs (Bi-Po coincidence). Therefore, it is possible to use the time correlation among events to efficiently identify decays from ^{214}Po. The Fig. 4.19-right shows the time difference (t_{diff}) of pairs of consecutive events. A baseline corresponding to a 1% random coincidences is observed for $t_{diff} > 200$ μs. At lower values of t_{diff}, a pronounced excess is visible and is interpreted as a Bi-Po coincidence. By selecting the events with a $t_{diff} < 200$ μs in the Fig. 4.19-left, the original spectrum with three outstanding identified peaks is reduced to a single peak. Therefore, the peaks from the α energy spectrum are unambiguously identified as the different products of the ^{222}Rn decay chain.

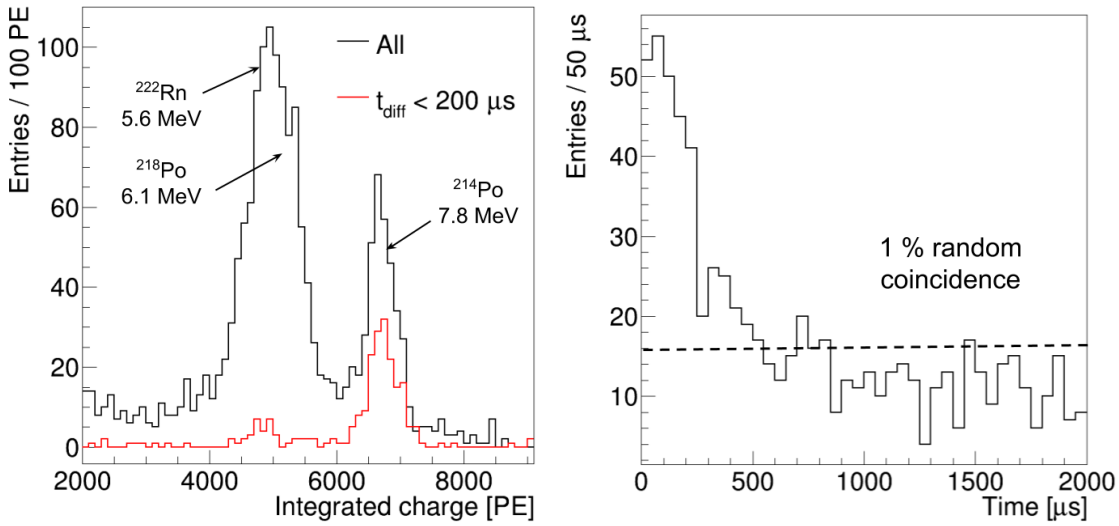

Figure 4.19: (Left) Energy spectrum of the α events before (black) and after (red) applying the Bi-Po coincidence requirement. The peaks of the ^{222}Rn chain are clearly identified. (Right) Time difference of pairs of consecutive events. An excess is observed for $t_{diff} < 200$ μs, associated with the Bi-Po coincidence.

The light yield obtained for the different peaks is depicted in Fig. 4.20-left. The average value obtained for the light yield is 0.96 $\pm$ 0.02 PE/keV. It is corrected for the measured liquid argon purity. For the energy resolution, values between 2% and 4% are obtained.

The relative light yield of scintillating materials differs for particles of distinct ionisation densities. For particles with high ionisation densities, there are two processes that reduce the light yield. One is the quenching of the primary excitation by the high density of ionised molecules/atoms around the particle. The second process

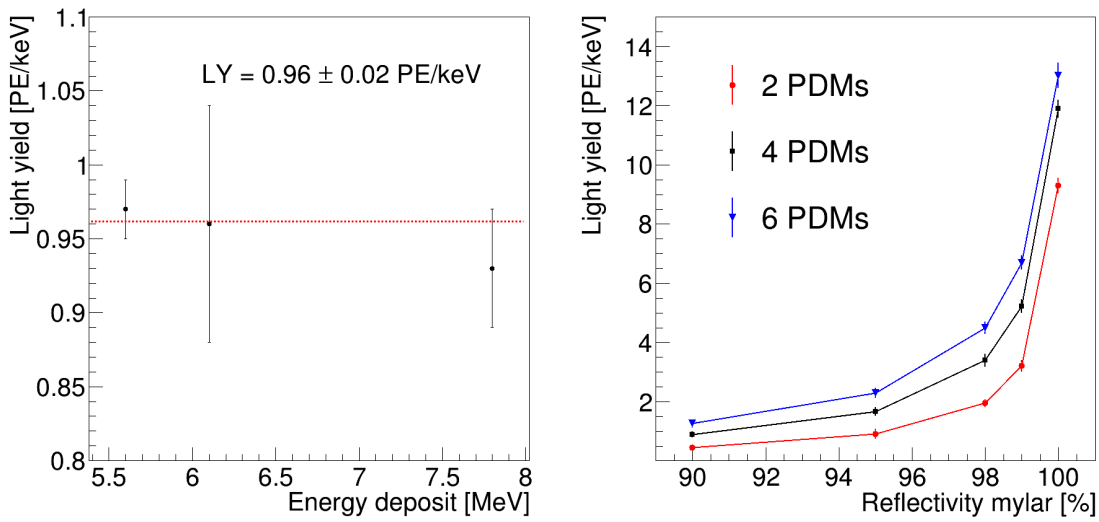

Figure 4.20: (Left) Light yield estimated with the different α peaks of the ^{222}Rn chain, with an average value of 0.96 ± 0.02 PE/keV. (Right) Dependence of the light yield with the mylar reflectivity for different numbers of PDMs.

is due to interactions between neighbouring excimers that lead to a non-radiative dissipation of the excitation energy. Particles with a high ionisation density appear at a lower apparent energy in scintillation spectra than electrons or gammas of the same actual energy. For the case of α particles, the ratio between the apparent electron equivalent energy of the α and its actual energy is referred to as α quenching factor. The α quenching factor depends, in general, on the energy of the α particle, but for the energy range from 5 to 8 MeV it is found to be constant around 0.72 [148]. Applying the α quenching factor, a light yield of 1.33 ± 0.03 PE/keV is obtained for electron-like particles in DArT.

The value obtained for the light yield is lower than that expected from the simulations (9 PE/keV). These are based on different unmeasured optical parameters such as the mylar reflectivity. In order to study the impact of this parameter, several simulations of 1000 events are carried out with a constant energy deposit of 100 keV. Fig. 4.20–right shows the dependence of the light yield on the mylar reflectivity for different numbers of PDMs, decreasing from 9.5 to 0.5 PE/keV when the reflectivity is reduced from 1 to 0.9. Assuming a 98% reflectivity, in good agreement with [149], a light yield of 1.95 ± 0.05 PE/keV is obtained with two PDMs. This value is close to the measured value of 1.33 ± 0.03 PE/keV. Eventually, the light yield can be increased to 3.4 and 4.95 PE/keV using 4 and 6 PDMs, respectively.

The full spectrum of integrated charge is displayed in Fig. 4.21, expressed in keV after applying the light yield calibration factor of the previous paragraph. The contribution of the cosmic muons is observed as a flat distribution that reaches 15 MeV, after applying a saturation cut, consistent with the length of the active volume (18 cm). At low energy, two excesses are observed which could be associated with β-decays of the ^{39}Ar (with an end point of 564 keV) and γ-rays of the ^{40}K (1.46 MeV). However, it is necessary to reduce the environmental background and the contribution of cosmic muons to make an accurate estimation of the amount of ^{39}Ar in the atmospheric argon.

The surface tests have allowed us to characterize the detector completely and

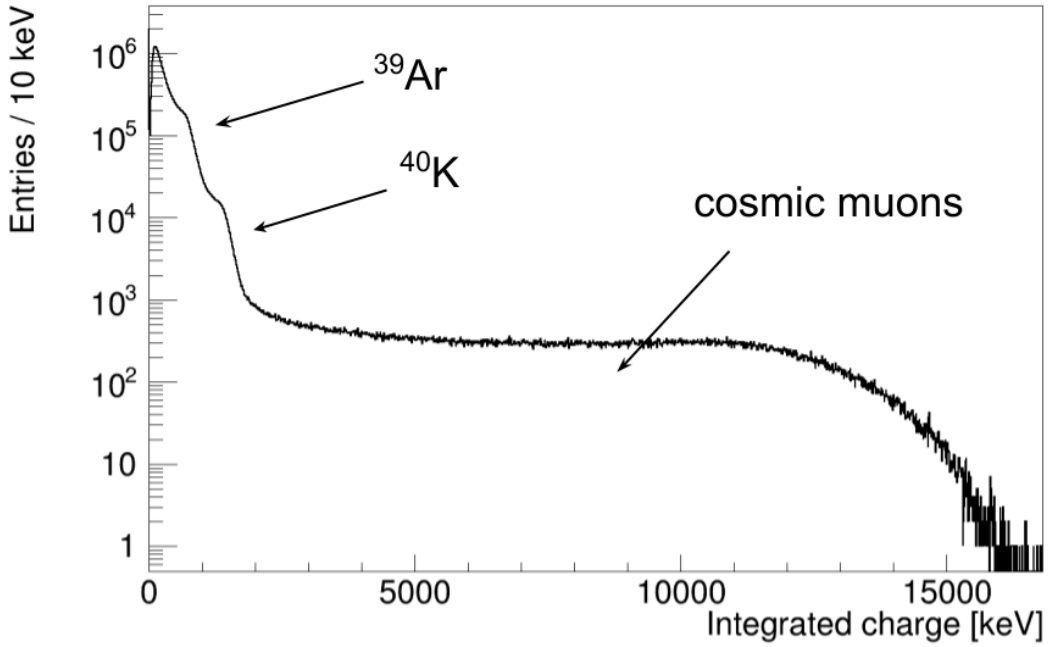

Figure 4.21: Integrated charge spectrum of DArT in keV.

improve our simulations. Also, the event discrimination capability in DArT has been demonstrated and fundamental parameters such as light yield and energy resolution have been obtained using isotopes of the ^{222}Rn chain. During these tests, the detector has been operated on surface continuously for several days satisfactorily, leading to the successful integration tests of DArT. These results are a crucial step in the development of the DArT in ArDM program, being the first measurements of the project. The next milestone is the DArT assembly at the LSC, scheduled in summer 2021.

4.4 Upgrade of DArT detector: EDArT

DArT has been designed to measure with high precision the amount of ^{39}Ar in the argon that will be used in DarkSide-20k.

The Aria project will be the facility to develop active depletion of ^{39}Ar from the UAr to possibly provide depleted argon (DAr) targets for LAr detectors. It is designed to separate ^{39}Ar from ^{40}Ar by exploiting the tiny difference in the relative volatility of the two isotopes. The current design of DArT may not be sufficient to provide an accurate measurement of the level of ^{39}Ar in the DAr in a short period of time. For this reason, I have proposed an enhanced version of DArT (EDArT).

EDArT would be a dual-phase detector with an active volume of 10 L of liquid argon. It would be installed inside ArDM in a similar way to DArT. The light would be detected by two PDM arrays at the top and bottom. The larger volume would make it possible to increase the number of ^{39}Ar events, which is fundamental to have enough data with large depletion factors.

The γ-rays of the environmental background, with energy over 100 keV, would interact several times in the detector, unlike the β decays of 39Ar. The secondary electroluminescence signal (S2) produced in EDArT would allow to reconstruct the

position of the interactions in the detector, and to tell multi-scattering γ-ray events from β decays, increasing significantly the signal-to-background ratio (S/B).

A preliminary geometry has been simulated to estimate the capabilities of such detector. It has been found that for the different background contributions (external and material) 80% are multi-scattering events. The number of signal events for UAr (0.73 mBq/kg), background events and S/B in a week of operation for DArT and EDArT, operating in single and dual-phase, are listed in Table 4.1.

Table 4.1: Number of signal events, background events and S/B in a week of operation for DArT and EDArT, operating in single (SP) and dual-phase (DP).

Configuration	**Signal UAr [evt/week]**	**Background [evt/week]**	**S/B**
DArT-SP	613	471	1.33
EDArT-SP	6130	4042	1.56
EDArT-DP	6130	830	7.59

The number of signal events increases from 630 events per week in DArT to 6300 in EDArT. The number of background events also increases from 471 to 4042. However, it is possible to reduce it to 830 events per week by rejecting multi-scattering events. This means that S/B increases from 1.3 in DArT to 7.6 in EDArT-DP. The statistical uncertainty of the ^{39}Ar depletion factor measured per week in EDArT-DP is reduced with respect to DArT from 7% to 1% for $DF = 1400$ and from 40% to 6% for $DF = 14000$.

More studies are necessary to determine the resolution in the event position reconstruction and the impact of saturation on the S2 events, in order to demonstrate the feasibility of EDArT-DP

In conclusion, this section presents a possible improvement in the design of DArT to increase sensitivity to DF over 1400. Preliminary studies show that an uncertainty of 6% for $DF = 14000$ can be reached using EDArT-DP.

Chapter 5

Spectroscopic studies with argon and xenon gas at high pressure

Over the last decade, argon and xenon detectors have attracted a lot of interest for their use in direct dark matter search [2, 90, 92, 91, 150] and neutrino experiments [87, 151], given their unique ionization and scintillation properties. In these experiments, the high-purity noble element bulk is used as target, as well as active and tracking medium for particles [88, 152], attaining overall performances better than the ones reachable with other technologies.

A central aspect of the single or dual (gas-liquid) phase noble element detectors is the efficient collection and detection of the vacuum ultraviolet (VUV) scintillation photons, which provides calorimetric data, event time for the 3D event reconstruction, and particle identification capability [153, 154]. However, the details of the photon production mechanisms as well as the wavelength and temporal spectra are not fully understood. Experimental information, obtained largely from the closely related fields of photo-chemistry, plasma and laser physics, provides abundant evidence that the light emission mechanism relies on the bond created between excited and ground state atoms through 3-body collisions. As densities are similar or above those of noble gases at standard (STP) conditions, Ar_2^* and Xe_2^* *excimers*, Rydberg states with a dimer core and a binding electron, form. Singlet and triplet excimer states undergo radiative de-excitation, giving rise to the so-called *second excimer continuum*. This feature dominates the scintillation spectrum for gas pressures above 100 mbar, and results in relatively narrow emission bands ($\approx$ 10 nm wide) at 128 nm (argon) and 172 nm (xenon).

Under the above paradigm, there has been so far little motivation towards exploiting spectroscopic information in this kind of particle detectors. As a consequence, the light detection systems of argon and xenon chambers are based on broad-band optical sensors, possibly coupled to photon wavelength-shifters, that effectively integrate the light signal over a wide spectral range, missing the potential information provided by the scintillation wavelength.

Some studies were carried out (mostly prior to the 90's) to investigate the temporal evolution of characteristic spectral components of the argon and xenon scintillation. This experimental program was performed through irradiation with strong X-ray [155], electron [156, 157], proton [158] or heavy ion [159, 160] beams. Although a high intensity beam can produce, in a relatively simple way, the photon yield required for the study of scintillation in pure gases, spurious effects (associative

processes, interactions with walls and emission from the window) are often introduced. Comparatively, it is more difficult to study the time-resolved spectroscopy with individual particles, and, for this reason, the systematic investigation of the spectral characteristics and absolute scintillation yields in particle detectors is much scarcer, and seems to be almost entirely circumscribed to α-particles [161, 162, 163].

With regard to the particle detectors field, the demonstration of a light emission mechanism more complex than the one so far considered in the literature, with well separated emission bands for different particle types, could trigger the interest on a novel detector concept sensitive to the photon wavelength. This technology would allow to exploit distinctive features of the noble gases scintillation emission, a possibility currently not conceived by the present experiments.

To this aim, we have built a high-pressure gas detector in the CIEMAT laboratory (Sec. 5.2). The use of photon sensors with different spectral sensitivities allowed us to detect the Ar scintillation in the near, middle and far UV ranges, and to investigate, in detail, aspects of the photon production mechanism and light emission spectrum particularly relevant for particle detectors based on noble elements.

Results obtained with α and β sources deployed in the gas chamber, operated up to 20 bar, evidenced a substantial emission in the middle-UV region, which is consistent with the so-called *third continuum emission* (Secs. 5.1 and 5.3). Despite being still sub-dominant, overall, compared to the second continuum, the third continuum is markedly fast, hence representing the main contribution to the photon signal during the first tens of ns (Secs. 5.3 and 5.4) below 10 bar.

To the best of our knowledge, this is the first systematic study of the third continuum carried out with α and β sources operated in a noble-gas chamber. Our findings significantly boost the importance of the spectral information in noble-element detectors. Although the two continua can be unambiguously differentiated spectroscopically, the widespread use of wavelength shifter coatings in dark matter and neutrino detectors spoils any possibility of exploiting the spectroscopic information of the argon scintillation.

5.1 Brief review of the scintillation in noble gases

In this section we revisit briefly the experimental situation, starting with the 1$^{\text{st}}$ and 2$^{\text{nd}}$ continuum, that have their origin on the emission from vibrationally-relaxed singlet ($Ar_2^*(^1\Sigma_u)$) and triplet ($Ar_2^*(^3\Sigma_u)$) excimer states, when transitioning to the dissociative ground state of the Ar dimer ($Ar_2(^1\Sigma_g)$). The importance of this emission stems from the fact that, for pressures above few 100's of mbar, low-lying excited atomic states (resonant: $Ar^*(s_4)$, metastable: $Ar^*(s_5)$) are quickly and predominantly populated through a collision-dominated atomic cascade; given that singlet and triplet excimer states are formed from those atomic states through termolecular (3-body) reactions, this emission displays a high universality. Focusing on the $Ar^*(s_4)$ state, the scintillation process can be characterized in general through the

following (dominant) pathways:

$$\mathrm{Ar}^{**} + \mathrm{Ar} \xrightarrow{\text{(cascade)}} \mathrm{Ar}^{*}(s_4) + \mathrm{Ar} \quad \text{collisional quenching} \tag{5.1}$$

$$\mathrm{Ar}^{**} \xrightarrow{\text{(cascade)}} \mathrm{Ar}^{*}(s_4) + h\nu\text{'s} \quad \text{atomic radiation} \tag{5.2}$$

$$\mathrm{Ar}^{*}(s_4) + \mathrm{Ar} + \mathrm{Ar} \xrightarrow{K_{s_4 \to 0_u}} \mathrm{Ar}_2^{*}(0_u^+) + \mathrm{Ar} \quad \text{exc. form.} \tag{5.3}$$

$$\mathrm{Ar}_2^{*}(0_u^+) \xrightarrow{K_{0_u \to s_4}} \mathrm{Ar}^{*}(s_4) + \mathrm{Ar} \quad \text{exc. dissociation to } s_4 \tag{5.4}$$

$$\mathrm{Ar}_2^{*}(0_u^+) \xrightarrow{K_{0_u \to s_5}} \mathrm{Ar}^{*}(s_5) + \mathrm{Ar} \quad \text{exc. dissociation to } s_5 \tag{5.5}$$

$$\mathrm{Ar}_2^{*}(0_u^+) \xrightarrow{1/\tau_{0_u}} \mathrm{Ar} + \mathrm{Ar} + h\nu \quad \text{first continuum} \tag{5.6}$$

$$\mathrm{Ar}_2^{*}(0_u^+) + \mathrm{Ar} \xrightarrow{K_{bind,1}} \mathrm{Ar}_2^{*}({}^1\Sigma_u(v)) + \mathrm{Ar} \quad \text{exc. binding} \tag{5.7}$$

$$\mathrm{Ar}_2^{*}({}^1\Sigma_u(v)) + \mathrm{Ar} \xrightarrow{K_{cool,1}} \mathrm{Ar}_2^{*}({}^1\Sigma_u(v=0)) + \mathrm{Ar} \quad \text{exc. cooling/relaxation} \tag{5.8}$$

$$\mathrm{Ar}_2^{*}({}^1\Sigma_u(v=0)) \xrightarrow{1/\tau_{e2}^{s}} \mathrm{Ar}_2({}^1\Sigma_g) + \mathrm{Ar} + h\nu \quad \text{second continuum} \tag{5.9}$$

Here Ar^{**} refers to any excited atomic state above the two lowest ones, $\mathrm{Ar}_2^{*}(0_u^+)$ is the weakly bound Ar_2^{*} excimer associated with $\mathrm{Ar}_2^{*}({}^1\Sigma_u(v))$, in Hund's notation corresponding to *case c*, and the quantum number v refers to the vibrational state, with $v = 0$ corresponding to the bottom of the potential well. If considering, instead, that the cascade proceeds through the $\mathrm{Ar}^{*}(s_5)$ state, the situation is analogous:

$$\mathrm{Ar}^{**} + \mathrm{Ar} \xrightarrow{\text{(cascade)}} \mathrm{Ar}^{*}(s_5) + \mathrm{Ar} \quad \text{collisional quenching} \tag{5.10}$$

$$\mathrm{Ar}^{**} \xrightarrow{\text{(cascade)}} \mathrm{Ar}^{*}(s_5) + h\nu\text{'s} \quad \text{atomic radiation} \tag{5.11}$$

$$\mathrm{Ar}^{*}(s_5) + \mathrm{Ar} + \mathrm{Ar} \xrightarrow{K_{s_5 \to 0_u}} \mathrm{Ar}_2^{*}(1_u/0_u^-) + \mathrm{Ar} \quad \text{exc. form.} \tag{5.12}$$

$$\mathrm{Ar}_2^{*}(1_u/0_u^-) \xrightarrow{K_{0_u \to s_5}} \mathrm{Ar}^{*}(s_5) + \mathrm{Ar} \quad \text{dissociation to } s_5 \tag{5.13}$$

$$\mathrm{Ar}_2^{*}(1_u/0_u^-) \xrightarrow{1/\tau_{1_u}} \mathrm{Ar} + \mathrm{Ar} + h\nu \quad \text{first continuum} \tag{5.14}$$

$$\mathrm{Ar}_2^{*}(1_u/0_u^-) + \mathrm{Ar} \xrightarrow{K_{bind,3}} \mathrm{Ar}_2^{*}({}^3\Sigma_u(v)) + \mathrm{Ar} \quad \text{exc. binding} \tag{5.15}$$

$$\mathrm{Ar}_2^{*}({}^3\Sigma_u(v)) + \mathrm{Ar} \xrightarrow{K_{cool,3}} \mathrm{Ar}_2^{*}({}^3\Sigma_u(v=0)) + \mathrm{Ar} \quad \text{exc. cooling/relaxation} \tag{5.16}$$

$$\mathrm{Ar}_2^{*}({}^3\Sigma_u(v=0)) \xrightarrow{1/\tau_{e2}^{t}} \mathrm{Ar}_2({}^1\Sigma_g) + \mathrm{Ar} + h\nu \quad \text{second continuum} \tag{5.17}$$

and $\mathrm{Ar}_2^{*}(1_u/0_u^-)$ refers to the degenerate weakly bound excimers associated with $\mathrm{Ar}_2^{*}({}^3\Sigma_u(v))$. A detailed diagram compiling these pathways can be found for instance in [164]. Reaction rates (K) will be assumed in this work to be in units of $[\mathrm{t}^{-1}]$, therefore being number density (N) dependent. Experimentally, it is has been determined that, for pressures above 100 mbar, the dominant time constants are the (3-body) formation times $\tau_{f_2} = 1/K_{s_{5(4)} \to 0_u}$, and the decay times τ_{e2}^{s}, τ_{e2}^{t}.

At high ionization densities, characteristic of high pressures and/or highly ionizing radiation, charge recombination provides additional scintillation channels [165, 166]. From

$$\mathrm{Ar}^{+} + \mathrm{Ar} + \mathrm{Ar} \rightarrow \mathrm{Ar}_2^{+} + \mathrm{Ar} \tag{5.18}$$

$$\mathrm{Ar}_2^{+} + e \rightarrow \mathrm{Ar}_2^{**} \tag{5.19}$$

$$\mathrm{Ar}_2^{**} \rightarrow \mathrm{Ar}^{**} + \mathrm{Ar} \tag{5.20}$$

the 1st and 2nd continua follow, according to reactions 5.1, 5.2, 5.10, 5.11. This leads to a perfect correlation between recombined charge and excess scintillation, with reaction 5.19 being regulated by the external electric field [167]. As a result, the effective energy to create a UV photon at zero-field varies, under α-particles, from W_{sc}=50.6 eV at 2 bar to W_{sc}=25.3 eV at 10 bar [168].

On the other hand, mechanisms leading to scintillation mainly in the region [180, 300] nm are grouped under the generic denomination of "3^{rd} continuum", despite it is possible that a number of different species contribute, as hinted by the study in [160]. The identification of the precursors to this continuum has been subject of hot debates throughout the 80's and 90's [169, 170]. The most complete study to date, combining the two leading hypothesis, doubly ionized (Ar^{++}) and excited (Ar^{+*}) ions, seems to be [160], however it does not allow quantitative predictions of the scintillation yields, nor it has been fully substantiated. In a nutshell, doubly ionized states would lead to scintillation around 200 nm through three-body reactions, as:

$$Ar^{++} + Ar + Ar \rightarrow (Ar_2)^{++} + Ar \quad (5.21)$$

$$(Ar_2)^{++} \rightarrow Ar^{+} + Ar^{+} + h\nu \quad (5.22)$$

At high pressures, the presence of new peaks in the range [200, 300] nm led to the consideration of additional contributions, finding a good theoretical correspondence with Ar^{+*} decays:

$$Ar^{+*} \rightarrow Ar^{+} + h\nu \quad (5.23)$$

Contrary to the 1st and 2nd continua, the pathways leading to formation of Ar^{+*} species have not been unambiguously identified. According to experimental data obtained in [161] for α-particles, electron-ion recombination is not competing with process 5.21, so the 3rd continuum would be largely field-independent except perhaps for very highly ionizing radiation.

5.2 Experimental setup

The wavelength-sensitive chamber is shown in Fig 5.1. It consists of a 7 cm side stainless steel cube with one CF-40 flange on each face. The top and bottom flanges are connected to the service lines for the vacuum and the gas filling. The lateral flanges are equipped with four custom-made optical view-ports necessary to decouple the pressurized region from the optical readout system. A custom-designed steel frame keeps the windows in place. Grooves in the mechanical assembly hold viton o-rings which seal the window, making the view-port vacuum and pressure-tight up to 20 bar. The windows are made of 8.0 mm thick UV-grade MgF_2 crystals (38.1 mm–$\varnothing$), whose transmission is $\approx$ 95% for wavelengths above 180 nm (Fig. 5.2-left). A transmission of $\approx$ 33% at 128 nm is measured comparing the light detected with and without the MgF_2 crystals installed in the chamber.

Four 1" Hamamatsu photomultipliers (PMT) are hosted in canisters attached to the optical view-ports. They are built with KF-40 tee and cross fittings and equipped with a connection for the vacuum line, separated from the main pressure chamber, and two electrical feedthroughs for the HV and PMT signals.

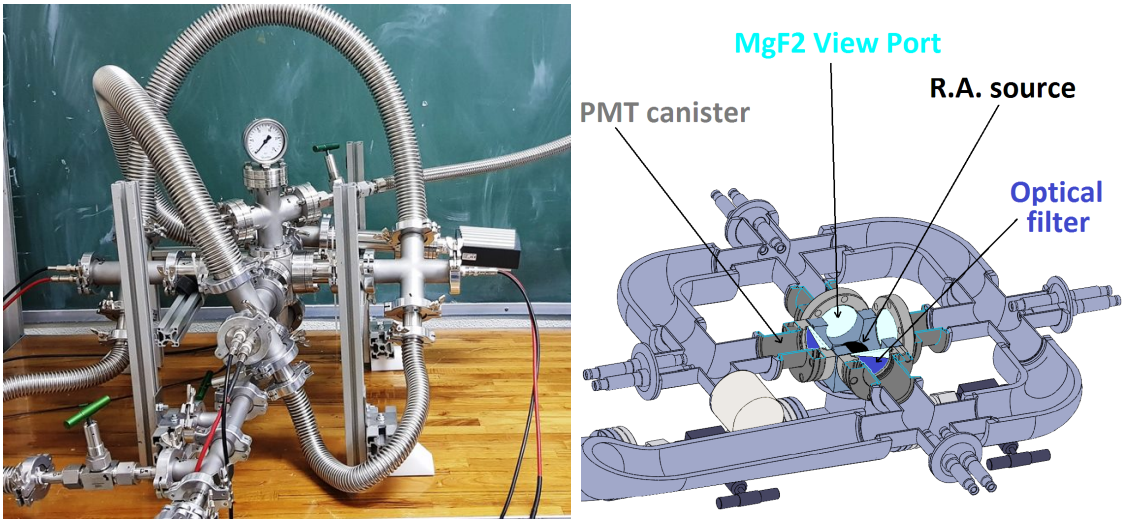

Figure 5.1: (Left) Photograph of the experimental setup. (Right) Top view of detector. The pressurized region with the radioactive source is in the centre of the chamber.

PMTs with different spectral sensitivities are used in the experiment. Two Hamamatsu R7378A phototubes are placed in opposite sides of the central chamber. In the other two confronting faces, one Hamamatsu R6095 and one Hamamatsu R6835 are set. The Hamamatsu R6095 PMT is coated with a 200 μg/cm^2 layer of tetraphenyl butadiene (TPB), a wavelength shifter that converts the UV photons to 420 nm with approximately 100% efficiency [126]. The nominal quantum efficiencies (QE) of these phototubes and the MgF_2 window's transmission coefficient are plotted in Fig. 5.2-right as a function of the photon wavelength [171, 172].

The TPB coating makes the R6095 response independent of the wavelength of the incident photon in the VUV-UV region, so its spectral sensitivity is considered constant in the range of interest ([100, 300] nm). The QE of this tube is considered equal to half of the nominal value at 420 nm (30 %) to take into account the 50 % probability of backward emission of the TPB-converted photons. The CsI photocathode of the R6835 is solar blind, thus the 420 nm photons, diffused backwards by the TPB coating of the R6095 placed in front of it, do not produce a signal. Specific tests performed in our laboratory with the R6835 PMT and a blue LED proved that this phototube is not sensitive to the 420 nm light. The geometry of the setup reduces the optical cross-talk between the 420 nm photons and the R7378 phototubes to a level which is negligible for our purposes.

Special runs with 1" ($\varnothing$) Al_2O_3 (Sapphire) crystals from Thorlabs [173] and long-pass filters form Asahi [174]), placed in front of the R6835 and R7378 respectively, are also taken in order to narrow the spectral sensitivity of these phototubes. The cross-comparison of the signals with and without the filters placed in front of the PMTs allows to study the Ar scintillation in well defined UV ranges. This work

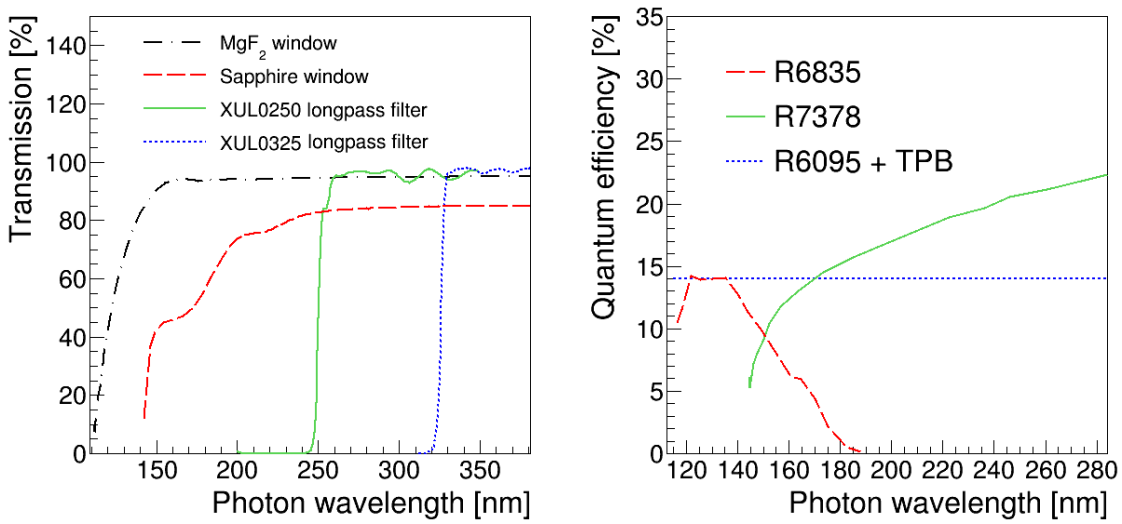

Figure 5.2: (Left) Curves of light transmission as a function of wavelength, for the windows and filters used in the experiment. (Right) Quantum efficiencies of the PMTs used in the detector, measured by Hamamatsu as a function of the wavelength of the incident photons.

investigates the argon scintillation in the spectral ranges [110, 140] nm (called UV2 region in the following) and [160, 325] nm (UV3 region) using the signals of the R6835 PMT with the Al_2O_3 window and of the R7378 PMT with the Asahi filters, respectively (Table 5.1). The upper limits are identified by the fact that no light signal is detected with the filters placed in front of the PMTs.

The detector is equipped with two pressure sensors (ITR-90) and a set of 1/2" VCR valves that allow to set the pressure in the chamber and the optical readout system independently. The optical filters can be put or removed without the need to open or evacuate the pressure chamber. Before each run, the system is pumped with a TURBOVAC 350i for 24 hours and a pressure of 2×10^{-5} mbar is typically reached in the central volume. Pure argon gas (AirLiquide ALPHAGAZ^{TM}-2, purity $\geq$ 99.9999 %) is used to fill the chamber. The PMT region is evacuated and continuously pumped during the data taking (pressure $<9\times10^{-5}$ mbar) to minimize the absorption of the UV-VUV photons by the air between the optical view-port and the PMT window.

The PMTs are powered independently with a negative bias voltage through custom-made bleeder circuits with SMD components mounted on PCBs. The signal is amplified 10 times with a CAEN N979 module. One of the two outputs of the fast amplifier goes to a leading edge discriminator (CAEN N841), with a threshold set to 0.5 photoelectrons. Different trigger logics (CAEN N455 quad logic unit), based on the coincidence of the R6095 and R7378 phototubes, are used in the experiment. The second output of the fast amplifier is fed to a CAEN DT5725 sampling ADC (14-bit resolution and 250 MS/s sampling rate). Different runs are taken with digitization windows from 4 μs to 16 μs. The data are transferred via optical link to a computer for the analysis. The gain of the PMTs is obtained from dark-rate data taken in vacuum, by fitting the single photoelectron peak with a Gaussian function. The calibration of the R6835 is performed directly with the tail of the argon light pulse, given its very low dark pulse rate. The high voltage of the PMTs is set independently,

Table 5.1: Definition of the UV2 and UV3 spectral ranges. The lower bounds are set by the spectral sensitivity of the PMTs. The upper limits are defined from the filters' transmission edge.

Region	Range	Lower bound	Upper bound
UV2	[110, 140] nm	R6835 lower spectral sensitivity limit	R6835 + Al_2O_3 crystal
UV3	[160, 325] nm	R7378 lower spectral sensitivity limit	R7378 + XUL0325 filter

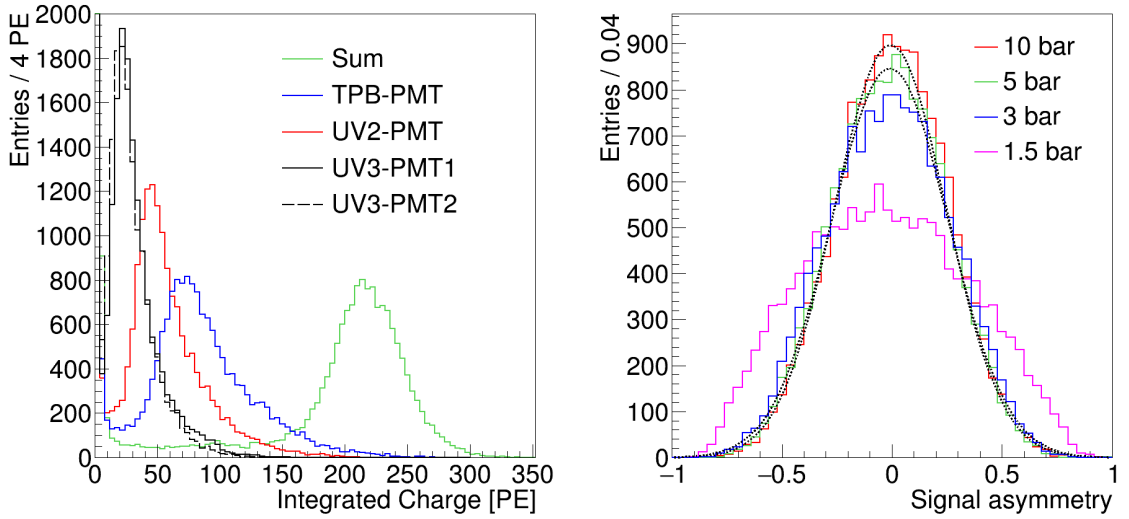

Figure 5.3: (Left) Integrated charge signal of the four different PMTs used in the experiment, obtained with the ^{241}Am α source in argon at 2 bar. The signal in the UV3 region is detected with two R7378 PMTs (UV3-PMT1 and UV3-PMT2). The light collected on the four photo detectors (Sum) is around 220 PE. (Right) Asymmetry between the two R7378 PMTs for different pressures. The Gaussian functions fitted to the data are overlaid.

in order to equalize the gains to the level of 500 ADC counts per photoelectron.

The gas purity is assessed through the decay time of the slow component of the argon second continuum emission. Values of ≈ 3 μs were obtained depending on the gas pressure and flow. Simple selection criteria are applied to reject a few percent of the total triggers which are produced by electronic noise and cross-talk events.

The results presented in this study are obtained with ^{241}Am (activity $\approx$ 500 Bq) and ^{90}Sr/Y (activity $\approx$ 100 Bq) radioactive sources electrodeposited on stainless steel disks. The pressure chamber is equipped with a PTFE support structure able to host one radioactive source in the centre.

5.3 Wavelength-resolved UV/VUV emission with a ^{241}Am source

Initial measurements were carried out with a ^{241}Am α-source in argon gas up to 16 bar using two R7378 (UV3-PMT1 and UV3-PMT2 in the following), one R6835

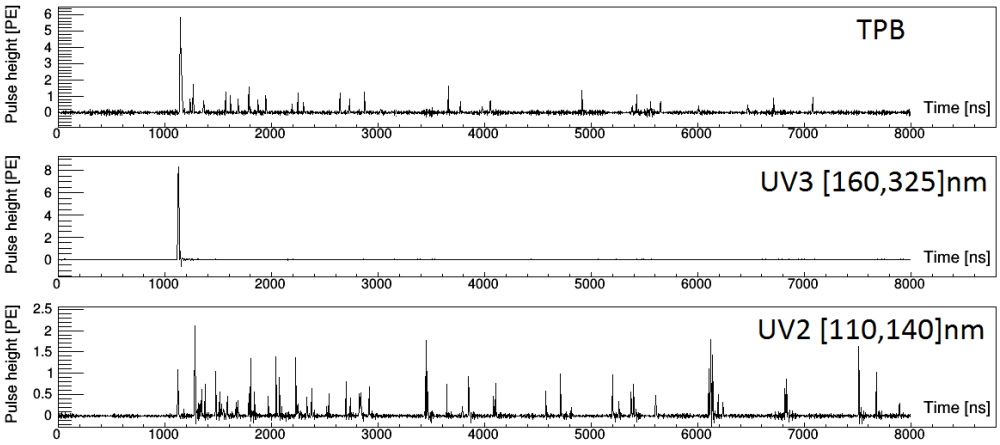

Figure 5.4: Typical Ar scintillation signals from 5.5 MeV α-particle interaction detected in three spectral regions, with argon gas at 1.5 bar. A clear separation of the components is possible by wavelength discrimination.

(UV2-PMT) and one TPB-coated R6095 PMT (TPB-PMT). Taking into account the W-values reported in [168], 1.1$\times$ 10^6 photons are produced in argon at 2 bar. Considering the solid angle between the PMTs photocathode and the source, the MgF_2 transmission coefficient and the nominal PMTs QE, (1.0 $\pm$ 0.2) $\times$ 10^2 photoelectrons (PE) are expected to be detected by the TPB-PMT, which is sensitive to the entire spectral range. The average solid angle between the PMTs photocathode and the source is estimated by means of a toy Monte Carlo which includes the detailed description of the chamber geometry and takes into account the refraction of the light on the MgF_2 crystals. Values in the range [0.008, 0.011] are obtained for the different PMTs depending on the nominal photocathode size and the average length of the alpha track as a function of the gas pressure.

The α-peak is clearly visible in the integrated charge spectra (Fig. 5.3-left). Depending on the gas purity and pressure, more than two hundred of photoelectrons (PE) are detected in the full energy peak (green histogram) produced by the $\approx$ 5.5 MeV α particles, allowing wavelength and time-resolved analysis of the light pulses. The TPB-PMT detects $\approx$ 90 PE on average (blue histogram in Fig. 5.3-left), a value which is in good agreement with the expected one. The UV2-PMT (red histogram) mean value is approximately 60 PE, while the two UV3-PMTs (black histograms), which are only sensitive to wavelengths above 160 nm, detect $\approx$ 30 PE each on average. This clearly establishes that there is a significant component of the argon scintillation light at wavelengths significantly longer than the 128 nm line from the second continuum.

The signal asymmetry, defined as the ratio between the difference and the sum of a pair of PMTs integrated signals, is plotted in Fig. 5.3-right for the two UV3 phototubes at different pressure values. The data are fitted with a Gaussian function with a mean value compatible with zero, confirming that the source is at the centre of the chamber. The width of the distribution decreases with pressure due to the reduction of the mean range of the particles in the gas, indicating that the influence of any geometrical correction in the measured scintillation is negligible above 3 bar.

The pulse shape of a typical signal, produced by an α event in argon at 1.5 bar, is presented in Fig. 5.4, as registered by the different PMTs. The TPB-PMT detects

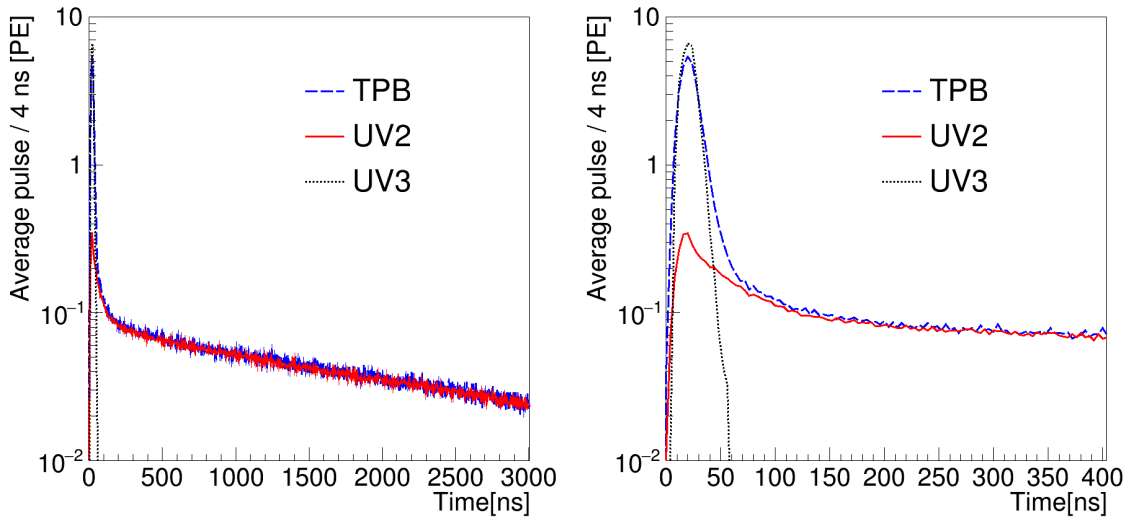

Figure 5.5: Pulse shapes of the argon scintillation signals averaged over 3×10^4 events per PMT type, registered with the ^{241}Am source in Ar at 1.5 bar, in two time windows: (left) $[0, 3000]$ ns and (right) $[0,\ 400]$ ns.

the characteristic fast and slow components of the argon emission. However, only the slow component of the scintillation is detected in the UV2 region, in form of a long train of pulses (μs scale) at the single photoelectron level. The UV3 sensitive phototubes are able to detect only the prompt emission, with a pulse amplitude similar to the one detected by the TPB-PMT.

A signal consistent with dark current is registered by the UV2-PMT with the sapphire crystal placed between the PMT window and the MgF_2 optical view-port, proving that the slow component of the Ar scintillation is entirely in the range $[110,\ 140]$ nm. The light signal detected by the UV3-PMTs with the 250 nm long-pass filter is of the order of 20% of the total signal without filter. No light is detected with the 325 nm long-pass filter.

The 1.5 bar argon scintillation pulses, averaged over 3×10^4 events, are displayed in Fig. 5.5 in two time ranges. Only the α-particle interactions from the ^{241}Am source are considered, using an energy threshold cut. LED calibration runs taken in vacuum evidenced an after-pulsing component, between 60 ns and 100 ns after the maximum pulse height, in the UV3-PMTs signal. This second pulse is removed from the analysis with a software cut, after confirming that the impact in our study is negligible.

In this analysis, only the raw number of PEs have been reported without any signal correction. The combination of the plots in Figs. 5.3 (left) and 5.5 suggests that the amplitude of the signal detected by the TPB-PMT, which is sensitive to the entire spectral range, is very similar to the sum of the signals of two other PMTs, sensitive only to either of the two UV2 and UV3 regions. In Fig. 5.6, the integrated charge spectra (left) and the average pulse shape of the argon scintillation (right) are shown with the ^{241}Am source in argon gas at 1.5 bar, selecting the events in the center of the detector through two symmetry cuts between the different couples of confronting PMTs. Given the symmetry of the setup and the similar size of the PMTs, the fact that the tube signals are similar in the two regions UV2 and UV3 respectively also suggests that the QEs are comparable.

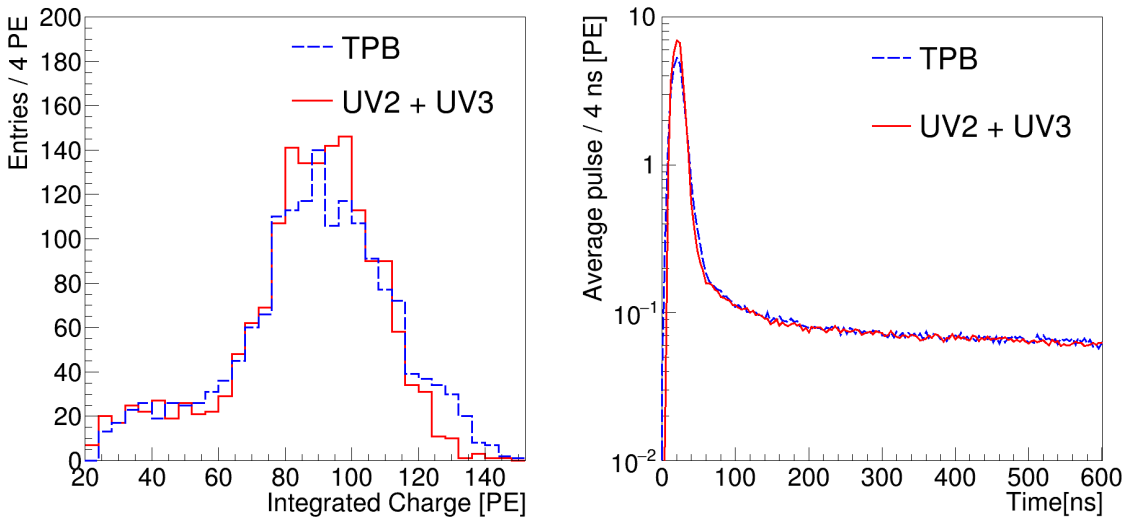

Figure 5.6: (Left) Integrated charge spectrum obtained in the PMT with the wavelength shifter compared with the sum of the spectra in the UV2 and UV3 regions, with ^{241}Am data in argon gas at 1.5 bar. (Right) Average argon pulse detected with the TPB and sum of the UV2 and UV3 pulses at 1.5 bar.

These results prove that the two components of the scintillation with Ar gas at 1.5 bar are characterized by distinct wavelengths and can be unambiguously differentiated spectroscopically. The slow component is consistent with the second continuum emission (Sec. 5.1), which gives rise to the 128 nm photons. The fast component of the scintillation, on the other hand, is entirely in the UV3 region and it is compatible with the third continuum emission.

In our experiment the actual purity of the argon gas was estimated through the decay time constant of the triplet excimer states $Ar_2^*(^3\Sigma_u)$. The values obtained between 2.5 and 3 μs set the level of impurities in the range 0.1–1 ppm [175], which is consistent with the gas contamination certified by the producer. The measured triplet decay time rejects the possible explanation of the UV3-photon production in terms of parasitic re-emissions from N_2, H_2O and O_2 contamination, which can only produce a sub-dominant component in the UV band and over a wide time scale. Any explanation, other than the third continuum emission, in terms of unusual Ar contaminants is considered implausible.

The fast/slow component ratio obtained at 1.5 bar gas pressure and maximum purity (3.2 μs) is 5.4, in good agreement with the value 5.5 $\pm$ 0.6 at 1.1 bar absolute pressure measured in [176].

5.4 Spectroscopic analysis of the argon scintillation as a function of the gas pressure

In order to quantitatively compare signals in the two spectral regions UV2 and UV3, we calculate the total numbers of photons produced by the α interactions considering the MgF_2 transmission values (33% for the UV2 region and 95% for the UV3), the nominal QEs (0.15 for the UV2-PMT and TPB-PMT, 0.18 for the UV3-PMT) and the solid angle estimated through the toy Monte Carlo (Sec. Sec:ES). The analog

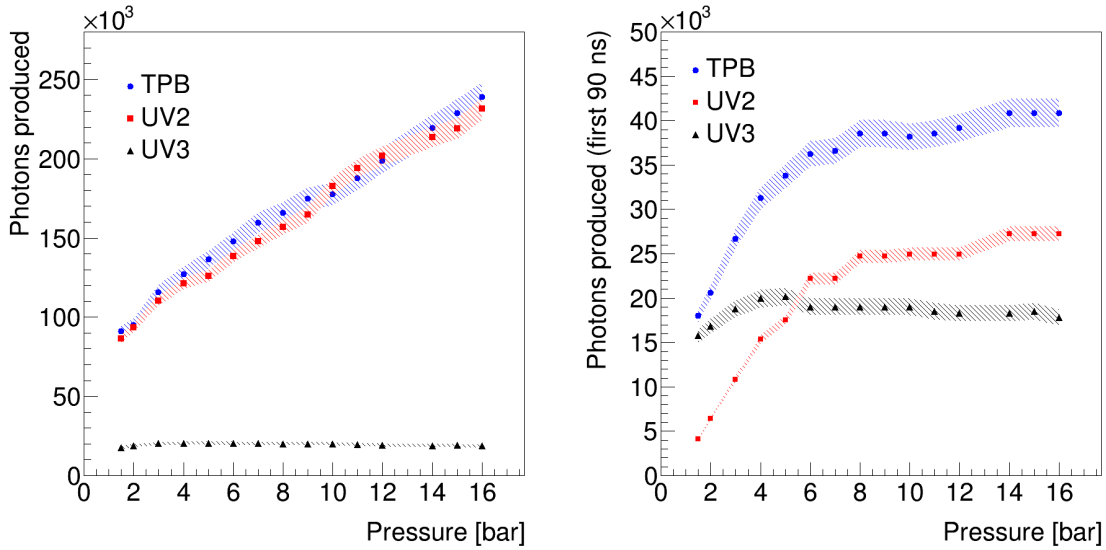

Figure 5.7: (Left) Mean α signal detected in the different spectral ranges as a function of the pressure. (Right) Variation with the pressure of the fast component (first 90 ns) of the argon scintillation. In both graphs, the bands indicate the systematic uncertainties.

manometer introduces an uncertainty of 0.2 bar on the pressure measurement.

The variation of the average ^{241}Am signal, defined as the mean value of a Gaussian fit to the α peak, is presented in Fig. 5.7-left as a function of the gas pressure. The light yield of the chamber is sufficient to clearly identify the alpha peak in the charge spectra (Fig. 5.3-left), and the statistical uncertainty from the fit is negligible for all the PMTs. The fluctuations in the number of photons are taken into account with a pressure independent systematic uncertainty of $\pm$ 3 – 5%, that is related to the uncertainty on the gain calibration and to the different spectral responses of the PMTs.

The light in the UV2 region (red square in Fig. 5.7-left) increases to more than twice the initial value in the [1.5, 16] bar pressure range, an effect which is consistent with the enhanced electron-ion recombination probability at higher gas pressure [163]. On the other hand, the signal in the UV3 region (black triangles) is stable within the uncertainties in that pressure range: this result suggests that the recombination light is consistent only with 128 nm photons production and no other emission is observed at longer wavelengths.

In Fig. 5.7-right the evolution of the charge signal in a fixed 90 ns time window after the trigger ("fast" component) is shown as a function of the gas pressure. The UV2 signal rises up to 25 PE and gets nearly stable at pressures above 7 bar, demonstrating that more photons are emitted promptly in the UV2 region (red dots) when the gas pressure increases. The UV3 component (black dots) barely depends on the pressure and represents the dominant light emission during the first 90 ns, up to 5 bar.

A typical signal from an α interaction in argon at 16 bar is plotted in Fig. 5.8. When it is compared with the signal at 1.5 bar (Fig. 5.4), a fast component can be now observed in the UV2 region. In the UV3 region, though, the pulse shape and the amplitude of the signal is similar to the 1.5 bar case. This is consistent with the fast component of the scintillation signal detected by the TPB-PMT being

significantly larger at 16 bar than at 1.5 bar.

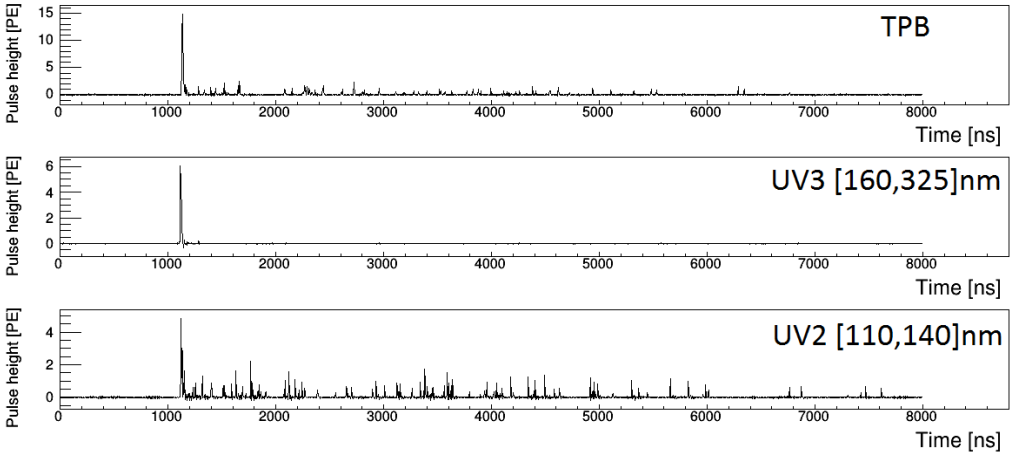

Figure 5.8: Typical Ar scintillation signals from 5.5 MeV α-particle interaction detected in three spectral regions, for argon gas at 16 bar. Compared to the typical signal at 1.5 bar (Fig. 5.4), a fast component appears in the UV2 region when the pressure is increased.

The argon scintillation pulse, averaged over 3×10^4 α interactions, is depicted in Fig. 5.9 for different pressures and spectral regions. The pulse heights are normalized to the maximum values, which are observed at 1.5 bar for the UV3 and 16 bar for the UV2 emissions, respectively. A relatively small decrease of the UV3 signal is evident as the pressure increases from 5 to 16 bar (Fig. 5.9-right). The enhancement of the fast argon scintillation component at higher pressure is evident in the UV2 region (Fig. 5.9-left). This effect is consistent with the reduction of the average distance among the argon molecules at higher pressure, which allows the formation of the excimer in shorter time and leads to an increase in the fast component through the decay of the singlet $^1\sum_u$ states. This result is in agreement with an old study that evidenced the dependence of the Ar_2^*-excimer formation-time on the gas pressure [177]. The change of slope around 6 bar in Fig. 5.7-right can be explained by the singlet state excimer formation time becoming smaller than the 90 ns fast signal integration window.

The use of sensors with different spectral sensitivity allows to study the second and the third continuum emissions separately. The average light pulse (from 2×10^4 events) in the UV3 region with argon at 1.5 bar is shown in Fig. 5.10-left. Data are fitted using the following expression:

$$I_{UV3}(t) = \frac{L}{\tau_{f_3} - \tau_{e_3}}(e^{-t/\tau_{e_3}} - e^{-t/\tau_{f_3}}) \otimes G(t - t_0, \sigma), \tag{5.24}$$

where L is a normalization constant, G a gaussian function, with mean t_0 and width σ, that accounts for the detector response and τ_{f_3}, and τ_{e_3} are the time necessary for the formation of the third continuum precursors and their characteristic photon emission time. In each bin of Fig. 5.10-left the pulse error is calculated through the statistical distribution of the set of waveforms and a fixed uncertainty of $\pm$ 2 ns is introduced by the sampling rate of the ADC.

The τ_{f_3} time constant is fast and it cannot be precisely measured from the fit due to the 250 MHz maximum sampling rate of our ADC, thus a limit $\tau_{f_3} \lesssim 1$ ns

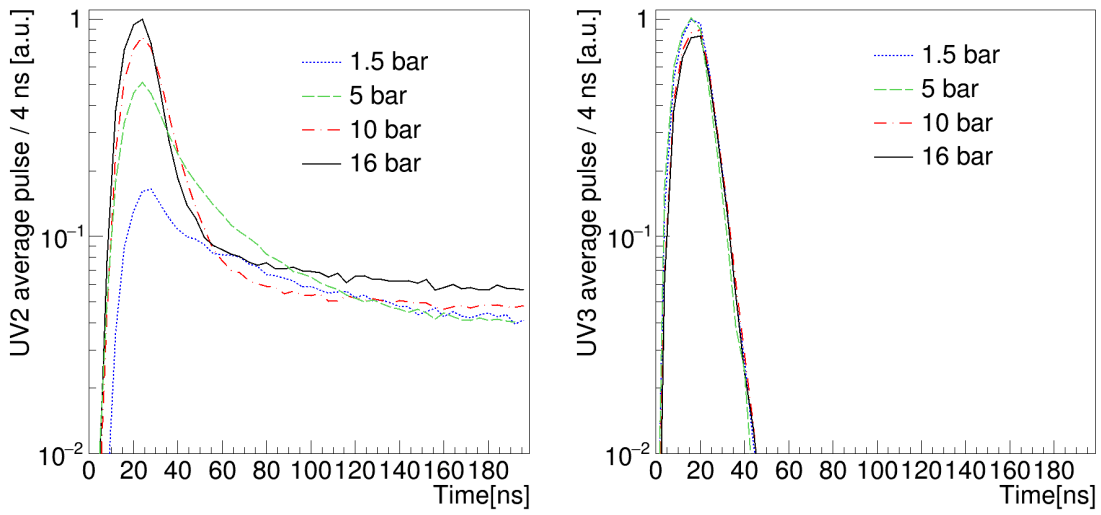

Figure 5.9: Average signals in the [1.5, 16] bar pressure range for the (left) UV2 and (right) UV3 regions. For UV3, only slight variations on the shapes are observed for different pressures. In the UV2 region, the fast component is more significant at higher pressure.

is set on the molecular-ions formation time. The photon emission time constant τ_{e_3} is independent of the gas pressure in the range [1, 16] bar (Fig. 5.10-right) and its value is 5.02 $\pm$ 0.11 ns, calculated as the average of the fit results in the pressure range of interest. This result is compatible with previous works [169, 162], where values of $\approx$ 5 ns have been obtained for the lifetime of these radiative molecular states.

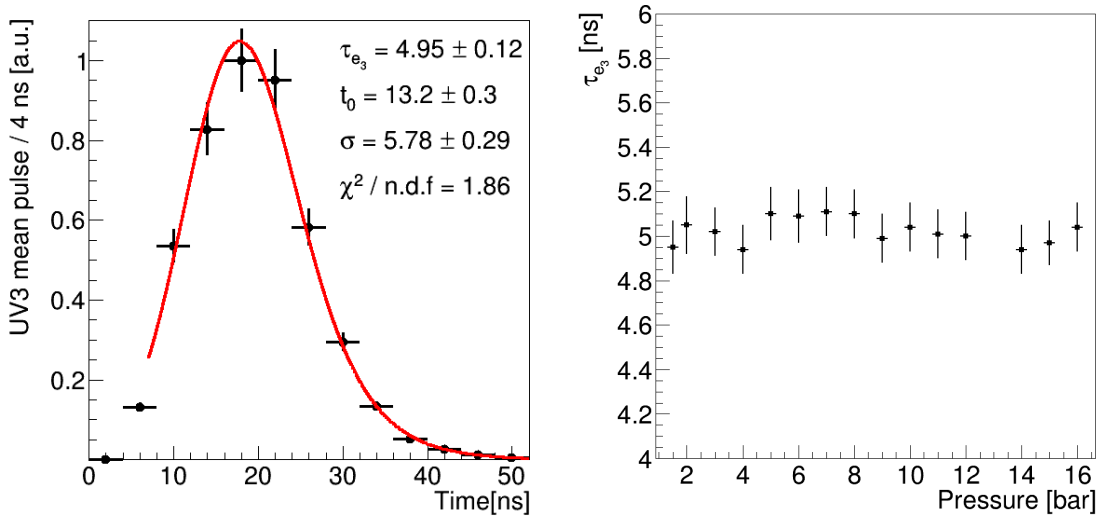

Figure 5.10: (Left) Result of the fit (red line) of the mean pulse for 2×10^4 α interactions in argon at 1.5 bar in the UV3 region (black) using Eq. 5.25. (Right) Dependence of the emission time constant with pressure in the 1.5 to 16 bar range.

The time constants of the argon second continuum in the UV2 region are obtained in the [1.5, 8] bar pressure range, fitting the average light pulse in the UV2 region

with the following function [176]:

$$I_{UV2}(t) = \left[\frac{L_1}{\tau_{f_2} - \tau^s_{e_2}} (e^{-t/\tau_{f_2}} - e^{-t/\tau^s_{e_2}}) + \frac{L_2}{\tau_{f_2} - \tau^t_{e_2}} (e^{-t/\tau_{f_2}} - e^{-t/\tau^t_{e_2}}) \right] \otimes G(t - t_0, \sigma), \tag{5.25}$$

The two exponential differences account for the singlet (s) and triplet (t) contributions, independently, with the corresponding τ_{e_2} parameters labeled accordingly. The formation times have been assumed to be identical for both contributions. The result of the fit of the UV2-PMT average charge spectrum at 1.5 bar (Fig. 5.11-left) proves that Eq. 5.25 represents an accurate description of the argon scintillation signal at that pressure.

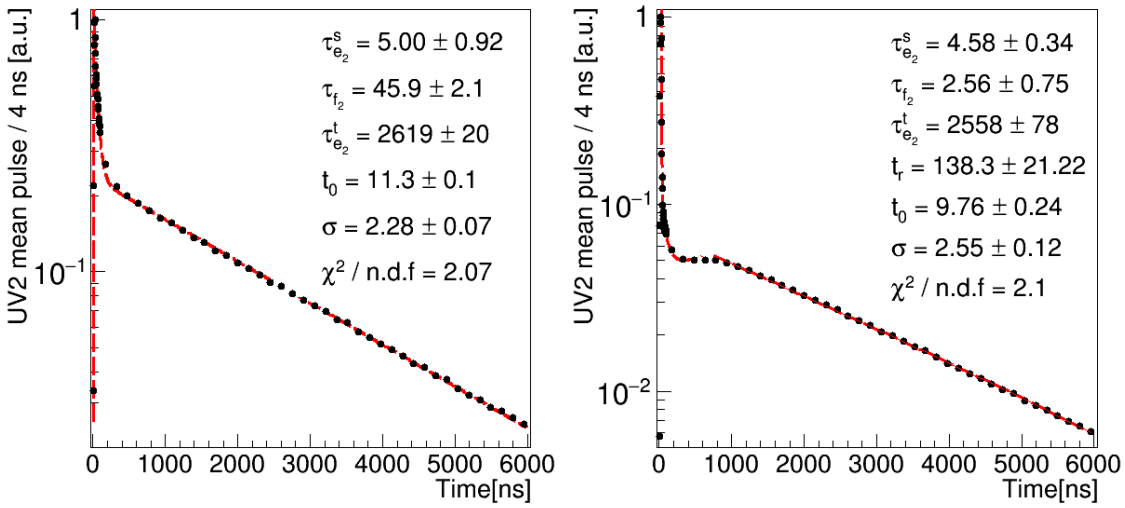

Figure 5.11: Results of the fits (red lines) of the mean pulses for 2×10^4 α interactions in argon at (left) 1.5 bar and (right) 16 bar, in the UV2 region (black dots). A 4 ns binning is used up to 100 ns and it is increased to 160 ns for larger times. Eq. 5.25 is used for the fit on the left, and Eq. 5.25 + Eq. 5.26 for the fit on the right.

At pressures larger than 8 bar, the UV2 signal shape is characterized by a new structure a few μs after the maximum pulse height, and Eq. 5.25 no longer describes the spectrum. A tentative explanation of this feature is taken from the model proposed in [103], that addresses the electron-ion recombination luminescence in the absence of electric field. This model considers a region of uniform ionization density and neglects the diffusion process out of the α track for the thermalized electrons. The recombination time τ_r is proportional to $P^{-2.7\pm0.3}$ for pressures larger than 10 bar [163] and it becomes shorter at higher pressures. In liquid argon, this time is below 1 ns, where the time dependence of the recombination is dominated by the molecular de-excitation time.

A new term is added to Eq. 5.25 in order to describe the scintillation from the charge recombination, I^R_{UV2}, which depends on the characteristic recombination time, t_r, and the excimer lifetime, τ_e, (discussed in Sec. 5.1):

$$\begin{aligned} I^R_{UV2}(t) &= L_3\ (e^{-t/\tau^t_e} - e^{-2t/t_r}), \qquad \text{for } t < t_r, \\ I^R_{UV2}(t) &= L_3\ e^{-t/\tau^t_e}, \qquad\qquad\quad \text{for } t > t_r, \end{aligned} \tag{5.26}$$

where L_3 is a normalization constant. The result of the UV2 signal fit to Eq. 5.25, after including the additional term $I^R_{UV2}(t)$, is shown in Fig. 5.11-right. The signal is successfully described by the fit above 8 bar up to 16 bar. The dependence of the excimer formation time and the singlet decay time in the UV2 region are summarized in Fig. 5.12-left for different pressures.

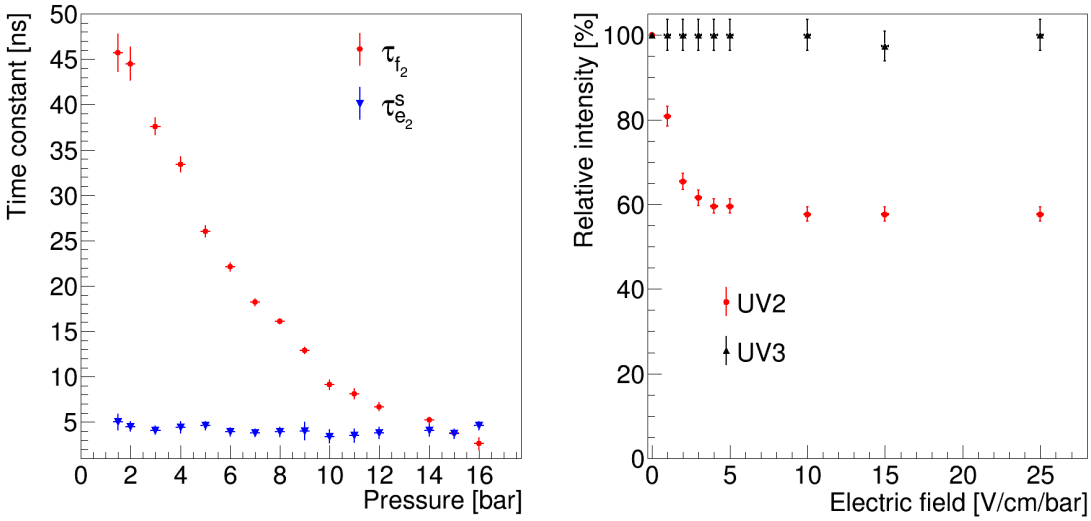

Figure 5.12: (Left) Dependence of the excimer formation time constant (red dots) and singlet de-excitation lifetime (blue triangles) with pressure in the 1.5 to 16 bar range. (Right) Dependence of the luminescence with the electric field intensity in the UV2 (red dots) and UV3 (black triangles) regions. The UV3 signal is not affected by the electric field.

The excimer formation time has a strong pressure dependence, decreasing from 46 ns at 1.5 bar to 2.6 ns at 16 bar. On the other hand, the singlet decay time emission is independent of the pressure with values around 4-5 ns. The triplet lifetime is measured to be ≈ 3 μs depending on the gas flow as expected. These results are in good agreement with previous studies [177]. At argon pressures below 5 bar, the excimer formation time is the dominant factor that determines the photon emission during the first hundred of ns. In this case, the singlet component of the second continuum emission is smeared over tens of ns. At higher gas pressures, the typical excimer formation time decreases.

5.5 Electric field dependence of the scintillation and spectroscopic studies of the electron-ion recombination

With the aim of establishing the nature of the new structure that appears in the UV2 range at large pressures and to study the field dependence of the UV3 emission, a small field cage (2 cm height) with the ^{241}Am source on the anode plate was introduced in the central volume of the pressure chamber.

Data at 10 bar of pressure were taken in order to fully contain the α track in the field region. In this setup the anode is grounded and the reduced electric field (E/P)

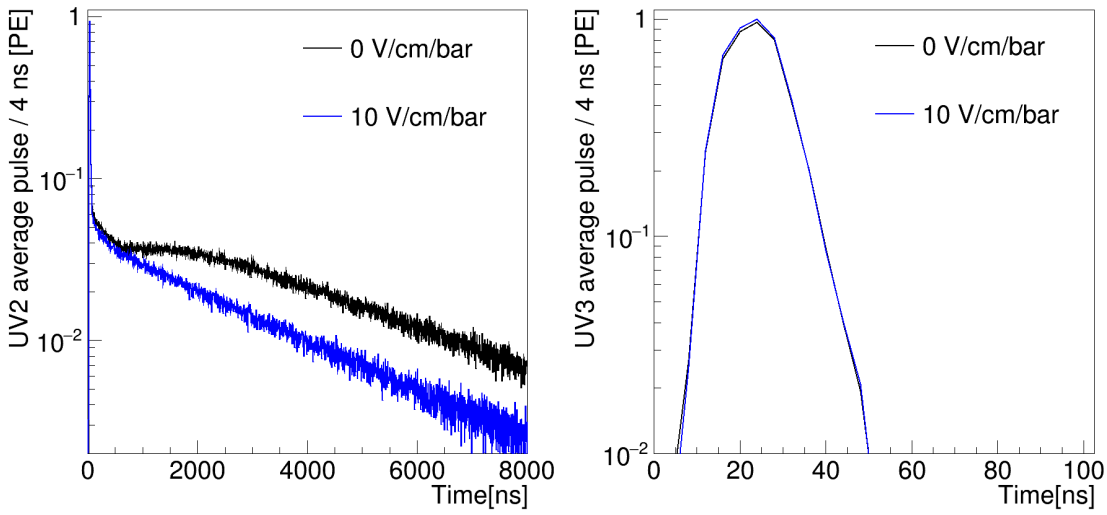

Figure 5.13: Mean pulse shape of the UV2 (left) and UV3 (right) signals with (blue line) and without (black line) electric field with argon at 10 bar. The bump in the UV2 graph disappears when the electric field is applied. The UV3 signal is not affected by the electric field.

applied in the range from 0 to 25 V/cm/bar. The number of PE measured with the ^{241}Am peak as a function of the electric field is shown in Fig. 5.12-right, evidencing that the emission in the UV2 wavelength range decreases with electric fields up to 4 V/cm/bar and then remains constant. The saturation in the collection of the charge above this field value is consistent with the measurements reported in [163] for the second continuum. On the other hand, the emission in the UV3 spectral region is not affected by the electric field up to 25 V/cm/bar.

The scintillation pulses at 10 bar with and without a 100 V/cm field, averaged over 2×10^4 events and normalized to the maximum value of the distribution, are shown in Fig. 5.13, both for the UV2 and UV3 spectral ranges. The bump over 1 μs in the UV2 range (left graph) disappears by increasing the amplitude of the reduced field. This result confirms the interpretation of this structure in terms of electron-ion recombination given in Sec. 5.4. When a sufficiently strong field is applied, the charge recombination is suppressed and the overall signal shape is similar to the scintillation pulse at pressures below 8 bar. In these conditions, the argon slow component is well described by a single exponential function.

The distribution for UV3 (right plot) proves that the photon emission in this spectral region is not affected by the electric field. This result demonstrates that the recombination light is consistent only with the second continuum emission at 128 nm.

5.6 First evidence of the third continuum emission with a β source

Our experiments with α particles in argon at different pressures have proved that a substantial component of the scintillation is in the range [160, 325] nm and is not related to the radiative de-excitation of the singlet and triplet excimers. We

interpret this photon production through the mechanism responsible for the third continuum emission (Sec.5.1). Additional studies have been performed replacing the ^{241}Am α source with a weak ^{90}Sr/Y β source (activity $\approx$ 100 Bq), with 546 keV and 2280 keV Q-values of the decays. We collected several runs with argon in the pressure range [15, 21] bar. The β's from the source are typically not fully contained in our detector, unlike for the case of α interactions. To increase the light collection, the UV2-PMT (R6835) is replaced by another phototube coated with TPB (R6095). In this configuration, the trigger is produced by the coincidence of the two TPB-PMTs.

The integrated charge spectrum of one TPB-PMT, obtained with the ^{90}Sr/Y β source and gas argon at 20 bar is compared with a background spectrum taken without any source (Fig. 5.14). A prominent excess is present at low energy, between 6 and 25 PE, giving us a solid evidence of the actual identification of the β interactions. A typical signal produced by one UV-PMT and one TPB-PMT in this region is displayed in Fig. 5.15. A clear pulse, similar to the one detected with the α source but with an amplitude consistent with the different energy scale, is shown in the UV3 region in coincidence with the TPB-PMT signal. To the best of the authors knowledge, this result is the first evidence of the third continuum emission produced by a β interaction in argon gas.

This demonstration of the third continuum emission from α and β interactions in argon, provides evidence that the temporal and spectroscopic information of the argon scintillation are strongly related. Further studies are necessary to assess the possibility to perform particle identification with this method.

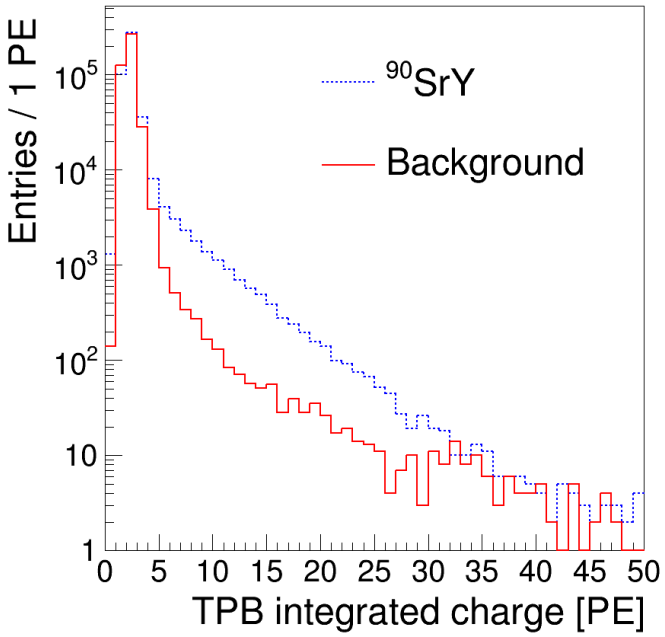

Figure 5.14: Integrated charge for events collected without (red line) and with (blue line) the ^{90}Sr/Y β source in the center of the detector. The number of events is normalized to the same acquisition time.

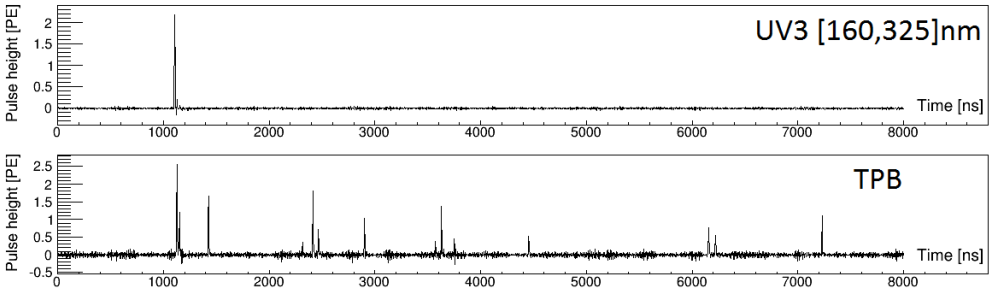

Figure 5.15: Typical Ar scintillation signals detected for a β event in two spectral regions, with argon gas at 20 bar.

5.7 Pulse shape discrimination of α and β events in argon gas

It is necessary to demonstrate the capability of performing a pulse shape discrimination (PSD) in our detector, and distinguish α and β events in order to study the possibility of novel particle discrimination technique based on the spectroscopic information.

A new variable, F_{90}, is defined as the ratio of the light detected in the first 90 ns to the total. The TPB integrated signal is represented respect to the F_{90} value for events from the ^{241}Am (Fig. 5.16-left) and the ^{90}SrY (Fig. 5.16-right) sources. In Fig. 5.16-left, one distribution is distinguished at high energy with a F_{90} value around 0.25. This population of events is associated with α decays from the source. The low energy events are associated with environmental radioactivity.

On the other hand, two distributions are identified in Fig. 5.16-right. Comparing with Fig. 5.16-left, the F_{90} value and the energy scale are compatible with α decays around 5 MeV. For this reason, these events are identified as α interactions from the ^{222}Rn decay chain. The second distribution at low energy is associated with β interactions from the ^{90}SrY source and environmental γ-rays. An asymmetry is applied to select the events produced in the center of the detector.

The F_{90} ratio is depicted in Fig. 5.17 for the two distributions detected with the ^{90}SrY source. The α and β interactions are selected with two energy cuts, over 150 PE and below 60 PE for α and β decays, respectively. The integral of both distributions are normalized to 1 for visualization. The α events have a $F_{90} = 0.25$, while the β interactions has a width range of F_{90} values between 0.4 and 0.8, with its mean value close to 0.6. The F_{90} value is larger for β than for α interactions in gas argon. An opposite behaviour to the one found in the liquid argon scintillation components (0.3 for β and 0.7 for α events). One possible explanation is the absence of recombination for electrons in gas argon.

The PSD capability of the detector is demonstrated, enabling the setup to evaluate the possibility of a new discrimination technique based in the wavelength emission of the scintillation components. The viability of this technique and its potential in argon gas detectors is under study.

Future tests in liquid argon will be done to estimate the impact over dark matter and neutrino detectors of the effects reported in this chapter.

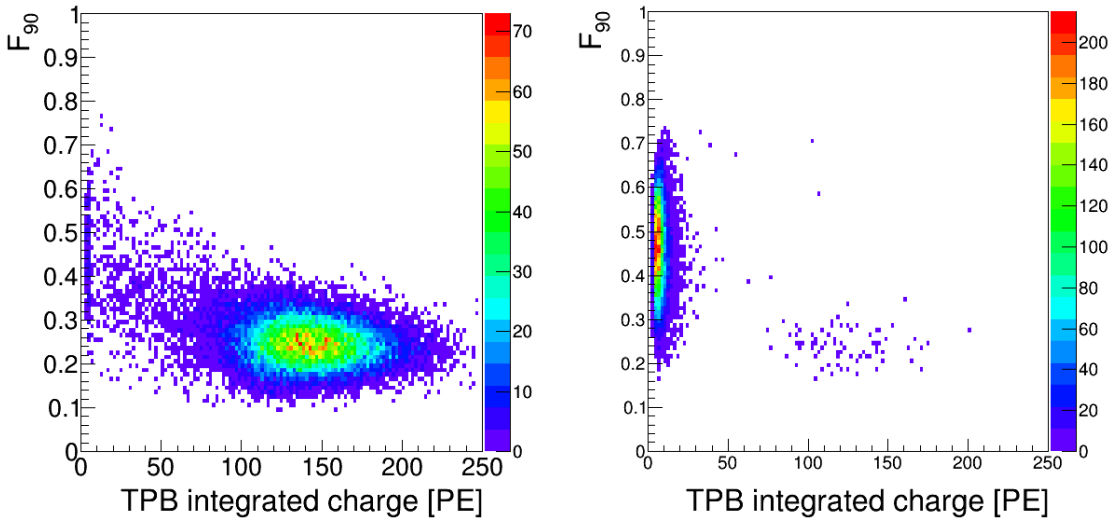

Figure 5.16: F_{90} ratio respect to the total integrated charge using the ^{241}Am (left) and ^{90}SrY (right) sources. The signal is studied in the full wavelength range with the TPB-PMT.

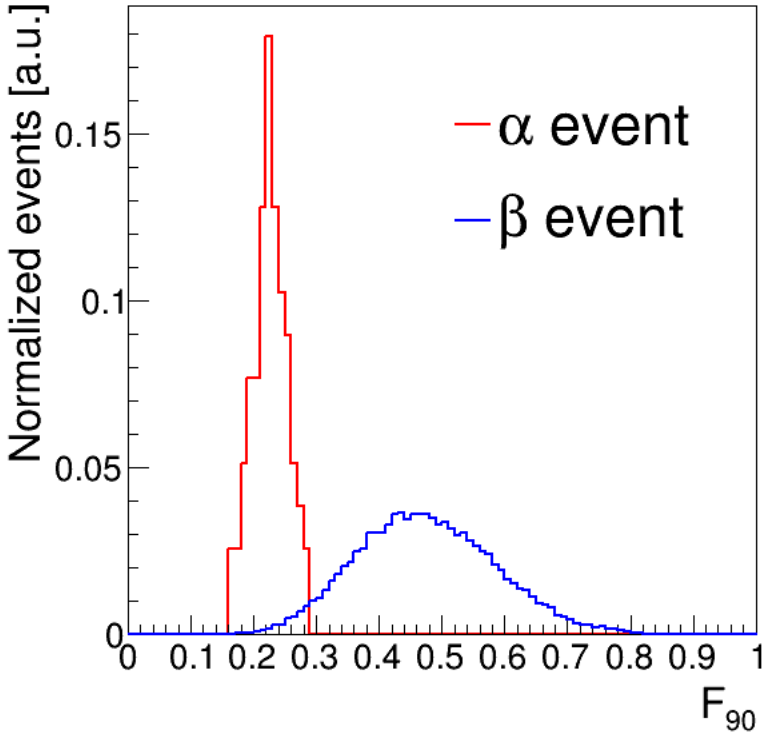

Figure 5.17: F_{90} ratio for the distributions under 60 PE and over 150 PE detected with the ^{90}SrY source. The integral of both distributions is normalized to 1. The ratios are 0.25 and 0.6 for α and β events, respectively.

5.8 Spectroscopic studies with xenon gas

The characteristics of the xenon scintillation are well established. However, usually the emission spectrum assumed in xenon gas experiments consists only of a 2nd continuum centered around 172 nm. This is in contrast to observations under α

particles of another continuum around 300 nm [160, 169, 170].

Additionally, electrons have a special interest for the study of nuclear reactions, in particular for

We have designed and assembled a sensitive wavelength-sensitive chamber in collaboration with IGFAE (see Fig. 5.18), to study the spectroscopic characteristics of the xenon scintillation light emission. It consists of two CF-100 40 cm length stainless steel cylinders. It is equipped with one electric feedthrough, three service lines for the vacuum and the gas filling and recirculation, and 2 CF-40 flanges for the PMT power supply and the signal extraction.

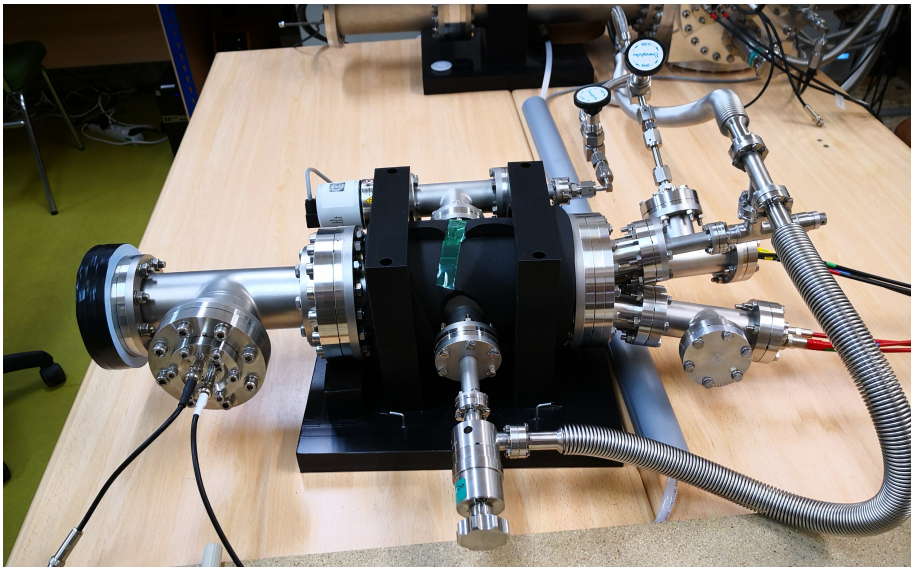

Figure 5.18: High pressure xenon chamber at IGFAE.

Four 1" Hamamatsu R7378A phototubes are placed in a PTFE support (see Fig 5.19-left). The nominal QE of these PMTs is plotted in Fig. 5.2-right as a function of the photon wavelength. Two long-pass filters from Asahi [174]) are placed in front of the PMTs, making them sensitive only to the third continuum. This work investigates the xenon scintillation in the spectral ranges [170, 550] nm and [250, 550] nm called UV and UV4 regions in the following, respectively.

The PMTs are placed in front of an electrified region of 4 cm diameter and 4 cm height, delimited by an aluminum field cage. The internal part is covered with a Teflon jacket, as a reflector, and the anode consisted of a 71% transparency mesh, situated at a distance of 1.5 cm from the PMT plane (see Fig. 5.19-right).

The PMT signals are fed to a CAEN DT5725 ADC (14-bit resolution and 250 MS/s sampling rate). The trigger is generated with a R7378 PMT without filter using a leading-edge discriminator (CAEN N841), with a threshold set to 0.5 photoelectrons. Different runs are taken with digitization windows from 4 μs to 8 μs.

The system is equipped with a recirculation system with hot and cold getters and a circulating compressor. The chamber was pumped until a residual pressure level of 10^{-4} mbar and then filled with gas xenon. The scintillation yield steadily increases until it reached saturation after a few minutes with the recirculation system.

The results presented in this study are obtained with ^{241}Am (activity $\approx$ 500 Bq) and ^{90}Sr/Y (activity $\approx$ 100 Bq) radioactive sources. The pressure chamber is

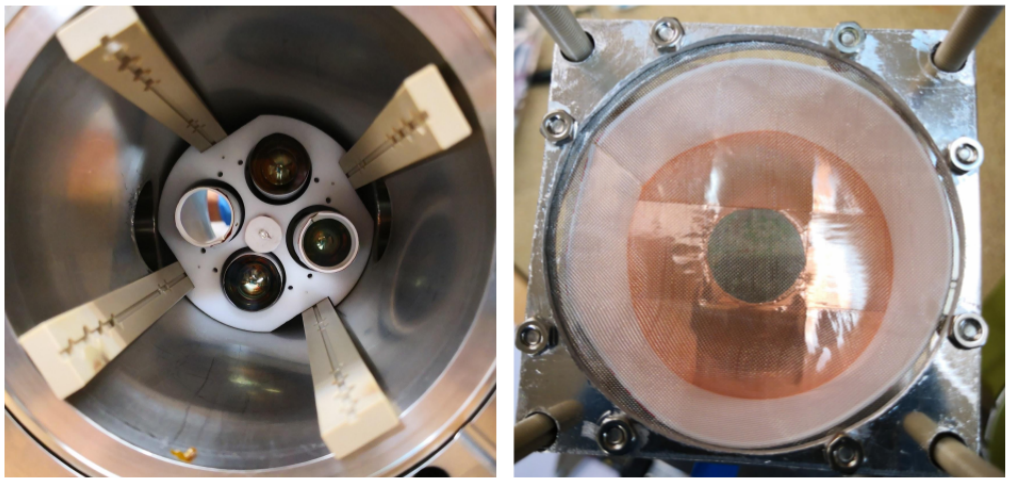

Figure 5.19: (Left) Photo of the 4 R7378A phototubes in the PTFE support structure. Two filters are placed in from of two PMTs. (Right) Photo of drift field cage. The internal part is covered with a Teflon jacket. The radioactive source installed in the cathode is visible behind the mesh, which works as the anode.

equipped with an acrylic support structure able to host one radioactive source in the centre (see Fig. 5.19-right).

5.8.1 Preliminary results with α and β sources

Initial measurements were carried out with a ^{241}Am α-source in gas xenon up to 10 bar using four R7378-PMTs: two without filter (UV-PMT1 and UV-PMT2 in the following) and the other two with a long-pass filter (UV4-PMT1 and UV4-PMT2). Preliminary results will be reported in this section.

The pulse shape of a typical signal, produced by an α event in xenon at 2 bar, is presented in Fig. 5.20, as registered by the different PMTs. The UV-PMTs detect the characteristic fast and slow components of the xenon emission. However, only the fast component of the scintillation is detected in the UV4 region, in form of a short pulse (10 ns scale).

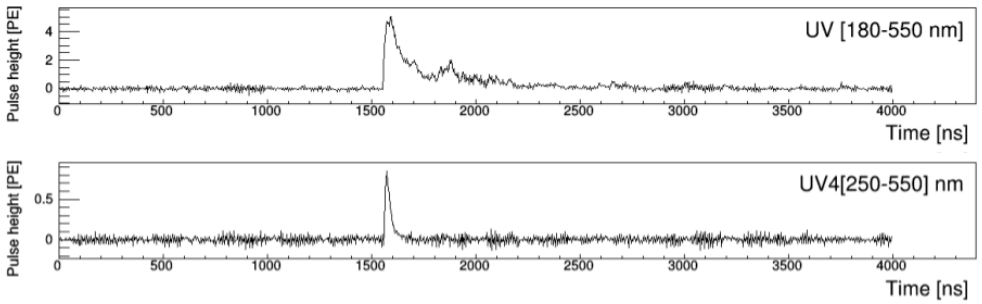

Figure 5.20: Typical Xe scintillation signals from 5.5 MeV α-particle interaction detected in two spectral regions, with xenon gas at 2 bar.

The gas purity is assessed through the decay time of the slow component of the xenon second continuum emission. Values in the range [80-95] ns were obtained

depending on the gas pressure and flow. Simple selection criteria are applied to reject a few percent of the total triggers which are produced by electronic noise and cross-talk events. The time constant for the third continuum emission measured is around 8 ns.

The relative intensity of the ^{241}Am peak (respect to 0 V/cm/bar peak) as a function of the electric field is shown in Fig. 5.21-left for different pressures. The emission in the UV wavelength range decreases with the electric field. The saturation in the collection of the charge above a 50 V/cm/bar field value is consistent with the measurements reported in [163] for the second continuum. On the other hand, the emission in the UV4 in the spectral region, Fig. 5.21-right, is not affected by the electric field up to 100 V/cm/bar.

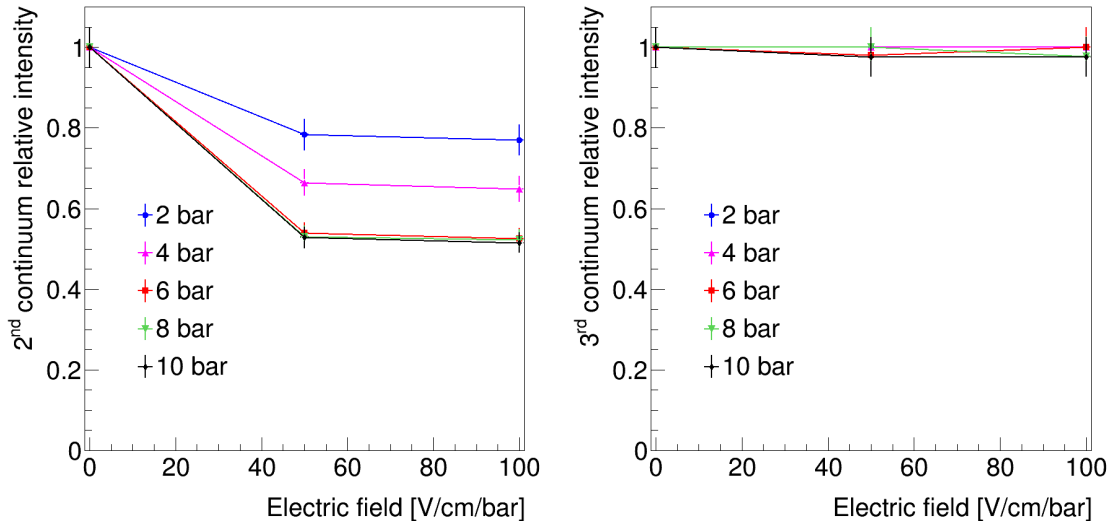

Figure 5.21: Relative intensity of the ^{241}Am peak (respect to 0 V/cm/bar peak) in the UV (left) and UV4 (right) ranges as a function of the electric field.

Additional studies have been performed replacing the ^{241}Am α source with the ^{90}Sr/Y β source. We collected several runs with xenon in the pressure range [1, 10] bar. The β's from the source are typically not fully contained in our detector for pressures lower than 2 bar, unlike for the case of α interactions.

The relative intensity of the ^{90}Sr/Y mean value as a function of the electric field is shown in Fig. 5.22-left for different pressures. The emission in the UV wavelength range remains stable with the electric field up to 100 V/cm/bar. This is the first direct evidence that electrons do not produce recombination in xenon gas up to at least 10 bar.

A signal is detected in the UV4 range with the β source over 2 PE. The dependence with the electric field is depicted in Fig. 5.22-right, as expected, it is not affected by the electric field up to 100 V/cm/bar. The shape of this signal is similar to the third continuum previously identified in argon. Thus, we can state the detection of the third continuum in the range [2-10] bar pressure for α and β events in xenon gas.

In conclusion, direct evidence has been obtained for the first time that electrons do not produce recombination in xenon gas in the pressure range [2-10] bar. Furthermore, the third continuum emission produced by α and β interactions in xenon gas has been also obtained for the first time using a ^{241}Am and a ^{90}Sr/Y source.

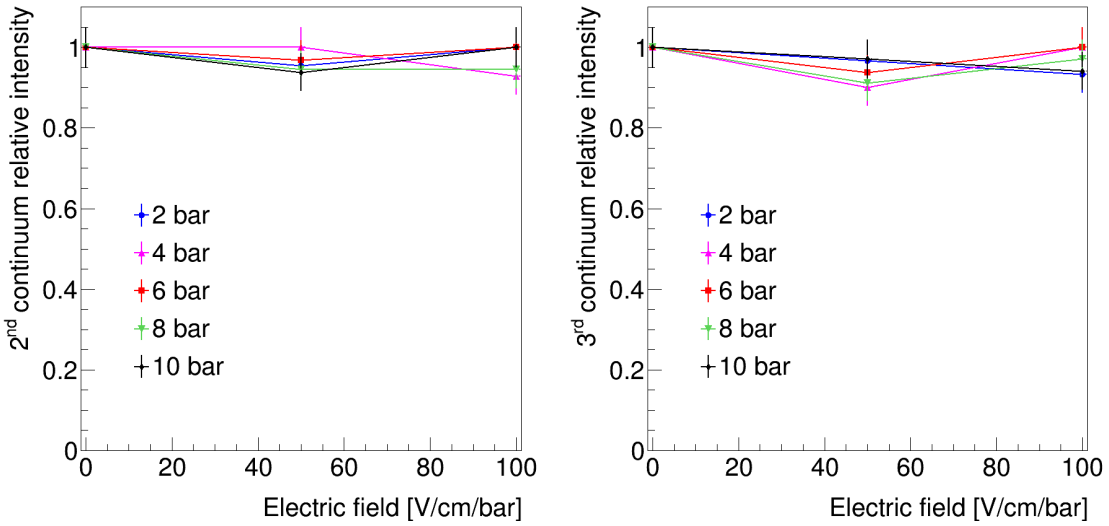

Figure 5.22: (Relative intensity of the ^{90}Sr/Y mean value (respect to 0 V/cm/bar peak) in the UV (left) and UV4 (right) ranges as a function of the electric field.

Chapter 6

Experimental aspects of the positive ion current on large size Argon detectors

Particle interactions in argon produce simultaneous excitation and ionization of the atoms, generating photons in the VUV range and ion/electron pairs. The mechanism of primary photon emission is similar for all the noble elements and goes through the formation of excimers, diatomic molecules in an excited state (see Chapter 5). At the same time, molecular ions are formed in short time (of the order of the ps) after the ionization of the atom. The electrons, produced contemporary, can travel of the order of 10^3 nm [178] in liquid argon (LAr), and, after being thermalized by interactions with the surrounding medium, they can recombine with nearby molecular ions within a time-scale of the order of 1 ns [101]. The columnar model of Jaffe [179] is the favorite one to describe the recombination, and it depends on the overall electron and ion charge density produced by ionization in a cylindrical volume surrounding the particle trajectory. The process leads, finally, to the formation of an excimer in the final state, thus an additional photon emission is possible with the same wavelengths and decay times of the excitation states.

In a typical liquid argon time projection chamber an electric field E_d prevents the full recombination of the charges allowing the collection of the ionization electrons at the anode. Under the effect of the electric field, the ions drift to the cathode following the same field lines of the electrons, however the former have a drift speed much smaller than that of the latter. The ion mobility is not very well known, and the values reported in the literature range between $\mu_i \approx 2 \times 10^{-4}$ cm^2 V^{-1}s^{-1} [180] and $\mu_i \approx 1.6 \times 10^{-3}$ cm^2 V^{-1}s^{-1} [181, 182] with the liquid in steady state. Even considering the more conservative larger value, the expected ion velocity v_i is five orders of magnitude lower than that of the electrons v_e at the same field. Once the drift field is turned on, the electrons are collected in relatively short time ($v_e \approx 2$ m/ms at $E_d \sim 1$kV/cm [117]) while, in a detector with maximum drift of the order of a few meters, the ions can stay in the liquid for some minutes before they get collected and neutralized on the cathode ($v_i \approx 1.6{\times}10^{-5}$ m/ms at $E_d \sim 1$kV/cm). Hence, a positive volume charge is created in liquid argon depending on the particle interaction rate in the active volume.

This space charge can locally modify the drift lines, the amplitude of the electric field, and ultimately the velocity of the electrons, thus, a displacement in the

reconstructed position of the ionization signal can be produced. Additionally, for relatively large values of the average density of positive ions, the positive-charge density can be sizable such that the probability of a "secondary electron/ion recombination", different than the recombination that occurs within the ionization track [101], has to be considered between the drifting electrons and the free positive ions. This effect can cause an additional signal loss, with a probability dependent on the electron drift path, that could resemble the charge quenching given by the contamination of the electronegative impurities in LAr. At the same time it can produce the emission of photons through channels similar to the recombination light.

This effect can be particularly relevant for dual-phase detectors foreseeing large charge amplification factors, where the ions, created in the vapor volume, may cross the gas-liquid interface and further increase the average density of positive ions in the active LAr volume.

In this chapter, I studied the impact of the space charge effects in liquid argon detectors. Additionally, preliminary results concerning the study of the space charge effects in a small (≈1 L) liquid argon chamber are presented.

6.1 Secondary recombination in liquid argon detectors

In case of large detectors with drift fields of some meters, the probability of a secondary recombination, different than the primary columnar recombination, has to be considered between the drifting electrons and the molecular ions, called "secondary ions" onwards. The recombination cross section σ between free charges can be defined as the transverse area whose crossing field lines end on one ion. Given a free positive charge q in the active volume (Fig. 6.1), which is steady with respect to the drifting electrons, the total number of field lines emerging from the ion, q/ϵ, is equal to the number of lines traversing the cross section, $E_d \times \sigma$, therefore the cross section can be simply given by [183]:

$$\sigma = \frac{q}{\epsilon E_d}, \tag{6.1}$$

where q is the elementary charge, ϵ the absolute permittivity of the liquid argon and E_d the amplitude of the drift field. It has a value of $\sigma = 1.2\ 10^{-9}$ cm^2 for a field of 1 kV/cm in liquid argon. Any electron located in a field line that crosses this surface recombines. Fig. 6.1 shows the field paths approaching an ion positioned at (0,0), which has a negligible size at the micron scale, in case of $E_d = 1$ kV/cm. The red curve is the envelope of all the lines ending on the ion.

In liquid argon time projection chambers, ions and electrons are constantly created by the particle interactions. Given the ≈ 1 Bq/kg [184] contamination of ^{39}Ar in atmospheric argon, a minimum ionization rate, of approximately 1.1×10^7 pairs/(m^{3}s) is expected in liquid [183, 185]. In case the detector is located on the Earth surface, the dominant contribution to the total ionization is typically given by the muons, and the ion production rate can be calculated as 1.5×10^9 pairs/(m^{3}s), two orders of magnitude greater than that given by the ^{39}Ar contamination.

The secondary ions are not uniformly dispersed within the detector but are grouped, either in a trace of a muon or in a globule around the disintegrated isotope.

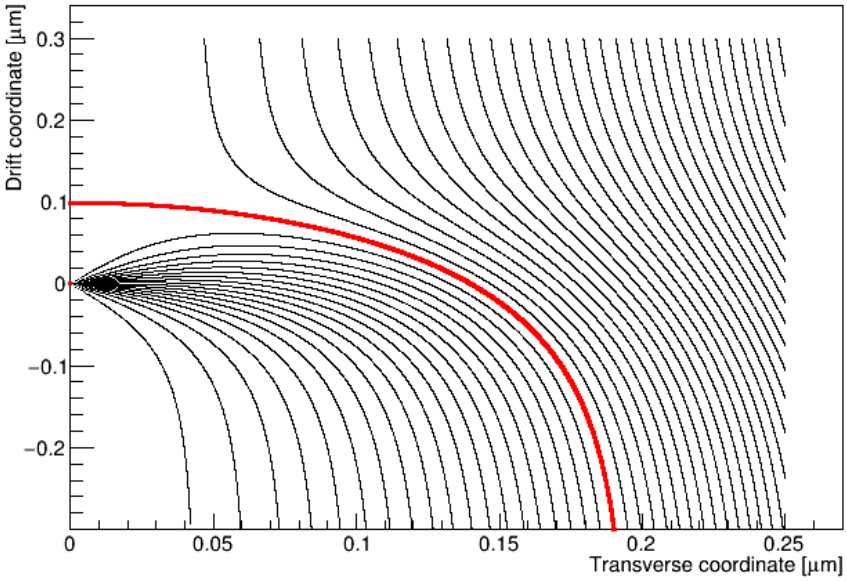

Figure 6.1: Configuration of the drift lines near a positive ion placed at (0,0) for a nominal drift field of 1 kV/cm. The drift field is along the vertical axis. The thick red line is the envelope of the field lines ending on the ion [183].

Since the electric field is linear, the field lines, and the surfaces defined by them, add up. Therefore, the area projected in a plane normal to the field by a grouped set of secondary ions is equal to the sum of all the areas due to the individual ions, independently of the shape of the set. The trace of a muon will produce on its projection in the normal plane a surface in the form of an elongated rectangle and an area defined by the ions contained in the trace. The ^{39}Ar decay will be projected in an approximately circular shape.

Suppose that a primary event of interest occurs in the detector at a distance L from the anode. In this place, an ionizing particle is generated, normally an argon nucleus, which produces positive ions, which we do not deal with here, and primary electrons that drift towards the anode through the action of the electric field. On their way, the electrons recombine with the secondary ion clouds previously produced by ^{39}Ar beta emissions and by cosmic muons. Given the difference in velocities between electrons and ions, these can be considered static during the transit time of the electrons to the anode. In the same way as ions, the cloud of primary electrons generates field lines, this time incoming, that project into an area, normal to the field, of surface proportional to the charge of the cloud. Since the projected range of the argon nuclei in LAr is very small, the primary ionization can be considered point-like and the projected area can be considered circular, with a center at the point of primary interaction and with a characteristic size defined by a primary radius r_p.

Recombination between primary electrons and secondary ions is given by the intersection of the normal surfaces to the field generated by the electrons and by the ions. To simplify the study of the recombination of the primary signal, we introduce an impact parameter α that describes the position, in units of r_p, of the center of

the primary electron cloud with respect to the edge of a secondary ion area. If $\alpha > 1$ this distance is greater than r_p, the primary signal is outside the ion area and there is no recombination. If $\alpha = 0$, the center of the negative cloud is just on the edge of the positive area and the recombination is approximately half. Finally, if $\alpha \leq$-1, the cloud will completely recombine since it is entirely within the ion area. The amount of recombined signal is given, in a first approximation, by the parameter α.

If we consider real signals, with a high number of electrons covering a large cross section, we have to take into account, not only a degradation of the signal due to scattered recombination but also the possibility that the signal will be recombined in much or all of it through a zone of high concentration of secondary ions. This effect can be expressed by the difference between the probability of having some recombination, case of $\alpha = 1$, and the probability of having complete recombination, case of $\alpha =$ -1. The smaller this difference, the greater the impact of high recombination.

The recombination is calculated with the following process. The detector is divided into infinitesimal slabs normal to the x-direction of the field. The rate of charge production per unit of area is calculated in each slab, and it is integrated respect to time and x. This calculation gives us the relationship between the recombination area and the total detector sectional area, that is, the probability that an isolated electron will be recombined. To study extensive primary signals we increase or decrease the edges of the secondary ionization zone by an amount of αr_p to consider the size of the primary electronic cloud. We repeat the integration to obtain the probability that an extensive primary signal finds an ion zone that recombines at least the part of the signal determined by α.

The amount of electrons produced by the primary particle is $N_p = FE_p$, where $F = 30$ e$^-$/keV is the energy efficiency of ionizing the argon and, E_p, is the energy of the primary particle. The disk, perpendicular to the field, containing the generated lines has an area of $A_p = N_p\ \sigma$ and a radius: $r_p = \sqrt{N_p\sigma/\pi}$.

Three different primary energies have been considered: 10 keV, 100 keV, and 1 MeV. The radii of the primary disks for these energies are 3.3 10^{-4} cm, 1.1 10^{-3} cm, and 3.3 10^{-3} cm. As a comparison, the projected ranges of an alpha particle at these energies in LAr are 1.9 10^{-5} cm, 7.3 10^{-5} cm, and 6.5 10^{-4} cm [186], values much less than the radius of the primary disks.

6.1.1 Underground TPC

In the case of an underground detector, there are no cosmic muons. The secondary ions are exclusively due to the beta decay of the ^{39}Ar isotope that is uniformly distributed in the volume of the LAr. The electrons emitted by the ^{39}Ar have an energy spectrum $\Phi(E_{Ar})$ which covers a range from 0 to a maximum E_Q worth 565 keV.

Each ^{39}Ar decay produces an ionization zone of a size limited by the range of beta particles in LAr, this range is 0.34 mm [186] for average energy of 175 keV. Although this range is 10 to 100 times greater than the radii of the primary discs previously shown, to facilitate the analysis, the energy deposition has been considered punctual. The electrons resulting from the decay are immediately withdrawn by the electric field, leaving the slowly drifting ions. These generate a disk of recombination field lines of area: $S_{Ar} = F\sigma E_{Ar}$, and radius $r_{Ar} = \sqrt{S_{Ar}/\pi}$. The beta spectrum has been taken from [187] and normalized so that its integral over energy is equal to the

activity of ^{39}Ar in the atmospheric argon (1 Bq/kg).

To determine the probability of recombination of an isolated electron, produced at a distance L from the anode, we divided the detector into slabs normal to the direction-x of the field. In each slab, of thickness dx, the rate of production of recombination area per unit of detector cross section is:

$$\frac{d^2A_{Ar}^{1e^-}}{dtdx} = \int S_{Ar}\rho\Phi(E_{Ar})dE_{Ar} = \int F\sigma E_{Ar}\rho\Phi(E_{Ar})dE_{Ar}, \tag{6.2}$$

where $\sigma = 1.2\ 10^{-9}$ cm^2 is the equivalent area of recombination of an individual ion and $\rho = 1500$ kg/m^3 is the density of the LAr.

To determine this integral, the beta spectrum was fitted to a 4th degree polynomial $\Phi(E_{Ar}) = \sum_{i=0}^{4} a_i E_{Ar}^i$, resulting in:

$$\frac{d^2A_{Ar}^{1e^-}}{dtdx} = F\sigma\rho\int E_{Ar}\left(\sum_{i=0}^{4} a_i E_{Ar}^i\right)dE_{Ar} = F\sigma\rho\left(\sum_{i=0}^{4}\frac{a_i E_Q^{i+2}}{i+2}\right). \tag{6.3}$$

This expression is not time dependent, so, to integrate with respect to time we just multiply by the lifetime of ions, $(L - x)/v_i$. This is the time to remove the ions by the field:

$$\frac{dA_{Ar}^{1e^-}}{dx} = F\sigma\rho E_Q^2\frac{L-x}{v_i}\left(\sum_{i=0}^{4}\frac{a_i E_Q^i}{i+2}\right), \tag{6.4}$$

where v_i is equal to the drift speed of the ions. The value of v_i is approximately $1.6\ 10^{-5}$ m/ms with an electric field of 1 kV/cm. Finally, integrating with respect to the variable x from 0 to L:

$$A_{Ar}^{1e^-} = \frac{F\sigma\rho L^2 E_Q^2}{2v_i}\left(\sum_{i=0}^{4}\frac{a_i E_Q^i}{i+2}\right). \tag{6.5}$$

The calculated value of this electron recombination probability for an underground detector of $L = 10$ m is 0.37%.

The recombination of the signal, parameterized by α, occurs when the primary disk, of radius r_p, intersects some secondary effective disk, of radius r_{Ar}, with a distance between centers less than an effective radius $r_{eff} = r_{Ar} + \alpha r_p$. The effective area $S_{eff} = 2\pi r_{eff}^2$ is the probability that the secondary effective disk will recombine a signal fraction equal to or greater than that determined by α.

The total probability of loss of a signal fraction is given by the relative weight of the sum of all the secondary effective disk areas with respect to the total section of the detector. To determine this value we divide the detector into slabs normal to the field of thickness dx and we integrate with respect to the energy, in each slab, the area of the disks:

$$\frac{dA_{Ar}}{dt} = \int S_{eff}\rho dx\Phi(E_{Ar})dE_{Ar} = \rho dx\int\pi(r_{Ar} + \alpha r_p)^2\Phi(E_{Ar})dE_{Ar}. \tag{6.6}$$

To integrate the previous equation, we change the variable from E_{Ar} to r_{Ar} using $E_{Ar} = \pi\ r_{Ar}^2/F\sigma$. The minimum integration radius is obtained using the fact that

the effective radius has to be defined positive $r_{eff} = r_{Ar} + \alpha\ r_p > 0$ and therefore $r_{Ar} > -\alpha\ r_p$. The integral is:

$$\frac{d^2 A_{Ar}}{dtdx} = \frac{2\pi^2 \rho}{F\sigma} \sum_{i=0}^{4} a_i \left(\frac{\pi}{F\sigma}\right)^i \left(\frac{r_Q^{2i+4} - r_{min}^{2i+4}}{2i+4} + 2\alpha r_p \frac{r_Q^{2i+3} - r_{min}^{2i+3}}{2i+3} + \alpha^2 r_p^2 \frac{r_Q^{2i+2} - r_{min}^{2i+2}}{2i+2}\right). \tag{6.7}$$

Where r_Q and r_{min} are the integration limits. Integrating again with respect to time first and variable x after:

$$A_{Ar} = \frac{\pi^2 \rho L^2}{F\sigma v_i} \sum_{i=0}^{4} a_i \left(\frac{\pi}{F\sigma}\right)^i \left(\frac{r_Q^{2i+4} - r_{min}^{2i+4}}{2i+4} + 2\alpha r_p \frac{r_Q^{2i+3} - r_{min}^{2i+3}}{2i+3} + \alpha^2 r_p^2 \frac{r_Q^{2i+2} - r_{min}^{2i+2}}{2i+2}\right). \tag{6.8}$$

Fig. 6.2 shows the probability of recombination respect to the α parameter value for an underground detector with a drift distance of 10 m. This probability plummets to a null value in the case of 1 MeV. This is because the size of the primary disk, r_p = 3.3 10^{-3} cm, is greater than the largest possible size of an ion disk, which has a radius $r_Q = 2.54^{-3}$ cm. For $\alpha = 0$ the calculated value is equal to the recombination probability of an isolated electron, 0.37%.

6.1.2 Surface TPC

At the surface, the recombination charge is mainly produced by the cosmic muons. The muons pass entirely through the detector leaving a straight trace of ionization from the anode to depth L where the primary particle is produced. The ion density produced is $Q \approx 5\ 10^4$ ions/cm. The traces impinge obliquely, with an angle θ with respect to the vertical, and have a length of $L/\cos\theta$.

In case of a vertical drift field, the positive charge of the muon traces is projected in the horizontal plane, normal to the field, to define a recombination area of the primary electrons. In the case of perfect vertical incidence ($\theta = 0$) the projected area normal to the field resembles a circle. In this case, and for L = 10 m, the number of ions produced is $QL = 5\ 10^7$, which corresponds to an area of $Q\sigma L = 6\ 10^{-2}$ cm^2. The radius of this circle is 1.4 mm.

In general, an oblique trace is projected on a long, narrow rectangle, of length $l_\mu = L\tan\theta$, area $S_\mu = Q\sigma L/\cos\theta$ and width $w_\mu = Q\sigma/\sin\theta$. For small θ angles the segment does not diverge, approaching the circular shape discussed earlier.

The muon flux distribution varies as: $\Phi(\theta,\ \phi) = \Phi(0)\cos^2\theta$ muons / (m^2 s sr), where $\Phi(0)$ is the vertical flux. The flow through a horizontal surface, which has

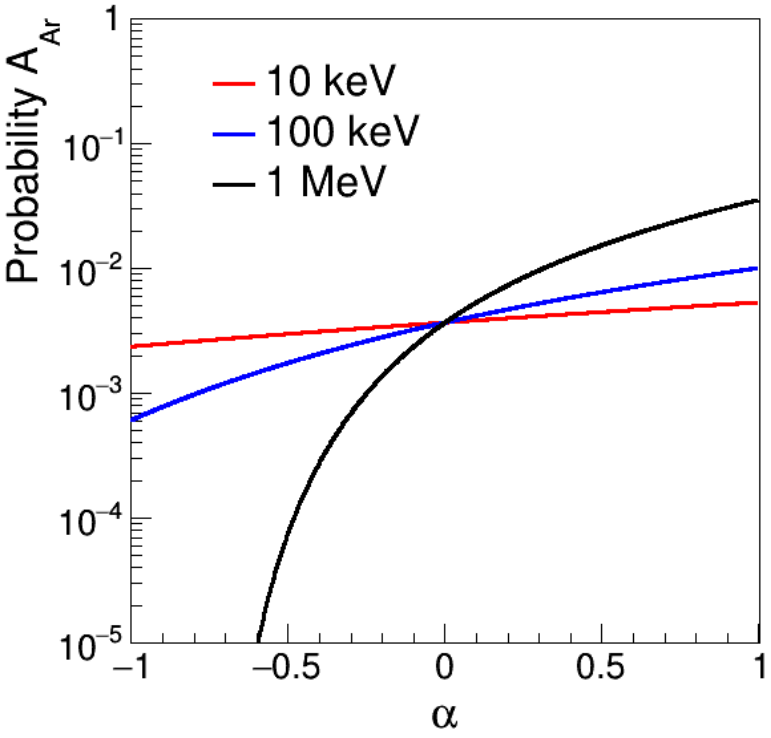

Figure 6.2: Recombination probability respect to the α parameter value for an underground detector with a drift distance of 10 m. Three different initial values for the primary disk energy are considered: 10 keV (red), 100 keV (blue) and 1 MeV (black).

been measured as $\Phi = 200$ muons / (m^2 s), is equal to the integral of the flow in all directions:

$$\Phi = \iint \cos\theta \Phi(\theta, \phi) d\Omega = \frac{\pi}{2}\Phi(0), \tag{6.9}$$

thus,

$$\Phi(\theta, \phi) = \frac{2\Phi}{\pi}\cos^2\theta. \tag{6.10}$$

To determine the probability of recombination of an isolated electron, produced at a distance L from the anode, we divided the detector into slabs normal to the field. Assuming a vertical electric field the trace length included in each slab of thickness dx is: dx/cos θ and the rate of production of recombination area per unit of cross section is:

$$\frac{d^2 A_\mu^{1e^-}}{dtdx} = Q\sigma \iint \frac{1}{\cos\theta}\cos\theta\Phi(\theta, \phi)d\Omega = \frac{4}{3}Q\sigma\Phi. \tag{6.11}$$

Integrating with respect to time and the variable x:

$$A_\mu^{1e^-} = \frac{2}{3}Q\sigma\Phi\frac{L^2}{v_i}. \tag{6.12}$$

An identical expression is found for a detector with a horizontal field, so the probability of recombination of an isolated electron is exactly the same. This is

reasonable since this probability should only depend on the amount of positive charge interposed in the path of the electron towards the anode, the same in both cases. The calculated value of the electron recombination probability for a surface detector with a drift length of 10 meters is 50%.

Let's look at the recombination, in a vertical drift field, of a primary signal that has a projected disk of radio r_p. In each differential slab, the transverse recombination surface produced by each trace of muon is considered the product of an element of transverse length times the width of the trace $dS_\mu = \frac{Q\sigma dx}{\cos\theta} = dl_\mu\, w_\mu$, where $dl_\mu = \mathrm{dx}\tan\theta$ and $w_\mu = Q\sigma/\sin\theta$.

To incorporate the size of the primary disk we consider an effective width of the trace as $w_{eff} = w_\mu + 2\alpha r_p$. When α = -1, any primary disk whose center is within the effective trace will be fully recombined. When $\alpha = 0$, at least half of the signal from these primary disks will be recombined. For $\alpha = 1$, the primary signal is recombined in any ratio.

Furthermore, the width of the actual trace must be large enough to recombine the part of the primary signal determined by α, which is $\mathrm{w}_\mu \geq (1 - \alpha) r_p$. This limit determines the angle of incidence:

$$\theta = \arcsin\frac{Q\sigma}{w_\mu} \leq \arcsin\frac{Q\sigma}{(1-\alpha}) r_p = \theta_{max}. \tag{6.13}$$

The integration domain of θ ranges from 0 to θ_{max}. The maximum angle of incidence is limited to 90°, so the argument of the arcsine function must be less than unity. The total effective recombination area in each slab is obtained by integrating with respect to the angles:

$$\frac{d^2 A_V^{1e^-}{}_\mu}{dtdx} = \iint \frac{dl_\mu}{dx} w_{eff} \cos\theta \Phi(\theta,\phi) d\Omega =$$

$$= 4\Phi\left[Q\sigma\frac{1-\cos^3\theta_{max}}{3} + \frac{\alpha r_p}{2}\left(\cos\theta_{max}\sin^3\theta_{max} + \frac{\theta_{max}}{2} - \frac{\cos\theta_{max}\sin\theta_{max}}{2}\right)\right]. \tag{6.14}$$

Integrating with respect to time and the variable x:

$$A_{V\mu} = 2\Phi\frac{L^2}{v_i}\left[Q\sigma\frac{1-\cos^3\theta_{max}}{3} + \frac{\alpha r_p}{2}\left(\frac{\theta_{max}}{2} + \cos\theta_{max}\sin\theta_{max}(\frac{1}{2} - \cos^2\theta_{max})\right)\right]. \tag{6.15}$$

The recombination of a primary signal that has a projected disk of radio r_p for the horizontal electric field case, is obtained with a similar approach. We use an alternative polar coordinate system with λ, the angle that the muon trace forms with the electric field axis, as the zenith angle and ϵ, the angle that traces form-s with the vertical axis as the azimuth angle. The probability of recombination of at

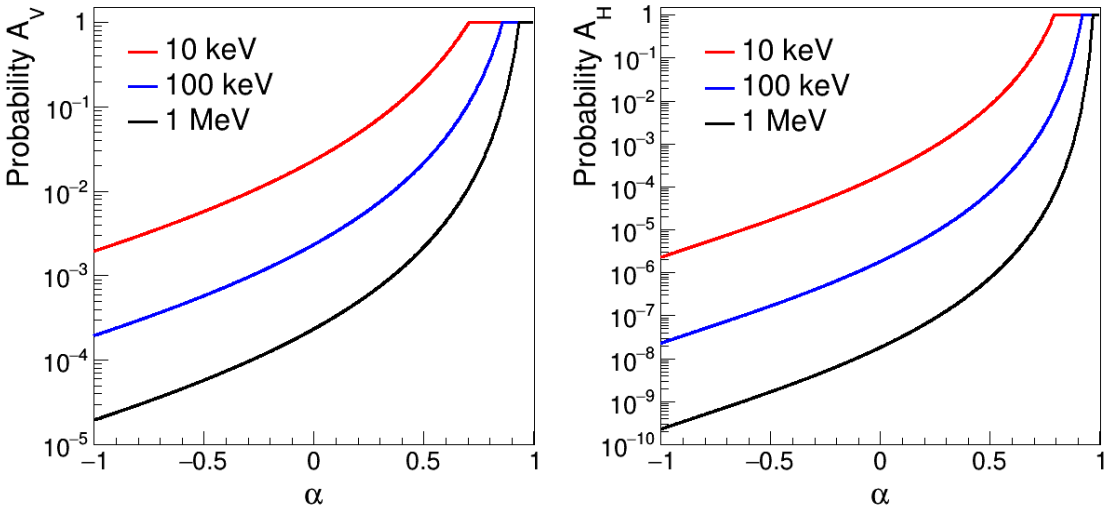

Figure 6.3: Recombination probability of the α parameter value for a surface detector with a drift distance of 10 m, with vertical (left) and horizontal (right) drift field. Three different initial values for the primary disk energy are considered: 10 keV (red), 100 keV (blue) and 1 MeV (black)

least the part of the primary disk determined by α is:

$$A_{H\mu} = \Phi \frac{L^2}{v_i} (Q\sigma \left[\frac{cos^3 \lambda_{max}}{3} - cos\lambda_{max} + \frac{2}{3} \right] \\ \alpha r_p \left[\frac{-\sin^3 \lambda_{max} \cos \lambda_{max}}{2} + \frac{2}{3} \left(\frac{-\sin \lambda_{max} \cos \lambda_{max}}{2} + \frac{\lambda_{max}}{2} \right) \right]) \, . \tag{6.16}$$

Fig. 6.3 shows the probability of recombination as function of the α parameter value for a surface detector with a drift distance of 10 m, with vertical and with horizontal drift field. The primary energy disks have a low probability of being absorbed in their totality or an appreciable fraction.

A trace perpendicular to the field produces a long but extremely fine area, of a width $w_\mu = Q\sigma = 6\ 10^{-5}$ cm, only traces aligned with the field within a value of θ_{max} can generate a trace projection thick enough to recombine a primary disk of radius r_p. For energies of 10 keV, 100 keV, and 1 MeV these maximum angles are 5.2 ^{o}, 1.6 ^{o}, and 0.5 ^{o}, respectively. Muon flux at such a small solid angle is strongly suppressed and hence also recombination for negative α values. The graphs for vertical and horizontal fields are very similar in the area close to $\alpha = 1$ because small recombination fractions can be caused by a large number of muons in both cases. However, the drop in the probability of recombination when moving towards values of α = -1 is greater, in orders of magnitude, in the horizontal field type. This is because the maximum muon flow occurs vertically, aligned with the field of a vertical detector, and transverse to the field of a horizontal detector.

The main difference between a surface and underground detector is the amount of charge, and therefore recombination, that exists. While the probability of re-

combination of an isolated electron in a 10-meter detector is 50% on the surface, it reduces to 0.37% in an underground detector.

The recombination by ^{39}Ar presents a small difference for energies less than the maximum of the beta spectrum, with values of 0-1 orders of magnitude. Muon recombination, on the other hand, presents much larger differences, of 3-5 orders of magnitude for vertical field and 6-11 orders of magnitude for the vertical field. This fact allows us to conclude that, despite being counter-intuitive, ionization is produced more diffusely by muons than by ^{39}Ar.

In conclusion, we can point out the irrelevance of ion accumulations in LAr-TPCs in regards to recombination. The probabilities of recombining entire signals, or significant fractions of them, are very small and the secondary ionization behaves as if it were uniformly dispersed in the LAr.

6.1.3 Gas amplification

In a dual-phase detector, the ionization electrons, produced by the particle interaction in the active volume, drift to the gas region where they are extracted and accelerated with the production of a Townsend avalanche. At the same time, given the low diffusion of the ions in gas argon relative to the typical size of the amplification region, a non-negligible fraction of the Ar ions produced by the avalanche can drift back to the liquid interface along the same field lines followed by the extracted electrons.

Each electron extracted from the liquid to the gas undergoes a charge avalanche process. The effective gain, G_{eff}, is defined as the number of electrons reaching the readout electrode divided per primary electron. Effective gains of 150 in LAr DP detectors were reported [188]. The number of back drifting ions, reaching the drift volume, can be calculated by:

$$N_d^{ion} = N_e^0 \cdot (G_{eff}^e - 1) \cdot f_{bflow} \cdot \epsilon_{liq} \cdot \epsilon_{grid} \tag{6.17}$$

Here, N_e^0 is the number of electrons entering the amplification region, f_{bflow} is the fraction of ions which drift towards the liquid, ϵ_{liq} is the efficiency with which the ions enter the liquid and is assumed to be 1 for the moment and ϵ_{grid} is the efficiency with which the ions cross the extraction grid to reach the drift volume: $\frac{E_d}{E_e x}$ being E_d the drift field and E_{ex} the extraction field.

We define the gain as the number of ions that are reinjected in the liquid argon respect to the arriving electrons, $G = N_d^{ion}/N_e^0$. This cloud of ions generates a new recombination zone, with an area, G times greater, that adds to the original, in addition, this new disk must cross the entire distance L from the anode, so its duration will be twice that of the average duration of the ions produced within the detector. The calculated recombination probability will be increased by a factor of $1 + 2G$.

It is important for a dual-phase massive detector with drift of many meters and charge amplification to investigate the ion feedback from the gas, possibly measuring G. We designed a small (≈1 L) liquid argon chamber, ARION (ARgon ION experiment), to study space charge effects and the dynamics of the ions at the interface gas/liquid. Preliminary results will be presented in the next section.

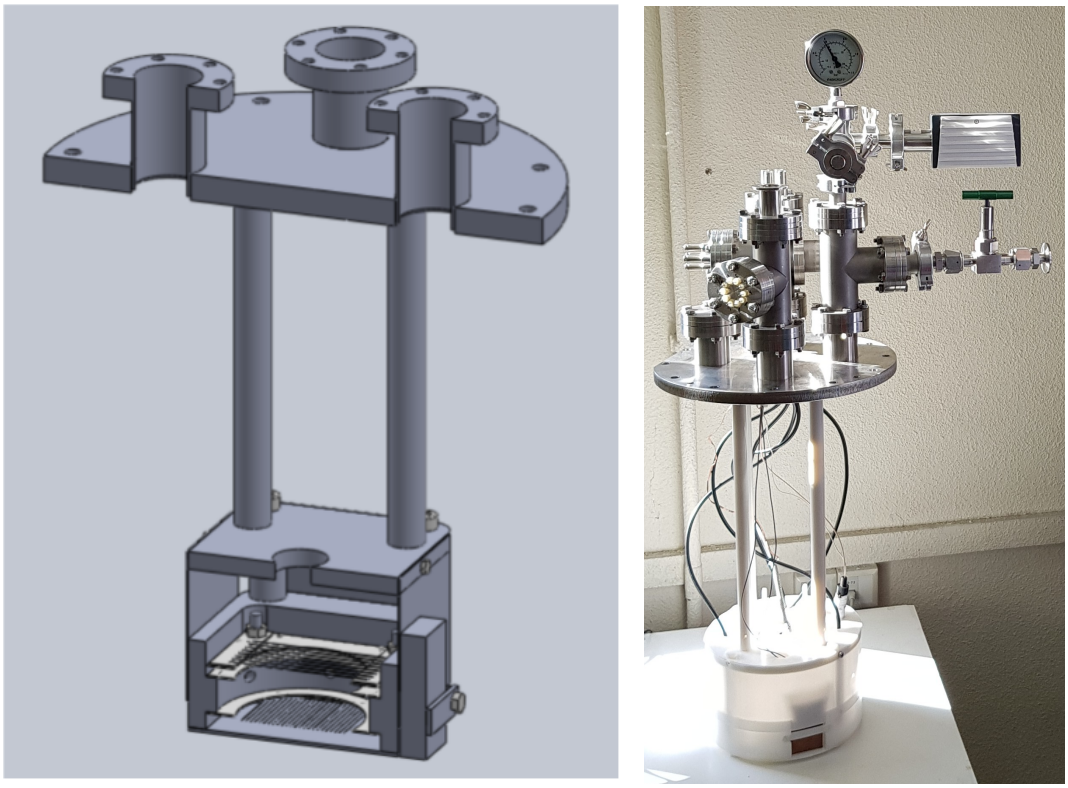

Figure 6.4: (Left)Design of the ARION internal structure. (Right) Photo of ARION internal structure assemble.

6.2 The ARION experiment

A liquid argon drift chamber was constructed (Fig. 6.4) at CIEMAT laboratory to study the dynamics of the ions at the interface gas/liquid and to measure the ion velocity dependence with the electric field in gas and liquid argon.

In order to produce a sizeable positive current from the anode, in a controlled way, a tungsten nail able to withstand a HV up to 5 kV is placed at the anode. The cathode is made of stainless steel (SS) wires, and two shaping rings (SS) maintain an uniform electric field. The distance between the anode and the cathode is variable, with a maximum distance of 7 cm. Four bars connect the support structure (ERTALITE with a teflon envelope) to a SS vacuum flange. The chamber is hosted in a cryostat and it is equipped with temperature and liquid level sensors. Five connections allow to power independently anode, cathode, the two shaping rings, and the conductive plane around the nail. The pressure is kept under 1.5 bar with a release valve.

The liquid argon level is measured by two custom made level sensors installed inside the detector (Fig. 6.5-left). They are fixed at a vertical position with the bottom part at 0.5 cm from the cathode. The first one consists of two concentric copper cylinders with a length of 12 cm and the second one in a series of parallel planes of 7 cm height. The variation of the capacity allows estimating the LAr level with an error of 7.5 mm and 0.7 mm, respectively. The temperature is measured with two PT100 resistors at the bottom of the level sensors.

The sensors are calibrated measuring the capacity in air and fully covered with LN_2. The corresponding capacity for LAr, C_{LAr} can be estimated from the following

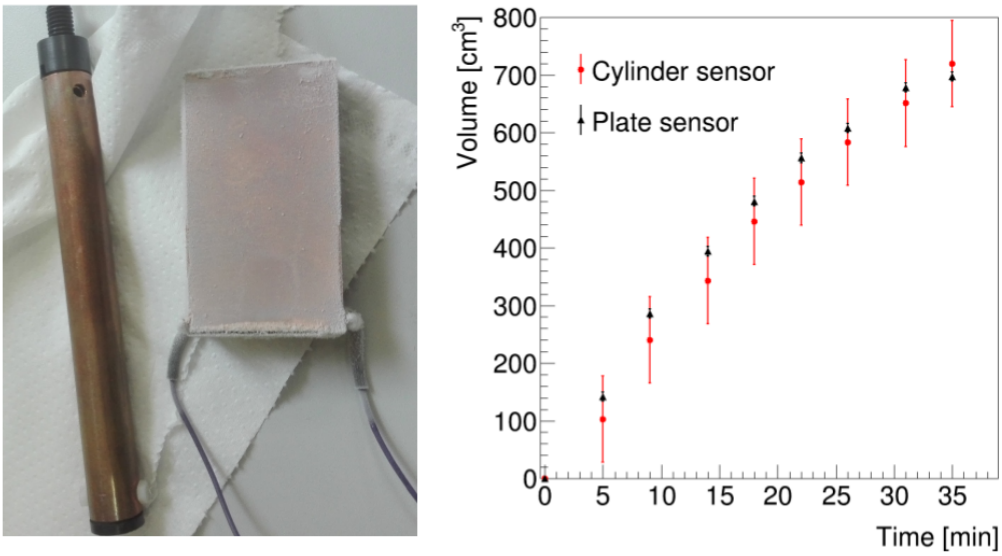

Figure 6.5: (Left)Photo of the two level sensors installed in ARION. (Right) Filling rate estimated with both sensors.

expression:

$$C_{LAr} = (\epsilon_{LAr}/\epsilon_{LN2})C_{LN2}, \tag{6.18}$$

where ϵ_{LAr} and ϵ_{LN2} are the dielectric constants for LAr (1.6) and LN_2 (1.4), and C_{LN2} is the capacity measured in LN_2. Fig. 6.5-right depicts the volume of LAr in the detector respect to time. A filling rate of 0.02 L/min is estimated. The plate sensor has a higher accuracy, but due to its length it saturates at 700 cm^3. On the other hand, the cylinder sensor has a larger measurement range but with a considerably higher error. The combination of both allows the precise estimation of the LAr level in the detector.

The electrons created near the nail are directly collected, but the positive charge is drifted towards the wires at the cathode. The current is measured with a digital pico-amperemeter with eight channels and a maximum range of ±130 nA. The mean value is extracted every second with the corresponding standard deviation.

A finite element simulation was implemented in COMSOL [189] to study the voltage configuration and field lines. The detector has been simulated with a mesh of 4.5 M tetrahedral elements with varying sizes, from 0.3 to 12.1 mm, as shown in Fig. 6.6. The element size, the maximum element growth rate, the curvature factor, and the resolution of narrow regions have been tuned to achieve the optimal configuration. The dielectric constant for the different materials are included.

The behavior of the field lines produced in the needle in gas argon with different temperature conditions is represented in Fig. 6.7. The voltage configuration is set to 3 kV at the anode, -3 kV at the cathode, -1 KV at the top shaping ring (T-SR), and -1.5 kV in the bottom (B-SR). The plane (P) around the needle is set to 1 kV. The intensity of the field is represented in logarithmic scale. The argon dielectric constant vales used at 293 K (1.0005) and 98 k (1.0016) are alike, thus electric field behavior is similar in both configurations. As expected, the electric field is stronger around the needle and uniform in the drift region.

The dynamic of the field in the gas-liquid interface is simulated in Fig. 6.8 with

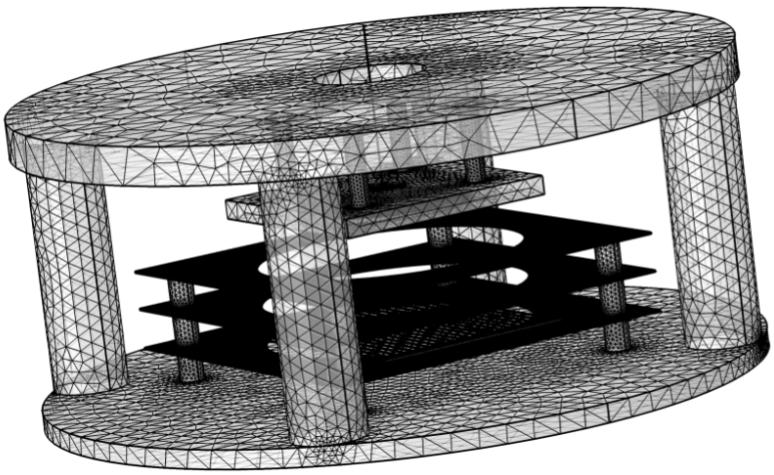

Figure 6.6: ARION geometry implemented in COMSOL.

the same voltage configuration. The liquid argon level is set between the top and bottom shaping rings (dashed line). A dielectric constant of 1.4955 is assumed for liquid. The temperature in the gas phase is 98 K while for liquid argon a value of 83 K is considered. The electric field is uniform in the drift region and most of the field lines produced in the anode finish in the wires at the cathode.

In conclusion, an uniform electric field is obtained with the current detector design in the three cases simulated. Most of the field lines produced in the anode are collected at the cathode. From the electrostatic point of view, the detector provides stable conditions to study the ion dynamics in the gas-liquid argon interface.

6.2.1 Test with a continuous ion current

The detector has been operated with different voltage configurations to maximize the charge transfer between the needle (anode) and the wire plane (cathode). A previous vacuum of to 10^{-4} mbar is reached before filling the detector with argon Alphagaz-1 up to 1.5 bar at room temperature.

The voltage configuration is maintained stable to 2 kV in the anode, -3 kV in the cathode, 0.5 kV in the plane around the needle, and 0.7 kV and 0 kV in the T-SR and the B-SR. The current is measured using the picoamperimeter every second. The evolution of the currents detected in the various parts likely to collect or produce charge is depicted in Fig. 6.9-left with argon gas in the range [1-1.5] bar and 293 K. The Fig. 6.9-right shows the values of the currents averaged every 5 s to reduce oscillations in the measurements.

The ions are generated at the anode producing an stable current of -100 nA, they are drifted to the cathode where are collected with an efficiency of about 100%, generating a current of 98 nA. The current detected on the plane and the two shaping rings is < 2 nA. Different decreases in the current produced at the anode are observed, which are correlated with increases in the pressure of the argon. As expected, the same effect is observed on the cathode current.

The behaviour at cryogenic temperatures ($\approx$ 100 K) is similar. A collection efficiency close to 100% is obtained with the appropriate configuration of voltages. The current produced in the anode is smaller due to the increase in the density of the argon gas. The voltage difference necessary to produce a continuous ion current

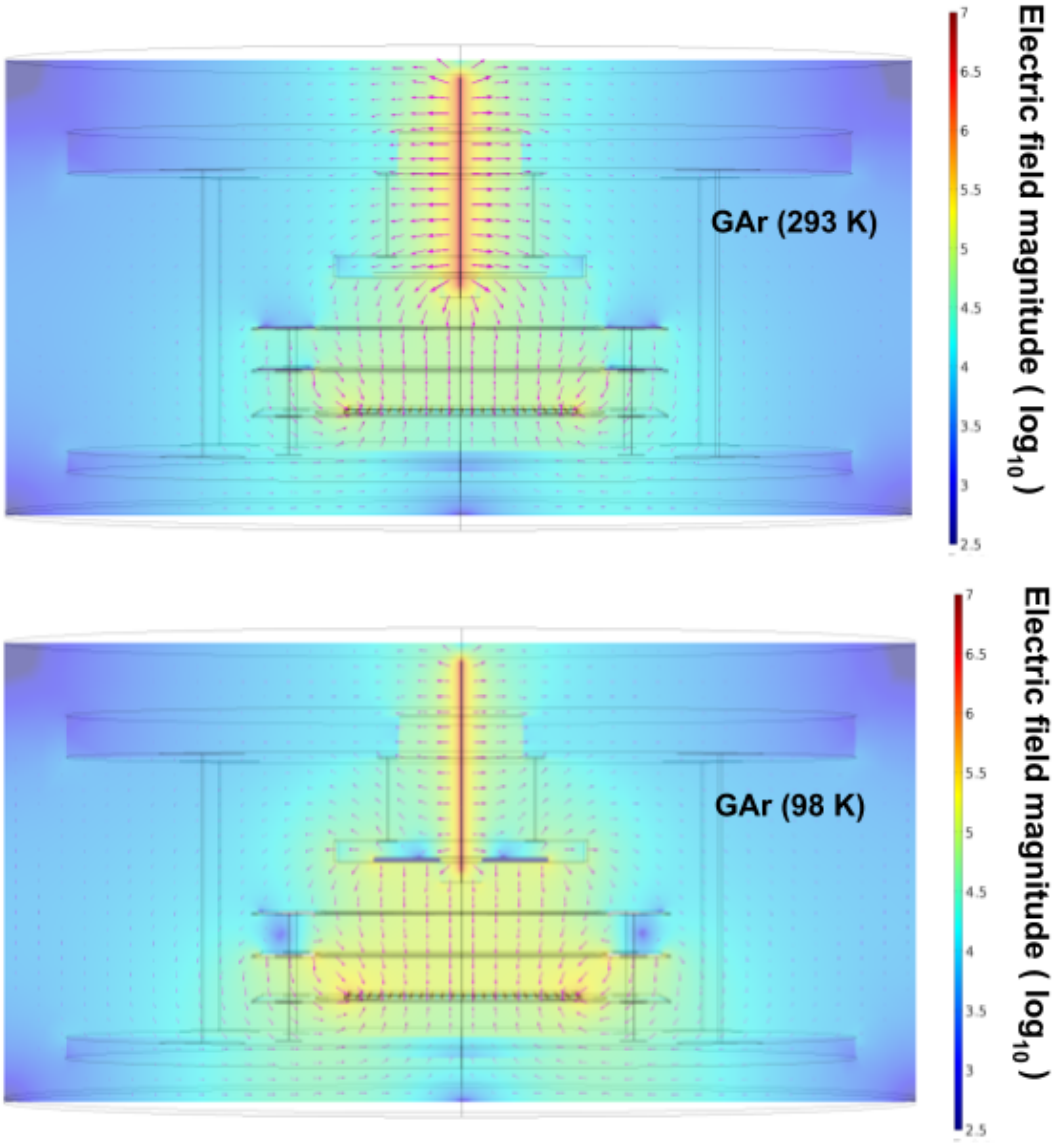

Figure 6.7: (Top) Simulation of the electric field in detector with argon gas at 293 K It is considered a dielectric constant of 1.0005. (Bottom) Simulation of the electric field in detector with argon gas at 98 K It is considered a dielectric constant of 1.0016.

is related to the density of the medium (pressure and temperature). At the bottom of Fig. 6.9 the value of the leakage currents is shown, defined as the value remaining after the sum of all currents. No leak currents values above 5 nA were found during the setup operation with gas argon.

Another important aspect to study is the impact of impurities in the detector over the ion drift. In Fig. 6.10 the currents produced at the anode and detected at the cathode are depicted for different initial vacuum conditions. In the different measurements the same configuration of the electric field, temperature and pressure of the argon are considered. The percentage difference between the two signals is illustrated at the bottom of Fig. 6.10. The current generated in the anode is constant up a contamination level of hundreds of mbar and disappear in the air as expected. The ion drift is not affected by impurities with differences smaller to 4%

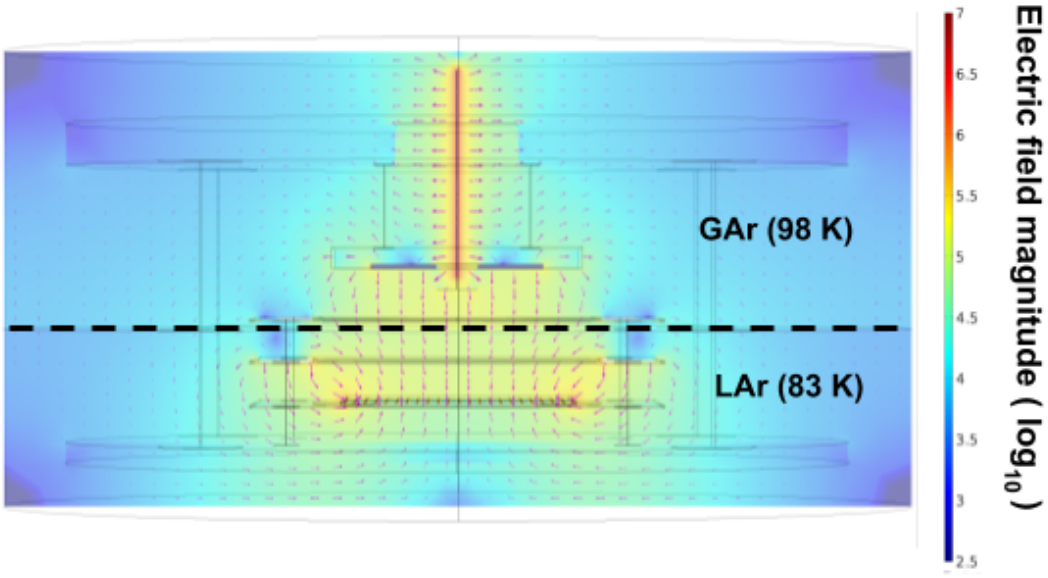

Figure 6.8: Simulation of the electric field in detector filled with liquid argon up to the dashed line. A dielectric constant of 1.4955 is assumed for LAr.

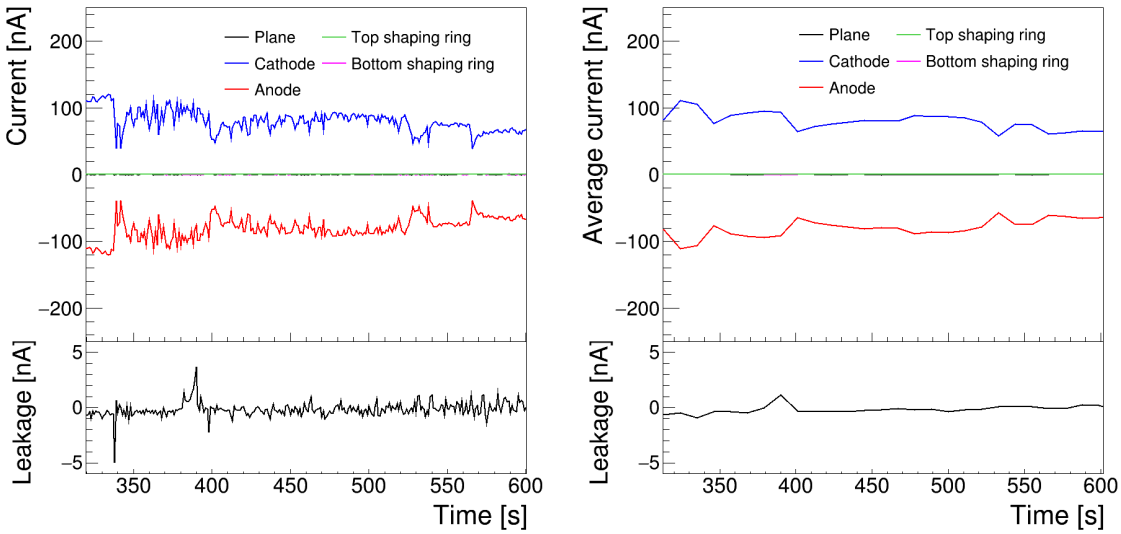

Figure 6.9: (Left)Evolution of currents measured in the plane (black), cathode (blue), anode (red), T-SR (green) and B-SR (pink). The leakage current, defined as the sum of all currents, is shown at the bottom. (Right) Currents measured at the detector averaged over 5 s. The average leakage current is shown at the bottom.

up to 100 mbar. The difference increases up to 8% at 500 mbar. Therefore, it is concluded that the impact of impurities on ion drift is practically negligible.

In conclusion, we have proven that we can produce a stable ion stream between the cathode and the anode with a collection efficiency of 100% at room temperature and cryogenic conditions. Our aim is to demonstrate the positive charge transfer between the gas and liquid phase of argon. This would have a considerable impact on the dual-phase detectors, increasing the space charge effects due to the ion feedback of the charge produced in the gas phase.

For this reason, the detector is filled with liquid argon. The collection efficiency

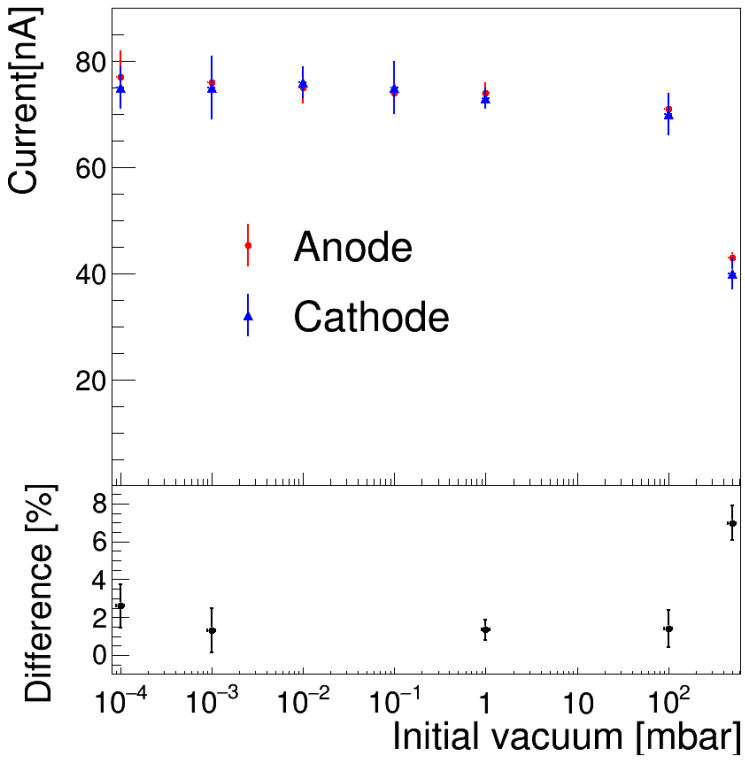

Figure 6.10: Mean value of current generated at cathode and anode for different initial vacuum conditions, with a pressure of 1.2 bar and a fixed electric field configuration. The percentage difference between the two signals is shown at the bottom.

is depicted in Fig. 6.11 for different LAr levels. The position of the cathode is indicated by the dashed line. The collection efficiency is close to 100% (consistent with previous tests in gas) when the cathode is not covered with LAr. The collection efficiency decreases when the level increases and the cathode begins to be covered with LAr. However, we measured an ion current when the LAr level is over the cathode, probing for the first time the ion feedback from gas to the liquid phase.

The ion current over the cathode disappears after covering it with a few centimeters of LAr. We explain this effect with the distortion of the electric field due to the accumulation of positive charge in the LAr due to the small mobility of ions.

To our knowledge this is the first time that the space charge effects are observed and studied with a small liquid argon detector. There is a first evidence of the ion feedback from gas to liquid phase. However, the accumulation of positive charge in liquid argon limits the possibilities of the operation with a continuous ion current.

6.2.2 Test with ion pulses

The operation with a continuous ion current has some limitations. For this reason, the setup has been modified in order to generate ion pulses in a controlled way. This will allow to confirm the ion feedback from gas to liquid phase and measure the ion drift velocity in gas and liquid argon for different field conditions.

An external circuit is designed to generate the ion pulses. A mechanical button allows the impulses to be generated in a controlled way. A voltage divider is used to duplicated the signal fed into the anode. This signal is acquired with a 1 MHz

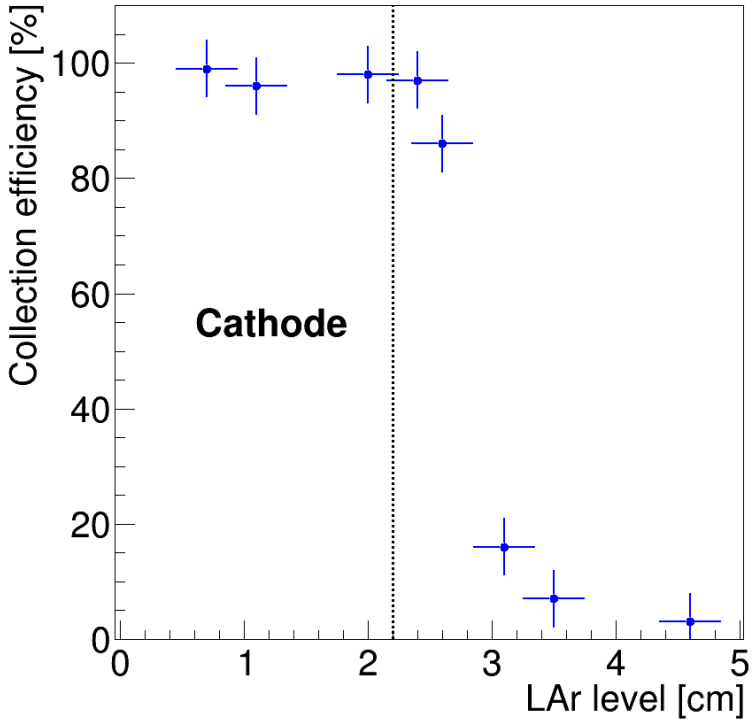

Figure 6.11: Collection efficiency respect to the LAr level. The position of the cathode is indicated by the dashed line.

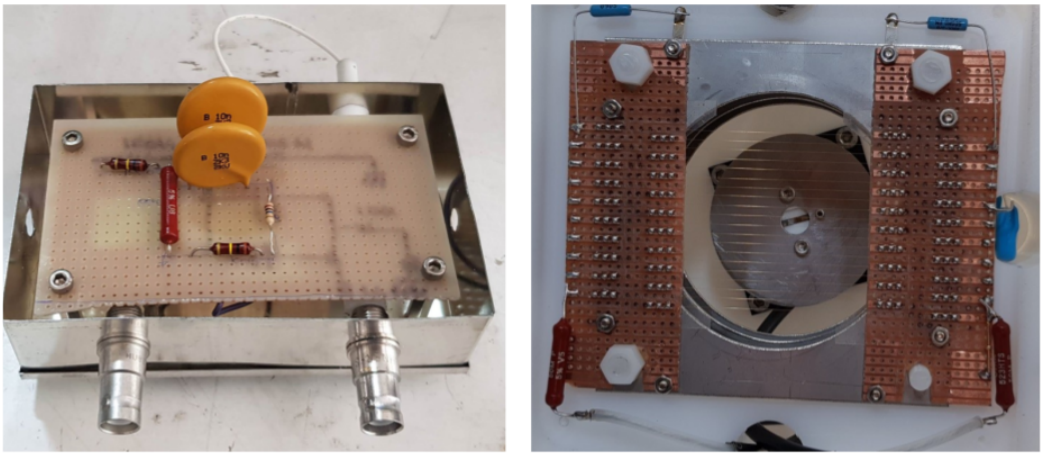

Figure 6.12: (Left) Circuit to generate the ion pulse at the needle. (Right) Double coplanar grid at the cathode.

oscilloscope. The external circuit inside a protection box is shown Fig. 6.12-left.

The ion cloud produced at the needle drifts in a constant field to the cathode immersed in LAr. In order to accurately obtain the mobility of the ions we have to measure the arrival time of the ion package. The signal from the cathode is not produced at the time of arrival of the ions, but is induced as the packet travels along its path according to the approximate law of Shockley-Ramo:

$$i = qvE_r, \tag{6.19}$$

where i is the instantaneous electric intensity induced in the cathode, q is the value of the charge packet, v is the velocity of the packet and E_r the component of a reduced field along the velocity.

Due to the extremely low speed of the ions in the LAr, the induced signal is very small and difficult to measure. The electric field with a flat cathode is constant, along the path of the charge packet, so that a uniform induced signal is produced throughout the transit time of the ions. Therefore, it is not possible to measure the arrival time of the ions precisely.

One solution to this problem is to include at the end of the path either a charge multiplier, LEM or GEM, which is not possible because the cathode is in LAr, or a very high electric field region that induces a strong signal at the cathode. For this reason the wire plane is replaced by a double coplanar grid (see Fig. 6.12-right), in which one of the two grids is the cathode, that is interlocked with the second grid, which provides a high electric field. Both grids are at different potentials, with a higher voltage in the cathode (V_1) than that of the amplification grid (V_2). Assuming that the needle is grounded, the drift voltage is V_{drift} =(V_1+V_2)/2 and the amplification voltage $V_{ampl} = V_1 - V_2$.

The average pulse over 10 events is shown in Fig. 6.13-left with argon gas at room temperature at 1 bar. The anode is fed with a 2.5 kV pulse, the amplification grid is set to -1 kV and the cathode to -2 kV. The signals are normalized to the maximum height of each pulse to facilitate their visualization. The anode signal rises quickly and discharges with a time constant of several milliseconds. A signal is measured at the cathode when the drift field is applied, with a delay of several milliseconds with respect to the signal provided to the anode.

Fig. 6.13-right illustrates the average pulse at the cathode with a V_{drift} of 1 kV and without potential at the cathode. When the drift field is removed, only fast pulses are detected, associated with induction signals. In addition, the position of the bump observed in the cathode when a drift field is applied, changes when the values of the field or the pressure are modified. Therefore, it is confirmed that the detected signal corresponds to the positively charged package generated at the needle.

We estimate the drift time of the ion cloud between the anode and the cathode, t_{drift} as the time difference between the maximum of the signal introduced in the anode and the average value of the bump detected in the cathode. The distance between the anode and the cathode, D_{drift} = 33 mm, so assuming that the field is uniform in the drift region it is possible to obtain the drift velocity of the ions $v_{drift} = D_{drift}/t_{drift}$.

Fig. 6.14 depicts the average v_{drift} calculated over 10 events in argon gas at 1 bar. The drift field is increased from 150 to 450 V/cm/bar. As expected, v_{drift} raises as the electric field is increased, a value around 4 m/s is obtained with an electric field close to 0.5 kV/cm/bar.

The electron drift velocity in argon gas with a field of 300 V/cm/bar was measured in [190] to be 330 m/s, two orders of magnitude larger than our estimations for the ion drift velocity with the same field value. This is consistent with the differences of several orders of magnitude observed between the drift times for ions and electrons in liquid argon.

In conclusion, with a small detector (1 L) we have been able to study the dynamics of ions in liquid argon and give a first evidence of ion feedback from the gas into

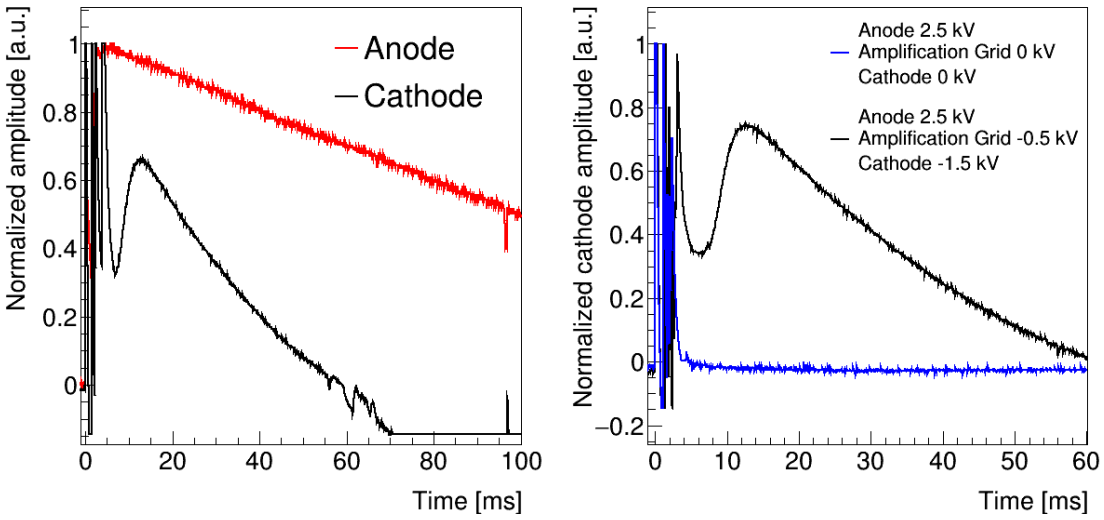

Figure 6.13: (Left)Average signal introduced to the anode (red) and detected at the cathode (black). The voltage configuration is: anode 2.5 kV, amplification grid -1 kV and cathode -2 kV. The signals are normalized to the maximum for visualization. (Right) Average signal detected at the cathode with a drift field of 300 V/cm (black) and without it (blue).

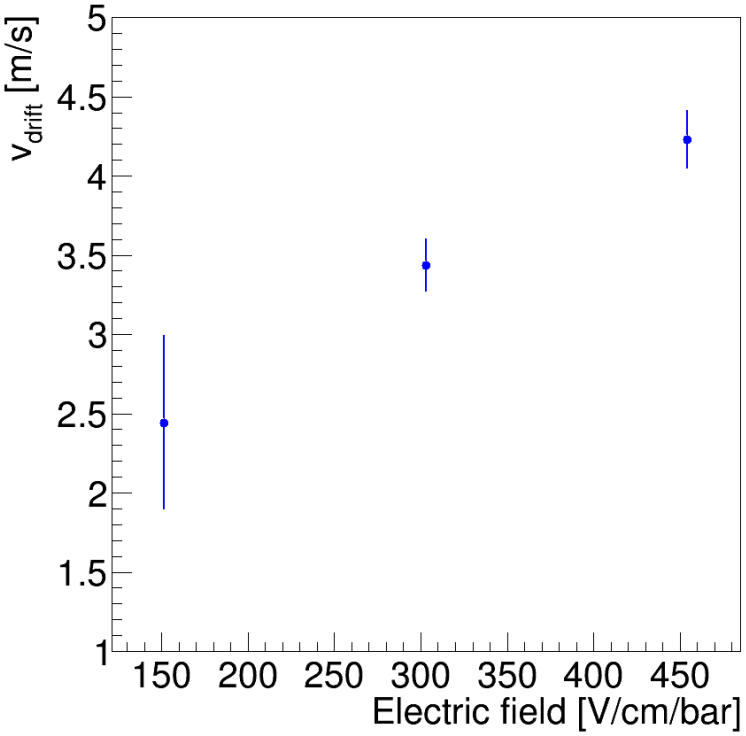

Figure 6.14: Drift velocity of the ions in argon gas at room temperature with respect to the intensity of the drift field.

the liquid phase. This is an important effect which has not been investigated and is typically neglected, evidencing for the first time an intrinsic limit of the technology and limiting the maximum electron drift achievable even in presence of infinite liquid

purity.

We are now upgrading the setup to operate the detector in dual-phase generating ion pulses in a controlled way. The detector has been commissioned with argon gas succesfully and it has been proved that it is possible to measure the drift velocity of the ions. Operations with liquid argon are planned for 2021.

Conclusions

I have performed my thesis within the DarkSide-20k [2] experiment. Specifically, I have developed simulations for background estimation and light propagation in DArT. I have been in charge of the characterisation of the light detection modules developed for DArT, and the commissioning of the detector on the surface. I have been involved in two other lines of research related to R&D for liquid argon detectors. The first one consists of the development of a novel particle discrimination technique using the wavelength produced by the argon and xenon scintillation emissions. The second is related to the study of the effects produced by the space charge in large liquid argon detectors with a small chamber.

I have designed the DArT experiment capable of measuring with high precision the amount of ^{39}Ar in the argon that will be used in current and future dark matter search experiments. The detector is under construction. The sensitivity of DArT was studied using a detailed background model and light response simulations. These studies show that the detector will allow measuring UAr depletion factors above 1000 with statistical accuracy better than 10% in one week of counting time. The main results of this work have been the basis of the DArT Technical Design Report [4] presented and approved by the LSC Scientific Committee in 2019. Additionally, I have published an article in JINST with these studies of which I am corresponding author [5].

I have been in charge of the characterisation of the 10 PDMs produced for DArT using a specific setup. They have been tested to work at room temperature and after several cryogenic cycles with liquid nitrogen. I have measured the I-V curves and the dark current spectrum. Additionally, I have designed and built the DArT calibration system.

I have participated in the detector assembly, the first data collection with atmospheric argon and their corresponding analysis. Currently, there is a paper in preparation based on the results shown in Chapter 4. These results are a crucial step in the development ofDArT in ArDM program. The next milestone is the DArT installation at the LSC that is scheduled to take place during 2021.

In November 2019, I participated in the operation of the first prototype of DarkSide, Proto-0, for several weeks at CERN. In particular, I have contributed to the assembly of Proto-0 and the data collection at CERN, the analysis software development and the detector characterization. Besides, I have developed the database for Proto-0 to monitor the motherboard stability over time.

Apart from the work done within the DarkSide collaboration. I have studied the primary and the recombination scintillation of the argon gas with a wavelength sensitive detector operated with α and β sources electrodeposited on stainless steel disks. For this purpose, I have designed and operated a high pressure chamber (up to 21 bar) equipped with photomultipliers (PMTs) sensitive at different wavelength

ranges.

The results evidence the emission of photons at wavelengths larger than the 128 nm line through a production mechanism which is not based on the excimer formation associated with the low-lying atomic states. This component of the argon scintillation is interpreted as the third continuum emission.

I have proven that up to 20% of the scintillation obtained with an ^{241}Am source in 1.5 bar argon gas is in the range [160, 325] nm. The photon yield and the typical emission time of this component are largely independent of the gas pressure up to 16 bar, and the emission is not significantly affected by an external electric field. Compared to the second continuum, which is dominated by the excimer formation time, the third continuum is remarkably fast and represents the main contribution to the argon light signal during the first tens of ns, for pressures below 10 bar. The spectroscopic studies of the electron-ion recombination light revealed that this component is consistent with the 128 nm emission. Evidence of the third continuum emission produced by β interactions in argon gas has been also obtained for the first time using a ^{90}Sr/Y source. An article with the main results, of which I am the corresponding author, has been accepted for publication in Europan Physics Journal C [6].

Additionally, I demonstrated the PSD capability of the detector, enabling the setup to evaluate the possibility of a new discrimination technique based on the wavelength emission of the scintillation components. The viability of this technique and its potential in argon gas detectors is under study. Future tests in liquid argon will be done to estimate the impact over dark matter and neutrino detectors.

I have designed and assembled a sensitive wavelength-sensitive chamber in collaboration with IGFAE, to study the spectroscopic characteristics of the xenon scintillation light emission. For the first time, I have obtained direct evidence that electrons do not produce recombination in xenon gas in the pressure range [2-10] bar. Furthermore, the third continuum emission produced by α and β interactions in xenon gas has been also measured for the first time using a ^{241}Am and a ^{90}Sr/Y source. The results obtained in xenon will be published in a paper that is under development.

I have established that the argon and xenon second and the third continuum scintillation can be distinguished experimentally using sensors with different spectral sensitivities, making it possible to exploit distinctive features of the noble gases photon emission that are not envisaged by the present experiments. Particularly, my investigations provide suggest the possibility of a novel particle identification technique based on the spectral information of the noble-elements scintillation light.

I have performed theoretical calculations of the secondary recombination probabilities expected in liquid argon detectors operating in single and dual-phase, both on the surface and underground. In addition, I have built a small detector (1 L) to study the dynamics of the ions in liquid argon. I have obtained the first evidence of ion feedback from the gas into the liquid phase. This is an important effect which has not been investigated and is typically neglected, this evidences for the first time an intrinsic limit of the technology and limits the maximum electron drift achievable even in presence of infinite liquid purity.

I am upgrading the setup to operate the detector with ion pulses generated in a controlled way. I have commissioned the detector with argon gas successfully and I demonstrated that it is possible to measure the drift speed of the ions with the setup. Liquid argon operations are planned for 2021. An article is at an advanced

stage with all these results.

I have presented all the results shown throughout the thesis at several international and national conferences. I have also discussed DArT related activities at the DarkSide-20k collaboration meetings. I have reported the progress of my work in weekly meetings. Specifically, within DarkSide-20k I have been part of the working groups related to software development, DArT and Proto-0 activities.

Bibliography

[1] N. Aghanim *et al.* [Planck], [arXiv:1807.06209 [astro-ph.CO]].

[2] C. E. Aalseth *et al.* [DarkSide] Eur. Phys. J. Plus **133** (2018), 131 doi:10.1140/epjp/i2018-11973-4 [arXiv:1707.08145 [physics.ins-det]].

[3] P. Agnes *et al.* [DarkSide], Phys. Rev. D **93** (2016) no.8, 081101 doi:10.1103/PhysRevD.93.081101 [arXiv:1510.00702 [astro-ph.CO]].

[4] https://indico.in2p3.fr/event/19093/contributions/71453/attachments/53086/68943/DART_in_ArDM_TDR-6.pdf

[5] C. E. Aalseth *et al.* (Corresponding author: E. Sanchez Garcia)[DarkSide-20k], JINST **15** (2020) no.02, P02024 doi:10.1088/1748-0221/15/02/P02024 [arXiv:2001.08106 [astro-ph.IM]].

[6] R. Santorelli, E. Sanchez Garcia, P. G. Abia, D. González-Díaz, R. L. Manzano, J. J. M. Morales, V. Pesudo and L. Romero, [arXiv:2012.08262 [physics.ins-det]].

[7] A. Marchionni *et al.* [ArDM], J. Phys. Conf. Ser. **308** (2011), 012006 doi:10.1088/1742-6596/308/1/012006 [arXiv:1012.5967 [physics.ins-det]].

[8] P. Agnes *et al.* [DarkSide], Phys. Lett. B **743** (2015), 456-466 doi:10.1016/j.physletb.2015.03.012 [arXiv:1410.0653 [astro-ph.CO]].

[9] P. A. Amaudruz *et al.* [DEAP-3600], Astropart. Phys. **108** (2019), 1-23 doi:10.1016/j.astropartphys.2018.09.006 [arXiv:1712.01982 [astro-ph.IM]].

[10] A. Hime [MiniCLEAN], [arXiv:1110.1005 [physics.ins-det]].

[11] A. Caminata [GADMC], PoS **EPS-HEP2019** (2020), 077 doi:10.22323/1.364.0077

[12] F. Zwicky, Helv. Phys. Acta **6** (1933), 110-127 doi:10.1007/s10714-008-0707-4

[13] P. Coles and F. Lucchin,

[14] V. C. Rubin and W. K. Ford, Jr., Astrophys. J. **159** (1970), 379-403 doi:10.1086/150317

[15] A. Del Popolo, AIP Conf. Proc. **1548** (2013) no.1, 2-63 doi:10.1063/1.4817029

[16] J. I. Read, J. Phys. G **41** (2014), 063101 doi:10.1088/0954-3899/41/6/063101 [arXiv:1404.1938 [astro-ph.GA]].

[17] N. W. Evans, C. A. J. O'Hare and C. McCabe, Phys. Rev. D **99** (2019) no.2, 023012 doi:10.1103/PhysRevD.99.023012 [arXiv:1810.11468 [astro-ph.GA]].

[18] M. C. Smith, S. H. Whiteoak and N. W. Evans, Astrophys. J. **746** (2012), 181 doi:10.1088/0004-637X/746/2/181 [arXiv:1111.6920 [astro-ph.GA]].

[19] O. Bienaymé, B. Famaey, A. Siebert, K. C. Freeman, B. K. Gibson, E. K. Grebel, G. Kordopatis, U. Munari, J. F. Navarro and W. Reid, *et al.* Astron. Astrophys. **571** (2014), A92 doi:10.1051/0004-6361/201424478 [arXiv:1406.6896 [astro-ph.GA]].

[20] J. Ehlers and P. Schneider,

[21] D. Clowe, M. Bradac, A. H. Gonzalez, M. Markevitch, S. W. Randall, C. Jones and D. Zaritsky, Astrophys. J. Lett. **648** (2006), L109-L113 doi:10.1086/508162 [arXiv:astro-ph/0608407 [astro-ph]].

[22] G. Gamow, Nature **162** (1948) no.4122, 680-682 doi:10.1038/162680a0

[23] A. A. Penzias and R. W. Wilson, Astrophys. J. **142** (1965), 419-421 doi:10.1086/148307

[24] E. Komatsu and D. N. Spergel, Phys. Rev. D **63** (2001), 063002 doi:10.1103/PhysRevD.63.063002 [arXiv:astro-ph/0005036 [astro-ph]].

[25] D. N. Spergel *et al.* [WMAP], Astrophys. J. Suppl. **148** (2003), 175-194 doi:10.1086/377226 [arXiv:astro-ph/0302209 [astro-ph]].

[26] B. D. Fields, P. Molaro and S. Sarkar, Chin. Phys. C **38** (2014), 339-344 [arXiv:1412.1408 [astro-ph.CO]].

[27] M. Milgrom, Astrophys. J. **270** (1983), 365-370 doi:10.1086/161130

[28] P. Gondolo, NATO Sci. Ser. II **187** (2005), 279-333 [arXiv:astro-ph/0403064 [astro-ph]].

[29] M. Davis, G. Efstathiou, C. S. Frenk and S. D. M. White, Astrophys. J. **292** (1985), 371-394 doi:10.1086/163168

[30] G. R. Blumenthal, S. M. Faber, J. R. Primack and M. J. Rees, Nature **311** (1984), 517-525 doi:10.1038/311517a0

[31] Q. R. Ahmad *et al.* [SNO], Phys. Rev. Lett. **89** (2002), 011301 doi:10.1103/PhysRevLett.89.011301 [arXiv:nucl-ex/0204008 [nucl-ex]].

[32] Y. Ashie *et al.* [Super-Kamiokande], Phys. Rev. Lett. **93** (2004), 101801 doi:10.1103/PhysRevLett.93.101801 [arXiv:hep-ex/0404034 [hep-ex]].

[33] S. Dodelson and L. M. Widrow, Phys. Rev. Lett. **72** (1994), 17-20 doi:10.1103/PhysRevLett.72.17 [arXiv:hep-ph/9303287 [hep-ph]].

[34] G. Mention, M. Fechner, T. Lasserre, T. A. Mueller, D. Lhuillier, M. Cribier and A. Letourneau, Phys. Rev. D **83** (2011), 073006 doi:10.1103/PhysRevD.83.073006 [arXiv:1101.2755 [hep-ex]].

[35] D. Abercrombie, N. Akchurin, E. Akilli, J. Alcaraz Maestre, B. Allen, B. Alvarez Gonzalez, J. Andrea, A. Arbey, G. Azuelos and P. Azzi, *et al.* Phys. Dark Univ. **27** (2020), 100371 doi:10.1016/j.dark.2019.100371 [arXiv:1507.00966 [hep-ex]].

[36] L. D. Duffy and K. van Bibber, New J. Phys. **11** (2009), 105008 doi:10.1088/1367-2630/11/10/105008 [arXiv:0904.3346 [hep-ph]].

[37] M. Zumalacarregui and U. Seljak, Phys. Rev. Lett. **121** (2018) no.14, 141101 doi:10.1103/PhysRevLett.121.141101 [arXiv:1712.02240 [astro-ph.CO]].

[38] B. J. Carr, K. Kohri, Y. Sendouda and J. Yokoyama, Phys. Rev. D **81** (2010), 104019 doi:10.1103/PhysRevD.81.104019 [arXiv:0912.5297 [astro-ph.CO]].

[39] B. Carr, F. Kuhnel and M. Sandstad, Phys. Rev. D **94** (2016) no.8, 083504 doi:10.1103/PhysRevD.94.083504 [arXiv:1607.06077 [astro-ph.CO]].

[40] B. J. Carr, Astrophys. J. **201** (1975), 1-19 doi:10.1086/153853

[41] C. Munoz, Nucl. Instrum. Meth. A **692** (2012), 13-19 doi:10.1016/j.nima.2012.01.053 [arXiv:1203.0678 [hep-ph]].

[42] V. Bonvicini *et al.* [PAMELA], Nucl. Instrum. Meth. A **461** (2001), 262-268 doi:10.1016/S0168-9002(00)01221-3

[43] W. B. Atwood *et al.* [Fermi-LAT], Astrophys. J. **697** (2009), 1071-1102 doi:10.1088/0004-637X/697/2/1071 [arXiv:0902.1089 [astro-ph.IM]].

[44] M. Aguilar *et al.* [AMS], Phys. Rev. Lett. **117** (2016) no.9, 091103 doi:10.1103/PhysRevLett.117.091103

[45] D. Ferenc [MAGIC], Nucl. Instrum. Meth. A **553** (2005), 274-281 doi:10.1016/j.nima.2005.08.085

[46] H. Abdalla *et al.* [HESS], Astron. Astrophys. **612** (2018), A1 doi:10.1051/0004-6361/201732098 [arXiv:1804.02432 [astro-ph.HE]].

[47] B. S. Acharya *et al.* [CTA Consortium], doi:10.1142/10986 [arXiv:1709.07997 [astro-ph.IM]].

[48] C. Arpesella [ANTARES], Nucl. Instrum. Meth. A **409** (1998), 454-457 doi:10.1016/S0168-9002(98)00125-9

[49] S. R. Klein [IceCube], IEEE Trans. Nucl. Sci. **56** (2009) no.3, 1141-1147 doi:10.1109/TNS.2009.2015300 [arXiv:0807.0034 [physics.ins-det]].

[50] K. K. Young [Super-Kamiokande],

[51] O. Adriani *et al.* [PAMELA], Nature **458** (2009), 607-609 doi:10.1038/nature07942 [arXiv:0810.4995 [astro-ph]].

[52] M. Aguilar *et al.* [AMS], Phys. Rev. Lett. **110** (2013), 141102 doi:10.1103/PhysRevLett.110.141102

[53] M. Aguilar *et al.* [AMS], Phys. Rev. Lett. **113** (2014), 121102 doi:10.1103/PhysRevLett.113.121102

[54] M. Aguilar *et al.* [AMS], Phys. Rev. Lett. **122** (2019) no.4, 041102 doi:10.1103/PhysRevLett.122.041102

[55] H. Abdallah *et al.* [H.E.S.S.], Phys. Rev. Lett. **117** (2016) no.11, 111301 doi:10.1103/PhysRevLett.117.111301 [arXiv:1607.08142 [astro-ph.HE]].

[56] M. Ackermann *et al.* [Fermi-LAT], Phys. Rev. Lett. **115** (2015) no.23, 231301 doi:10.1103/PhysRevLett.115.231301 [arXiv:1503.02641 [astro-ph.HE]].

[57] V. A. Mitsou [ATLAS and CMS], PoS **CORFU2019** (2020), 050 doi:10.22323/1.376.0050

[58] M. Bravin *et al.* [CRESST], Astropart. Phys. **12** (1999), 107-114 doi:10.1016/S0927-6505(99)00073-0 [arXiv:hep-ex/9904005 [hep-ex]].

[59] P. L. Brink *et al.* [CDMS-II], eConf **C041213** (2004), 2529 [arXiv:astro-ph/0503583 [astro-ph]].

[60] J. Amaré, I. Coarasa, S. Cebrián, C. Cuesta, E. García, M. Martínez, M. A. Olivan, Y. Ortigoza, A. Ortiz de Solorzano and J. Puimedon, *et al.* J. Phys. Conf. Ser. **1342** (2020) no.1, 012056 doi:10.1088/1742-6596/1342/1/012056 [arXiv:1710.03837 [physics.ins-det]].

[61] R. Bernabei *et al.* [DAMA], Nucl. Instrum. Meth. A **592** (2008), 297-315 doi:10.1016/j.nima.2008.04.082 [arXiv:0804.2738 [astro-ph]].

[62] E. Aprile [XENON1T], Springer Proc. Phys. **148** (2013), 93-96 doi:10.1007/978-94-007-7241-0_14 [arXiv:1206.6288 [astro-ph.IM]].

[63] S. Hanany *et al.* [NASA PICO], [arXiv:1902.10541 [astro-ph.IM]].

[64] K. Freese, J. A. Frieman and A. Gould, Phys. Rev. D **37** (1988), 3388-3405 doi:10.1103/PhysRevD.37.3388

[65] J. D. Lewin and P. F. Smith, Astropart. Phys. **6** (1996), 87-112 doi:10.1016/S0927-6505(96)00047-3

[66] R.H. Helm, Phys. Rev. 104 (1956) 1466.

[67] http://pisrv0.pit.physik.uni-tuebingen.de/darkmatter/

[68] F. Spoto *et al.* [GAIA], Astron. Astrophys. **616** (2018), A13 doi:10.1051/0004-6361/201832900 [arXiv:1804.09379 [astro-ph.EP]].

[69] R. Bernabei *et al.* [DAMA], Eur. Phys. J. C **56** (2008), 333-355 doi:10.1140/epjc/s10052-008-0662-y [arXiv:0804.2741 [astro-ph]].

[70] R. Bernabei *et al.* Universe **4** (2018) no.11, 116 doi:10.3390/universe4110116

[71] G. Adhikari *et al.* [COSINE-100], Phys. Rev. Lett. **123** (2019) no.3, 031302 doi:10.1103/PhysRevLett.123.031302 [arXiv:1903.10098 [astro-ph.IM]].

[72] J. Amaré *et al.* J. Phys. Conf. Ser. **1468** (2020) no.1, 012014 doi:10.1088/1742-6596/1468/1/012014 [arXiv:1910.13365 [astro-ph.IM]].

[73] M. Schumann, J. Phys. G **46** (2019) no.10, 103003 doi:10.1088/1361-6471/ab2ea5 [arXiv:1903.03026 [astro-ph.CO]].

[74] C. Savage, K. Freese, P. Gondolo and D. Spolyar, JCAP **09** (2009), 036 doi:10.1088/1475-7516/2009/09/036 [arXiv:0901.2713 [astro-ph.CO]].

[75] V. Sanglard [EDELWEISS], [arXiv:astro-ph/0306233 [astro-ph]].

[76] F. Petricca *et al.* [CRESST], J. Phys. Conf. Ser. **1342** (2020) no.1, 012076 doi:10.1088/1742-6596/1342/1/012076 [arXiv:1711.07692 [astro-ph.CO]].

[77] P. Agnes *et al.* [DarkSide], Phys. Rev. Lett. **121** (2018) no.8, 081307 doi:10.1103/PhysRevLett.121.081307 [arXiv:1802.06994 [astro-ph.HE]].

[78] M. Ibe, W. Nakano, Y. Shoji and K. Suzuki, JHEP **03** (2018), 194 doi:10.1007/JHEP03(2018)194 [arXiv:1707.07258 [hep-ph]].

[79] R. Ajaj *et al.* [DEAP], Phys. Rev. D **100** (2019) no.2, 022004 doi:10.1103/PhysRevD.100.022004 [arXiv:1902.04048 [astro-ph.CO]].

[80] E. Aprile *et al.* [XENON], Phys. Rev. Lett. **121** (2018) no.11, 111302 doi:10.1103/PhysRevLett.121.111302 [arXiv:1805.12562 [astro-ph.CO]].

[81] E. Aprile *et al.* [XENON], [arXiv:2007.08796 [physics.ins-det]].

[82] D. S. Akerib *et al.* [LZ], [arXiv:1509.02910 [physics.ins-det]].

[83] APPEC dark matter report (to be published)

[84] J. Aalbers *et al.* [DARWIN], JCAP **11** (2016), 017 doi:10.1088/1475-7516/2016/11/017 [arXiv:1606.07001 [astro-ph.IM]].

[85] C. A. J. O'Hare, J. Billard, E. Figueroa-Feliciano, A. M. Green and L. E. Strigari, doi:10.3204/DESY-PROC-2015-02/ohareciaran [arXiv:1510.04079 [hep-ph]].

[86] E. Baracchini *et al.* JINST **15** (2020) no.07, C07036 doi:10.1088/1748-0221/15/07/C07036 [arXiv:2007.12627 [physics.ins-det]].

[87] R. Acciarri *et al.* [MicroBooNE], JINST **12** (2017) no.02, P02017, https://doi.org/10.1088/1748-0221/12/02/P02017 [arXiv:1612.05824 [physics.ins-det]].

[88] V. Alvarez *et al.* [NEXT], JINST **7** (2012), T06001, https://doi.org/10.1088/1748-0221/7/06/T06001 [arXiv:1202.0721 [physics.ins-det]].

[89] R. Acciarri *et al.* [DUNE], [arXiv:1601.05471 [physics.ins-det]].

[90] P. Agnes *et al.* [DarkSide], Phys. Rev. Lett. **121** (2018) no.8, 081307, https://doi.org/10.1103/PhysRevLett.121.081307 [arXiv:1802.06994 [astro-ph.HE]].

[91] R. Ajaj *et al.* [DEAP], Phys. Rev. D **100** (2019) no.2, 022004, https://doi.org/10.1103/PhysRevD.100.022004 [arXiv:1902.04048 [astro-ph.CO]].

[92] J. Calvo *et al.* [ArDM], JCAP **03** (2017), 003, https://doi.org/10.1088/1475-7516/2017/03/003 [arXiv:1612.06375 [physics.ins-det]].

[93] E. Aprile *et al.* [XENON], Phys. Rev. Lett. **119** (2017) no.18, 181301, https://doi.org/10.1103/PhysRevLett.119.181301 [arXiv:1705.06655 [astro-ph.CO]].

[94] M. Schumann, [arXiv:1206.2169 [astro-ph.IM]].

[95] Platzman, J. Appl.Radiat. Isot.10, 116-127 (1961)

[96] Doke et al. Nuclear Instruments and Methods, 134, 353 (1976)

[97] M. Miyajima, T. Takahashi, S. Konno, T. Hamada, S. Kubota, H. Shibamura and T. Doke, Phys. Rev. A **9** (1974), 1438-1443 doi:10.1103/PhysRevA.9.1438

[98] T. Takahashi, S. Konno, T. Hamada, M. Miyajima, S. Kubota, A. Nakamoto, A. Hitachi, E. Shibamura and T. Doke, Phys. Rev. A **12** (1975), 1771-1775 doi:10.1103/PhysRevA.12.1771

[99] T. Doke, Portugal. Phys. **12** (1981), 9-48.

[100] S. Kubota and M. Hishida and J. Raun, J. Phys. C: Solid State Phys. **11** (1978), 2645, https://doi.org/10.1088/0022-3719/11/12/024.

[101] V. Chepel and H. Araujo, JINST **8** (2013), R04001, https://doi.org/10.1088/1748-0221/8/04/R04001 [arXiv:1207.2292 [physics.ins-det]].

[102] E. Aprile and T. Doke, Rev. Mod. Phys. **82** (2010), 2053-2097, https://doi.org/10.1103/RevModPhys.82.2053 [arXiv:0910.4956 [physics.ins-det]].

[103] S. Kubota, M. Hishida, M. Suzuki and J. Ruan, Phys. Rev. B **20**, 3486 (1979), https://doi.org/10.1103/PhysRevB.20.3486.

[104] S. Kubota, A. Nakamoto, T. Takahashi, T. Hamada, E. Shibamura, M. Miyajima, K. Masuda and T. Doke, Phys. Rev. B **17** (1978) no.6, 2762-2765 doi:10.1103/PhysRevB.17.2762

[105] G. Jaffe Ann. der. Phys. 42, 303 (1913)

[106] D. R. Nygren, eConf **C740805** (1974), 58 PEP-0144.

[107] G. Charpak, R. Bouclier, T. Bressani, J. Favier and C. Zupancic, Nucl. Instrum. Meth. **62** (1968), 262-268 doi:10.1016/0029-554X(68)90371-6

[108] C. Rubbia, CERN-EP-INT-77-08.

[109] B. Abi *et al.* [DUNE], [arXiv:1807.10334 [physics.ins-det]].

[110] B. Abi *et al.* [DUNE], [arXiv:2007.06722 [physics.ins-det]].

[111] J. P. Brodsky, doi:10.2172/1212164

[112] R. Acciarri *et al.* [WArP], JINST **5** (2010), P06003 doi:10.1088/1748-0221/5/06/P06003 [arXiv:0804.1217 [nucl-ex]].

[113] R. Acciarri *et al.* [WArP], JINST **5** (2010), P05003 doi:10.1088/1748-0221/5/05/P05003 [arXiv:0804.1222 [nucl-ex]].

[114] J. Calvo *et al.* [ArDM], Astropart. Phys. **97** (2018), 186-196 doi:10.1016/j.astropartphys.2017.11.009 [arXiv:1611.02481 [astro-ph.IM]].

[115] D. W. Swan, Proc. Phys. Soc. **82** (1963), 74-84 doi:10.1088/0370-1328/82/1/310

[116] E. Buckley *et al.* Nucl. Instrum. Meth. A **275** (1989), 364-372 doi:10.1016/0168-9002(89)90710-9

[117] W. Walkowiak, Nucl. Instrum. Meth. A **449** (2000), 288-294 doi:10.1016/S0168-9002(99)01301-7

[118] Y. Li *et al.* Nucl. Instrum. Meth. A **816** (2016), 160-170 doi:10.1016/j.nima.2016.01.094 [arXiv:1508.07059 [physics.ins-det]].

[119] S. Cova, M. Ghioni, A. Lacaita, C. Samori, and F. Zappa, Appl. Opt. 35, 1956-1976 (1996)

[120] F. Acerbi and S. Gundacker, Nucl. Instrum. Meth. A **926** (2019), 16-35 doi:10.1016/j.nima.2018.11.118

[121] D. Renker Nucl. Instrum. Meth. A 571 (2007) 1-6.

[122] M. D'Incecco, C. Galbiati, G. K. Giovanetti, G. Korga, X. Li, A. Mandarano, A. Razeto, D. Sablone and C. Savarese, IEEE Trans. Nucl. Sci. **65** (2017) no.1, 591-596 doi:10.1109/TNS.2017.2774779 [arXiv:1706.04220 [physics.ins-det]].

[123] R. Madden, L. Canfield, and G. Hass, J. Opt. Soc. Am. 53, 620-625 (1963). doi:10.1364/JOSA.53.000620

[124] Monica Fernandez-Perea, Juan I. Larruquert, Jose A. Aznarez, Alicia Pons, and Jose A. Mendez, Appl. Opt. 46, 4871-4878 (2007) doi:10.1364/AO.46.004871

[125] C. Silva, J. Pinto da Cunha, A. Pereira, V. Chepel, M. I. Lopes, V. Solovov and F. Neves, J. Appl. Phys. **107** (2010), 064902 doi:10.1063/1.3318681 [arXiv:0910.1056 [physics.ins-det]].

[126] C. Benson, G.D. Orebi Gann and V. Gehman , Eur. Phys. J. C **78**, 329 (2018) https://doi.org/10.1140/epjc/s10052-018-5807-z

[127] B. J. P. Jones, J. K. VanGemert, J. M. Conrad and A. Pla-Dalmau, JINST **8** (2013), P01013 doi:10.1088/1748-0221/8/01/P01013 [arXiv:1211.7150 [physics.ins-det]].

[128] M. Kuźniak, B. Broerman, T. Pollmann and G. R. Araujo, Eur. Phys. J. C **79** (2019) no.4, 291 doi:10.1140/epjc/s10052-019-6810-8 [arXiv:1806.04020 [physics.ins-det]].

[129] J. Strait *et al.* [DUNE], [arXiv:1601.05823 [physics.ins-det]].

[130] Heraeus Deutschland GmbH Co. KG, CleviosTM PEDOT, (2021) https://www.heraeus.com/media/media/hec/documents_hec/brochures_en/CLEVIOS_FL_Innovate.pdf.

[131] E. Aprile *et al.* [XENON100], Phys. Rev. D **84** (2011), 052003 doi:10.1103/PhysRevD.84.052003 [arXiv:1103.0303 [hep-ex]].

[132] P. Agnes *et al.* [DarkSide], [arXiv:2101.08686 [physics.ins-det]].

[133] P. A. Amaudruz *et al.* [DEAP-3600], Phys. Rev. Lett. **121** (2018) no.7, 071801 doi:10.1103/PhysRevLett.121.071801 [arXiv:1707.08042 [astro-ph.CO]].

[134] P. Agnes *et al.* [DarkSide], Phys. Rev. D **98** (2018) no.10, 102006 doi:10.1103/PhysRevD.98.102006 [arXiv:1802.07198 [astro-ph.CO]].

[135] P. Agnes *et al.* [DarkSide], Phys. Rev. Lett. **121** (2018) no.11, 111303 doi:10.1103/PhysRevLett.121.111303 [arXiv:1802.06998 [astro-ph.CO]].

[136] J. Calvo *et al.* [ArDM], JCAP **03** (2017), 003 doi:10.1088/1475-7516/2017/03/003 [arXiv:1612.06375 [physics.ins-det]].

[137] P. A. Amaudruz *et al.* Astropart. Phys. **62** (2015), 178-194 doi:10.1016/j.astropartphys.2014.09.006 [arXiv:1211.0909 [astro-ph.IM]].

[138] A. Langenkämper *et al.* Nucl. Instrum. Meth. A **884** (2018), 40-44 doi:10.1016/j.nima.2017.11.054 [arXiv:1703.07152 [astro-ph.IM]].

[139] T. Alexander *et al.* [arXiv:1901.10108 [physics.ins-det]].

[140] F. Acerbi *et al.* IEEE Trans. Electron. Dev. **64** no.2, 521-526 doi:10.1109/TED.2016.2641586 [arXiv:1610.01915 [physics.ins-det]].

[141] M. D'Incecco, C. Galbiati, G. K. Giovanetti, G. Korga, X. Li, A. Mandarano, A. Razeto, D. Sablone and C. Savarese, IEEE Trans. Nucl. Sci. **65** (2018) no.4, 1005-1011 doi:10.1109/TNS.2018.2799325 [arXiv:1706.04213 [physics.ins-det]].

[142] W. H. Lippincott, S. B. Cahn, D. Gastler, L. W. Kastens, E. Kearns, D. N. McKinsey and J. A. Nikkel, Phys. Rev. C **81** (2010), 045803 doi:10.1103/PhysRevC.81.045803 [arXiv:0911.5453 [astro-ph.IM]].

[143] J. Allison *et al.* IEEE Trans. Nucl. Sci. **53** (2006), 270 doi:10.1109/TNS.2006.869826

[144] P. Agnes *et al.* [DarkSide], JINST **12** (2017) no.10, P10015 doi:10.1088/1748-0221/12/10/P10015 [arXiv:1707.05630 [physics.ins-det]].

[145] J. Calvo *et al.* [ArDM], JCAP **12** (2018), 011 doi:10.1088/1475-7516/2018/12/011 [arXiv:1712.01932 [physics.ins-det]].

[146] D. M. Mei, Z. B. Yin, L. C. Stonehill and A. Hime, Astropart. Phys. **30** (2008), 12-17 doi:10.1016/j.astropartphys.2008.06.001 [arXiv:0712.2470 [nucl-ex]].

[147] https://encyclopedia.airliquide.com/nitrogen.

[148] J. P. Peiffer, 2007

[149] F. Padera, C. Lynch, Field Application Report, UV/Vis/NIR spectroscopy (2019)

[150] XENON colalboration, E. Aprile et al., Phys. Rev. Lett. **121** (2018) no.11, 111302.

[151] DUNE collaboration, B. Abi et al., [arXiv:1706.07081 [physics.ins-det]].

[152] DUNE collaboration, [arXiv:1910.06422 [physics.ins-det]].

[153] DEAP collaboration, P. Adhikari et al., Eur. Phys. J. C **80** (2020) no.4, 303.

[154] ArDM collaobration, J. Calvo et al., JCAP **12** (2018), 011.

[155] E. Robert, A. Khacef, C. Cachoncinlle, J. M. Pouvesle, Opt. Comm. **117** (1995), 179.

[156] H. A. Koehler, L. J. Ferderber, D. L. Redhead and P. J. Ebert, Phys. Rev. A **9** (1974), 768.

[157] R. Sauerbrey, F. Emmert and H. Langhoff, J. Phys. B **17** (1984), 2057.

[158] G. S. Hurst, T. E. Bortner and T. D. Strickler, Phys. Rev. **178** (1969), 4.

[159] A. Ulrich, et al, J. Appl. Phys. **62** (1987), 357.

[160] J. Wieser, A. Ulrich, A. Fedenev, M. Salvermoser, Opt. Comm. **173** (2000), 233.

[161] G. Klein, M. J. Carvalho, J. Phys. B: At. Mol. Phys. **14** (1981), 1283.

[162] A. Birot, H. Brunet, J. Galy, P. Millet, and J. L. Teyssier, J. Chem. Phys. **63** (1975), 1469.

[163] M. Suzuki, J. Ruan and S. Kubota, Nucl. Instr. and Meth. **192** (1982), 565.

[164] C. D. R. Azevedo, D. González-Díaz, S. F. Biagi, C. A. B. Oliveira, Nucl. Inst. and Meth. A **877** (2018), 157.

[165] T. Robert Connor and M. Biondi, Phys. Rev. **150** (1965), A778.

[166] L. Frommhold and M. A. Biondi, Phys. Rev. **185** (1969), 244.

[167] M. Suzuki, J. Ruan and S. Kubota, Nucl. Instr. and Meth. **192** (1982), 623.

[168] K. Saito, H. Tawara, T. Sanami, E. Shibamura, and S. Sasaki, IEEE Trans. Nucl. Sci, **49** (2002), 4.

[169] H. Langhoff, Optics communications **68** (1988), 1.

[170] A. Boichenko, V. Tarasenko, S. Yakovlenko, Proc. SPIE. **4071**, International Conference on Atomic and Molecular Pulsed Lasers III.

[171] https://www.hamamatsu.com/resources/pdf/etd/R7378A_TPMH1288E.pdf.

[172] https://www.hamamatsu.com/resources/pdf/etd/R6835_TPMH1263E.pdf.

[173] https://www.thorlabs.com/NewGroupPage9.cfm?ObjectGroup_ID=3982.

[174] https://www.asahi-spectra.com/opticalfilters/detail.asp?key=XUL0250.

[175] M. Akashi-Ronquest et al., Eur. Phys. J. A **55** (2019) no.10, 176.

[176] C. Amsler, V. Boccone, A. Buchler, R. Chandrasekharan, C. Regenfus and J. Rochet, JINST **3** (2008), P02001.

[177] J. W. Keto, R. E. Gleason Jr., and G. K. Walters, Phys. Rev. Lett. **33** (1974), 1365.

[178] R. Acciarri et al., *JINST* **8** (2013).

[179] G. Jaffe, *Ann. Phys.* **58** (1940) pg. 968.

[180] T.H. Dey, T.J. Lewis, J. Phys. D: Applied Physics, vol. 1, n 8, p 1019, (1968).

[181] M. Torti EPJ Web of Conferences **126**, 05013 (2016)

[182] http://atlas.web.cern.ch/Atlas/GROUPS/LIQARGEXT/TDR/html.1812/LARG-TDR-690.html

[183] L. Romero, R. Santorelli, B. Montes, *Astropart.Phys.* **92** (2017) pg. 11-20.

[184] P. Benetti *et al.* [WARP Collaboration], Nucl. Instrum. Meth. A **574,** 83 (2007) [astro-ph/0603131].

[185] R. Santorelli et al., Published in *JINST* **13** (2018) no.04, C04015

[186] https://indico.in2p3.fr/event/19093/contributions/71453/attachments/53086/68943/DART_in_ArDM_TDR-6.pdf

https://www.nist.gov/pml/stopping-power-range-tables-electrons-protons-and-hel

[187] J. Kostensalo, J. Suhonen and K. Zuber, J. Phys. G **45** (2018) no.2, 025202 doi:10.1088/1361-6471/aa958e [arXiv:1705.05726 [nucl-th]].

[188] C. Cantini, L. Epprecht, A. Gendotti, S. Horikawa, L. Periale, S. Murphy, G. Natterer, C. Regenfus, F. Resnati and F. Sergiampietri, *et al.* JINST **10** (2015) no.03, P03017 doi:10.1088/1748-0221/10/03/P03017 [arXiv:1412.4402 [physics.ins-det]].

[189] COMSOL Multiphysics® v. 5.3. www.comsol.com. COMSOL AB, Stockholm, Sweden.

[190] L. Colli, U. Fachinni, Review of Scientific Instruments, Vol. 23, 1, 1951